Gas and Dust in Galactic Planetary Nebulae at Sub-Solar Metallicity

Thesis

Gas and dust in Galactic planetary nebulae at sub-solar metallicity

George James Steven Pagomenos

School of Physical Sciences, Faculty of STEM

The Open University

This thesis is submitted for the degree of

Doctor of Philosophy

August 2018

Abstract

Planetary nebulae are the final phases of evolution for low- to intermediate-mass stars ($\sim$ 0.8–8 $M_{\odot}$). They consist of a central star surrounded predominantly by a circumstellar envelope containing the products of nuclear processing, and a photodissociation region containing dust and molecules. These include silicates and large organic molecules such as polycyclic aromatic hydrocarbons (PAHs), which are ubiquitous throughout the Universe, and fullerenes, which are the largest molecules to be firmly detected in space. All of this material coasts away from the central star, causing enrichment of the interstellar medium.

Although there have been significant advances in studies of this circumstellar material, we still do not fully understand how the metallicity (i.e. the abundance of elements heavier than helium) of the local environment affects the dust composition around these stars, or the processes that govern the formation and evolution of these large organic molecules.

This thesis presents a series of studies in which the abundances and dust composition around planetary nebulae are characterised in the low metallicity regions of the Milky Way, with use of data from the *Spitzer Space Telescope* and *SOFIA*. These include investigations into the metallicity and dust content of planetary nebulae in the outer thin disk and the halo of the Galaxy, and the physical conditions in which large organic molecules form.

I find that the outer regions of the Galactic disk have a lower metallicity than the solar neighbourhood, and that regions of low metallicity favour carbon-rich dust production over oxygen-rich dust (i.e. silicates), except for within the Galactic halo. These regions show a greater diversity of carbonaceous material than observed towards the Galactic bulge and in the solar neighbourhood. Fullerenes are preferentially formed in environments with low hydrogen density.

Acknowledgements

Firstly, I could not have been able to chase my dream of being a scientist if it wasn't for my family. In particular, I would like to thank Mum, Dad, Gran, Mike, Yiayia, Pappou, Isabel, Tony, Nick and Chris for all their love and support over the years.

I am incredibly fortunate to have worked with my two supervisors, Jeronimo Bernard-Salas and Helen Fraser. Jeronimo, thank you for providing me with the incredible opportunity to carry out this research, and with another to get involved with the *JWST* Evolved Stars working group. You have always pushed me to strive to do better, and your support and patience has always been appreciated. Helen, thank you for keeping me on track, and for providing a positive outlook when I needed perspective. You have both been amazing.

To everyone else with whom I have collaborated, namely Jan Cami, Els Peeters, Greg Sloan, Albert Zijlstra and the late Stuart Pottasch: thank you for everything, it has genuinely been wonderful working with all of you. I would also like to thank Maria Lugaro and Carolyn Doherty for inviting me to give a seminar talk at the Konkoly Observatory, Harriet Dinerstein for the inspiring scientific conversations, all members of the Astrochemistry Group and Astronomy Journal Club at the Open University with whom I have been able to share ideas, Geoff Bradshaw for the IT assistance, and Stephen Serjeant, Nicolas Peretto and Judith Croston for reading this thesis and assessing my viva.

Thanks to Philip, for being like a brother; Kieran, for the wine evenings and the conversations in which we set the world to rights; Jack and Tania, for hosting us in Japan for the week; Laura and David, for helping me take the next steps in my career and generally being awesome people; Lawrence, Ashley and Paul for being brilliant flatmates; everyone in the DPS House Band; the Goat Army (you know who you are); Rachel, Mark, Helen and

Graham for the semi-regular chats over coffees; and the rest of the “DeanSoc” crew: Dean, Joe, Meredith, Heidi, Aaron and Andy. Thanks also to Helen, Amit, Dan, Catherine, Natalia, Olivier, Paul, Pam, Calum, James, Jana, Ayo, Brendan, Maria, Vincent, Pete, Rhian, Amy, George, Aleksi, Sabrina, Feargus, Tom, Candice, Matt, Anton, Yasmin, Mike, Joe, Chris, Joanna and Alex; and anyone else who has been an essential component of my past few years but I have regrettably forgotten to mention here.

And last but certainly not least, I wish to thank my partner of almost seven years, Anastasia. I am so lucky to have you in my life.

Table of contents

List of figures

List of tables

Chapter 1

Introduction

Stars of $\sim$ 0.8–8 solar masses ($M_{\odot}$) will evolve to become planetary nebulae (PNe, singular PN). Over the course of their evolution, these stars produce circumstellar dust and ionised gas, which are ejected into the interstellar medium (ISM) by stellar winds. The chemical composition of this ejected material is of particular interest; spectral lines of gaseous species can be used to infer the physical conditions and abundances of these PNe, whereas studies have shown that there may be a relationship between the dust composition and the metallicity (i.e. the abundance of elements heavier than helium) of the region in which the stars formed and evolved.

In this thesis, I present four spectroscopic studies of PNe in regions of the Milky Way that are either known or *a priori* assumed to be of low metallicity, in order to address the following major questions:

- How does metallicity influence dust composition?
- How diverse is the chemistry of large organic molecules in circumstellar environments?

These questions will be addressed by analysing the metallicity and dust content of PNe in the outer regions of the Milky Way and the Galactic halo, with some emphasis on a select few sources with unusual dust emission. But first, it is important to understand the fundamental physics and chemistry required for these studies.

1.1 Low- to intermediate-mass stellar evolution

This section explains the main physical and chemical processes experienced within a star of $\sim$ 0.8–8 $M_{\odot}$ as they evolve into PNe.

1.1.1 The life cycle of a star

All stars begin their lives as clouds of gas and dust accreted from the ISM. When regions of these dark molecular clouds contain enough mass, they gravitationally contract upon themselves to form protostars. This contraction causes hydrogen to burn in the core, at which point the star enters the evolutionary phase known as the Main Sequence, as shown by the Hertzsprung-Russell diagram in Figure 1.1. Onion shell diagrams of the main nucleosynthesis

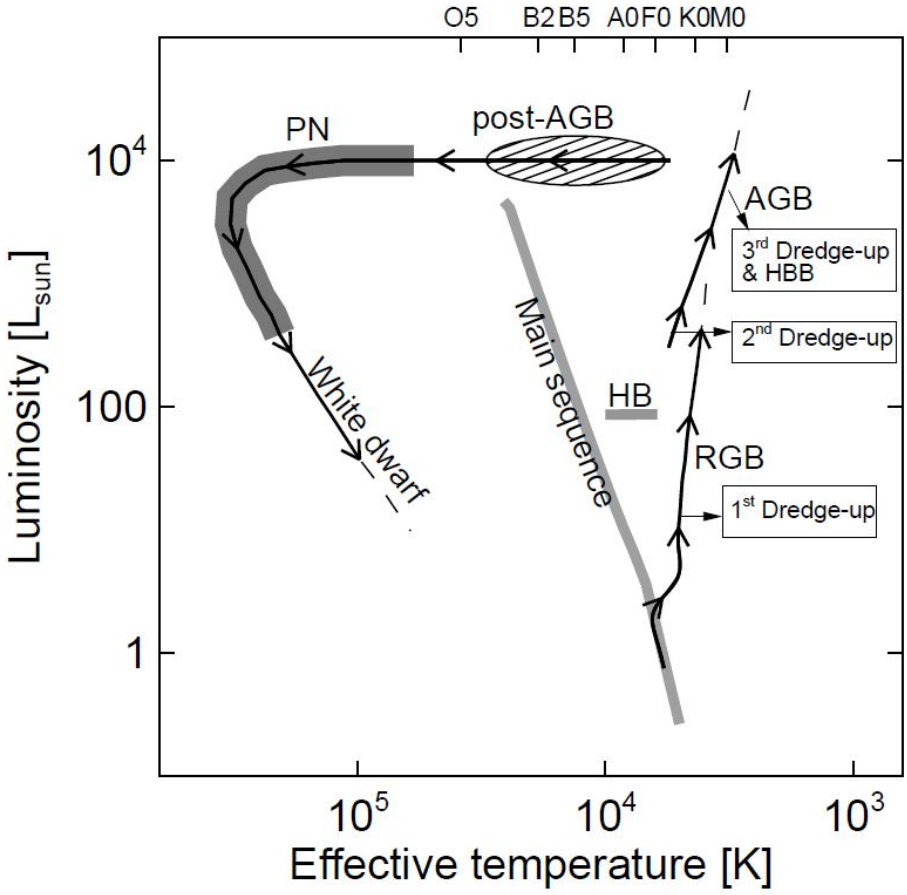

Fig. 1.1 Hertzsprung-Russell diagram showing the evolution of a low- to intermediate-mass star of $\sim$ 0.8–8 $M_{\odot}$. HB = horizontal branch, RGB = red giant branch, AGB = asymptotic giant branch, HBB = hot-bottom burning, PN = planetary nebula. (Bernard-Salas 2003, S. Hony & J. Bernard-Salas).

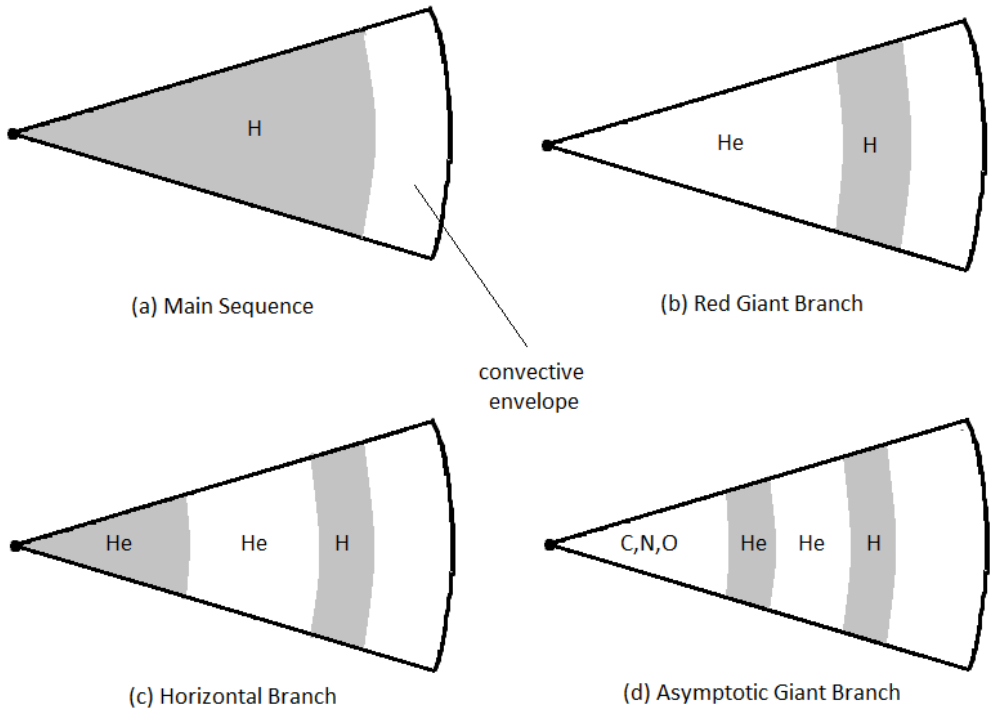

Fig. 1.2 Onion-shell diagrams of stars from the Main Sequence up to the AGB stages of evolution, with the stellar core on the left-hand side. Grey regions show that the indicated element is burning. The outer regions represent the convective envelopes of the stars. The widths of the regions are not to scale.

processes in Main Sequence stars and in the succeeding stages of evolution are shown in Figure 1.2 (see also Bernard-Salas 2003 and Ryan and Norton 2010).

The core hydrogen burning occurs through the proton-proton chain ('pp-chain'):

$$\begin{aligned} {}^1\mathrm{H} + {}^1\mathrm{H} &\longrightarrow {}^2\mathrm{H} + e^+ + \nu_e + 2\gamma \\ {}^2\mathrm{H} + {}^1\mathrm{H} &\longrightarrow {}^3\mathrm{He} \\ {}^3\mathrm{He} + {}^3\mathrm{He} &\longrightarrow {}^4\mathrm{He} + {}^1\mathrm{H} + {}^1\mathrm{H} \end{aligned} \tag{1.1}$$

The first step of this mechanism takes $\sim 10^9$ years, due to beta decay (in this case, ${}^2\mathrm{He} \longrightarrow {}^2\mathrm{H} + e^+ + \nu_e$) relying on the weak interaction. Hence, the main sequence is a relatively long-lived, stable phase of evolution. However, if there are a sufficient number of carbon atoms either from the ISM or formed from the triple-alpha (3α) process:

$$3 \times {}^4\mathrm{He} \longrightarrow {}^{12}\mathrm{C} \tag{1.2}$$

then these can be used as catalysts for the CNO-cycle, which is a quicker mechanism for burning hydrogen ($\sim 10^7$ years):

$$\begin{aligned} {}^{12}\mathrm{C} + {}^{1}\mathrm{H} &\longrightarrow {}^{13}\mathrm{C} + e^{+} + \nu_e + 2\gamma \\ {}^{13}\mathrm{C} + {}^{1}\mathrm{H} &\longrightarrow {}^{14}\mathrm{N} \\ {}^{14}\mathrm{N} + {}^{1}\mathrm{H} &\longrightarrow {}^{15}\mathrm{N} + e^{+} + \nu_e + 2\gamma \\ {}^{15}\mathrm{N} + {}^{1}\mathrm{H} &\longrightarrow {}^{12}\mathrm{C} + {}^{4}\mathrm{He} \end{aligned} \tag{1.3}$$

After around 10 billion years, the hydrogen in the core burns out and stable helium becomes the main core constituent. At this stage, the star is on the Red Giant Branch (RGB). Over time, the stellar temperature will become hot enough for the helium in the core to ignite, at which point the star enters the horizontal branch (HB). In this stage, there is a region of unburnt helium surrounding the core, as well as a hydrogen-burning shell. The HB is relatively short-lived ($\sim 10^8$ years), during which time the core helium fuses together to form carbon, as per equation (1.2). Once the core helium burning has exhausted, the star is on the Asymptotic Giant Branch (AGB).

While on the AGB, carbon and oxygen can be used in the formation of dust in the stellar envelope. Heavier elements can be formed through the slow neutron-capture process ("*s*-process"):

$$\begin{aligned} {}^{13}\mathrm{C} + {}^{4}\mathrm{He} &\longrightarrow {}^{16}\mathrm{O} + n \\ {}^{22}\mathrm{Ne} + {}^{4}\mathrm{He} &\longrightarrow {}^{25}\mathrm{Mg} + n \end{aligned} \tag{1.4}$$

Elements heavier than oxygen are not readily formed during the AGB evolutionary phase, but are instead likely to have originated from the outflows of high-mass stars (e.g. explosions of supernovae). These elements are typically formed from the addition of a helium atom, hence even-numbered elements up to iron are readily observed in spectra of evolved low- to intermediate-mass stars.

The AGB phase of evolution is terminated by a so-called "super-wind" reaching mass-loss rates as high as $\sim 10^{-4}\ M_{\odot}\ \mathrm{yr}^{-1}$ (e.g. Marshall et al. 2004; van Loon et al. 1999, 2003),

which eventually ejects enough of the material in the convective envelope for the central white dwarf star to become exposed and ionise this ejecta. At this point, the star becomes a planetary nebula.

The ejected gas and dust enriches the ISM, at which point they may be accreted into molecular clouds, assisting in their gravitational contraction and eventually leading to the formation of new stars.

1.1.2 Mixing episodes

Over the course of its evolution, a star will experience a series of convective mixing episodes known as 'dredge-ups', in which the various changes in temperature and pressure of the stellar cores cause the chemical material in the outer envelope of the star to penetrate further inwards, resulting in different elements being brought up to the surface. These main nucleosynthetic and convective mixing events alter the surface composition of a low- to intermediate-mass star over the course of its evolution. There are three dredge-up episodes; the first of these occurs on the RGB, the other two on the AGB.

The *first dredge-up* occurs as the convective envelope contracts towards the core, allowing products of the CN-cycle to be brought up to the surface. This results in the net abundances of ^{13}C and ^{14}N increasing at the expense of ^{12}C and hydrogen.

The *second dredge-up* can occur for stars on the AGB if their initial mass is $\gtrsim 4$ M$_\odot$ (Becker and Iben, 1979). The cores of stars with mass $\gtrsim 2.5$ M$_\odot$ will expand due to the production of the helium burning shell from the HB. However, the envelope will be contracting for stars $\lesssim 4$ M$_\odot$ through to the core as the hydrogen burning shell may have temporarily stopped. This leads to isotopes formed from the CNO-cycle being brought up to the stellar surface through convection, where the abundances of ^{4}He and ^{14}N increase and those of ^{12}C, ^{13}C and ^{16}O decrease.

The *third dredge-up* also occurs in the AGB phase. This is where instability causes a thermal pulse to occur outwards from the helium burning shell, allowing some ^{12}C, ^{16}O and ^{4}He to enter the area between the helium- and hydrogen-burning shells (see Figure 1.2). The

star then expands, causing it to cool. The hydrogen-burning shell is temporarily deactivated and the convective envelope can access the inner regions of the star, causing carbon, helium and a small amount of oxygen to enter the convective envelope. This can alter the carbon-to-oxygen (C/O) ratio of the star.

While not strictly a 'dredge-up' episode, a process known as *hot-bottom burning* can also occur during the AGB phase in stars of mass $\gtrsim 4$ $M_{\odot}$. During this process, the base of the convective envelope becomes heated by the hydrogen-burning shell, allowing for the CNO-cycle to occur (Delgado-Inglada et al., 2015; Karakas and Lattanzio, 2014). This causes the abundances of ^{12}C and ^{16}O to decrease in favour of ^{14}N.

Indeed, the abundances of carbon and oxygen are of particular interest in this thesis, as the C/O ratio governs the overall dust composition around a planetary nebula. The next section explains more about the roles of dust, and the molecules and spectral features associated with its emission.

1.2 Dust

Direct evidence for the existence of interstellar dust was first documented in a publication by Trumpler (1930), who concluded that there must have been "a considerable amount of finely divided matter" in a study of the absorption of light in the Milky Way. It has since been detected at redshifts of $z > 7$, corresponding to its presence approximately 740 Myr after the Big Bang (Venemans et al., 2012). It is the main source of opacity for non-ionising radiation, meaning that the spectral energy distribution of anything longer than 912 Å (the Lyman limit, corresponding to an energy value of 13.6 eV) is likely to be affected by dust (Tielens, 2005).

Despite contributing only 1% of the mass of the ISM (the other 99% coming from gas), dust is ubiquitous throughout the Universe. It is primarily produced in stars that lose large proportions of their mass during the course of their evolution, such as AGB stars and core-collapse supernovae (SNe) (e.g. Crowther 2007; Zhukovska and Henning 2013). There have been questions as to whether AGB stars and SNe are the main contributors of dust in the

ISM, as Wolf-Rayet stars (Gehrz, 1989) and red supergiants (Verhoelst et al., 2009) may also contribute.

Dust plays important roles in the ISM by acting as a catalytic surface for the formation of icy molecules such as H_2 (Gould and Salpeter, 1963) and reprocessing light from ultraviolet (UV) to infrared (IR) wavelengths (Cardiel et al., 2003; Li, 2009). Indeed, most of the emission from dust is observed at IR wavelengths.

The chemical composition of dust produced by AGB stars is defined by the C/O ratio; if C/O < 1, the source is oxygen-rich (O-rich), otherwise it is carbon-rich (C-rich). As the ISM has a greater abundance of oxygen than carbon, all stars begin as O-rich sources. These sources can become C-rich if the third dredge-up can efficiently bring enough carbon to their circumstellar envelopes. Carbon and oxygen in the stellar envelope will preferentially react with each other to form the stable and abundant carbon monoxide (CO) molecule. When one of these elements becomes depleted, the other reacts with other chemical species to form C-rich or O-rich dust (Lattanzio and Wood, 2003; Sloan et al., 2006). In metal-poor environments, less carbon needs to be dredged up to the stellar surface in order to exceed the amount of oxygen, resulting in there being more C-rich sources in regions of low metallicity.

In this thesis, we analyse the composition of circumstellar dust around Galactic PNe in environments of low metallicity. This section explains the different types of dust compositions observed at mid-IR wavelengths. The spectral features of many of these dust species are shown; the reader is referred to Chapter 2 for an explanation of the physics behind spectroscopy.

1.2.1 Carbon-rich dust

Infrared spectra of PNe display a wealth of carbon-rich dust emission, including large carbonaceous species such as polycyclic aromatic hydrocarbons (PAHs) and fullerenes (e.g. C_{60}, C_{70}). Other features, such as the so-called '30 μm feature' and the broad feature centered at 11 μm that is often attributed to silicon carbide (SiC), are regularly observed. The main C-rich dust features are described below.

Polycyclic aromatic hydrocarbons (PAHs)

PAHs are ubiquitous throughout the Universe and have been detected spectroscopically at redshifts z $\sim$ 2.8, which indicates their presence $\sim$ 3 Gyr after the Big Bang (Lutz et al., 2008). In evolved low- to intermediate-mass stars, the main PAH emission features are observed at 3.3, 6.2, 7.7, 8.6, 11.3 and 12.8 μm. Each of these come from the bending and stretching of different C$-$C and C$-$H bonds within the molecule (see Figure 1.3).

PAH features vary in profile, peak wavelengths and relative strength. Peeters et al. (2002) produced a classification system for these different profiles using *ISO* data, as shown in Figure 1.4. In particular, it was found that class *A* features correspond to H II regions and very hot, massive stars (particularly Harvard spectral types O and B), class *B* features from PNe and intermediate-mass stars, and class *C* features (peaking at the highest wavelengths)

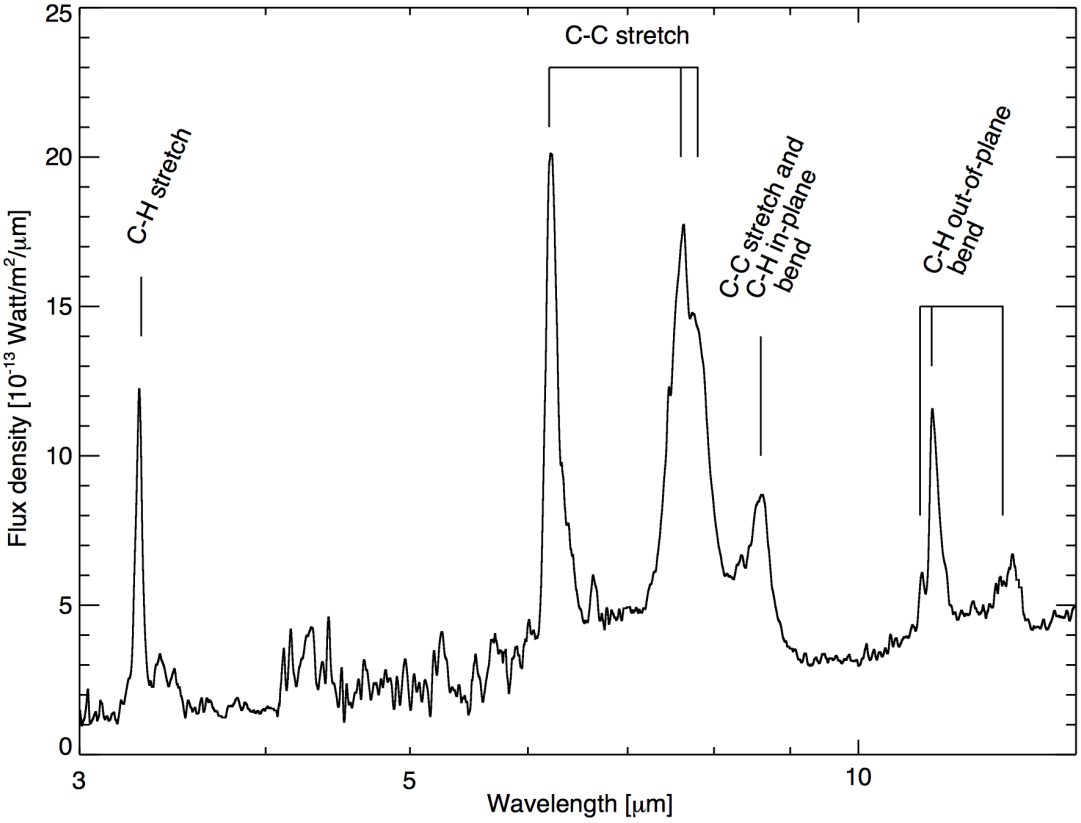

Fig. 1.3 A spectrum of a massive star forming region with atomic lines removed to emphasise the PAH features. The individual contributions of the hydrocarbons to each peak are shown. Figure reproduced from Peeters (2002).

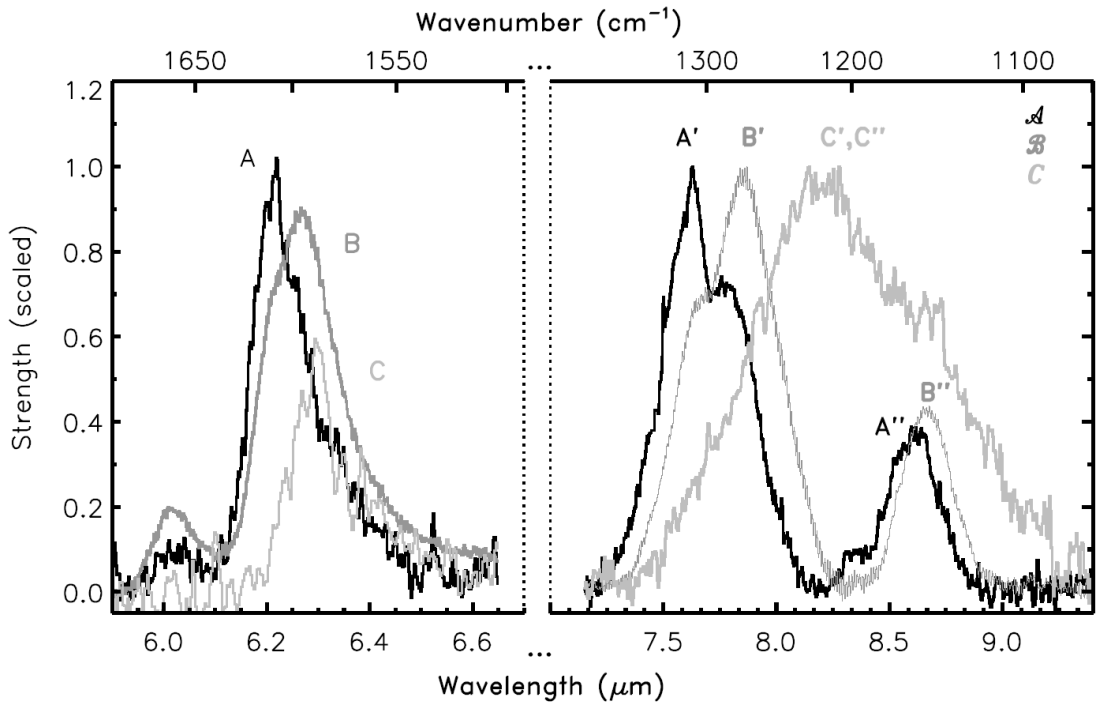

Fig. 1.4 The earliest PAH classification system within the range 6–9 μm, including the 6.2 μm (A, B, C), 7.7 μm (A', B', C') and 8.6 μm (A'', B'', C'') features. Figure reproduced from Peeters et al. (2002).

primarily from post-AGB stars. Matsuura et al. (2014) have since extended this classification system from a study of post-AGB stars and PNe in the Large Magellanic Cloud with the *Spitzer Space Telescope*. They introduce a class *D* for sources with one broad feature spanning from $\sim$ 7–9 μm, as well as a new system for PAH features from 10–14 μm.

While only two sources of Class *C* emission were detected in the work of Peeters et al. (2002), the study by Sloan et al. (2007) detected five more sources, including red giants. They proposed a relationship between the peak position of the Class *C* PAH feature with the effective temperature of the source. They also suggested that this emission class is consistent with a mixture of aliphatic (i.e. the atoms are bonded in a chain-like structure) and aromatic (i.e. the atoms form a ring) compounds known as hydrogenated amorphous carbon (HAC), which evolves with heat to become aromatised (PAHs). Carpentier et al. (2012) have also shown from a laboratory study that Class *C* PAH emission can evolve with heat into Class *A* emission.

PAH emission features within the 15–20 μm wavelength range has been attributed to C–C–C stretches (e.g. Boersma et al. 2010; Shannon et al. 2015). These are particularly weak in spectra of PNe.

Silicon carbide

There is a broad feature spanning from $\sim$ 9–13 μm, which peaks around 11 μm (see Figure 1.5). This is typically characterised as SiC emission, though this identification is still under debate. This feature is rarely observed in Galactic PNe; $\sim$ 30 of these sources have been found (Casassus et al., 2001a,b) out of a total of $\gtrsim$ 1100 Galactic PNe, although it is more frequently observed in Galactic AGB stars (e.g. Bernard-Salas et al. 2009). Hence, there may be a relationship between low metallicity regions and the presence of this feature. Studies of carbon stars and PNe from the Magellanic Clouds, which are metal-poor relative to the Sun, have shown that SiC emission is relatively common in these regions (e.g. Bernard-Salas et al. 2009; Sloan et al. 2006, 2014, reinforcing the concept of a link between the metallicity of the local environment and the detection of SiC emission.

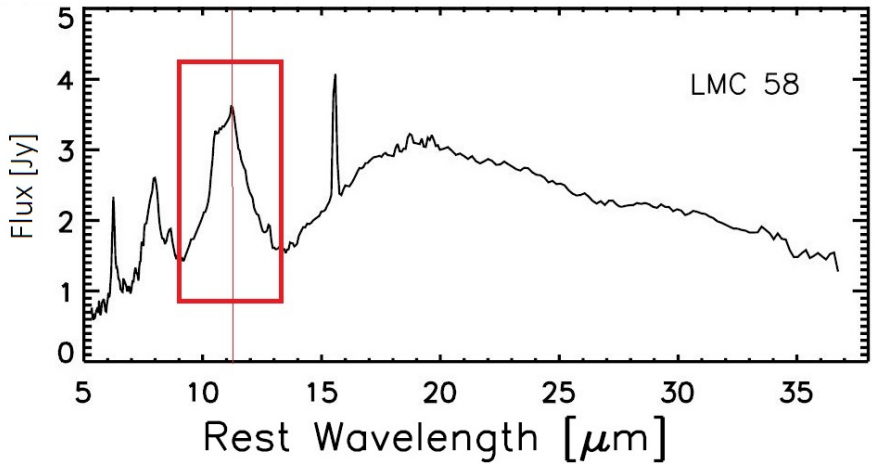

Fig. 1.5 The *Spitzer Space Telescope* IRS low-resolution spectrum for SMP LMC 58. The broad SiC feature is inside the box. The line coming through the peak of the SiC feature at about 11.3 μm has been added to show the presence of a PAH feature at this wavelength. Figure amended from Bernard-Salas et al. (2009).

Fullerenes

Discovered from laboratory experiments by Kroto et al. (1985), fullerenes are spheroidal or ellipsoidal molecular cage structures consisting solely of carbon atoms. Buckminsterfullerene (C_{60}) has 174 vibrational modes ($3N - 6$ degrees of freedom, N = number of atoms in the structure = 60), though only four are active at IR wavelengths (Nemes and Jelski, 2012), specifically at 7.0, 8.5, 17.4 and 18.9 μm (e.g. Bernard-Salas et al. 2012; Otsuka et al. 2014). They were discovered in the Galactic PN Tc 1 by Cami et al. (2010), and are currently the largest molecules that have been firmly indentified both in circumstellar and interstellar media. However, the mechanisms behind fullerene formation in Space are not yet understood (see § 1.4).

Fullerenes have now been observed in many diverse environments, such as YSOs, Herbig Ae/Be stars and post-AGB stars (Roberts et al., 2012). However, they are not common in Galactic PNe. Using the entirety of the *Spitzer* IRS data archives, only $\sim 3\%$ (11 out of 338) of the PNe that have been observed with this spectrograph show the associated emission features (Otsuka et al., 2014).

The C_{60}^{+} ion has now been confirmed as the carrier of four diffuse interstellar bands (DIBs) around 9500 Å (Campbell et al., 2015; Walker et al., 2015). DIBs are absorption features from optical and near-IR stellar spectra for which there have been no confirmed identifications since their first detection by Heger (1922), of which there are now more than 400 (e.g. Spieler et al. 2017; Tielens 2014). Hence, these detections suggest that fullerenes are widespread throughout the ISM and are therefore more common than inferred from Galactic PNe.

Other carbonaceous features

There are also other types of spectral feature that are attributed to carbon-rich dust. In particular, there is a broad '30 μm' feature that can produce as much as 25% of the total energy output of a star (Hony et al., 2002; Hrivnak et al., 2000). This feature spans from $\sim$ 23–45 μm and is sometimes associated with magnesium sulfide (MgS). However, this designation is under debate; Zhang et al. (2009) argued that dust mass of MgS in post-AGB

star HD 56126 needs to be greater in order to account for the power of the feature, though it has also been suggested that the power would be reached if MgS was in thermal contact with SiC and amorphous carbon (Lombaert et al., 2012).

Other less broad features with peaks at ~ 21 μm, ~ 15.8 μm and ~ 17.1 μm (the latter two are always observed together) have only been seen in the presence of the 30 μm feature. Their carriers are unknown, but they are expected to come from hydrocarbons (e.g. Sloan et al. 2014).

Another feature at 3.4 μm is often attributed to HAC (Duley and Williams, 1983), which has been shown from laboratory studies to accurately reproduce the corresponding feature in astronomical spectra (Furton et al., 1999).

1.2.2 Oxygen-rich dust

O-rich dust consists of silicates such as SiO or SiO_2, as well as olivine and forsterite, which contain significant amounts of magnesium. These silicates can be characterised as either amorphous or crystalline depending on their bonding structure.

Crystalline silicates show spectral features at 23.5, 27.5, 33.8, 40 and 60 μm (e.g. Górny et al. 2010; Molster et al. 2002; see Figure 1.6). The chemical bonding in these molecules is relatively organised and rigid. For instance, quartz has a hexagonal bonding structure with silicon on each vertex, where silicon atoms share covalent bonds with three oxygen atoms, and each oxygen atom is bonded to two silicon atoms.

Conversely, the chemical bonding within amorphous silicates is relatively haphazard; while the covalent bond structure between silicon and oxygen atoms remains the same, there is no overall molecular structure. They show spectral features at 9.7 and 18.7 μm, to represent Si$-$O and O$-$Si$-$O bonds respectively (see Figure 1.7).

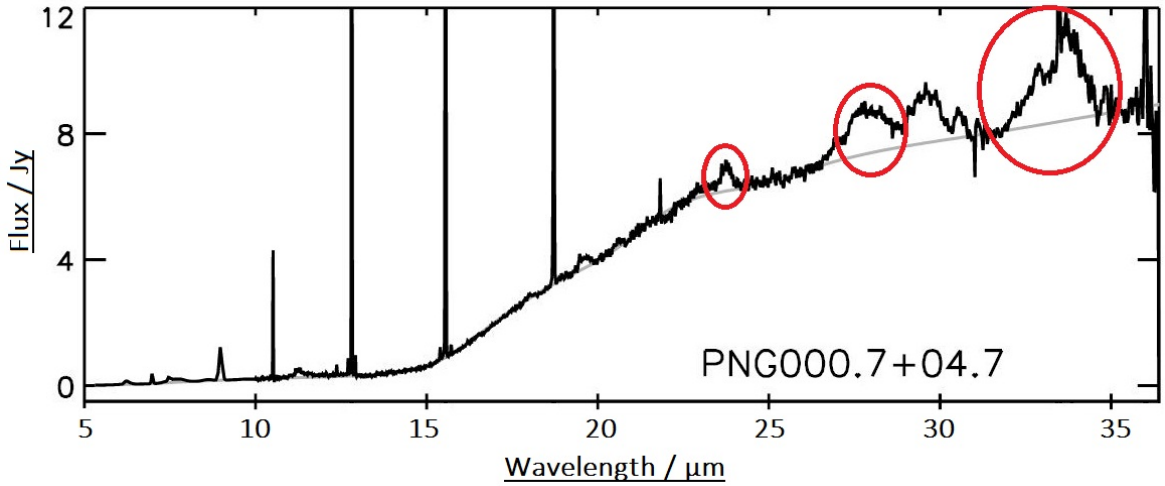

Fig. 1.6 A spectrum of the planetary nebula PNG000.7+04.7, with the crystalline silicate features circled. This was taken from *Spitzer* IRS, in low-resolution below 10 μm and in high-resolution above 10 μm. Figure amended from Gutenkunst et al. (2008).

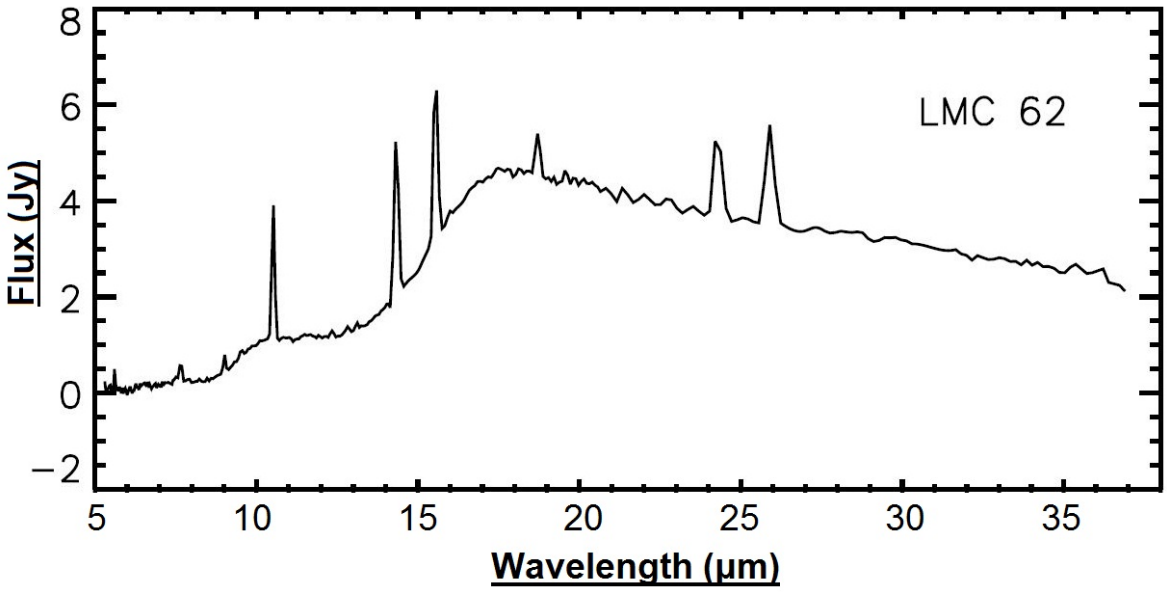

Fig. 1.7 A spectrum of the planetary nebula SMP LMC 62 from the Large Magellanic Cloud as taken with the *Spitzer Space Telescope*. The amorphous silicate features are represented by the plateau centered around 9.7 μm and the broad feature spanning beyond $\sim$ 15 μm but centred at 18.7 μm. Figure amended from Bernard-Salas et al. (2009).

1.2.3 Dual-dust chemistry

In addition to sources with spectra showing O-rich or C-rich dust emission, some PNe show features from both. The reasons for the occurrence of this dual-dust chemistry have not yet been fully established.

Several studies have been carried out on determining the origin of this phenomenon. One suggests that a late thermal pulse from the AGB stage of evolution could have occurred, causing another third dredge-up that could bring forth C-rich dust in an O-rich source (Waters et al., 1998). It has also been proposed that O-rich dust can exist in old, stable disks around post-AGB stars (Zijlstra et al., 1991), held in place through Keplerian motion. These two mechanisms differ significantly over the location of the dust components; the late thermal pulse would imply that the C-rich dust is located far from the star, whereas the O-rich dust disk places the C-rich dust closer to the star. In another study by Guzman-Ramirez et al. (2015), the dual-dust chemistry PN BD $+30^{\circ}$ 3639 was analysed with the *Stratospheric Observatory for Infrared Astronomy* (SOFIA) in order to spatially resolve the main PAH and silicate emission features. They applied radiative transfer models of dust to these observations and suggested that there is a silicate disk on the outer regions of the PN. However, they could not spatially resolve the 33 μm crystalline silicate emission from a particularly high dust continuum in their spectra. Hence, the origin of dual-dust chemistry in PNe requires further investigation.

1.3 Planetary nebulae

The planetary nebula phase of evolution officially commences when all of the material ejected from the convective envelope of the AGB star is ionised. PNe reach temperatures of $\sim 10^5$ K and have lifetimes of $\sim 10^4$ years. Eventually, all of the ionised material enriches the ISM, and the central white dwarf star cools until it becomes a black dwarf.

This section explores the structures of PNe, and explains the physics behind the formation of bow shocks, which may affect the chemical compositions of these stars.

1.3.1 Morphology

Planetary nebulae appear in all shapes and sizes. The morphologies of the ejected gas and dust around these stars have been of interest since Curtis (1918) deduced that they are important in determining their physical conditions. There have since been several classification systems (e.g. Balick 1987; Greig 1971; Stanghellini et al. 1993) in which PNe morphologies have been classed as round, bipolar/butterfly, elliptical/egg-shaped, irregular, etc. Figure 1.8 shows a variety of PNe observed by the *Hubble Space Telescope*, with a large variation of morphologies. Together with the classification system of Peimbert (1978) based on the PN abundances, estimates of the mass of the central stars and the chemical composition of the stellar ejecta can be obtained (Kwitter et al., 2014; Torres-Peimbert and Peimbert, 1997).

There have been several suggested causes for particular morphologies in PNe. One of the most heavily discussed causes in recent years has been the presence of binary star systems with common envelopes (e.g. Akashi and Soker 2017; Bond and Livio 1990; Hillwig et al. 2016;

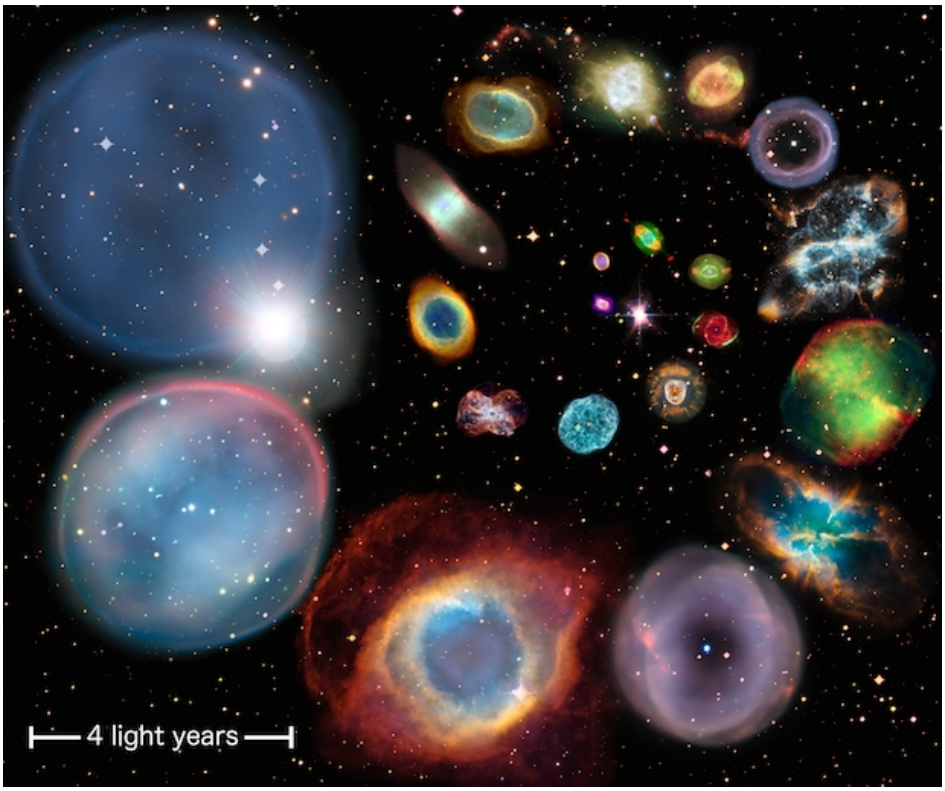

Fig. 1.8 Series of planetary nebulae, ordered by size. (ESA / Hubble / NASA / ESO / I. Bojicic / D. Frew / Q. Parker)

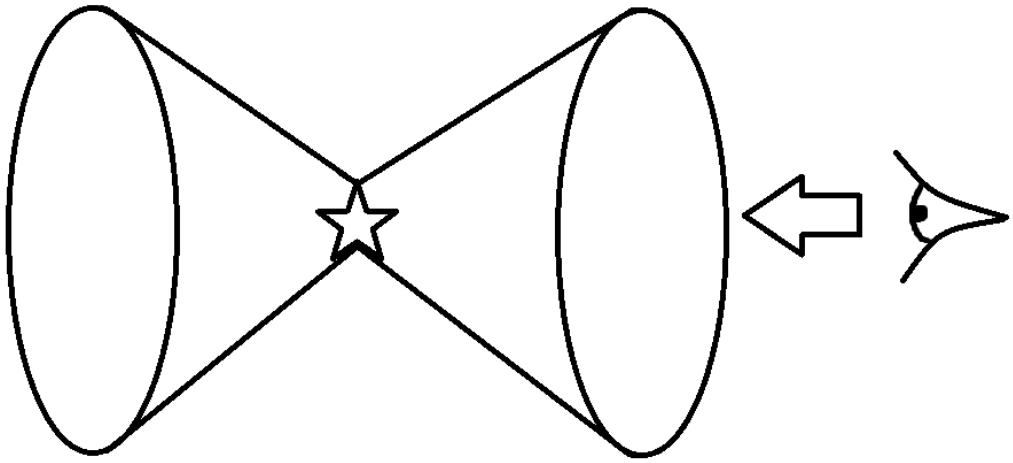

Fig. 1.9 Possible explanation for observations of spherical and elliptical PNe.

Jones 2015), and even triple-star systems (e.g. Soker et al. 1992). The interstellar magnetic field may also affect the morphology (e.g. Falceta-Gonçalves and Monteiro 2014; van Marle et al. 2014), theoretically producing either bipolar outflows or eye-shaped structures, although large magnetic field strengths are required ($\gtrsim 500\ \mu G$). Hence, magnetic fields were often considered to be relatively negligable in affecting the morphology of PNe compared to the presence of binary companions (e.g. Sabin et al. 2007; Soker 2005, 2006).

Samples of Galactic PNe have shown varying proportions of sources with a spherical morphology, such as Abell 30 and Abell 39, ranging from $\sim 4\%$ (Stanghellini et al., 2016) to $\sim 26\%$ (Manchado et al., 2000), whereas $\gtrsim 50\%$ of both samples consisted of elliptical PNe. Soker (2002) argued that most of the spherical PN population is detected towards the Galactic anti-centre, and suggested that metallicity effects contribute to this morphology. van Marle et al. (2014) suggested that the morphologies of PNe are also likely to be affected by the shaping of slow AGB winds and their interactions with the interstellar magnetic field. Figure 1.9 shows that it may also be possible for sources with spherical or elliptical morphologies to be bipolar, with one of the outflows pointed towards the observer.

Perhaps the most heavily studied morphology is that involving bipolar outflows, which are observed in PNe such as the Twin Jet Nebula (M2-9) and the Butterfly Nebula (NGC 6302), from which high-velocity jets from the central star interact with the ISM (Huggins, 2007). The origins of these outflows are not well understood, but studies have suggested one possible

method is the presence of an equatorial toroidal structure around the central star (e.g. Calvet and Peimbert 1983; Chen et al. 2016; Doan et al. 2017; Icke 1988; Icke et al. 1989), potentially from an optically thick region of gas. This structure may also be an accretion disk from within a binary system, which is formed either around the secondary companion by mass-loss from the primary star (e.g. Soker and Rappaport 2000) or around the primary star by the break-up of the companion (e.g. Nordhaus and Blackman 2006). Either way, binaries are believed to be the cause of bipolar jets (e.g. García-Segura et al. 2014, 2016; Soker 2016).

The presence of outflows in PNe indicates that shock processes are occurring. These will affect the chemical compositions observed from around these stars.

1.3.2 Shocks

When material moves into a region of low pressure from one of high pressure, a shock front is formed (e.g. Tielens 2005). A typical example is when a stellar outflow reaches the ISM; this does not exclusively apply to those of AGB stars and PNe, but also to those of Herbig-Haro objects and supernova explosions (e.g. Guerrero et al. 2013).

Two types of shocks occur in the ISM. The first type involves supersonic movement, in which there is a sudden heating of the gas at the shock front, up to temperatures of $\sim 10^5$ K (Draine, 1980; Kaufman and Neufeld, 1996). From the frame of reference of the shock front, the mass, momentum and energy are respectively conserved using the following equations, known as the Rankine-Hugoniot relations (Hugoniot, 1887, 1889; Macquorn Rankine, 1870):

$$\rho_0 v_0 = \rho_1 v_1 \tag{1.5}$$

$$P_0 + \rho_0 v_0^2 = P_1 + \rho_1 v_1^2 \tag{1.6}$$

$$\frac{P_0 + u_0}{\rho_0} + \frac{v_0^2}{2} = \frac{P_1 + u_1}{\rho_1} + \frac{v_1^2}{2} \tag{1.7}$$

where ρ is the density, v is the velocity, P is the pressure and u is the internal energy per unit volume of the gas in the shock, and the subscripts '0' and '1' respectively represent the regions

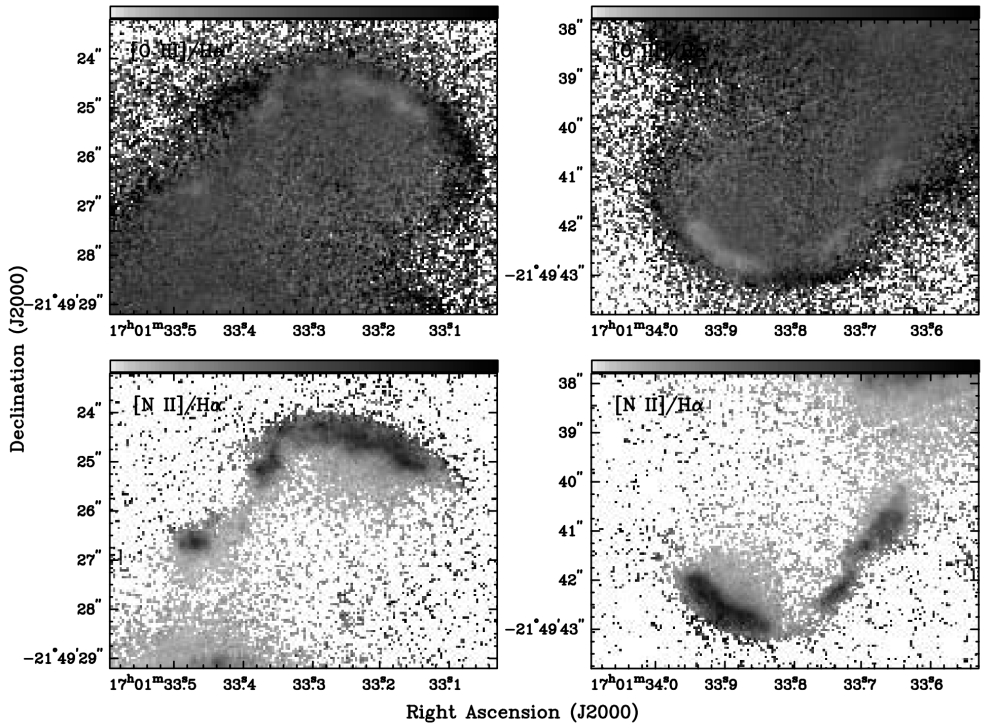

Fig. 1.10 Bow shocks in PN IC 4634, in [O III]/Hα (top) and [N II]/Hα (bottom). Figure reproduced from Guerrero et al. (2008).

upstream and downstream of the shock front, i.e. before and after the fast shock heating process (e.g. Tielens 2005). These types of shock are known as "J-shocks", as there is a "jump" in the physical conditions at the shock front. The second type of shock is formed from the interaction between low-ionisation species moving subsonically and the local magnetic field. These are known as "C-shocks", as the physical conditions of the gas are "continuous" upstream and downstream of the shock front.

Images of PNe have shown these structures in the form of bow shocks, which are both analogous to, and named after, the wave produced by the bow of a ship on water (c.f. an outflow moving into the quiescent ISM; e.g. Kakinami et al. 2013; Landau and Lifshitz 1959). These are easy to observe in the emission of temperature-dependent species such as O III or N II[1], as shown in Figure 1.10.

[1]Roman numerals indicate ions; the numeral itself is one greater than the positive charge of the species. Hence, O III = O^{2+} and N II = N^{+}. Square brackets around this notation are used in describing particular spectral lines, and indicate that the transition is forbidden in terms of the quantum selection rules. These are explained in Chapter 2.

Shocks can change the chemical composition around the star. For instance, dust grains can be destroyed in high-velocity shocks. This is discussed further in Chapters 4 and 5. However, the heating of interstellar gas by shocks is not as efficient as that from far-UV photons (Hollenbach and Tielens, 1999).

1.3.3 Photodissociation regions

Aside from the central star and the ejected circumstellar envelope of ionised material, there are regions of PNe in which atoms with ionisation potentials of less than that of hydrogen (13.6 eV) and molecules reside. These are known as photodissociation regions, or photon-dominated regions (PDRs), as the heating is governed by far-UV radiation (Tielens and Hollenbach, 1985). By this definition, PDRs are found not only around evolved stars, but also in interstellar environments.

A typical PDR schematic is shown in Figure 1.11. Lyman continuum photons (corresponding to energies of $\sim$ 6 to 13.6 eV) will be absorbed by an interlayer of H I and H II gas (Hollenbach and Tielens, 1997, 1999; Vasta, 2010), from which they can penetrate into the PDR. The incident flux of these photons, G_0, is measured relative to the average interstellar radiation field, 1.6×10^{-6} W m^{-2} (Habing, 1968). The depth of the PDR is typically measured in terms of the V-band extinction (A_V, measured in magnitudes), from which the column density of hydrogen (N_H) can be deduced from the following equation (Predehl and Schmitt, 1995):

$$N_H = (1.79 \pm 0.03\, A_V) \times 10^{21}\ \mathrm{cm}^{-2} \tag{1.8}$$

The chemical stratification in PDRs is such that most of the material at low-A_V is atomic or ionic (for low-ionisation species, e.g. C^+) and molecules are observed at high-A_V.

The modelling of PDRs has evolved over the past few decades (e.g. Hollenbach and Tielens 1999; Röllig et al. 2007); early models (e.g. Black and Dalgarno 1977; Glassgold and Langer 1974; Hollenbach and Salpeter 1971) focused primarily on the conversions of atomic hydrogen and carbon to molecules of H_2 and CO in interstellar clouds. These evolved

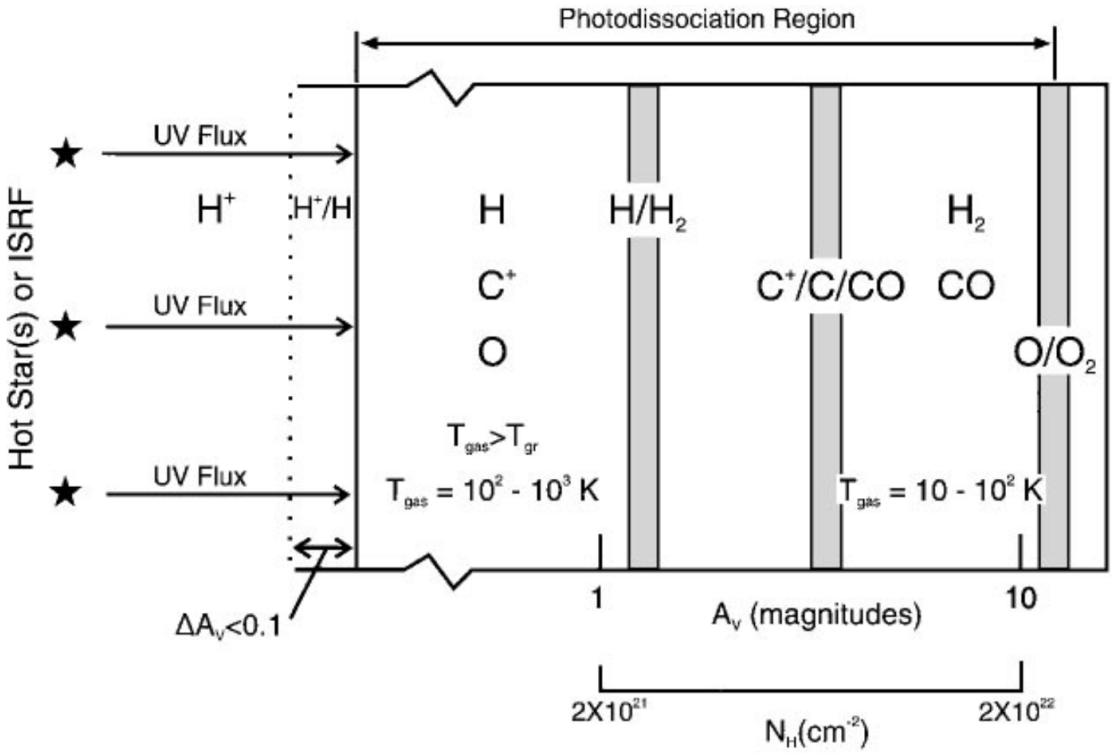

Fig. 1.11 Schematic diagram of a photodissociation region. The UV source, e.g. the cetral star of a planetary nebula, is on the left-hand side. Figure reproduced from Hollenbach and Tielens (1997).

into models investigating the chemistry with the consideration of an incident far-UV flux (e.g. Chokshi et al. 1988; Tielens and Hollenbach 1985; van Dishoeck and Black 1988), and these eventually became models which considered factors such as time-dependent chemistry (e.g. Genzel et al. 1989) and the presence of clumps (e.g. Burton et al. 1990). PDRs around evolved stars were the main focus of models by W. Latter (Fong et al., 2001) and Castro-Carrizo et al. (2001), who investigated carbon-rich and oxygen-rich sources, respectively (see § 1.2). Today, the modelling simulation *CLOUDY* (Ferland et al., 2017, 1998, 2013) is often used as a spectral prediction code for PDRs and other astrophysical systems in non-local thermodynamic equilibrium.

Observations have shown that the molecular emission expected to be observed in PDRs is stronger in bipolar PNe (e.g. Hora et al. 1999; Latter et al. 2000). For instance, the excited H_2 emission around the well-studied PN NGC 7027, which may contain multiple bipolar outflows (Huang et al., 2010), is shown in Figure 1.12. The emission in this PN is modelled

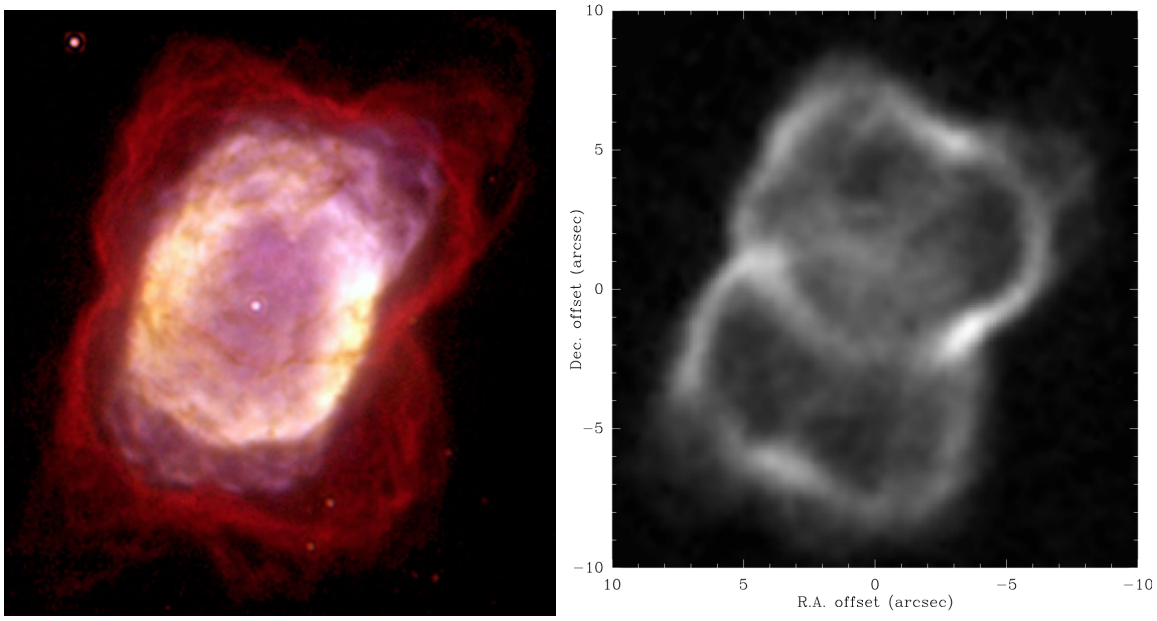

Fig. 1.12 The planetary nebula NGC 7027. Left: an RGB image (Hubble Legacy Archive / ESA / NASA; Delio Tolivia Cadrecha). Right: a velocity-integrated image of the H_2 1–0 S(1) transition. Figure reproduced from Cox et al. (2002).

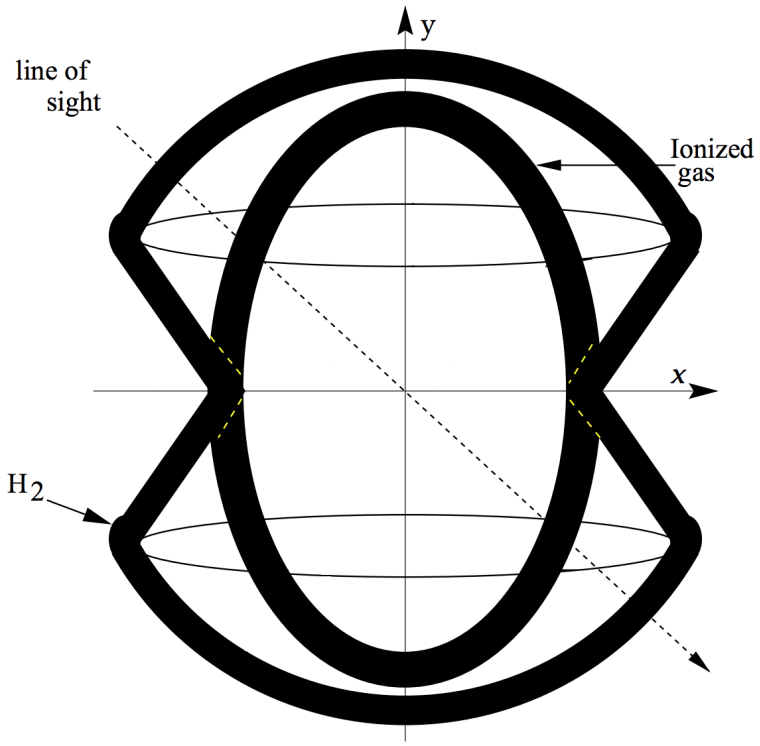

Fig. 1.13 The modelled geometry of the PDR around NGC 7027. Figure amended from Latter et al. (2000).

geometrically as an hourglass-shaped "bicone" around an ellipsoid of ionised material, as shown in Figure 1.13 (Cox et al., 2002; Latter et al., 2000). Hence, this morphology may be appropriate for the modelling of PDRs around other bipolar PNe. The molecular emission in the almost spherical proto-PN HD 56126 is clumped, but the morphology is relatively unchanged (Meixner et al., 2004).

1.4 Current status

This section shows the current understanding to be built upon by the work in this thesis, in terms of studies of metallicity and chemical diversity in circumstellar environments.

1.4.1 Influence of metallicity on dust composition

In this thesis, the chemical composition of the gas and dust around PNe within low-metallicity regions of the Milky Way is investigated. Figure 1.14 shows a side view of the Milky Way, consisting of the bulge, the disk, and the surrounding halo. The central bulge contains much of the Galaxy's population of old stars, as well as gas and dust, hence the metallicity within this region is greater than elsewhere in our Galaxy. The disk has a radius of $\sim$ 20–30 kpc and consists of two components: the 'thin disk' contains most of the gaseous material and stars, and the 'thick disk' encapsulates the thin disk but has a lower metallicity and low gas content (Gilmore and Reid, 1983). The bulge and disk together contain the vast majority of stars in the Milky Way. The Galactic halo contains few stars, and is consequently established as a region of low metallicity.

Within the Galactic plane (disk), there is a radial abundance gradient; the local metallicity decreases at greater distances from the Galactic centre. A visual representation of this is shown in Figure 1.15, in which the oxygen abundances from a sample of PNe studied by Pottasch and Bernard-Salas (2006) have been observed to decrease between Galactocentric distances (R_g) of $\sim$ 4–10 kpc. In Chapter 3 of this thesis, a sample of PNe located towards the Galactic

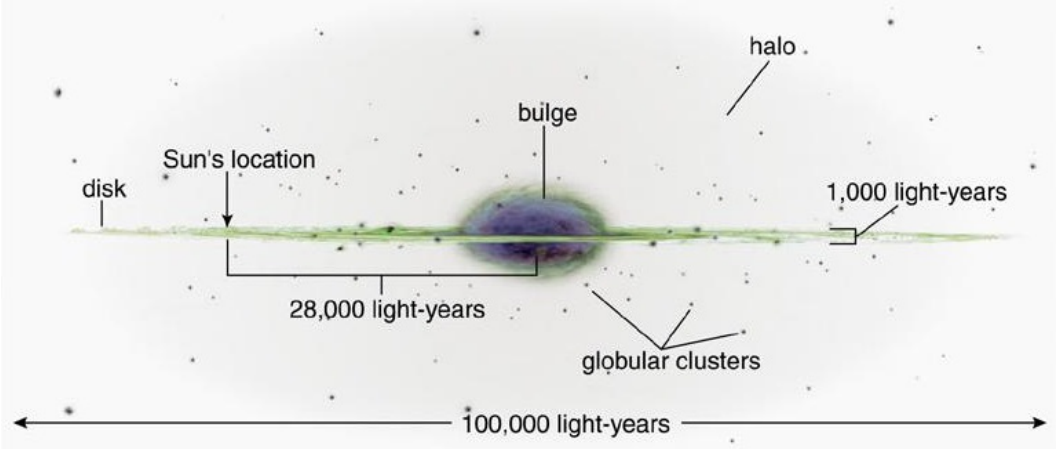

Fig. 1.14 Side view of the Milky Way. The Sun is located at $\sim$ 8 kpc from the Galactic centre; 1 kpc $\equiv$ 3261.56 light years. (F. Walter)

anti-centre ($R_g > 8$ kpc) are analysed in order to determine whether the radial abundance gradient of the Milky Way continues beyond the solar neighbourhood.

There are similarities of the dust compositions of PNe within particular regions of the Galactic disk. For instance, dual-dust chemistry is more commonly found close to the Galactic bulge (Górny et al., 2010; Gutenkunst et al., 2008; Perea-Calderón et al., 2009; Stanghellini et al., 2012). Similarly, oxygen-rich dust is typically observed closer to the Galactic centre, whereas carbon-rich dust is observed consistently in PNe throughout the Galactic disk. As mentioned in § 1.2, the overall dust composition of a PN is partly dependent on the metallicity of the local region, as the star will become C-rich faster if the stellar environment has less oxygen. Studies of PNe in the Magellanic Clouds, which are of sub-solar metallicity, have shown that C-rich dust emission is more commonly observed than O-rich emission in these sources (e.g. Bernard-Salas et al. 2009; Sloan et al. 2014; Ventura et al. 2016; Volk et al. 2011). However, the dust composition in the Magellanic Clouds is typically more diverse from that observed towards the Galactic bulge and in the solar neighbourhood, as there is a greater probability of observing features such as silicon carbide and fullerenes (see § 1.4.2). The Magellanic Clouds are of a similar metallicity to regions of the Milky Way, assuming the Galactic abundance gradient continues beyond $\sim$ 10 kpc. Hence, the dust compositions of Magellanic Cloud PNe are ideal for comparison with those located towards the Galactic anti-centre, which are investigated in Chapter 4.

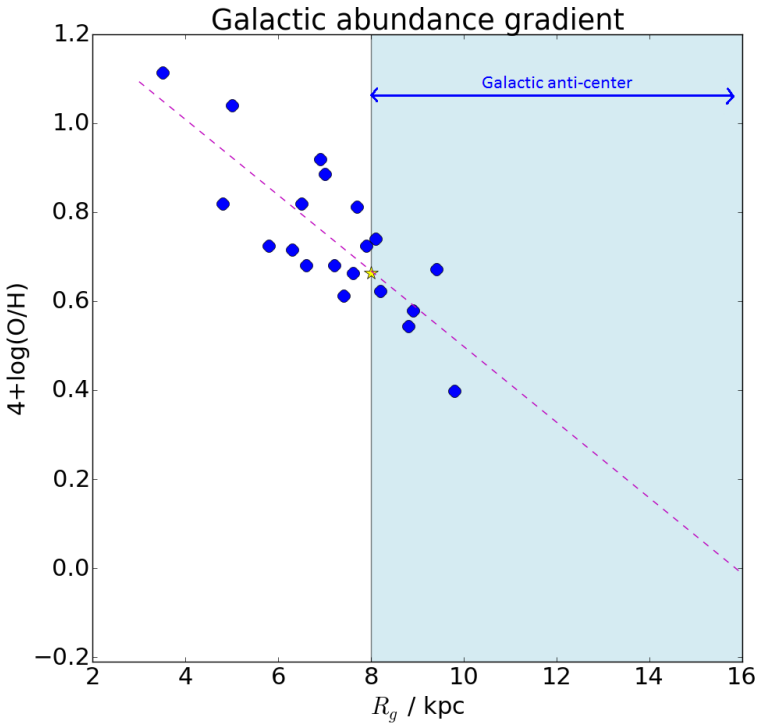

Fig. 1.15 The radial oxygen abundance gradient of the Milky Way, as shown by a sample of PNe from Pottasch and Bernard-Salas (2006). The Sun is represented by the yellow star.

The metal-poor Galactic halo contains few stars, which typically have masses $\lesssim 0.85\ M_{\odot}$ (e.g. Abate et al. 2015), hence PNe with these masses are not expected to undergo the third dredge-up. The chemical compositions of gas and dust from a sample of PNe from the Galactic halo, and the origins of these stars within this low metallicity region, are investigated in Chapter 5.

1.4.2 Diversity of large organic molecules

The ISM contains around 200 known molecular species, ranging from small molecules such as H_2 and CO, to large aliphatic species such as C_2H_5OCHO and isomers of C_3H_7CN (Belloche et al., 2014, 2009), to even larger aromatic compounds such as fullerenes (Cami et al., 2010). A full list of the detected interstellar molecules is shown in the *Cologne Database for Molecular Spectroscopy*[2] (Endres et al., 2016; Müller et al., 2005; Müller et al., 2001). The physical conditions of circumstellar environments are such that long aliphatic compounds

[2]http://www.astro.uni-koeln.de/cdms/molecules

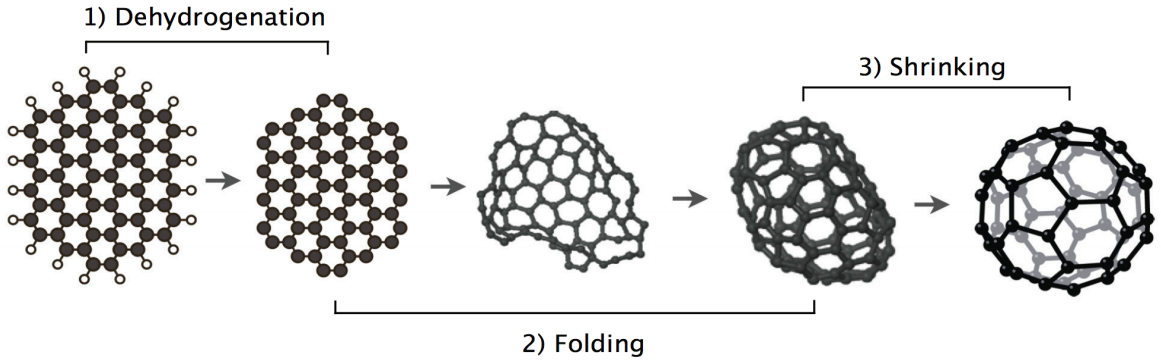

Fig. 1.16 Proposed 'PAH striptease' method of fullerene formation. Figure reproduced from Berné et al. (2015).

cannot survive around them (with the possible exception of HAC), compared to the strong double- and triple-bonds between carbon atoms in aromatic species.

PAHs are the most predominant C-rich dust emission, athough features attributed to silicon carbide and fullerenes are also occasionally detected in circumstellar environments. Fullerenes are particularly interesting as they are the largest known molecules that have been detected in space. Hence, by studying the environments in which they inhabit, we may get an insight into the formation requirements for many organic molecules.

The emission from these molecules is likely to be observed within the PDRs of PNe. By analysing the emission of the main cooling lines, such as those of [O I] and [C II], the physical conditions of the regions in which these molecules have formed and evolved can be analysed. However, the pathways by which fullerenes form and evolve are still not well understood. Analysing the PDRs around evolved stars with fullerene emission may help in understanding the processes leading to the formation of many complex organic molecules around evolved stars.

Several mechanisms for the formation of fullerenes in space have been proposed, such as the photo-processing of PAHs (Berné et al., 2015) or HAC (García-Hernández et al., 2010) via a 'striptease' mechanism, as shown in Figure 1.16, in which the outer hydrogen atoms are removed by strong UV radiation, causing the remaining carbon skeleton to curve in on itself and form a fullerene molecule. Aside from this top-down method of fullerene formation, there is also the bottom-up method of 'closed network growth', in which atomic carbon and C_2 are

added to a smaller PAH or fullerene molecule, causing it to grow (e.g. Dunk et al. 2012a,b). Determining the balance between top-down and bottom-up processes in the formation of carbonaceous molecules remains a significant challenge in the field of astrochemistry (van Dishoeck, 2017).

In Chapter 6 of this thesis, the PDRs of a sample of Galactic PNe known to exhibit C_{60} emission features are analysed through the analysis of data from *SOFIA*, in order to examine the physical conditions of the environments in which these large organic molecules are located.

1.5 Thesis overview

This thesis includes four science chapters. Chapter 2 explains the methodologies and fundametal physics used in these science chapters, which includes the basics of spectroscopy and the technical details of the telescopes and instruments used. Chapters 3 and 4 respectively provide an analysis of the gas and dust in a sample of PNe from the Galactic anti-centre, as measured by the *Spitzer Space Telescope*. Chapter 5 shows a study of the gas and dust composition of PNe in the Galactic halo, and probes the origins of these stars. In Chapter 6, the *SOFIA* telescope is used to investigate the physical conditions of the PDRs around a sample of PNe with known fullerene emission. Finally, in Chapter 7, the implications of the work carried out in this thesis are explained, and the future of astrochemical planetary nebula studies is discussed.

Chapter 2

Methods of data reduction and analysis

This thesis consists of four studies involving the use of infrared spectroscopy, particularly from the *Spitzer Space Telescope* and the *Stratospheric Observatory for Infrared Astronomy*. Data from these telescopes are analysed to obtain ionic and elemental abundances, measure the flux from molecular emission (particularly for carbonaceous species), and output spatial maps of the emission of particular lines.

This chapter explains the fundamentals of spectroscopy, with emphasis on infrared spectroscopy of planetary nebulae, such as the emission of forbidden lines and the use of these lines to determine the physical conditions around these stars. The use of infrared airborne and Space telescopes is discussed in contexts that are both historical and directly relevant to the science carried out in this thesis, and the software packages used for the data analysis in the upcoming science chapters are also explained.

2.1 Spectroscopy

Spectroscopy is the method by which we can determine the chemical composition of any astronomical source. From spectra of planetary nebulae, most of the observed emission originates from either quantum-forbidden electronic transitions, recombination lines of atomic hydrogen, or from dust. The spectra analysed in this thesis are observed at infrared wavelengths, which are ideal for detecting the vibrational transitions of carbonaceous or silicate

molecules associated with dust; further advantages of observing IR spectra are explained in § 2.2.

In this section, the concepts of atomic and molecular spectroscopy concerning the studies of PNe in future chapters are outlined. There is a broad literature on the subject, and the reader is encouraged to look at Matthews (1985) and Atkins and de Paula (2002) for more regarding the physical chemistry processes, and Tennyson (2011) for more on the applications of spectroscopy in astronomy.

2.1.1 Atomic spectroscopy

Atomic spectroscopy is entirely governed by electrons. Every single atom or ion consists of a system of quantised electronic energy levels, as shown in Figure 2.1. Between these energy states, the electrons can become excited by the absorption of a photon with energy equal to the difference in energy levels, or de-excited by emitting a photon of this energy. The absorption and emission of these photons can be detected by observing at these wavelengths:

$$E = \frac{hc}{\lambda} = h\nu \tag{2.1}$$

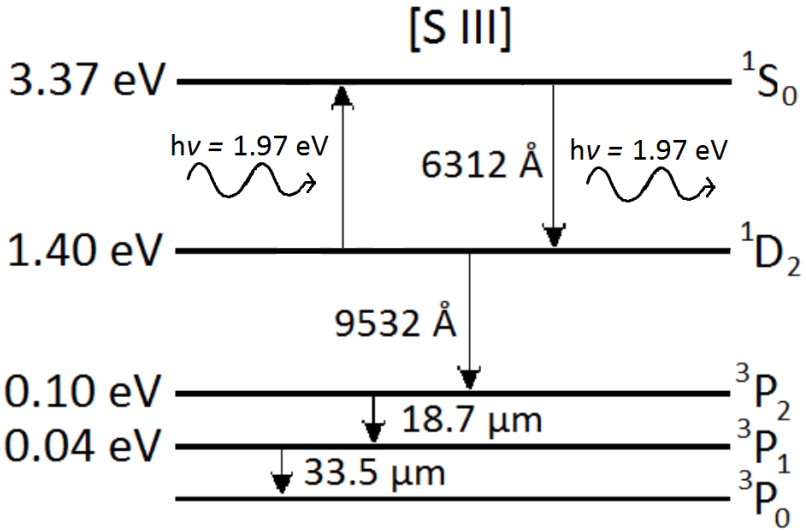

Fig. 2.1 The lowest five electronic energy levels of the S^{2+} ion. The term symbols for each level are shown on the right; these are explained throughout this section. The energy values above the ground state ($^3P_0$) are shown on the left.

where E is the photon energy in Joules (J); h is Planck's constant, 6.626×10^{-34} J s; c is the speed of light, 3×10^{8} m s^{-1}; λ is the wavelength of light in metres and ν is the light frequency in Hertz.

If an electron absorbs enough energy to become unbound from all energy levels within the atom or ion, then this chemical species is ionised and gains a positive ionic charge. A free electron can also be taken in by an atom or ion, and may initially occupy a high energy state; de-excitation will take place via several energy levels ("cascade") and multiple photons will be produced. This process is known as recombination.

The rates at which photons are absorbed and spontaneously emitted by an electron are:

$$\frac{dn_l}{dt} = -B_{lu} n_l \rho_\nu \tag{2.2}$$

$$\frac{dn_u}{dt} = -A_{ul} n_u \tag{2.3}$$

where n_l and n_u are respectively the number densities of electrons in the lower and upper energy states of the transition, B_{lu} is the Einstein absorption coefficient (units: m^3 J^{-1} s^{-2}), A_{ul} is the Einstein coefficient for spontaneous emission (units: s^{-1}), which indicates the probability of a given electronic transition, and ρ_ν is the radiation energy density at the transition frequency (units: J m^{-3}). Photons can also be emitted by stimulated emission, i.e. from the influence of another photon. This is an important mechanism for observing spectral lines from lasers and astronomical maser sources, but is not a focus of this thesis.

Quantum numbers and term symbols

Each of the electrons in an atom or ion is given a unique set of quantum numbers. This originates from the Pauli exclusion principle, which states that no two electrons can occupy the same quantum state within a particular chemical species at any given time.

Quantum numbers for electrons are always represented by lower case letters. The principal quantum number, n, defines the distance of the electron from the atomic nucleus ($n \in \mathbb{Z}$, $n > 0$). The orbital angular momentum quantum number, l, indicates the ability of an electron

to penetrate into the nucleus ($l \in \mathbb{Z}$, $l \geqslant 0$). Together, these two quantum numbers define the occupied electron shells in a species. These follow a naming convention based on the 'sharp', 'principal', 'diffuse' and 'fundamental' series of atomic lines based on the l quantum number, e.g. 1s, 2s, 2p, ... where s, p, d and f respectively represent l = 0, 1, 2 and 3 (for greater l values, this continues alphabetically from f). The spin angular momentum quantum number, s, represents the intrinsic spin ($s = \frac{1}{2}$ for an electron). The total angular momentum, j, is the vector sum of the l and s quantum numbers ($j = | \, l + s \, |$). There are also magnetic components to the three angular momentum quantum numbers: m_l, m_s and m_j, defining the behaviour of the electron in a magnetic field (m_l takes all integer values between $-l$ and l; $m_s = \pm\frac{1}{2}$; m_j takes all values between $-j$ and j in integer steps).

Each electronic energy state is assigned a *term symbol* based on the total quantum numbers of the unpaired electrons, which is denoted as ${}^{2S+1}L_J$, where:

$$\underline{L} = \sum_e \underline{l}_e \tag{2.4}$$

$$\underline{S} = \sum_e \underline{s}_e \tag{2.5}$$

$$\underline{J} = \underline{L} + \underline{S} \tag{2.6}$$

where the subscript e is used to indicate that these are the sums over the quantum numbers of all unpaired electrons. Note the use of vector notation in the above equations; this implies a range of values for L, S and J. For instance, in situations where an atom or ion has two unpaired electrons, L takes all values from $| \, l_1 - l_2 \, |$ to $l_1 + l_2$ in integer steps. Each combination of these three quantum numbers represents an electronic energy state. As with its electronic counterpart, the quantum number L is represented by letters S, P, D, F, etc.

The ordering of the term symbols representing the electronic energy states in a chemical species are governed by Hund's rules. The complete set of quantum numbers for the electrons must be calculated. Hund's rules state that for a given electron configuration:

- States with the largest multiplicity (i.e. $2S + 1$) have the lowest energy;

- If multiple states share the same multiplicity, the state with the largest orbital angular momentum has the lowest energy;

- If an electron shell is less than half-filled, the state with the lowest J value has the lowest energy. If it is more than half-filled, the state with the greatest J value has the lowest energy.

The Pauli exclusion principle imposes a further condition: for electrons with the same n and l quantum numbers, $(L + S)$ must be even.

For clarity, consider the electron states of S^{2+}, as shown in Figure 2.1. The electron configuration, in accordance with the Periodic Table, is $1s^2 2s^2 2p^6 3s^2 3p^2$. Only the electrons in the 3p shell are considered, as the other shells are full (and therefore stable) and hence these do not contribute to the energetic processes within the ion. Two electrons are considered with $s = \frac{1}{2}$, therefore $S = 0, 1$ and $(2S + 1) = 1, 3$. For both electrons, $l = 1$, therefore $L = 0, 1, 2$. The energy states that satisfy the Pauli exclusion principle are therefore ^1S, ^3P and ^1D. The values for J are $(0 + 0 =)\ 0$ for ^1S and $(2 + 0 =)\ 2$ for ^1D, whereas the ^3P state takes J values of 0, 1 and 2 (this is known as "fine splitting"). In accordance with Hund's first rule, the triplet states (i.e. those with a multiplicity of 3) are lowest in energy, and because the $3p$ shell contains two electrons out of a maximum of six, Hund's third rule shows that $\mathrm{E}(^3P_0) < \mathrm{E}(^3P_1) < \mathrm{E}(^3P_2)$. Of the two singlet states, the $^1D_2$ state has a larger orbital angular momentum than the $^1S_0$ state, and is therefore the next lowest in energy, in accordance with Hund's second rule.

Quantum selection rules for electric dipole transitions

There are several sets of quantum selection rules that govern the states between which an electronic transition occurs. The most important type for atomic spectroscopy in planetary nebulae involves electric dipole transitions, i.e. those involving the separation of a positive and negative electric charges (other types include the weaker electric quadrupole and magnetic dipole transitions).

Some rules are always followed in electric dipole transitions. These are known as the rigorous selection rules:

- $\Delta J = 0$ or $\pm$ 1, but not from 0–0;
- $\Delta M_J = 0$ or $\pm$ 1;
- The parity, calculated by $(-1)^{\sum_e l_e}$, changes.

There is also a further set of propensity rules, which lead to strong "allowed transitions" when followed:

- $\Delta S = 0$;
- One electron jumps, $\Delta l = \pm$ 1;
- $\Delta L = 0$ or $\pm$ 1, but not from 0–0.

However, this set of rules (particularly the last two) may be broken, in which case the transition is "forbidden". These are denoted by a pair of square brackets around the ion, e.g. [S III]. For this particular ion (see Figure 2.1), the $^1S_0 \rightarrow {}^1D_2$ transition is forbidden as $\Delta L = 2$ (also, the parity does not change and $\Delta J = 2$, suggesting that this is an allowed electric quadrupole transition). The $^1D_2 \rightarrow {}^3P_2$ breaks the rule by changing the spin angular momentum quantum number. The transitions between the ^3P fine structure states break the $\Delta l = \pm$ 1 rule for one electron, and the unchanging parity again suggests that these are not electric dipole transitions.

Forbidden transitions are commonly observed from spectra of planetary nebulae; their particularly low densities allow for long-lasting radiative decay processes to occur without being affected by collisional excitation or de-excitation. These transitions are typically observed from lower energy states, as electrons in higher states are likely to have several possible allowed routes to become de-excited. These low-level transitions are typically observed at visible and infrared wavelengths. This is one of several reasons why the work in this thesis focuses primarily on the analysis of IR spectra (see also § 2.2).

Alongside these forbidden emission lines, infrared spectra of PNe also show transitions from recombination in hydrogen atoms. These transitions often show similar flux ratios relative to one another, as shown by Hummer and Storey (1987).

2.1.2 Molecular spectroscopy

The infrared spectra of planetary nebulae analysed in this thesis are ideally suited for observations of photons from ions close to the ground electronic state, as well as those from the vibrations of bonds in carbonaceous molecules, and some from the changes in vibrational energy from the abundant H_2 molecule. The spectroscopy of molecules is much more intricate than that of atoms, as their internal energies consist of electronic, vibrational and rotational components. This is a consequence of the Born-Oppenheimer approximation, which states that the difference in mass between electrons ($\sim 9 \times 10^{-31}$ kg) and nucleons ($\sim 2 \times 10^{-27}$ kg) within a molecule is large enough to consider their motion separately. The differences between electronic energy states are greater than those of vibrational energy states, which in turn are greater than those of rotational energy states. Hence, these different components are observed within separate wavelength regions.

In this thesis, IR spectra showing the vibrational emission of carbonaceous molecules (see Chapter 1) are studied in detail. While not a main focus, molecular hydrogen ro-vibrational features are also regularly observed in these spectra. For more information regarding the electronic and rotational spectroscopy of molecules, the reader is again referred to Atkins and de Paula (2002) and Tennyson (2011).

Vibrational spectroscopy

In molecules, photons can be emitted from the bending and stretching of the bonds that hold the constituent atoms together; a good example is shown by the spectrum of PAHs in Chapter 1 (Figure 1.3). For a molecule with N atoms, there are $3N-6$ vibrational modes if non-linear and $3N-5$ if linear. This is because there are $3N$ ways to organise the atoms

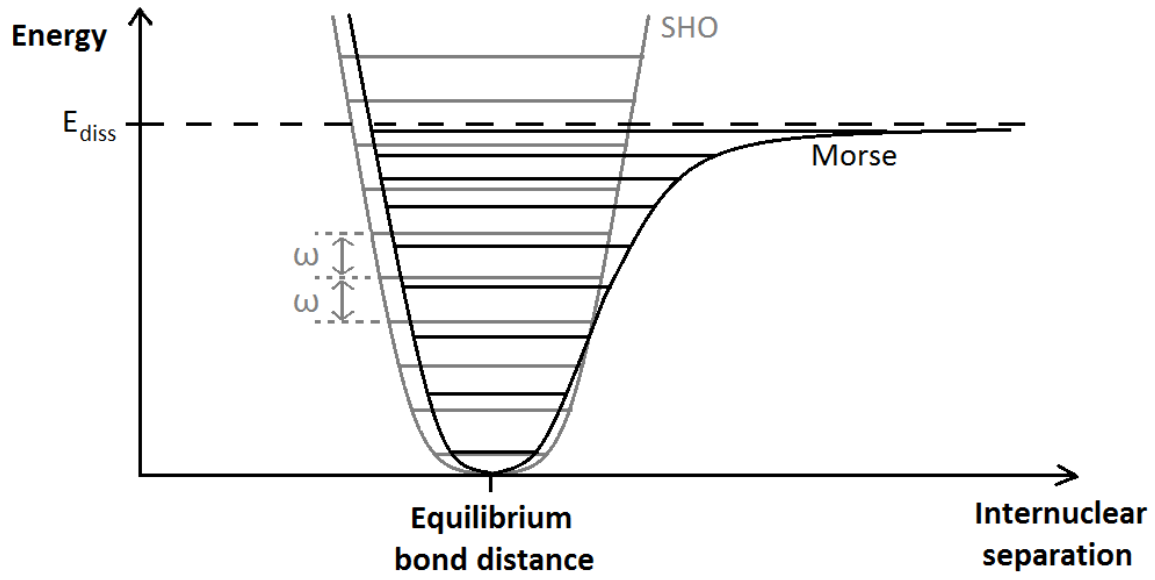

Fig. 2.2 Schematic showing the vibrational levels within the simple harmonic oscillator (SHO) and Morse potential models. The dissociation energy of the Morse potential is given by E_{diss}.

in three-dimensional space, though three are required to define the centre of mass for the molecule and another two or three (depending on linearity) define the molecular orientation.

The structure of vibrational modes in a molecule can be estimated by modelling the molecule as a harmonic oscillator, as in Figure 2.2. In this model, the vibrational energy states are equally spaced and all transitions follow the quantum rule $\Delta v \pm 1$, implying that only one emission feature will be observed. However, the ability for the bond to dissociate after being subjected to enough energy is not considered. Realistically, the vibrational energy states get closer together as the dissociation energy is approached, and there are no quantum rules governing the change in energy level, hence a wide range of emission features are observed. This is known as the Morse potential.

Vibrational transitions are typically observed at infrared wavelengths, and are often attributed to large molecules, such as PAHs and fullerenes. Indeed, with a variety of potential chemical compositions for circumstellar PAHs, the vibrations of particular functional groups can help identify families within these molecules.

For small molecules, e.g. diatomics such as H_2, the rotational components become equally important when analysing their spectral features.

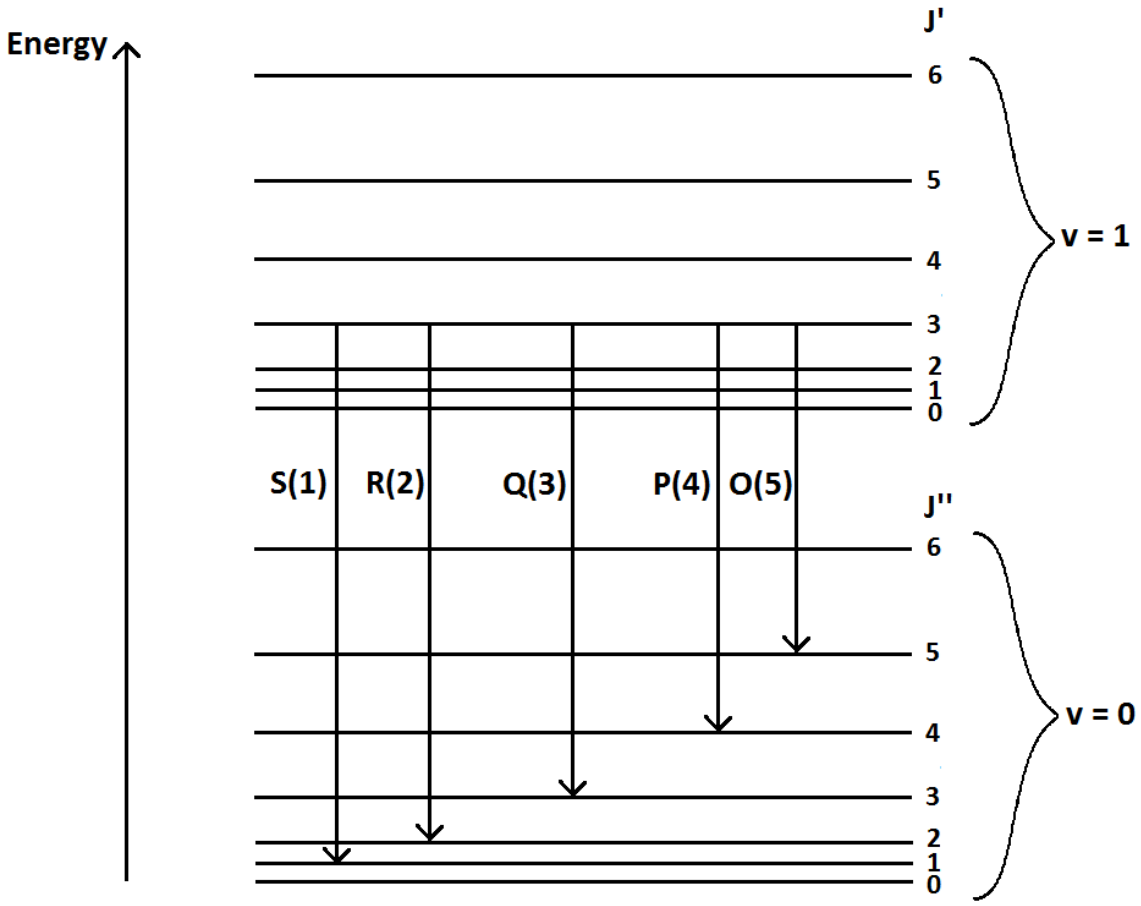

Fig. 2.3 Typical ro-vibrational transitions observed from molecules. The names of the transitions between rotational states (J) and vibrational states (v) are explained in the text.

Ro-vibrational spectroscopy

Molecules simultaneously vibrate and rotate. Each vibrational energy level is modelled to consist of several rotational energy levels, as shown in Figure 2.3. For a given molecule, particular sets of transitions will occur as different sets of quantum rules apply depending on the molecule. For example, many diatomics show strong emission in the P- and R-branches, which respectively describe emission features where the change in rotational energy state, ΔJ, is $+1$ and -1[1]. Similarly, the Q-branch describes transitions in which $\Delta J = 0$, and the O- and S-branches describe those where ΔJ is $+2$ or -2 in emission, respectively. The name of each transition is taken from the rotational energy level in the lower vibrational energy state.

[1]Note that the signs are reversed when considering these transitions in absorption.

Hence, the transition from $J' = 1$ to $J'' = 2$ is known as P(2). In all of the above cases, there are no restrictions on Δv.

The P- and R-branches are the most commonly observed types of ro-vibrational transition in molecules, such as from the emission of small hydrocarbons (e.g. C_2H_2 and C_4H_2) in the PN SMP LMC 11 (Bernard-Salas et al., 2006). Q-branch transitions are only observed when the ground electronic state of a molecule has an orbital angular momentum that is non-zero. The O- and S-branches are observed in homonuclear diatomic molecules such as H_2, and these transitions are typically associated with Raman scattering, in which a photon is absorbed and quickly re-emitted at a slightly different wavelength.

In summary: the infrared spectra of PNe are dominated by the emission of atomic lines from quantum-forbidden fine structure electronic energy states, molecules and dust. The next section explains how IR emission lines can be used to obtain specific astrophysical information in sources such as PNe.

2.2 Infrared emission lines

The forbidden emission lines observed within a PN spectrum provide information on the chemical compositions and physical conditions around the star. This section explains how the analysis of the emission lines at IR wavelengths is advantageous, relative to those in other wavelength regions, for the work in this thesis.

2.2.1 Metallicity and abundance

A standard method of describing the chemical composition of a star or region is by the mass fraction of hydrogen (X), helium (Y) and metals (Z), where metals are defined as any element heavier than helium. The quantity Z is also known as the metallicity. For the Sun: $X \sim 0.7$, $Y \sim 0.28$ and $Z \sim 0.02$ (e.g. Osterbrock and Ferland 2006; Wheeler et al. 1989).

For studies of PNe, it is more characteristic to refer to their chemistry in terms of abundances. These are often given in the form 12 + log(M/H), where M is the element for which the abundance is being measured.

In order to calculate ionic abundances from spectra of planetary nebulae, radiative transfer processes must be considered. The equations of radiative transfer are the following (e.g. Simpson 1975):

$$\frac{dI_\nu}{ds} = j_\nu - \kappa_\nu I_\nu \tag{2.7}$$

$$\frac{dI_\nu}{d\tau_\nu} = \frac{j_\nu}{\kappa_\nu} - I_\nu \tag{2.8}$$

where I_ν is the specific intensity of a light ray (units: erg cm^{-2} s^{-1} Hz $^{-1}$ steradian^{-1}), s is the displacement along the ray, j_ν is the emissivity (i.e. the ratio of the energy radiated from the stellar surface compared to that of a blackbody; units: erg cm^{-3} s^{-1} Hz^{-1} steradian^{-1}), κ_ν is an absorption coefficient (units: cm^{-1}) and τ_ν is the optical depth (dimensionless). From spectra of PNe, the abundances of many elements can be calculated from the emission of forbidden lines which originate from the more optically thin regions of the stars, where there are low probabilities of absorption.

The abundance of an ion in a planetary nebula is effectively defined as its density relative to the density of protons in this source. These values can be obtained by examining the intensities of the relevant spectral lines, as well as their wavelengths (which are related to the energy of the photons), the statistical populations of the electronic energy levels and the relevant coefficients of spontaneous emission and recombination. Hence, ionic abundances are measured by:

$$\frac{n_{ion}}{n_p} = n_e \frac{I_{ion}}{I_{H\beta}} \frac{\lambda_{ul}}{\lambda_{H\beta}} \frac{\alpha_{H\beta}}{A_{ul}} \left(\frac{n_u}{n_{ion}}\right)^{-1} \tag{2.9}$$

where n_p is the proton density, n_e is the electron density, I_{ion} is the intensity of the ionic line, λ_{ul} is the line wavelength, $\alpha_{H\beta}$ is the effective recombination coefficient for $H\beta$, A_{ul} is the Einstein coefficient of spontaneous emission, and n_u/n_{ion} is the ratio of the upper level

population of the transition to the entire population of the ion. Note that the line intensities, defined as the extinction-corrected flux values, require relatively small extinction corrections at IR wavelengths compared to those in other wavelength regions. At these wavelengths, the main ionic emission states of neon, sulphur and argon are observed. To account for ionisation states that are not observed at IR wavelengths, there are two options: either obtain complementary information from studies at other wavelengths, or apply ionisation correction factors for the missing ions. All of this is explained in more detail in Chapter 3.

In the literature, the abundance of iron is often used as a metric for metallicity, and the quantity Fe/H is often given in the form:

$$\mathrm{Fe/H} = \log_{10}\left[\frac{\mathrm{Fe/H}}{(\mathrm{Fe/H})_{\odot}}\right] \tag{2.10}$$

Hence, any iron abundances given as negative numbers in this thesis use this convention.

2.2.2 Probing physical conditions

At mid-IR wavelengths, the observed fine structure emission lines of ions, such as those from the ^3P states in S^{2+} and Ne^{2+}, can be used to determine the electron densities (n_e) of these species. With the inclusion of optical data, the electron temperatures (T_e) of many ions can also be calculated. Both of these quantities are required for calculating the ionic abundances as per equation (2.9); while n_e is directly applied, T_e governs the populations of upper electronic energy levels.

The spacing between energy levels is key in explaining how to obtain these physical conditions. In PNe, the energy is thermal, in accordance with:

$$E = \frac{3}{2}k_B T_e \tag{2.11}$$

where k_B is the Boltzmann constant, 1.381×10^{-23} J K^{-1}, and T_e is the electron temperature of the ion.

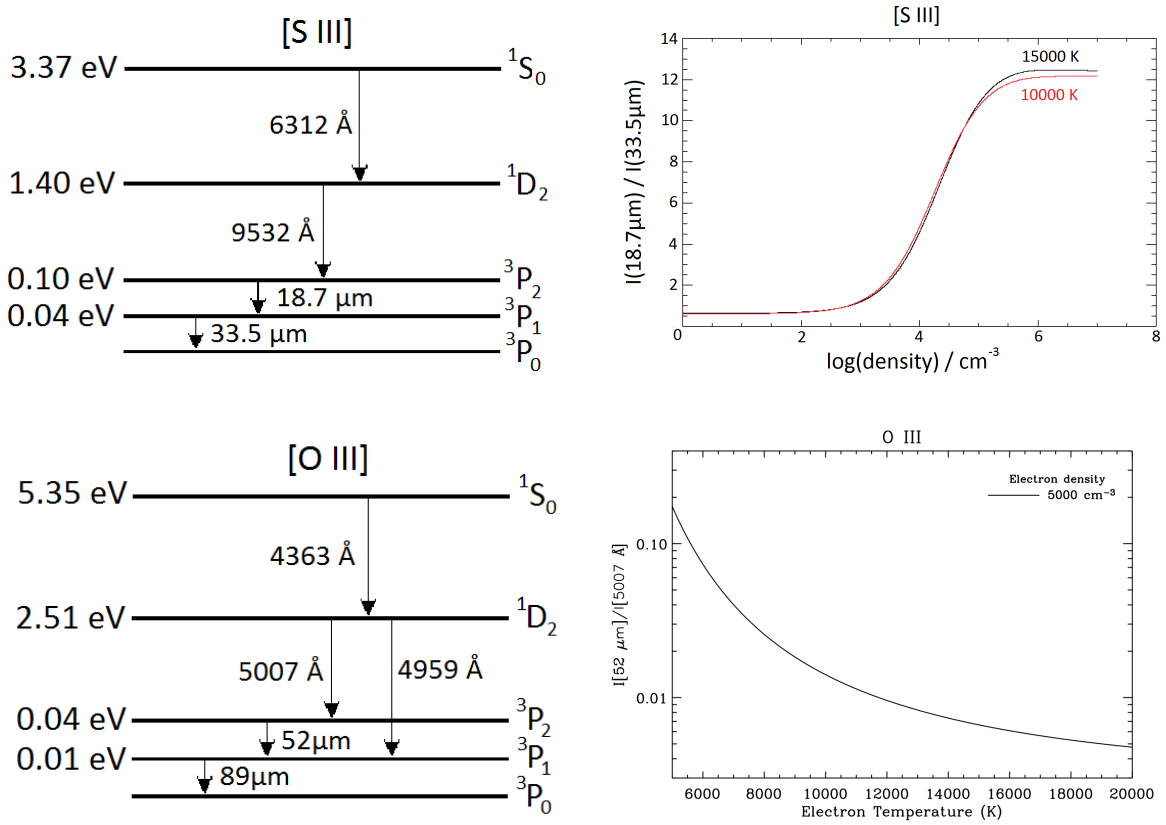

Fig. 2.4 Top: The energy level diagram for [S III] and density plot at two different temperatures. Bottom: The energy level diagram for [O III] and temperature plot (bottom-right diagram from Bernard-Salas 2003). The energy values on the left-hand plots represent those above the ground electronic state.

The top two panels of Figure 2.4 show how the intensity ratios of the two infrared fine structure lines show little temperature dependence, and are hence ideal for calculating the electron density (n_e) of S^{2+} around a PN. Indeed, the ratios of any two lines which have different probabilities of radiative transition or collisional de-excitation will exhibit a dependence on the electron density.

The populations of the upper electronic energy levels in PNe are governed by the amount of thermal energy available to excite the electrons (collisions are not a typical cause of excitation in PNe due to low densities). Hence, they are temperature-dependent. For a given ion, T_e can be calculated from the intensity ratios of electronic transitions originating from states with a large energy difference, as shown by the bottom panels of Figure 2.4 for O^{2+}. These typically use either optical lines, or a combination of optical and IR, due to the inverse relation between energy and wavelength from equation (2.1).

Infrared spectra show the emission of carbonaceous molecules that are associated with dust. They also show the atomic lines of low-excitation electronic transitions, which can be used in the analysis of both the chemical composition and the physical conditions around PNe. The next section gives a brief history of infrared astronomy, and details the two instruments used to obtain the data analysed in future chapters.

2.3 Infrared airborne and space telescopes

2.3.1 History

Spectral observations of PNe at mid- and far-IR wavelengths are best obtained from outside of Earth's atmosphere, as much of their emission are blocked by the absorption of water at these wavelengths. While current ground-based telescopes can accurately observe in the near-IR (e.g. the *William Herschel Telescope* or the *United Kingdom Infrared Telescope*), the emission of dust and atomic lines at greater IR wavelengths are more likely to be detected by telescopes that are either airborne or in space.

Indeed, airborne telescopes can detect most astronomical IR radiation from the lower stratosphere (Erickson, 1992). One of the pioneering airborne telescopes is the *Kuiper Airborne Observatory* (KAO, 1974–95), which operated with a 91 cm telescope that observed at IR wavelengths. *KAO* was the first telescope to detect the rings of Uranus (Elliot et al., 1977) and the atmosphere of Pluto (Elliot et al., 1989). It was capable of photometry and both echelle and heterodyne spectroscopy from ~ 0.3 to ~ 600 μm [2].

The first space telescope to operate at IR wavelengths was the *Infrared Astronomical Satellite* (IRAS, February–November 1983). Its main scientific goals were to carry out a sky survey that was unbiased from the effects of the Earth's atmosphere, and to detect point sources. It took photometric observations at wavelengths of 12, 25, 60 and 100 μm, as well as taking spectral observations in the range 7.5–23 μm with resolving power of 14–

[2] From "*NASA's Kuiper Airborne Observatory, 1971–1995: An Operations Retrospective With a View to SOFIA*", written by Erickson & Meyer (2013). URL: https://history.arc.nasa.gov/hist_pdfs/nasasp2013-216025.pdf

35 (Neugebauer et al., 1984). While it was active, it mapped around 96% of the entire sky. It has also been credited with the discovery of six comets and several other galaxies (e.g. Green et al. 1985; Meadows 1984).

IRAS was followed up by the *Infrared Space Observatory* (ISO, 1995–98). *ISO* improved upon *IRAS* through its greater wavelength coverage ($\sim$ 2–197 μm in spectroscopy with the *Short/Long Wavelength Spectrometers* (SWS/LWS) and up to 240 μm in photometry with *ISOCAM* and *ISOPHOT*), sensitivity and spatial resolution (Kessler et al., 1996), with which it enabled observations of many PNe within the Milky Way.

The JAXA-run *AKARI* (2006–11; Murakami et al. 2007) used a 68.5 cm telescope and consisted of two main instruments: the Infrared Camera (IRC), which carried out spectroscopy over the wavelength range 1.8–26.5 μm (Onaka et al., 2007), and the Far-Infrared Surveyor (FIS), producing photometry at 65, 90, 140 and 160 μm and Fourier transform spectroscopy from 50–180 μm (Kawada et al., 2007). The latter became defunct after August 2007 due to the crygoenic helium supply of *AKARI* running out. Studies of PNe from *AKARI* were able to utilise observations of dust emission features at 3.3 and 3.4 μm (respectively attributed to PAHs and HAC, e.g. Tielens 2005); this has not been possible with any other space telescopes since *ISO*.

The most recent infrared Space telescope, the *Herschel Space Observatory* (2009–13), specialised in far-IR wavelengths. It was capable of spectroscopy in the wavelength range 55–625 μm, including integral field unit (IFU) spectroscopy with the *PACS* instrument, heterodyne spectroscopy with *HIFI* and imaging Fourier transform spectroscopy with *SPIRE*, as well as photometry from 60–210 μm with *PACS* and at 250, 350 and 500 μm with *SPIRE* (Pilbratt et al., 2010). With *Herschel*, the first spatially resolved images of PNe at far-IR wavelengths were obtained (e.g. Ueta et al. 2014), providing information on the photodissociation regions of particular PNe, as can be detected from emission of cooling lines such as [O I] at 63 and 146 μm, and [C II] at 158 μm.

The next dedicated space telescope for infrared astronomy is the *James Webb Space Telescope* (JWST), estimated for launch in 2021 (at time of writing). A detailed description of its capabilities is given in Chapter 7.

2.3.2 The *Spitzer Space Telescope*

The *Spitzer Space Telescope* (2003 –) is the first telescope that has been sensitive enough to detect the infrared spectroscopic emission from PNe in the outer reaches of the Milky Way. The first reported publication based on the original ideas for the *Spitzer Space Telescope* came from NASA, dating back to 1976 (seven years before the launch of *IRAS*). The idea of an infrared telescope with a 1.2 m mirror (compared to the $\sim$ 60 cm mirrors of *IRAS* and *ISO*), that would be cooled below temperatures of 20 K with supercritical helium, was then introduced as the Spacelab Infrared Telescope Facility (SIRTF) (Witteborn and Young, 1976). Through its production, the primary mirror was scaled down to 85 cm, and SIRTF was renamed the "Spitzer Space Telescope" shortly after it was launched, after Lyman Spitzer Jr., the man credited for the idea of using telescopes in space.

Spitzer has three main instruments: the *Infrared Spectrograph* (IRS), the *Infrared Array Camera* (IRAC) and the *Multiband Imaging Photometer for Spitzer* (MIPS). *IRAC* carried out photometry at 3.6, 4.5, 5.8 and 8.0 μm, with the intention of viewing galaxies at redshifts of $1 < z < 5$ (Fazio et al., 2004), for which peak emission of stellar atmospheres is typically observed at a rest wavelength of 1.6 μm (John, 1988). While the rest of the instruments on board *Spitzer* have been inactive since 2009, the 3.6 and 4.5 μm cameras are still collecting data as part of the *Spitzer* "warm mission" (Fajardo-Acosta et al., 2007; Squires et al., 2007). *MIPS* specialised in mid- to far-IR astronomy, and was capable of both photometry (at 24, 70 and 160 μm) and spectroscopy from 52–100 μm (Rieke et al., 2004).

The Infrared Spectrograph (IRS)

All of the science involving *Spitzer* in this thesis will involve use of the *IRS*, as its mid-IR wavelength range of $\sim$ 5–37 μm is ideal for examining the emission of dust features, and

observing the main emission lines of neon, sulphur and argon ions for the calculation of their elemental abundances. *Spitzer* IRS produces both low- and high-resolution spectra from within four modules, as described in Table 2.1. The 'short' or 'long' refers to the wavelength range of the instrument, whereas the 'low' or 'high' describes the resolution. The sensitivity is greatest in the SL module, as shown in Figure 2.5, which is better suited for observing faint spectral features (e.g. weak dust emission); the high-resolution modules are better used for detecting atomic line emission. The wavelength ranges covered by these spectrographs are shown in Table 2.2.

The structure of the low-resolution modules is shown in Figure 2.6. These consist of two main orders (slits) plus a third 'bonus' order. Within each of these orders, the spectra are taken in two 'nod' positions, at one-third and two-thirds of the way along the order width. The two peak-up arrays obtain images at central wavelengths of 16 and 22 μm (for the blue and red arrays, respectively). These are used to locate the target and reposition the spectral slits so that it can be observed. The high-resolution modules are echelle spectrographs, i.e. they consist of several (in this case, ten) cross-dispersed orders, as shown in Figure 2.7.

The modules have different surface areas, and hence the amount of flux that each can detect is also different. The spectra analysed from *Spitzer* IRS in this thesis are scaled to the LH module, as it has the largest surface area and hence can detect the largest amount of flux from the observed source.

2.3.3 *Stratospheric Observatory for Infrared Astronomy* (SOFIA)

SOFIA (2010 –) is a 2.5 m telescope run by NASA that is fully operated on a Boeing 747 aeroplane, built as a successor to *KAO*. *SOFIA* has eight main instruments, covering wavelengths

Table 2.1 The four modules of the *Spitzer* IRS.

Name	Meaning	Wavelength range (μm)	Resolution	Angular size
SL	Short-Low	5.1 – 14.5	60 – 127	$3.6'' \times 57''$
LL	Long-Low	14.0 – 38.0	57 – 126	$10.5'' \times 168''$
SH	Short-High	9.8 – 19.5	~ 600	$4.7'' \times 11.3''$
LH	Long-High	18.7 – 37.2	~ 600	$11.1'' \times 22.3''$

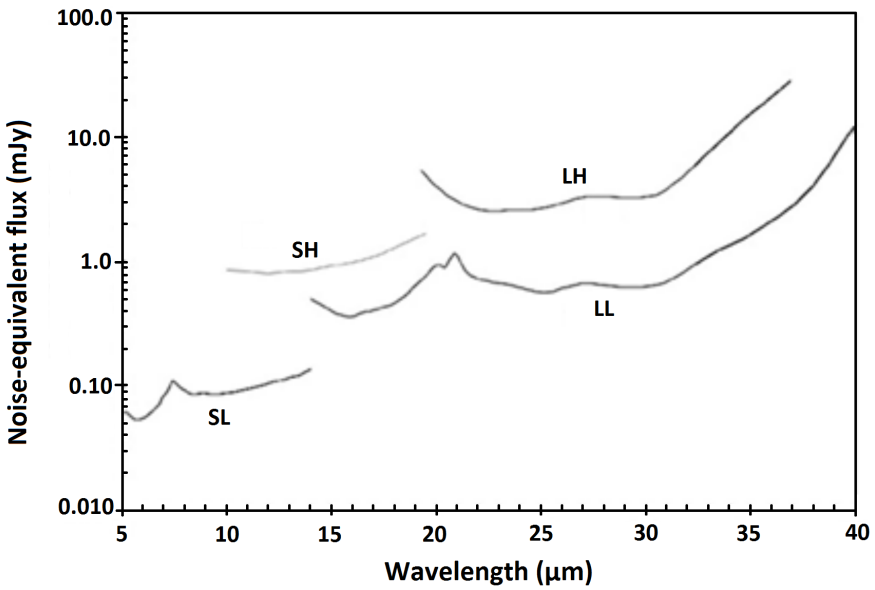

Fig. 2.5 Sensitivity of *Spitzer* IRS to 1-sigma detections, with a medium sky background, a 512 s integration time and an ecliptic latitude of 0°. Figure amended from the *Spitzer* IRS Instrument Handbook.

Table 2.2 The wavelengths of the *Spitzer* IRS orders.

Module	Order	Wavelength range (μm)	Module	Order	Wavelength range (μm)
SL	2	5.1 – 7.6	LL	2	14.0 – 21.3
	3	7.3 – 8.7		3	19.4 – 21.7
	1	7.4 – 14.5		1	19.5 – 38.0
SH	20	9.8 – 10.7	LH	20	18.7 – 20.7
	19	10.3 – 11.3		19	19.7 – 21.8
	18	10.9 – 12.0		18	20.8 – 23.0
	17	11.6 – 12.7		17	22.0 – 24.3
	16	12.3 – 13.6		16	23.4 – 25.9
	15	13.1 – 14.5		15	24.9 – 27.5
	14	14.0 – 15.5		14	26.7 – 29.4
	13	15.0 – 16.6		13	28.7 – 31.7
	12	16.3 – 18.0		12	31.0 – 34.2
	11	17.7 – 19.5		11	33.7 – 37.2

between 360 nm and 612 μm, through spectroscopy (*EXES*, *FIFI-LS*, *FORCAST*, *GREAT*) and photometry (*FLITECAM*, *FORCAST*, *FPI+*, *HAWC+*, *HIPO*). Of these instruments, *GREAT* covers heterodyne spectroscopy and *HAWC+* can also be used as a polarimeter.

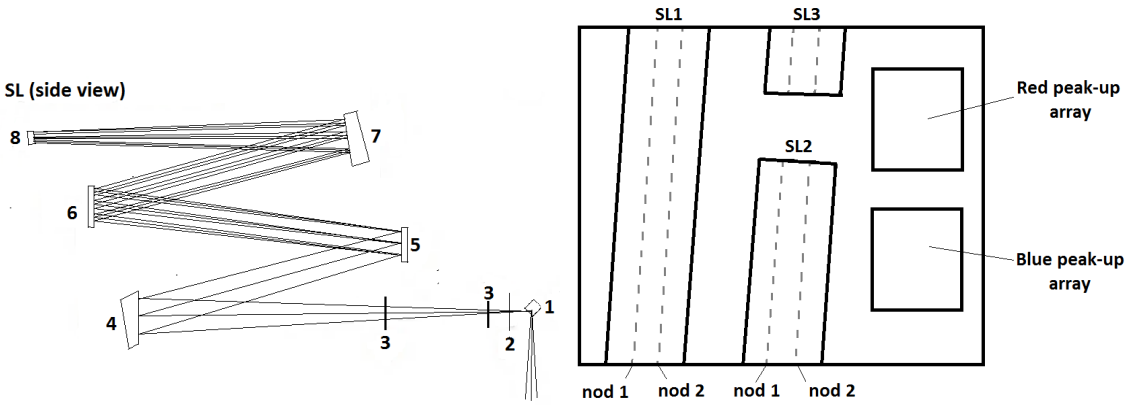

Fig. 2.6 Left: Schematic diagram of the *Spitzer* IRS short-low (SL) module with labels: (1) Pick-off mirror for incident light; (2) Slits; (3) Pass filters, which maintain light of the required wavelengths; (4) Collimator; (5) Grating; (6) Schmidt corrector lens, used to diffract the light to reach spherical lenses; (7) Schmidt camera; (8) Focal plane array, which shows the output. Figure amended from the IRS Instrument Handbook. Right: Schematic diagram of the output from the *Spitzer* IRS short-low (SL) module. The long-low (LL) module has a similar layout of the spectral orders, but does not include the peak-up arrays.

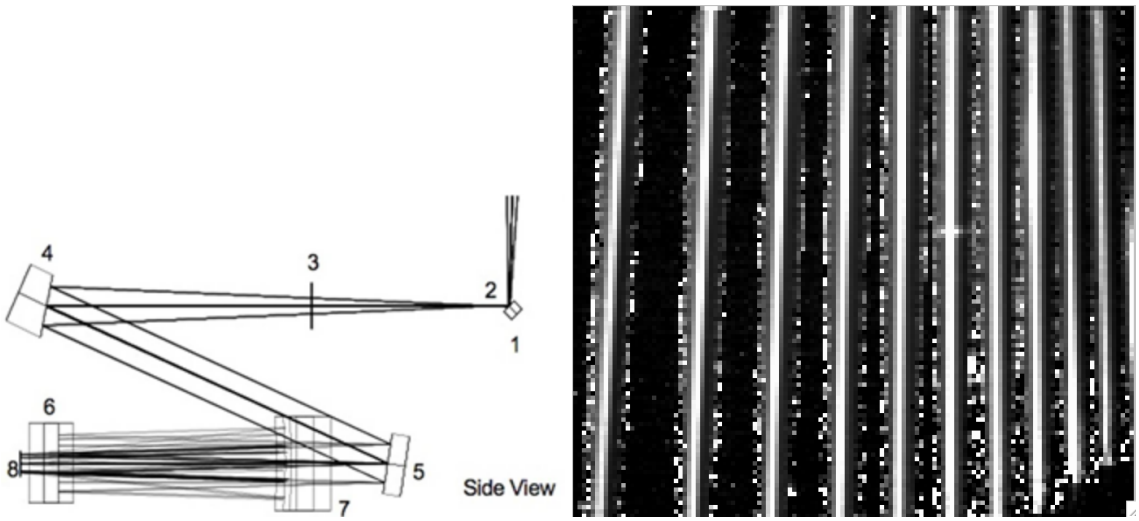

Fig. 2.7 Left: Schematic diagram of the *Spitzer* IRS short-high (SH) module with labels: (1) Pick-off mirror for incident light; (2) Slits; (3) Pass filter; (4) Collimator; (5) Cross-dispersion grating; (6) Echelle grating; (7) Camera mirror; (8) Focal plane array. Figure reproduced from the IRS Instrument Handbook. Right: Example SH nod 1 spectrum from PN M4-18, post-data handling; see § 2.4 for more information on these steps.

The Far-Infrared Field-Imaging Line Spectrometer (FIFI-LS)

FIFI-LS has a resolution R $\sim$ 500–2000, depending on the observed wavelength. Unlike *Spitzer* IRS, FIFI-LS works as an IFU spectrometer; it has two channels, the 'blue' channel (51–120 μm, FOV = 0.5 square arcminutes, $6'' \times 6''$ pixel size) and the 'red' channel (115–203 μm, FOV = 1 square arcminute, $12'' \times 12''$ pixel size), through which spectra can be obtained through each individual pixel. Both channels consist of 5×5 pixels, which can be reorganised as an effective 25×1 pixel slit, then the light is dispersed by a diffraction grating and picked up by a 16×25 pixel detector array. Figure 2.8 shows this schematically.

The far-IR wavelength range of FIFI-LS enables us to observe the spectra of cooling lines around a PN, particularly the [O I] 63 and 146 μm and [C II] 158 μm lines. These emission lines are typically observed within the neutral PDRs around PNe (see § 1.3), and therefore IFU spectra of these lines can provide insight into the environments in which the dust is located.

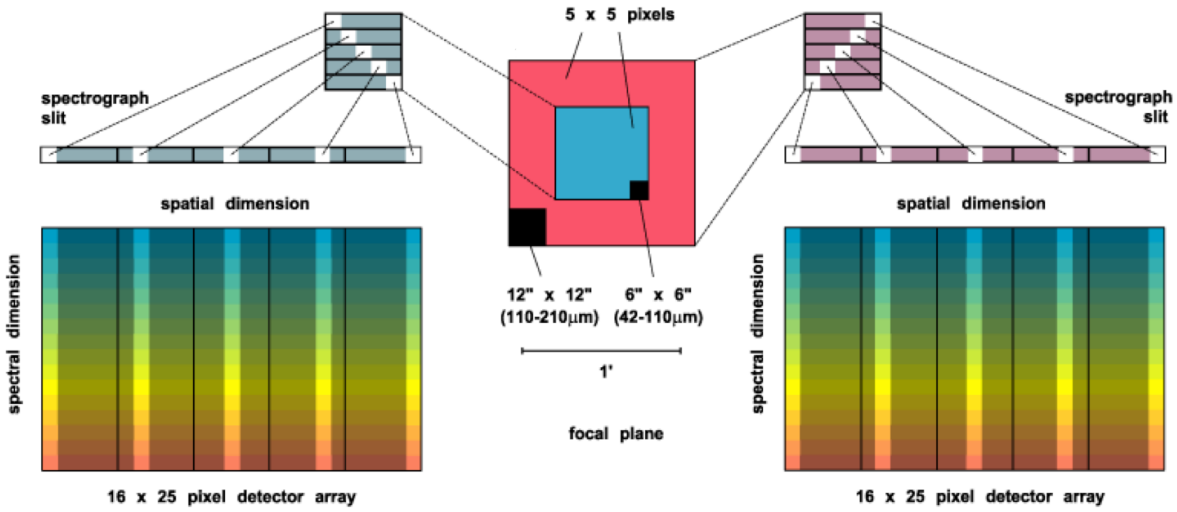

Fig. 2.8 Schematic diagram of the FIFI-LS instrument on board *SOFIA*. Figure reproduced from the Cycle 6 *SOFIA* Observers' Handbook.

2.4 Data processing

Data from *Spitzer* IRS and *SOFIA* FIFI-LS are ideal for examining the emission of atomic lines, dust, organic molecules and neutral species from PNe. This section explains the processes involved in the data handling from both instruments, using programs written in Interactive Data Language (IDL).

2.4.1 Spectroscopic Modelling Analysis and Reduction Tool (SMART)

The *SMART* program (Higdon et al., 2004) provides a graphical user interface designed to carry out the reduction of *Spitzer* IRS data. The reduction and extraction of spectra in Chapters 3, 4 and 5 of this thesis have been carried out using *SMART* version 8.2.9, released in September 2014. Figure 2.9 shows a flowchart of all involved processes, from downloading the data to extracting the spectra.

A full catalogue of *Spitzer* IRS data is available to download from the *Spitzer* Heritage Archive[3]. The *Spitzer* data analysed throughout this thesis have been reduced and handled

[3]http://sha.ipac.caltech.edu/applications/Spitzer/SHA/

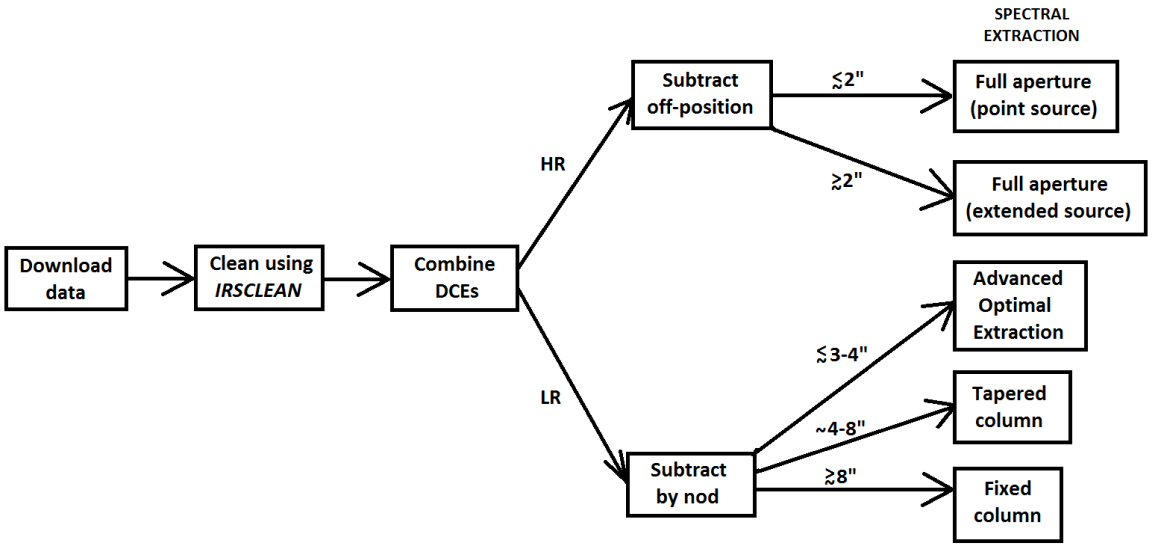

Fig. 2.9 Flowchart showing the processes of data handling and extraction through *SMART*. HR = high resolution; LR = low resolution. The extraction methods are explained in the text.

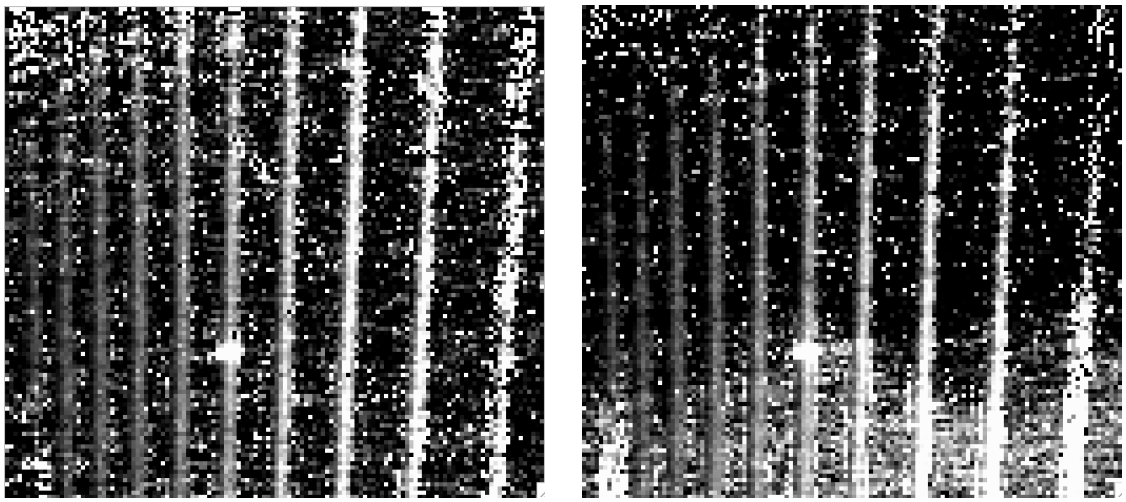

Fig. 2.10 Two DCEs from an exposure of the planetary nebula Y-C 2-5, from nod 1 of the LH module of *Spitzer* IRS. The DCE on the left is relatively typical, whereas the DCE on the right shows uneven dark current and is therefore disregarded. The bright spot slightly to the lower-left of centre is the [O IV] 25.9 μm emission line.

from the original uncalibrated Level 1 data. Each observation was cleaned of rogue pixels using the *IRSCLEAN*[4] program.

Several spectra were taken from both nod positions of a particular module. The spectra taken from each nod are known as data collection events (DCEs), which were used to produce a combined spectrum after cleaning rogue pixels. Before combination, care was always taken to remove DCEs from which there were issues with uneven dark current, such as in the image shown on the right of Figure 2.10. Otherwise, the flux observed in each of the orders would be greater towards blue wavelengths, which would make the stitching of orders difficult. To further reduce noise levels and glitches, low-resolution data were subtracted by those from the opposite nod, and high-resolution data were subtracted by off-position observations.

Spectra were then extracted using one of several methods offered by *SMART*. These were based on the resolution and the diameter of the source, as shown in Figure 2.9. For high-resolution data, full-aperture extractions were used. These involved summing the flux over the spectral slits, and pixels with "not-a-number" (NaN) values were replaced with average pixel values. Low-resolution data were extracted through one of three methods. The standard method is the "tapered column" extraction, which sums the flux over the slit using a

[4]Available from the *Spitzer* Science Center website: http://ssc.spitzer.caltech.edu.

column that increases with the point-spread function (PSF), i.e. the response of the instrument when observing a point source, which increases with wavelength. This is in accordance with:

$$\theta = \frac{1.22\lambda}{d} \tag{2.12}$$

where θ is the angular resolution of the instrument in radians, λ is the observed wavelength of light and d is the diameter of the observing aperture.

Spectra of smaller sources were extracted using the *Advanced Optimal Extraction* (AdOpt, Lebouteiller et al. 2010) method, which measures the PSF at each wavelength and weights each pixel by their signal-to-noise ratio, instead of weighting them equally. For more extended sources, a "fixed column" extraction was preferred, as this added the flux within a wider area than a tapered column extraction offers. In all cases, user interaction was required to identify the source within the spectral image.

After the spectrum was extracted, the edges of the orders (which are typically noisy) were masked en masse (though the edges of particular orders would be unmasked if they covered wavelengths with emission of dust features or atomic lines), and glitches were masked individually. Lines were measured using the *ISO Spectral Analysis Package* (ISAP, Sturm et al. 1998), in which a continuum was fit to data points specified by the user, and a Gaussian was fit by identifying the line. Flux values are given in W m^{-2}.

For broad dust emission features, *SMART* has been used to fit multiple Gaussians with specified wavelengths and full-width half-maxima (FWHM). The methods for this are detailed in Chapter 4. However, single-Gaussian flux measurements for dust emission features are carried out by use of an external program based on *SMART*, which fits the Gaussian within a specified wavelength range and with an extra central point, which may be user-defined or fit at the peak if chosen. If there is a relatively low signal-to-noise ratio in a spectrum, the recorded peak flux value may not represent that of the feature. Hence, I have defined each of the central points for the broad dust flux measurements.

2.4.2 FLUXER

The handling of *SOFIA* data was carried out using *FLUXER*. This is a program created by Christof Iserlohe[5], designed to handle IFU data from various telescopes such as *SOFIA*, *Keck* and the *Very Large Telescope* (VLT). Figure 2.11 shows the main processes involved in displaying the data and measuring flux values.

The *SOFIA* FIFI-LS data used in this thesis were reduced and corrected before being handled in *FLUXER*. A brief summary of the pipelines used for reduction, in accordance with the Guest Investigator Handbook for FIFI-LS Data Products[6], is as follows: background noise was removed through the chopping and nodding of the telescope, where "chopping" involves the subtraction of the sky background from the source flux and "nodding" infers the combination of images of the same source taken from two different observing slits. Wavelengths were calibrated to account for the motion of Earth with regard to the local standard of rest, i.e. the mean movement of material from the Galactic disk, as observed from within the solar neighbourhood (e.g. Shu 1982). Flat-field frames were removed and telluric corrections were made, resulting in data being masked at wavelengths corresponding to emission from Earth's atmosphere. Flux values were calibrated to nearby asteroids or moons, as few stars emit strongly at far-IR wavelengths.

[5]http://www.ciserlohe.de/fluxer/fluxer.html
[6]https://www.sofia.usra.edu/sites/default/files/FIFI-LS_GI_Handbook_RevB1.pdf

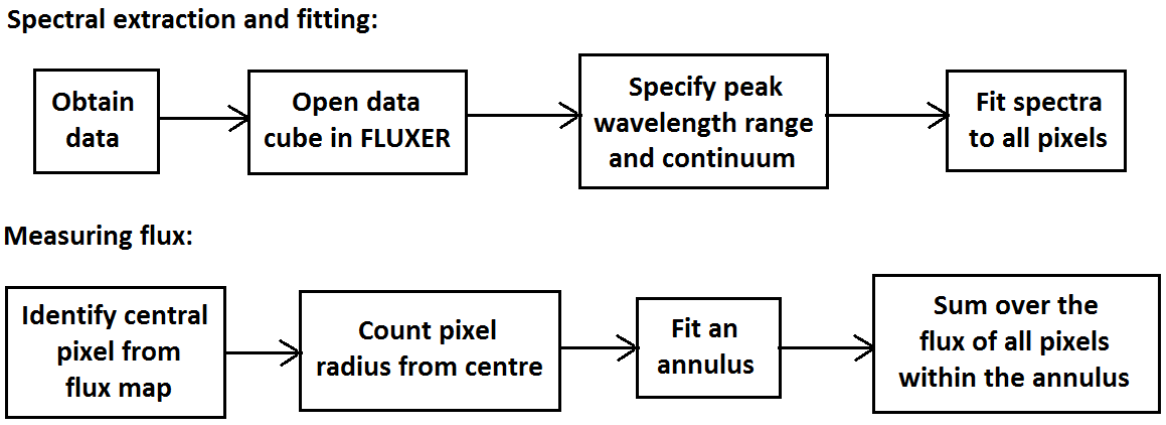

Fig. 2.11 Flowchart showing the processes of Level 4 data handling through *FLUXER*.

The reduced data cubes were accessed through *FLUXER*. Each data cube covered wavelengths within ~ 0.5 μm on both sides of the line of interest. Figure 2.12 shows examples from the user interface. The wavelength ranges for the peak and continuum were specified in one pixel by the user, and these wavelength bounds were fit to the spectra in all pixels. At this stage, spatial maps of quantities such as the flux values and peak wavelengths of the emission lines could be plotted.

Flux measurements from spectral lines were measured by applying an annulus of specified radius to cover as many pixels as possible, and summing over the flux values for each pixel. There are greater uncertainties in flux values when the emission map is not circular.

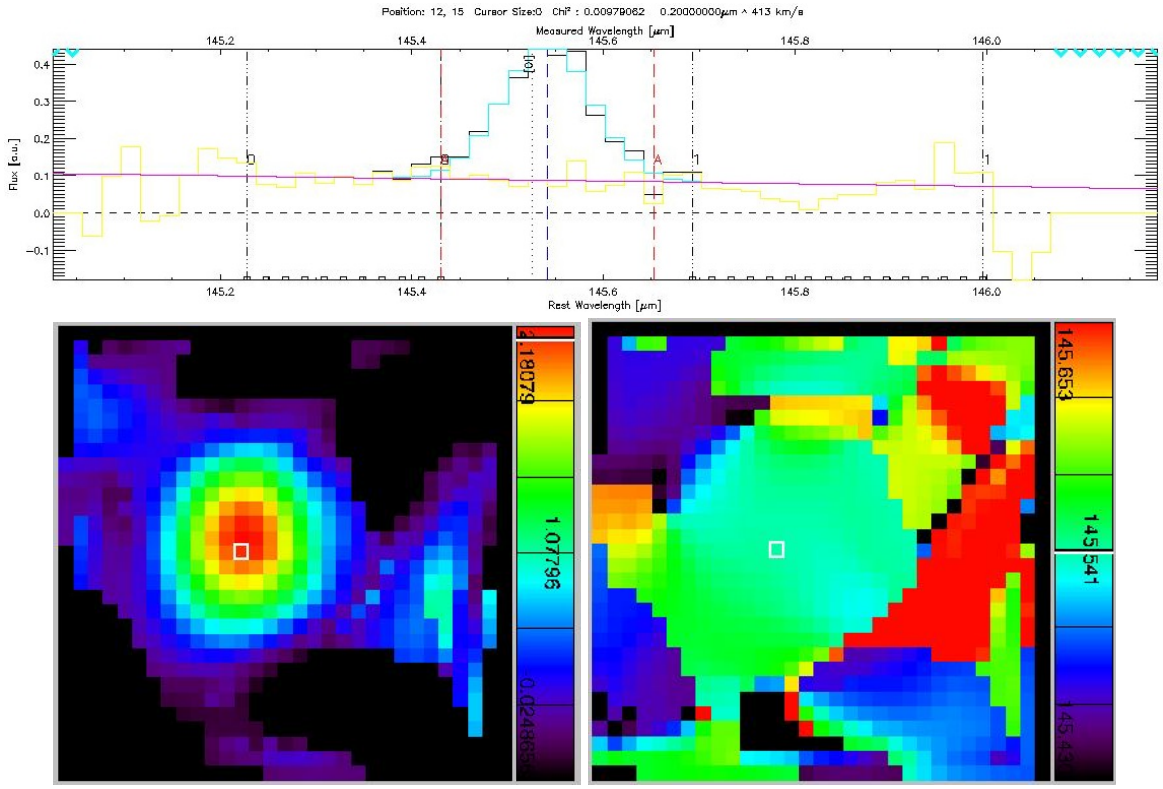

Fig. 2.12 Examples of spectra and IFU maps as shown from the *FLUXER* interface. Top: the spectrum of one pixel from the IFU ([O I] 146 μm in PN M1-11). The two red dashed vertical lines represent the peak wavelength range, the black dot-dashed vertical lines are the specified continuum wavelengths. The original spectum consists of the continuum (yellow) and the emission line (black), over which a Gaussian is fitted (cyan) with central wavelength shown by the dark blue dashed line. On the y-axis, flux is measured in Janskys. Bottom-left: intensity map of all pixels in the IFU using specified line limits from top figure. Black regions represent pixels where the Gaussian flux between the specified wavelengths is less than zero. Bottom-right: map of central wavelengths for all pixels in the IFU. In the bottom figures, the highlighted pixel represents the spectrum of the top figure.

The flux is given in Janskys, where:

$$1 \text{ Jy} = 10^{-26} \text{ W m}^{-2} \text{ Hz}^{-1} \tag{2.13}$$

By multiplying by the width of a wavelength bin in the spectrum, a value in Jy μm was obtained. These units were converted to W m^{-2} by:

$$F(\text{W m}^{-2}) = \frac{F(\text{Jy } \mu m)}{\lambda^2} \times 3 \times 10^{14} \tag{2.14}$$

where 3×10^{14} represents the speed of light in units of μm s^{-1}. If the observed area of the target was known in square arcseconds, the flux per steradian was given as:

$$F(\text{W m}^{-2} \text{ sr}^{-1}) = F(\text{W m}^{-2}) \times \frac{A \text{ (sq.arcsecs)}}{4.25 \times 10^{10}} \tag{2.15}$$

where 4.25×10^{10} is the number of square arcseconds in a steradian. These units are used with the models in Chapter 6.

2.5 Summary

Infrared spectra are ideal for observing dust features around PNe, such as PAHs and fullerenes, and for observing the forbidden line emission from the fine-splitting ground electronic states for ions of elements such as neon, sulphur and argon. The elemental abundances can be deduced from these observations, and the physical conditions of these sources, such as the electron temperatures and electron densities, can be calculated from the intensities of these mid-IR emission lines. With the *Spitzer Space Telescope*, all of these lines and features can be observed from PNe in the outskirts of the Milky Way. At far-IR wavelengths, emission from neutral and low-ionisation species can be observed with *SOFIA*. These lines originate from the PDRs of PNe, which also contain the dust around these stars, and hence this cooling line emission can be analysed to provide the physical conditions of the environments in which these dust features are observed.

The underlying physics and main methodologies applied throughout this thesis have now been introduced. In the next chapter, the abundances of a sample of PNe located towards the outskirts of the Milky Way galaxy, as observed with *Spitzer* IRS, are investigated in order to establish the potential continuation of the Galactic abundance gradient introduced in Chapter 1.

Chapter 3

Neon, sulphur and argon abundances of planetary nebulae in the sub-solar metallicity Galactic anti-centre

(The work presented in this chapter has been published in *Astronomy & Astrophysics* as Pagomenos et al. 2018. A preliminary version was also published in a conference proceedings as Pagomenos et al. 2017.)

3.1 Introduction

As Sun-like stars (of $\sim$ 0.8–8 $M_{\odot}$) evolve, they eventually become planetary nebulae (PNe). In this evolutionary phase, the star has lost enough of its convective envelope through stellar winds to expose its inner, hotter regions, causing this ejected material to become ionised. The ionic and elemental abundances of this PN ejecta can be determined by analysing the strong forbidden emission lines of the ions in the stellar spectrum.

Spectra of PNe taken at mid-IR wavelengths show numerous α-process elements, such as neon, sulphur and argon. While the abundances of elements like helium and carbon change significantly throughout the course of stellar evolution, those of neon, sulphur and argon are

unchanged (e.g. Marigo et al. 2003), making them useful probes of metallicity at the epoch of stellar formation. Abundance studies carried out at optical wavelengths commonly use oxygen as a metric for metallicity, as the observed emission lines of O^+ and O^{2+} are always strong. However, during the evolution of these low- to intermediate-mass stars, the abundances of oxygen are known to change. This particularly occurs within the asymptotic giant branch (AGB) phase, in which the third dredge-up brings helium, carbon and a small amount of oxygen to the outer envelope of the star. For stars with mass $\gtrsim 4$ $M_\odot$, some oxygen will also be destroyed by hot bottom burning (e.g. Delgado-Inglada et al. 2015; Karakas and Lattanzio 2014). An empirical study by Delgado-Inglada et al. (2015) has also shown that oxygen enrichment can occur in Galactic PNe with carbonaceous dust. It has been proposed by García-Hernández et al. (2016) that this can be explained by diffusive convective overshooting processes, i.e. those that extend core mixing beyond the Schwarzschild boundary of main sequence stars (Böhm-Vitense, 1958; Herwig et al., 1997), produce significant increases in oxygen abundances around solar metallicity (Marigo, 2001; Pignatari et al., 2016).

While most abundances from observational studies have been measured using optical spectra, there are some advantages to analysing PNe using infrared spectra. These are described in several studies (e.g. Bernard-Salas 2003; Pottasch and Beintema 1999; Rubin et al. 1988), but can be summarised as follows: extinction corrections are greatly reduced at IR wavelengths compared to those in the optical and ultraviolet regions; many ionic emission lines are observable for Ne, S and Ar within this wavelength range, and hence the need for ionisation correction factors (ICFs) in calculating elemental abundances is reduced; as these IR lines also originate from energy levels close to the ground state, both the uncertainties in the electron temperatures of any ion measured at IR wavelengths and temperature fluctuations within the PN can have little effect on the overall abundances. For this study in particular, the extinction corrections are reduced further as the Galactic anti-centre, a region with much less extinction than the bulge (e.g. Pottasch and Bernard-Salas 2015), is considered.

The presence of the Galactic metallicity gradient was made clear in a sample of H II regions by Shaver et al. (1983) for nitrogen, oxygen, sulphur and argon. Since then, it has

been further studied not only in H II regions (e.g. Esteban et al. 2017; Fernández-Martín et al. 2017; Martín-Hernández et al. 2002) but also in PNe (e.g. Maciel et al. 2015; Maciel and Quireza 1999; Pottasch and Bernard-Salas 2006), young B-type stars (e.g. Fitzsimmons et al. 1992; Rolleston et al. 2000), Cepheid variables (e.g. Andrievsky et al. 2002a,b,c; Genovali et al. 2015; Lemasle et al. 2013; Luck et al. 2003), open clusters (e.g. Friel 1995) and young stars (e.g. Magrini et al. 2017).

While the presence of the metallicity gradient in the Galactic disk is agreed upon over Galactocentric distances (R_g) in the range 4–10 kpc, its continuation towards the anti-centre is debated. Studies of H II regions (Esteban et al., 2017; Fernández-Martín et al., 2017) and B-type stars (Smartt, 2000) have found that there is little variation in the gradient far from the Galactic centre, yet a study of Cepheid variables from Andrievsky et al. (2002c) showed the gradient flattening with R_g. Samples of PNe have also been previously analysed in the anti-centre with conflicting results. Costa et al. (2004) showed that the oxygen abundances of a group of PNe, 8–15 kpc away from the Galactic centre, did not directly follow the gradient but instead flattened beyond 10 kpc. This has also been observed in the nearby spiral galaxies M31, M33, M81 and NGC 300 (Magrini et al., 2016). However, the sample of Henry et al. (2010) suggested that the gradient steepened beyond this distance.

Chemical evolution models of the Milky Way have predicted that the radial abudance gradient will flatten over time due to several factors, such as the methodologies of Galactic archaeology, in which metallicity increases over time due to the death of massive stars, causing enrichment in the ISM (e.g. Minchev et al. 2013), and radial migration (e.g. Kubryk et al. 2015; Minchev et al. 2014, 2012; Vera-Ciro et al. 2014), in which the angular momentum from stars is redistributed, leading to the movement of stars from the Galactic disk and hence contributing to a flattening radial metallicity gradient with Galactocentric distance (e.g. Sellwood and Binney 2002).

Investigations into the time evolution of the radial metallicity gradient have given varying results, with several studies of PNe finding an overall steepening with time (e.g. Chiappini et al. 2001; Kubryk et al. 2015; Maciel and Quireza 1999; Stanghellini and Haywood 2010),

suggesting that the Galactic disk formed slowly (Chiappini et al., 1997). However, Maciel et al. (2003) showed the gradient to flatten over time. Studies of open clusters and field stars have also given varying conclusions on this matter (Anders et al., 2017).

In this chapter, the abundances of neon, sulphur and argon are derived in a sample of 23 PNe located towards the Galactic anti-centre using IR data, in order to study the metallicity gradient beyond 10 kpc, and these are compared to other IR spectroscopic samples from the Milky Way that were analysed in the same way.

The layout of this chapter is as follows: In § 3.2, the source selection and the basic data reduction and extraction methods are discussed. In § 3.3, the methods used to calculate flux, intensity, abundance values and Galactocentric distances are explained. The implications of these data on the metallicity gradient in the further regions of the Milky Way are considered in § 3.4. Finally, in § 3.5, the main results are summarised.

3.2 Data

3.2.1 Observations

The observations were made with *Spitzer* IRS (Houck et al., 2004; Werner et al., 2004) through GTO program 40035 (PI: J. Bernard-Salas). The observations were carried out between December 2007 and December 2008 with the staring mode of the IRS using the Short-Low (SL), Short-High (SH) and Long-High (LH) modules (see Table 2.1), each allowing for simultaneous observations from two *nod* positions, at 1/3 and 2/3 of the way along the observing slit.

The 23 sources are listed in Table 3.1. These were chosen from the *Strasbourg-ESO catalogue* compiled by Acker et al. (1992), in order to meet the following two criteria: (a) the sources were located in the direction of the anti-centre (l = 120–240°, $b = 0° \pm 20°$); (b) the physical sizes of the PNe were generally small enough to fit in the widest observing slit of *Spitzer* IRS (LH, $11.1'' \times 22.3''$), thus minimising the aperture corrections required to account for the different slit sizes. These small angular sizes further suggest the location of

Table 3.1 The 23 PNe observed in the sample. 'AORkeys' represent the *Spitzer* IRS observation data.

Source *Name*	Source *PNG*	RA (J2000) *(h m s)*	Dec (J2000) *(d m s)*	AORkey	AORkey *off position*	R_g *(kpc)*
J320	190.3−17.7	05 05 34.32	+10 42 23.8	21946880	21947136	13.6 ± 1.6
K3-65	153.7−01.4	04 15 54.53	+48 49 40.1	21947392	21947648	11.5 ± 2.1*
K3-66	167.4−09.1	04 36 37.23	+33 39 30.0	21947904	21948160	15.8 ± 2.3
K3-67	165.5−06.5	04 39 47.93	+36 45 42.6	21948416	21948672	14.4 ± 4.3†
K3-68	178.3−02.5	05 31 35.86	+28 58 41.6	21948928	21949184	10.2 ± 1.8*
K3-69	170.7+04.6	05 41 22.13	+39 15 08.1	21949440	21949696	>13.9*
K3-70	184.6+00.6	05 58 45.34	+25 18 43.8	21949952	21950208	>14.0*
K3-71	184.8+04.4	06 13 54.98	+26 52 57.0	21950464	21950720	10.5 ± 2.0*
K3-90	126.3+02.9	01 24 58.70	+65 38 34.7	21950976	21951232	<8.7*
K4-48	201.7+02.5	06 39 55.84	+11 06 30.3	21952000	21952256	16.6 ± 5.0†
M1-1	130.3−11.7	01 37 19.43	+50 28 11.6	21952512	21952768	14.7 ± 2.4
M1-6	211.2−03.5	06 35 45.13	−00 05 37.5	21953024	21953280	9.8 ± 1.8*
M1-7	189.8+07.7	06 37 20.96	+24 00 35.4	21953536	21953792	14.5 ± 1.9
M1-8	210.3+01.9	06 53 33.79	+03 08 27.0	21954048	21954304	12.2 ± 1.4
M1-9	212.0+04.3	07 05 19.20	+02 46 59.5	21954560	21954816	16.2 ± 2.5
M1-14	234.9−01.4	07 27 56.50	−20 13 22.8	21955072	21955328	11.4 ± 1.1
M1-16	226.7+05.6	07 37 18.93	−09 38 48.0	21955584	21955840	13.0 ± 1.8
M1-17	228.8+05.3	07 40 22.19	−11 32 29.9	21956096	21956352	14.8 ± 2.3
M2-2	147.8+04.1	04 13 15.04	+56 56 58.1	21956608	21956864	>9.7*
M3-2	240.3−07.6	07 14 49.92	−27 50 23.3	21957120	21957376	15.3 ± 2.6
M4-18	146.7+07.6	04 25 50.85	+60 07 12.8	21957632	21957888	15.0 ± 2.2
SaSt2-3	232.0+05.7	07 48 03.67	−14 07 40.4	21958144	21958400	20.8 ± 4.1
Y-C 2-5	240.3+07.0	08 10 41.64	−20 31 32.6	21958656	21958912	13.2 ± 6.6‡

Notes: The Galactocentric distances and their errors were determined from heliocentric values determined statistically from Frew et al. (2016), assuming $R_{g,\odot} = 8.0 \pm 0.5$ kpc, except: * directly measured distances from Giammanco et al. (2011); † statistical distances from Phillips and Márquez-Lugo (2011); ‡ statistical distance from Costa et al. (2004), from which a 50% error is assumed.

Table 3.2 Aperture corrections applied to each of the line flux values.

PN	Diameter ($''$)	SL $\rightarrow$ SH	SH $\rightarrow$ LH
J320	7	1.40	1.47
K3-65	5	1.20	1.15
K3-66	2	1.05	1.00
K3-67	2	1.00	1.00
K3-68	12	1.50	2.00
K3-69	$<$1	1.00	1.00
K3-70	2	1.00	1.05
K3-71	3	1.00	1.00
K3-90	10	1.00	2.00
K4-48	2	1.15	1.08
M1-1	5	1.00	1.50
M1-6	4	1.20	1.12
M1-7	11	1.00	2.20
M1-8	18	1.00	2.00
M1-9	3	1.12	1.07
M1-14	5	1.50	1.30
M1-16	3.6	1.38	1.18
M1-17	3	1.18	1.05
M2-2	7	2.30	2.00
M3-2	8	1.00	1.00
M4-18	4	1.12	1.00
SaSt2-3	$<$1	1.00	1.00
Y-C 2-5	8	1.00	1.70

the PNe towards the anti-centre, as opposed to within the solar neighbourhood; many PNe with Galactocentric distances of less than $\sim$ 3 kpc typically have sizes of at least $30'' \times 30''$ (e.g. Frew et al. 2016). The sample size of 23 allows for significant statistical analysis in the upcoming abundance plots and metallicity gradients, and is comparable to those of other PN studies.

3.2.2 Data reduction and extraction

The basic calibration data (*bcd*) image files obtained from the *Spitzer* IRS were processed through the *Spitzer* Science Centre (SSC) pipeline, version S18.18, then reduced and analysed through the "Spectroscopic Modelling Analysis and Reduction Tool" (*SMART*) (Higdon et al., 2004).

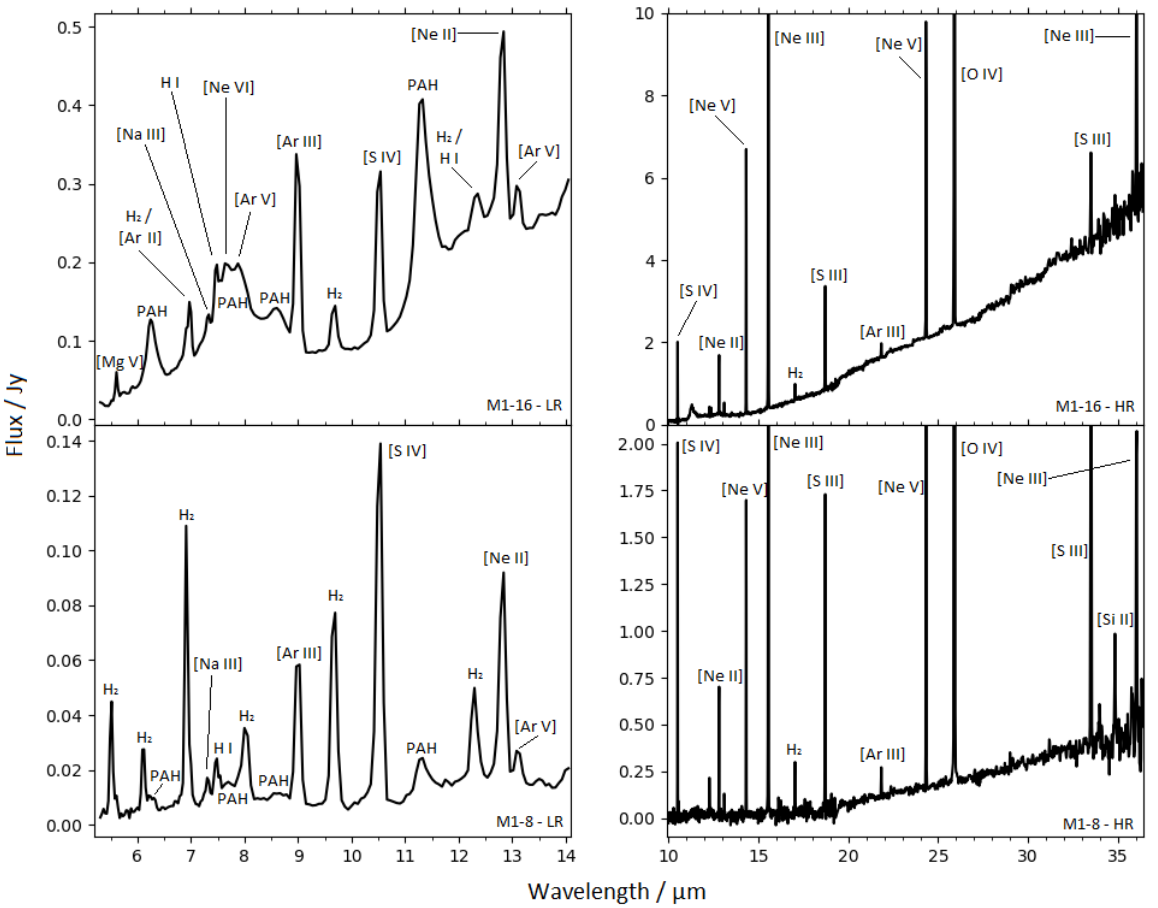

Fig. 3.1 The full *Spitzer* IRS spectrum of M1-16 (top) and M1-8 (bottom). The low resolution spectra (SL) are shown on the left, and the high resolution spectra (SH and LH) are on the right.

The data reduction processes are explained in detail in Chapter 2. Most of the PNe in this sample were chosen such that all of the source flux would fall within the LH module. In fact, 15 of the 23 targets also have a physical diameter of $\leqslant 5''$, so in these cases most of the flux would also be detected by the smaller and narrower SH module ($4.7'' \times 11.3''$). Some of the source flux still might not be detected by the SL and SH modules, resulting in jumps in the baseline continuum. To account for this, the SL and SH flux values are scaled by matching the continua in the overlapping wavelength regions. The scale factors are listed in Table 3.2.

Figure 3.1 shows the full low- and high-resolution spectra of two representative PNe in the sample, M1-16 and M1-8.

3.3 Analysis

3.3.1 Ionic abundances

The ionic abundances obtained from the spectra have been calculated using equation (2.9). For the derivation of the neon, sulphur and argon abundances, the emission lines have been observed for the most populated ions of these elements: Ne^{+}, Ne^{2+}, Ne^{4+}, S^{2+}, S^{3+}, Ar^{+}, Ar^{2+} and Ar^{4+}. These IR ionic abundances are complemented with those of the missing ionisation states from optical spectra (Ne^{3+}, S^{+} and Ar^{3+}) in the literature in order to avoid or reduce the need for ICFs. These values were primarily taken from Henry et al. (2010) and references included in Sterling and Dinerstein (2008). As IR and optical data are being compared, homogeneity is assumed in the slit sizes; this is a resonable assumption as Henry et al. (2010) use data from the Apache Point Observatory (APO), for which the slit size is $2'' \times 360''$, and most of the PNe from this sample that they have observed are $\lesssim 4''$ in diameter, so most of the flux will have been detected from these sources. S^{4+} is also considered, which is not directly detectable in IR or optical spectra, although it is only expected to contribute to the overall sulphur abundance for PNe with high IP values. Where there are no flux values available for any particular line in a PN, correction factors are applied (see § 3.3.6).

3.3.2 Line flux measurements

Flux values for the fine structure ionic emission lines with a $\geqslant 3\sigma$ detection were determined by applying Gaussian fits through the ISAP line fitting program (Sturm et al., 1998) in *SMART*. The raw $F(\lambda)$ values were calculated for each line in each of the two oberving positions (nods), which typically agreed to within 10%. These were then averaged; in the few cases where there were any remaining low-level glitches obstructing a particular line, these were discarded in favour of the flux value from the nod without glitches. The associated uncertainties were propagated from those calculated from the individual flux measurements within each nod, unless the difference in flux between the two nods was greater than the assumed uncertainties, in which case this difference was taken as more representative of the

Table 3.3 Selected line intensity values from the Galactic anti-centre PNe, in units of 10^{-14} erg cm^{-2} s^{-1}. Continued on next page.

PN	H I		[O IV]	[Ne II]	[Ne III]		[Ne V]	
	7.5μm	*12.4μm*	*25.9μm*	*12.8μm*	*15.6μm*	*36.0μm*	*14.3μm*	*24.3μm*
J320	21.3	7.82	...	6.60	761	50.9	...	...
K3-65	2.81‡	...	...	15.0	186	<24.5	...	...
K3-66	16.4†	6.40	3.20	94.7	185	...	<4.75	<3.74
K3-67	32.7	11.7	7.16	28.3	778	54.2	<5.12	<3.73
K3-68	...	...	1190	<2.95	37.4	...	23.0†	23.6
K3-69	4.88†	...	35.3	5.72	176	...	33.4	8.52
K3-70	3.56†	...	61.0	5.44†	92.7	...	23.4	15.4
K3-71	1.33‡	...	913	<2.12	18.6	...	32.6	43.4
K3-90	...	1.97†	2070	<2.55	32.6	...	131	152
K4-48	...	3.94†	143	20.0	497	23.0	22.4	8.02
M1-1	...	...	1620	<2.59	30.5	...	670	753
M1-6	104	36.2†	...	1320	57.5	...	...	...
M1-7	20.5	8.40†	371	61.4	874	52.7	2.89†	2.63
M1-8	6.31†	...	834	28.9	323	26.4†	63.9	55.9
M1-9	38.5†	8.94	...	111	371	...	...	...
M1-14	73.1	25.9	...	727	446	37.7	...	...
M1-16	20.3	8.68	854	61.7	1070	76.4	256	147
M1-17	42.9	9.84†	336	47.2	849	67.3†	20.4	11.8
M2-2	63.2	20.9†	216	7.86	1520	99.6	<3.78	<2.85
M3-2	...	...	27.8	2.59	10.4	...	5.53	10.7†
M4-18	...	...	...	334	<142	...	...	...
SaSt2-3	5.56†	...	...	32.4	<1.78	...	...	...
Y-C 2-5	2.62†	...	1190	<1.36	86.9	25.9†	...	...

Uncertainties are $< 10\%$, except: † uncertainties 10–20%, ‡ uncertainties 20–35%. * No line is observed, and the presence of the H_2 0–0 S(5) feature at 6.9μm prevents an accurate upper limit being taken.

uncertainty. The data were then corrected for extinction using the extinction law from Fluks et al. (1994). Table 3.3 shows all values for the extinction corrected intensities, $I(\lambda)$. Upper limits of 3σ or more were calculated for emission lines of the most important ions of neon, sulphur and argon when there were no clear detections.

3.3.3 Extinction corrections

The extinction law of Fluks et al. (1994) has been applied to the flux values, which extends that of Savage and Mathis (1979) into IR wavelengths. This law identifies values of $A_\lambda \,/\, E(B-V)$,

Table 3.3 (Continued)

PN	[S III]		[S IV]	[Ar II]	[Ar III]		[Ar V]	
	18.7μm	*33.5μm*	*10.5μm*	*7.0μm*	*9.0μm*	*21.8μm*	*7.9μm*	*13.1μm*
J320	82.1	34.4	1020	<1.72	28.0	<2.39	...	...
K3-65	49.8	38.4	53.7	8.31	17.9	<1.81	...	...
K3-66	51.9	22.2	30.2	18.1†	32.7	<2.82	...	...
K3-67	108	42.1	519†	8.89	66.2	5.00†	...	...
K3-68	10.6	11.1	98.8†	<5.60	<4.80	<1.02	<30.9‡	4.30
K3-69	8.74†	<10.4	20.7†	<8.57	17.6†	<3.04	...	...
K3-70	28.8	16.9†	39.5	2.96	11.6†	<1.48	...	...
K3-71	3.87†	8.42	57.2	<1.13	1.69‡	<1.34	3.16‡	2.64
K3-90	6.03†	7.07‡	170	<1.64	4.86†	<1.41	9.13	15.7†
K4-48	38.2	9.22†	56.4	9.91	45.8†	2.52†	...	...
M1-1	14.3	10.6	210	<2.03	4.61	<1.32	6.86†	27.6
M1-6	222	42.5†	<9.38	298	151	<10.5	...	...
M1-7	151	87.3	249	24.5†	77.7	6.10	...	...
M1-8	47.4	56.7	98.8	*	27.9	3.92	<6.00	6.51
M1-9	129	40.9	59.4	29.7†	49.7†	<3.73	...	...
M1-14	375	112	41.3	39.2	170	10.9	...	...
M1-16	68.7	32.1	91.3	43.2†	114†	8.09	<14.6	12.1†
M1-17	203	54.9	346	28.3	87.1†	5.89†	...	...
M2-2	112	74.7	1250	2.22‡	77.1	6.27	...	...
M3-2	3.59‡	6.33†	5.46†	*	1.93†	<1.05	...	...
M4-18	14.8‡	<13.5	...	110	...	...	...	...
SaSt2-3	7.12	7.11†	...	32.4†	...	...	...	...
Y-C 2-5	3.67	<4.77	87.5	*	3.16	<0.88	...	...

where $E(B-V) = A_B - A_V$; the 'B' and 'V' subscripts representing wavelengths of ~ 450 nm and ~ 550 nm respectively. The $A_\lambda \ / \ E(B-V)$ variable is often found in literature as the extinction ratio R, where R_V of interstellar space is commonly taken as 3.1.

To correct observed flux values for extinction, the relation is:

$$\begin{aligned} I(\lambda) \ = \ F(\lambda)_{\text{corr}} \ &= \ F(\lambda) \ \times \ 10^{0.4 \, A_\lambda} \\ &= \ F(\lambda) \ \times \ 10^{0.4 \ \times \ \frac{A_\lambda}{E(B-V)} \ \times \ E(B-V)} \end{aligned} \tag{3.1}$$

In PN abundance calculations, it is standard to use $I(H\beta)$ as a reference. In optical studies, this feature can be observed at 4861 Å, which corresponds with a value of $A_\lambda \ / \ E(B-V) \ = \ 3.664$. Hence, the multiplying factor in equation (3.1) becomes $10^{1.47 \ \times \ E(B-V)}$. Therefore, by defining the extinction correction:

$$C(H\beta) \equiv I(H\beta) - F(H\beta) \tag{3.2}$$

we obtain:

$$E(B-V) = C(H\beta)/1.47 \tag{3.3}$$

Here, $C(H\beta)$ values from literature have been used for all sources, and $I(H\beta)$ has been calculated from recombination lines of neutrally charged atomic hydrogen (H I) using the relationships from Hummer and Storey (1987).

From inputting values into equation (3.3) and following the corresponding Fluks extinction law, the IR extinction corrections typically take values of $A_\lambda \lesssim 0.2$, whereas at optical wavelengths $A_\lambda \lesssim 4.6$, emphasising that IR spectra require much lower corrections for extinction and hence the associated line intensity values will have smaller uncertainties.

3.3.4 Hβ intensity

In the wavelength range of *Spitzer* IRS the emission lines of several recombination transitions of H I are observed, the strongest of which are represented by the 7.5 μm and 12.4 μm lines. Both of these emission lines account for at least two transitions; the H I 6–5, 8–6, 11–7 and 17–8 lines are blended around 7.5 μm (H I 6–5 is the strongest of these transitions, contributing 74.43% of the total flux) whereas the H I 7–6 and 11–8 transitions both contribute to the emission line at 12.4 μm (H I 7–6 provides 89.08% of this flux). The Balmer decrement is applied to obtain values of $I(H\beta)$ from Hummer and Storey (1987), interpolated to account for the electron density and temperature values of the PNe. When both of these IR emission features were observed, their $I(H\beta)$ values agreed by up to $\sim 25\%$, and an average was taken.

The calculated $I(H\beta)$ values are shown in Table 3.4 alongside the $F(H\beta)$ and $I(H\beta)$ values from 4861 Å optical line measurements, and $C(H\beta)$ values from the literature. In the four cases when neither of the two recombination lines were observed in a spectrum, the Fluks extinction law (Fluks et al., 1994) was applied to these literature $F(H\beta)$ values. The

Table 3.4 $I(H\beta)$ values for the sample.

PN	$C(H\beta)$	IR log $I(H\beta)$	Lit. log $F(H\beta)$	Lit. log $I(H\beta)$
J320	0.24	-11.13	$-11.63^{(1)}$, $-11.39^{(2)}$	-11.15
K3-65	$1.83^{\dagger}$	-12.05	$-14.24*^{(1)}$	$-12.41*$
K3-66	0.98	-11.26	$-12.22^{(3)}$	-11.24
K3-67	1.02	-10.91	$-12.13^{(1)}$, $-12.07^{(3)}$	-11.05
K3-68	$0.80^{\dagger}$	...	$-12.90^{(V)}$	-12.10
K3-69	$1.34^{\dagger}$	-11.80	$-13.25^{(1)}$	-11.91
K3-70	1.45	-11.92	$-13.54^{(1)}$, $-13.59^{(3)}$	-12.09
K3-71	$1.14^{\dagger}$	-12.35	$-13.62^{(1)}$	-12.48
K3-90	1.02	-11.70	$-13.40^{(3)}$	-12.38
K4-48	1.47	-11.39	$-12.93^{(3)}$, $-12.82^{(4)}$	-11.46
M1-1	$0.6^{\ddagger}$	...	$-11.84^{(1)}$, $-11.88^{(5)}$	-11.24
M1-6	1.57	-10.49	$-12.28^{(1)}$, $-12.34^{(3)}$	-10.77
M1-7	0.40	-11.15	$-12.21^{(1)}$, $-12.20^{(3)}$	-11.80
M1-8	$1.1^{\ddagger}$	-11.69	$-13.12^{(1)}$, $-12.37^{(5)}$	-12.02
M1-9	0.46	-10.99	$-11.66^{(3)}$, $-11.73^{(4)}$	-11.20
M1-14	0.69	-10.63	$-11.58^{(1)}$, $-12.20^{(3)}$	-10.89
M1-16	0.59	-11.12	$-12.80^{(3)}$, $-11.99^{(6)}$	-11.40
M1-17	0.96	-10.94	$-12.00^{(1)}$, $-11.89^{(7)}$	-10.93
M2-2	1.26	-10.69	$-12.22^{(1)}$, $-12.63^{(3)}$	-10.96
M3-2	$0.22^{\#}$	...	$-13.26^{(1)}$, $-12.32^{(5)}$	-12.10
M4-18	0.77	...	$-12.01^{(3)}$, $-12.15^{(8)}$	-11.24
SaSt2-3	$0.73^{\#}$	-11.77	$-12.68^{(9)}$	-11.95
Y-C 2-5	0.00	-12.07	$-12.65^{(3)}$, $-12.26^{(4)}$	-12.26

Notes: (1) Acker et al. (1991); (2) Milingo et al. (2002); (3) Henry et al. (2010); (4) Cuisinier et al. (1996); (5) Carrasco et al. (1983); (6) Perinotto and Corradi (1998); (7) Costa et al. (2004); (8) De Marco and Crowther (1999); (9) Pereira and Miranda (2007); (V) VizieR catalogue, given reference unverified. * Large uncertainty. $C(H\beta)$ obtained from Henry et al. (2010) except: † from Giammanco et al. (2011); ‡ from Condon and Kaplan (1998); $^{\#}$ from Frew et al. (2013).

resulting values agree with those in literature mostly to within a factor of 2 (more for K3-90 and M1-7). In these situations the IR values are favoured, as the H I lines are measured in the same spectra as the ionic emission that has been derived. Another advantage of using these lines to determine $F(H\beta)$ is that the extinction corrections are far smaller compared to those from optical wavelengths; $A_\lambda < 4.6$ from the use of the 4861 Å $H\beta$ line, whereas $A_\lambda < 0.2$ from the IR recombination lines.

3.3.5 Electron densities and temperatures

Both n_e and T_e are needed to determine abundance values; n_e is a direct component of their calculation (see equation 2.9) whereas T_e designates the statistical populations of the excited electronic states present within the ion. These are listed in Tables 3.5 and 3.6 respectively, and the transition probabilities and collision strengths used in calculating these values are shown in Table 3.7. These values were taken from TIPbase, part of the IRON project (Hummer et al., 1993).

As explained in Chapter 2, IR lines originate from electronic transitions close to the ground state. Therefore, by analysing the ratio of $I(\lambda)$ values for two transitions of the same ion, n_e values can be obtained that are mostly independent of temperature. Of the line flux ratios available from the *Spitzer* spectra, those of the [S III] 18.7 / 33.5 μm transitions are favoured as both of these lines are easy to measure in high resolution spectra and are frequently seen together. While other line ratios were available in some PNe (e.g. [Ne III], [Ne V]), they were either detected in fewer of the PNe in the sample, or were detected at noisy wavelength regions. For instance, the [Ne III] line at 36.0 μm is found at the upper wavelength region of the LH module, which is highly susceptible to noise above $\sim$ 35 μm. The 14.3 and 24.3 μm lines of [Ne V] were only observed in 12 of the 23 PNe in the sample, though the associated density values agree well with those of [S III]. Uncertainties averaged $\sim$ 20% for values of $n_e > 1000$ cm^{-3}, though this becomes larger for the few sources where $n_e < 1000$ cm^{-3}. In the four cases where the two [S III] lines were not directly measurable and any other line ratios were either not observed or affected by noise, literature values were used to apply the [S II] 6716 Å / 6731 Å line intensity ratio. The mean value derived from the [S III] line ratios in this sample of $n_e = 3700$ cm^{-3} was applied for K3-69 and Y-C 2-5, as these lines were not observed in these PNe and there were no n_e values given in literature. In these cases, while the uncertainty in density is high, the abundances are affected little, with neon and argon showing little change at the density extremes and sulphur being affected by 20% at most. All density values are shown in Table 3.5, with the uncertainties reflecting those of the [S III] 18.7 / 33.5 μm ratios. It is noted that for K3-90, Henry et al. (2010) apply the high

Table 3.5 Electron density values of PNe (cm^{-3}).

PN	n_e (This work)	n_e (Lit.)	Sources
J320	3350 ± 600	4800	1,2,3,4
K3-65	1150 ± 200	...	...
K3-66	3150 ± 500	7700	1,5
K3-67	3900 ± 550	4400	5,6,7,8
K3-68	600 ± 300	500	6
K3-69	*3700 ± 3000*‡	...	...
K3-70	2000 ± 650	2250	2,5,9
K3-71	10000 ± 2000†	10000	8
K3-90	400 ± 300	20000*	5
K4-48	8100 ± 2250	2600	5,10
M1-1	1300 ± 450	4100	1,11
M1-6	11450 ± 4700	8500	2,5
M1-7	1900 ± 200	1050	2,5
M1-8	350 ± 150	440	2
M1-9	5050 ± 900	4600	2,5,10
M1-14	5450 ± 450	5400	2,5,12
M1-16	2800 ± 550	2300	2,5,10,13
M1-17	6450 ± 300	5000	2,9,14,15
M2-2	1550 ± 300	1600	5
M3-2	230†	230	2
M4-18	8000 ± 3000†	8000	16,17
SaSt2-3	600 ± 450	2400	9
Y-C 2-5	*3700 ± 3000*‡	...	2,5,10

Notes: (1) Aller and Czyzak (1983); (2) Costa et al. (2004); (3) Koeppen et al. (1991); (4) Milingo et al. (2002); (5) Henry et al. (2010); (6) Aller and Keyes (1987); (7) Kingsburgh and Barlow (1994); (8) Tamura and Shaw (1987); (9) Aksaker et al. (2015); (10) Cuisinier et al. (1996); (11) Aller et al. (1986); (12) Costa et al. (1996); (13) Perinotto and Corradi (1998); (14) de Freitas Pacheco et al. (1991); (15) Peimbert et al. (1995); (16) De Marco and Crowther (1999); (17) Goodrich and Dahari (1985). [S III] densities used when applicable. Literature values are averaged when there are multiple sources. No uncertainty was given for the literature value of M3-2. * High density limit. † Value from literature. ‡ Mean n_e value from those derived from [S III] in this sample, with the standard deviation of all other data points as the associated uncertainty.

density limit to estimate n_e despite having intensity values for the [S II] 6716 Å and 6731 Å lines. This is due to the two values having high uncertainties. A density of $n_e = 800$ cm^{-3} would have been calculated with these values, which is almost within the uncertainty margins of the calculated IR [S III] line ratio.

Measurements of T_e require electronic transitions with large differences in energy. For this study, temperatures calculated from optical line flux values based on the transition ratios

Table 3.6 Electron temperature values of PNe as averages of literature values.

PN	Ionic Lines	T_e / K
J320	[N II], [O III]	11900 ± 2300
K3-65	...	*11900 ± 2600*
K3-66	[N II], [O II], [O III], [S II], [S III]	10800 ± 2500
K3-67	[N II], [O II], [O III], [S III]	14400 ± 3200
K3-68	[N II], [O III]	19600 ± 2000
K3-69	...	*11900 ± 2600*
K3-70	[N II], [O II], [O III], [S III]	13700 ± 4500
K3-71	[O III]	12600 ± 2000
K3-90	[O II], [O III]	12000 ± 2500
K4-48	[N II], [O II], [O III], [S II], [S III]	12700 ± 2300
M1-1	[O III]	14900 ± 1500
M1-6	[N II], [O III], [S III]	9800 ± 1900
M1-7	[N II], [O II], [O III], [S II], [S III]	10600 ± 4200
M1-8	[N II], [O III]	12900 ± 1900
M1-9	[N II], [O II], [O III], [S III]	10800 ± 1800
M1-14	[N II], [O II], [O III], [S III]	10000 ± 3700
M1-16	[N II], [O II], [O III], [S III]	11700 ± 3000
M1-17	[N II], [O III]	10700 ± 2600
M2-2	[N II], [O III], [S III]	12500 ± 1500
M3-2	[N II]	10200 ± 1000
M4-18	[N II], [O II], [S II]	6100 ± 3000
SaSt2-3	[N II]	9800 ± 1400
Y-C 2-5	[N II], [O II], [O III]	13000 ± 2400

Notes: K3-65 and K3-69 adopt the average temperature of the other sources due to lack of literature values; their associated uncertainties are given to be the standard deviation of all other values. Sources are the same as those given in Table 3.5.

Table 3.7 Atomic data for ions shown in Table 3.3.

Ion	Transition Probability	Collision Strength
Ne^{+}	Griffin et al. (2001)	Griffin et al. (2001)
Ne^{2+}	Galavis et al. (1997)	Butler and Zeippen (1994)
Ne^{4+}	Galavis et al. (1997)	Griffin and Badnell (2000)
Ne^{5+}	Mendoza (1983)	Mitnik et al. (2001)
S^{2+}	Mendoza and Zeippen (1982)	Galavis et al. (1995)
S^{3+}	Johnson et al. (1986)	Saraph and Storey (1999)
Ar^{+}	Mendoza (1983)	Pelan and Berrington (1995)
Ar^{2+}	Mendoza and Zeippen (1983)	Galavis et al. (1995)
Ar^{4+}	Mendoza and Zeippen (1982)	Galavis et al. (1995)
O^{3+}	Galavis et al. (1998)	Zhang et al. (1994)

of the [N II], [O II], [O III], [S II] and [S III] lines calculated from the literature are applied. As no T_e values could be found in the literature for K3-65 and K3-69, for these two PNe the average value of $T_e = 11900$ K was adopted. All of these values can be found in Table 3.6.

3.3.6 Elemental abundances

One of the main advantages of analysing spectra at infrared wavelengths is that the main ionisation lines of neon, sulphur and argon can be observed. From these lines, the ionic abundances of Ne^{+}, Ne^{2+}, Ne^{4+}, S^{2+}, S^{3+}, Ar^{+}, Ar^{2+} and Ar^{4+} have been measured. These data are complemented with the ionic abundances of S^{+} and Ar^{3+} measured by Henry et al. (2010) from optical spectra, hence fewer corrections are required in determining their elemental abundances. Ne^{3+} is accounted for in sources with observable Ne^{4+} emission, and S^{4+} is considered in sources with O^{3+}, which has a greater IP (47.22 eV and 54.94 eV, respectively).

These missing ionic abundances are corrected for with ICFs. ICFs can either be determined empirically (e.g. Pottasch and Surendiranath 2005; Surendiranath et al. 2004), by considering lines with similar IP values (e.g. Peimbert and Costero 1969), or from photoionisation models (e.g. Delgado-Inglada et al. 2014; Kingsburgh and Barlow 1994; Kwitter and Henry 2001; Natta et al. 1980). In many cases, argon and particularly sulphur are highlighted as being complicated to correct for, as the low IPs of higher ionisation states may lead to their greater contributions towards the overall elemental abundances. Many variants of the ICFs for these elements have been given in literature (e.g. Kingsburgh and Barlow 1994; Kwitter and Henry 2001; Thuan et al. 1995) with significant disagreement between some of them (Vermeij and van der Hulst, 2002).

To account for the abundances of missing ionisation states, the calculated IR values are complemented with optical abundances derived by Henry et al. (2010) where possible. To correct for S^{+} and Ar^{3+} when these values are not available, the percentage contributions of these ions are calculated towards their respective elemental abundances for the PNe in the sample with these ionic abundances, and the mean values are applied as ICFs. In each

Table 3.8 Percentage contributions of ions that have required the use of empirically calculated ICFs towards their respective elemental abundances.

Ion	Range	Mean	Source
[Ne IV]	2–33%	17.5%	Bernard-Salas et al. (2008)
[S II]	1–20%	10%	This work
[S V]	7–23%	15%	Bernard-Salas et al. (2008)
[Ar II]	1–32%	13%	This work
[Ar IV]	3–46%	26%	This work

case, the minimum and maximum values are taken as the uncertainty limits. This method is also applied to account for Ar^{+} in three sources for which the 7.0 μm line intensity cannot be measured. For Ne^{3+} and S^{4+}, the range of contributions of these ions to their respective elemental abundances as given by Bernard-Salas et al. (2008) are considered; they calculated these values from the analysis of the PN sample of Pottasch and Bernard-Salas (2006) and also from the Galactic PN models of Surendiranath et al. (2004) and Pottasch and Surendiranath (2005). Each of these ranges are shown in Table 3.8. Note that ICFs correcting for these missing ionic states are only applied for PNe in which other ions with greater or similar IP values are observed.

Tables 3.9, 3.10 and 3.11 give the ionic and elemental abundance values for Ne, S and Ar respectively, with the empirical ICFs applied. As ICFs can be uncertain, the resulting abundances calculated with these empirical ICFs are also compared with abundances for which well-established ICFs from the literature have been applied, such as those of Kingsburgh and Barlow (1994), Kwitter and Henry (2001) and Delgado-Inglada et al. (2014). In all cases, the ionic abundances calculated in this work are applied. For the equations given in this section, the notation A(X) = ICF($X^{m+} + X^{n+}$) $\times$ ($X^{m+} + X^{n+}$)/H is applied, where A(X) is the elemental abundance of X. Table 3.12 shows the supplementary data used in the following calculations from optical abundance studies. Some ICF equations from other studies use ionic ratios that are particularly sensitive to the electron density and temperature, such as those involving O^{+} and O^{2+}, hence there may be additional uncertainties in some of the resulting abundance values.

Table 3.9 Ionic and total abundances of neon ($\times 10^{-5}$). Optical values for ionic abundances were used for ions not observable in IR spectra. $H\beta$ values were calculated from IR recombination lines.

Source	[Ne II] IP = 21.56eV	[Ne III] IP = 40.96eV	[Ne V] IP = 97.12eV	[Ne VI] IP = 126.21eV	ICF	Ne/H $\times 10^{-5}$	Ne/H lit. $\times 10^{-5}$
J320	0.109	6.20	...	...	1.00	6.3 ± 1.8	*5.3 ± 1.6*
K3-65	2.45	14.7	...	...	1.00	17.2 ± 5.9	...
K3-66	2.17	2.09	<0.007	...	1.00	4.3 ± 1.6	4.51 ± 1.79
K3-67	0.253	3.47	<0.003	...	1.00	3.7 ± 1.1	3.79 ± 0.93, *4.17 ± 1.46*
K3-68	<0.338	2.11	0.218	...	1.21	2.8 ± 1.6	...
K3-69	0.438	6.69	0.174	...	1.21	8.9 ± 3.3	...
K3-70	0.507	4.23	0.151	...	1.21	5.9 ± 2.9	7.01 ± 1.74
K3-71	<0.569	2.60	0.721	...	1.21	4.0 ± 1.8	...
K3-90	<0.155	0.952	0.500	...	1.21	1.8 ± 0.8	14.1 ± 8.0
K4-48	0.573	7.29	0.051	...	1.21	9.6 ± 3.0	10.5 ± 2.5
M1-1	<0.048	0.275	0.886	0.014	1.21	1.4 ± 0.5	*8.9 ± 2.7*
M1-6	5.65	0.129	...	...	1.00	5.8 ± 2.3	1.15 ± 1.53
M1-7	1.06	7.32	0.003	...	1.21	10.2 ± 6.0	20.8 ± 4.8
M1-8	1.62	8.73	0.235	...	1.21	12.8 ± 5.1	...
M1-9	1.39	2.32	...	...	1.00	3.7 ± 1.8	4.04 ± 1.18
M1-14	4.18	1.28	...	...	1.00	5.5 ± 2.2	1.61 ± 0.45
M1-16	0.991	8.44	0.270	0.008	1.21	11.8 ± 5.8	10.8 ± 2.6, *7.0 ± 2.0*
M1-17	0.539	4.91	0.017	...	1.21	6.6 ± 1.7	...
M2-2	0.045	4.24	<0.001	...	1.00	4.3 ± 1.0	4.89 ± 1.19, *5.89 ± 3.53*
M3-2	0.426	0.819	0.052	...	1.21	1.6 ± 0.9	...
M4-18	10.6	<2.32	...	...	1.00	10.6 ± 3.9	*0.54 ± 0.06*
SaSt2-3	2.56	<0.068	...	...	1.00	2.6 ± 1.5	...
Y-C 2-5	<0.188	5.90	<0.036	...	1.00	5.9 ± 3.4	...

Notes: ICFs applied for [Ne IV] contributions - see § 3.3.6. Literature values from Henry et al. (2010). Literature abundances in italics are from sources given by Sterling and Dinerstein (2008).

Table 3.10 Ionic and total abundances of sulphur ($\times 10^{-6}$). Optical values for ionic abundances were used for ions not observable in IR spectra. $H\beta$ values were calculated from IR recombination lines.

Source	[S II] lit. IP = 10.36eV	[S III] IP = 23.34eV	[S IV] IP = 34.79eV	ICF	S/H $\times 10^{-6}$	S/H lit. $\times 10^{-6}$
J320	...	1.25	3.16	1.33	5.8 ± 1.7	*14 ± 4*
K3-65	...	6.64	1.45	1.33	10.8 ± 3.7	...
K3-66	0.15 ± 0.10	1.13	0.126	1.18	1.7 ± 0.6	1.70 ± 0.55
K3-67	0.10 ± 0.04	0.880	0.886	1.18	2.2 ± 0.7	2.04 ± 0.76, *5.01 ± 1.75*
K3-68	...	0.899	1.92	1.33	3.8 ± 2.1	...
K3-69	...	0.629	0.302	1.33	1.2 ± 0.5	...
K3-70	0.30 ± 0.04‡	2.21	0.642	1.18	3.7 ± 1.8	3.44 ± 1.07
K3-71	...	1.37	3.73	1.33	6.8 ± 3.0	...
K3-90	0.36 ± 0.15	0.303	1.65	1.18	2.7 ± 1.2	1.86 ± 1.42
K4-48	0.19 ± 0.06	1.32	0.370	1.18	2.2 ± 0.7	1.65 ± 0.51, *1.95 ± 0.59*
M1-1	...	0.207	0.656	1.33	1.2 ± 0.4	...
M1-6	(0.48 ± 0.78)	1.45	<0.011	1.11	1.6 ± 0.6	2.66 ± 1.29, *1.91 ± 0.57*

Notes: ICFs applied to account for [S II] and [S V] contributions - see § 3.3.6. Literature values from Henry et al. (2010). Literature abundances in italics are from sources given by Sterling and Dinerstein (2008). † Abundance calculated from flux data of De Marco and Crowther (1999). ‡ Abundances calculated from flux data of Aksaker et al. (2015).

Table 3.10 (Continued)

Source	[S II] lit. IP = 10.36eV	[S III] IP = 23.34eV	[S IV] IP = 34.79eV	ICF	S/H $\times 10^{-6}$	S/H lit. $\times 10^{-6}$
M1-7	0.75 ± 0.17	2.24	0.743	1.18	4.4 ± 2.6	3.88 ± 1.10
M1-8	...	2.17	0.888	1.33	4.1 ± 1.6	...
M1-9	0.16 ± 0.10	1.69	0.151	1.00	2.0 ± 1.0	2.10 ± 0.64, *1.29 ± 0.39*
M1-14	0.14 ± 0.07	2.35	0.049	1.00	2.5 ± 1.0	2.19 ± 0.67, *0.81 ± 0.24*
M1-16	0.24 ± 0.07	0.981	0.265	1.18	1.8 ± 0.9	1.55 ± 0.46, *1.80 ± 0.50*
M1-17	$0.37 \pm 0.03^{\ddagger}$	2.69	0.857	1.18	4.6 ± 1.2	*9.55 ± 2.87*
M2-2	0.01 ± 0.00	0.526	1.21	1.18	2.1 ± 0.5	1.10 ± 0.51
M3-2	...	0.512	0.141	1.33	0.87 ± 0.49	...
M4-18	$2.89 \pm 0.74^{\dagger}$	0.665	...	1.00	3.6 ± 1.6	3.56 ± 3.85, *1.45 ± 0.20*
SaSt2-3	$0.24 \pm 0.04^{\ddagger}$	0.476	...	1.00	0.70 ± 0.42	...
Y-C 2-5	...	0.462	2.27	1.33	3.6 ± 2.1	...

Table 3.11 Ionic and total abundances of argon ($\times 10^{-7}$). Optical values for ionic abundances were used for ions not observable in IR spectra. $H\beta$ values were calculated from IR recombination lines.

Source	[Ar II] IP = 15.76eV	[Ar III] IP = 27.63eV	[Ar IV] lit. IP = 40.74eV	[Ar V] IP = 59.81eV	ICF	Ar/H $\times 10^{-7}$	Ar/H lit. $\times 10^{-7}$
J320	<0.180	3.55	...	...	1.35	4.8 ± 1.4	*9.4 ± 2.8*
K3-65	8.45	22.0	...	...	1.35	41.2 ± 14.2	...
K3-66	2.66	5.64	...	...	1.35	11.2 ± 4.4	5.4 ± 1.1
K3-67	0.487	4.48	1.73 ± 0.353	...	1.00	6.7 ± 2.0	6.0 ± 1.2, *10.0 ± 3.5*
K3-68	<3.83	<3.96	...	1.05	1.35	$<6.7 \pm 4.2$	...
K3-69	<4.13	10.3	...	...	1.35	13.9 ± 6.7	...
K3-70	1.70	8.17	3.16 ± 1.09	...	1.00	13.0 ± 6.6	14.6 ± 3.0
K3-71	<1.89	3.59	...	1.98	1.35	7.5 ± 3.6	...
K3-90	<0.350	2.23	3.44 ± 0.64	1.78	1.00	7.5 ± 3.4	13.3 ± 2.4
K4-48	1.78	10.2	4.21 ± 0.80	...	1.00	16.2 ± 5.3	19.9 ± 3.7, *5.4 ± 4.1*
M1-1	<0.227	0.632	...	1.05	1.64	2.8 ± 1.3	*21.0 ± 8.6*
M1-6	8.32	5.21	...	...	1.35	18.3 ± 7.2	9.1 ± 2.3, *40.7 ± 12.2*

Notes: ICFs applied to account for [Ar II] and [Ar IV] contributions - see § 3.3.6. Literature values from Henry et al. (2010). Literature abundances in italics are from sources given by Sterling and Dinerstein (2008). * Upper limits for 6.99 μm [Ar II] are inaccurate due to the contribution of the H_2 0–0 S(5) line at 6.9 μm.

Table 3.11 (Continued)

Source	[Ar II] IP = 15.76eV	[Ar III] IP = 27.63eV	[Ar IV] lit. IP = 40.74eV	[Ar V] IP = 59.81eV	ICF	Ar/H $\times 10^{-7}$	Ar/H lit. $\times 10^{-7}$
M1-7	2.69	10.2	3.27 ± 0.59	...	1.00	16.2 ± 9.5	36.4 ± 6.4
M1-8	*	11.7	...	0.703	1.64	20.3 ± 10.6	...
M1-9	2.38	4.85	0.22 ± 0.08	...	1.00	7.5 ± 3.7	8.0 ± 2.0, *10.0 ± 3.0*
M1-14	1.46	7.67	...	...	1.35	12.3 ± 4.9	9.5 ± 2.0, *20.4 ± 6.1*
M1-16	4.35	13.9	3.56 ± 0.68	0.400	1.00	22.2 ± 11.1	22.2 ± 4.0, *18.0 ± 3.0*
M1-17	2.07	7.83	...	...	1.35	13.4 ± 3.9	*33.1 ± 9.9*
M2-2	0.079	3.32	3.00 ± 0.57	...	1.35	8.7 ± 2.0	6.8 ± 1.2, *8.9 ± 5.4*
M3-2	*	2.41	...	...	1.64	4.0 ± 2.5	...
M4-18	24.8	...	...	...	1.00	24.8 ± 9.4	...
SaSt2-3	16.6	...	...	...	1.00	16.6 ± 10.0	...
Y-C 2-5	*	3.30	...	...	1.64	5.4 ± 3.4	...

Table 3.12 Ionic and elemental abundances from optical data in the literature, used in the calculations of neon, sulphur and argon ICFs in Tables 3.13–3.15.

PN	He^+/H^+ $\times10^{-3}$	He^{2+}/H^+ $\times10^{-3}$	N^+/H^+ $\times10^{-6}$	N/H $\times10^{-6}$	O^+/H^+ $\times10^{-5}$	O^{2+}/H^+ $\times10^{-5}$	O/H $\times10^{-5}$
J320	...	...	*0.23 ± 0.08*	*14.8 ± 4.4*	*0.42 ± 0.13*	25.7 ± 7.7	27.5 ± 8.3
K3-66	88 ± 11	0.32 ± 0.10	12.6 ± 4.1	34.1 ± 8.1	59 ± 38	10.0 ± 2.2	16.0 ± 4.8
K3-67	93 ± 14	0.24 ± 0.04	3.6 ± 0.9	79 ± 23	5.9 ± 1.8	12.5 ± 3.2	13.1 ± 3.3
K3-70	98 ± 15	21.5 ± 3.2	52 ± 12	305 ± 81	20.4 ± 5.6	*7.8 ± 2.0*	*12.0 ± 2.7*
K3-90	4.9 ± 2.5	105 ± 17	...	...	1.3 ± 0.7	*2.7 ± 0.7*	*62 ± 33*
K4-48	107 ± 14	17.3 ± 2.6	22.5 ± 5.4	206 ± 50	35 ± 11	*24.3 ± 5.8*	*32.3 ± 7.1*
M1-6	...	...	42 ± 20	58 ± 26	241 ± 87	9.5 ± 2.9	34 ± 11
M1-7	110 ± 14	15.7 ± 2.4	61 ± 14	252 ± 70	115 ± 30	*29.9 ± 6.8*	*47.3 ± 9.2*
M1-9	104 ± 14	0.11 ± 0.04	8.8 ± 2.8	37 ± 13	47 ± 31	14.5 ± 3.3	19.2 ± 5.0
M1-14	96 ± 12	0.10 ± 0.05	14.0 ± 3.9	46 ± 13	89 ± 47	20.1 ± 4.4	29.0 ± 6.9
M1-16	105 ± 15	25.2 ± 3.8	81 ± 20	543 ± 145	50 ± 14	*21.8 ± 5.3*	*33.2 ± 7.2*
M2-2	104 ± 14	7.8 ± 1.2	0.36 ± 0.12	15.8 ± 6.6	4.5 ± 0.8	17.9 ± 4.3	19.8 ± 4.7
Y-C 2-5	39.7 ± 5.9	62.4 ± 9.2	0.15 ± 0.05	55 ± 34	0.79 ± 0.39	11.1 ± 2.9	28.6 ± 7.7

Notes: All values have been taken from Henry et al. (2010), except for those of J320 which are from Costa et al. (2004) with an assumed 30% uncertainty applied. Values in italics are not involved in any future calculations, and have only been included for completeness.

Neon

At mid-IR wavelengths, lines of Ne^{+}, Ne^{2+}, Ne^{4+} and Ne^{5+} can be measured, though Ne^{3+} is best observed in the optical and near-UV regions, respectively at $\sim$ 4720 Å and $\sim$ 2424 Å. Unfortunately, no literature values exist for the abundance of Ne^{3+} in any of the PNe in the anti-centre sample.

The photoionisation model of Kingsburgh and Barlow (1994), also used by Kwitter and Henry (2001), used the following ICFs:

$$\mathrm{ICF}(Ne^{2+} + Ne^{4+}) \;=\; 1.5 \tag{3.4}$$

$$\mathrm{ICF}(Ne^{2+}) \;=\; \frac{O}{O^{2+}} \tag{3.5}$$

However, the abundances of sources with weak radiation fields are underestimated due to the disregard of the Ne^{+} ionic contribution to the total neon abundance (e.g. Tsamis et al. 2013). This problem is also observed in the ionic abundances of several sources in the anti-centre PN sample, in which Ne^{+} sometimes contributes more to the overall elemental abundance than Ne^{2+}. These include K3-66, M1-6 and M1-14 (see Table 3.9).

Recently, Delgado-Inglada et al. (2014) produced a newer set of ICF models to account for parameters such as effective temperatures and stellar luminosities. For Ne/H corrections, they apply:

$$\mathrm{ICF}(Ne^{2+} + Ne^{4+}) \;=\; (1.31 + 12.68\nu^{2.57})^{0.27} \tag{3.6}$$

where $\nu = He^{2+}/(He^{+} + He^{2+})$. However, the requirement for Ne^{4+} limits the usability of this correction. They also state that the ICFs will overestimate the neon abundances unless $0.4 \lesssim \nu \lesssim 0.6$. The He^{+} and He^{2+} abundances given for 12 of the 23 PNe in the anti-centre sample from Henry et al. (2010) give ν values outside this range, 10 of these sources having values of $\nu < 0.2$ and 5 of these with $\nu < 0.005$. PNe with very low ν values have small He^{2+} ionic abundances, which typically indicates low-ionisation sources with little or no

Table 3.13 Comparison of the neon abundances and ICFs used in this study with those in which ICFs from other sources have been applied – see equations (3.4), (3.5) and (3.6).

	This work		KB94		DI14	
	Ne/H		Ne/H		Ne/H	
PN	$\times 10^{-5}$	ICF(Ne)	$\times 10^{-5}$	ICF(Ne)	$\times 10^{-5}$	ICF(Ne)
J320	$6.3 \pm 1.8^{*\dagger}$	1.00	$6.6 \pm 3.3^{\dagger}$	1.07	...	...
K3-66	$4.3 \pm 1.6^{*\dagger}$	1.00	$3.4 \pm 1.8^{\dagger}$	1.61	...	...
K3-67	$3.7 \pm 1.1^{*\dagger}$	1.00	$3.6 \pm 1.7^{\dagger}$	1.05	...	...
K3-68	$2.8 \pm 1.6^{*\dagger\ddagger}$	1.21	$3.5 \pm 0.7^{\dagger\ddagger}$	1.50	...	...
K3-69	$8.9 \pm 3.3^{*\dagger\ddagger}$	1.21	$10.3 \pm 3.3^{\dagger\ddagger}$	1.50	...	...
K3-70	$5.9 \pm 2.9^{*\dagger\ddagger}$	1.21	$6.6 \pm 3.2^{\dagger\ddagger}$	1.50	$4.9 \pm 2.4^{\dagger\ddagger}$	1.11
K3-71	$4.0 \pm 1.8^{*\dagger\ddagger}$	1.21	$5.0 \pm 2.2^{\dagger\ddagger}$	1.50	...	...
K3-90	$1.8 \pm 0.8^{*\dagger\ddagger}$	1.21	$2.2 \pm 0.9^{\dagger\ddagger}$	1.50	$2.9 \pm 1.2^{\dagger\ddagger}$	1.98
K4-48	$9.6 \pm 3.0^{*\dagger\ddagger}$	1.21	$11.0 \pm 3.1^{\dagger\ddagger}$	1.50	$8.0 \pm 2.6^{\dagger\ddagger}$	1.09
M1-1	$1.4 \pm 0.5^{*\dagger\ddagger\#}$	1.21	$1.7 \pm 0.6^{\dagger\ddagger}$	1.50	...	...
M1-6	$5.8 \pm 2.3^{*\dagger}$	1.00	$0.46 \pm 0.26^{\dagger}$	3.54	...	...
M1-7	$10.2 \pm 6.0^{*\dagger\ddagger}$	1.21	$11.0 \pm 5.0^{\dagger\ddagger}$	1.50	$8.0 \pm 1.9^{\dagger\ddagger}$	1.09
M1-8	$12.8 \pm 5.1^{*\dagger\ddagger}$	1.21	$13.4 \pm 3.2^{\dagger\ddagger}$	1.50	...	...
M1-9	$3.7 \pm 1.8^{*\dagger}$	1.00	$3.1 \pm 1.3^{\dagger}$	1.32	...	...
M1-14	$5.5 \pm 2.2^{*\dagger}$	1.00	$1.8 \pm 0.9^{\dagger}$	1.44	...	...
M1-16	$11.8 \pm 5.8^{*\dagger\ddagger\#}$	1.21	$13.1 \pm 6.9^{\dagger\ddagger}$	1.50	$9.7 \pm 3.0^{\dagger\ddagger}$	1.11
M1-17	$6.6 \pm 1.7^{*\dagger\ddagger}$	1.21	$7.4 \pm 2.3^{\dagger\ddagger}$	1.50	...	...
M2-2	$4.3 \pm 1.0^{*\dagger}$	1.00	$4.7 \pm 1.9^{\dagger}$	1.11	$4.6 \pm 1.8^{\dagger\ddagger}$	1.08
M3-2	$1.6 \pm 0.9^{*\dagger\ddagger}$	1.21	$1.3 \pm 0.5^{\dagger\ddagger}$	1.50	...	...
Y-C 2-5	$5.9 \pm 3.4^{*\dagger}$	1.00	$15.2 \pm 6.9^{\dagger}$	2.58	...	...

Notes: KB94 = Kingsburgh and Barlow (1994); DI14 = Delgado-Inglada et al. (2014). In all cases, ICFs are applied to the neon ionic abundances from Table 3.9. Superscript symbols show the ions considered in the calculations: $^{*} = Ne^{+}$; $^{\dagger} = Ne^{2+}$; $^{\ddagger} = Ne^{4+}$; $^{\#} = Ne^{5+}$. M4-18 and SaSt2-3 are not included on this table as their Ne^{2+} abundances are upper limits. K3-65 is not included as its helium and oxygen abundances have not been found in the literature.

Ne^{4+} emission. However, this is not true for Y-C 2-5, which has a relatively large ν (0.61) but no observable Ne^{4+} emission in its *Spitzer* IRS spectrum.

Table 3.13 shows a comparison between the neon abundances calculated with both the empirical ICFs and the well-established ICFs of Kingsburgh and Barlow (1994) and Delgado-Inglada et al. (2014). There is good agreement in almost all cases between the two sets of values, though the disregard of Ne^{+} leads to major underestimates from the Kingsburgh and Barlow (1994) model for M1-6 and M1-14. For Y-C 2-5, the applied ICF of 2.58 leads to a much greater abundance than predicted empirically. However, as the mid-IR spectrum of this

PN shows the strong emission line of Ne^{2+} but not those of Ne^{+} or Ne^{4+}, it is possible that the Ne^{3+} that is being corrected for may give a significant contribution to the neon abundance. The fact that large amounts of He^{2+} are seen compared to He^{+} in this source shows that the radiation field in Y-C 2-5 is greater than 54.4 eV (the IP of He^{2+}), and as Ne^{3+} ionises at 63.5 eV, a large ICF may be required.

Sulphur

As ionisation models are typically applied to optical spectra, it is normal to only see corrections for S^{3+} from S^{+} and S^{2+} ionic abundance measurements. In these studies, the low IP of S^{2+} (34.8 eV) has always been taken as an indication that larger ionic states are likely to be present in PNe, and the similar IP of O^{+} (35.1 eV) is generally considered in obtaining an ICF for sulphur. Dinerstein (1980) carried out an IR spectroscopic survey of 12 PNe and found that the commonly used ICF of O/O^{+} can overpredict the measured abundances of S^{3+}. However, the presence of even greater ionisation states must also be considered.

Based on models of H II regions from Stasińska (1978), the ICF for sulphur from optical spectra was calculated by Barker (1980) to be:

$$\mathrm{ICF}(S^{+}+S^{2+}) = \left[1-\left(1-\frac{O^{+}}{O}\right)^{\alpha}\right]^{-1/\alpha} \tag{3.7}$$

where $\alpha = 3$, though subsequent studies argued that $\alpha = 2$ (French, 1981) or $2 \leqslant \alpha \leqslant 3$ (Garnett, 1989) better represented the sulphur abundances. Kingsburgh and Barlow (1994) also used this equation, with $\alpha = 3$.

A different method of determining the ICF for sulphur was calculated by Kwitter and Henry (2001), who considered newer atomic data and incorporated the charge exchange rates into the ICF values. They used the equation:

$$\mathrm{ICF}(S^{+}+S^{2+}) = \exp[-0.017+0.18\beta-0.11\beta^{2}+0.072\beta^{3}] \tag{3.8}$$

where $\beta = \log(O/O^{+})$.

The models of Delgado-Inglada et al. (2014) calculate ICFs for the S/O ratio, and multiply by the O/H abundance:

$$\log \mathrm{ICF}((\mathrm{S}^{+}+\mathrm{S}^{2+})/\mathrm{O}^{+}) = \frac{-0.02-0.03\omega-2.31\omega^{2}+2.19\omega^{3}}{0.69+2.09\omega-2.69\omega^{2}} \tag{3.9}$$

$$\log \mathrm{ICF}(\mathrm{O}^{+}+\mathrm{O}^{2+}) = \frac{0.08\nu+0.006\nu^{2}}{0.34-0.27\nu} \tag{3.10}$$

where ν is as defined in equation (3.6) and $\omega = \mathrm{O}^{2+}/(\mathrm{O}^{+} + \mathrm{O}^{2+})$. In all cases, $\omega > 0.5$ and for K3-67, M2-2 and Y-C 2-5, $\omega > 0.95$.

The sulphur abundances calculated using these ICFs are shown in Table 3.14. Again, the values calculated using empirical ICFs compare well with those from photoionisation models. ICFs obtained with equation (3.7) are often large when $\alpha = 2$, and provide much greater estimates than those of the compared studies. However, the agreement is greatly improved when $\alpha = 3$. The uncertainties in the ICF calculated from Kwitter and Henry (2001) are larger due to their propagation, but the ICFs themselves are smaller, with most of them having values of $\leqslant 1.35$. The only exception to this is K3-90, which has a stronger radiation field than the others ($\mathrm{S}^{3+}/\mathrm{S}^{2+} = 5.4$). Despite these uncertainties, the S/H values calculated from equation (3.8) show a good agreement with the other values. The abundances calculated using ICFs from Delgado-Inglada et al. (2014) are similar in that their uncertainties are relatively high, though in almost all cases they show better agreement with the abundances calculated using empirically determined ICFs than those from Kwitter and Henry (2001).

Argon

In optical spectra, the Ar^{2+}, Ar^{3+} and Ar^{4+} ions can all be observed. The most abundant of these ions is thought to be Ar^{2+}, though this largely depends on the radiation field of the source.

Argon abundances calculated by Kingsburgh and Barlow (1994) applied the following ICFs.

Table 3.14 Comparison of the sulphur abundances and ICFs used in this study with those in which ICFs from other sources have been applied – see equations (3.7) to (3.10).

	This work		B80 / KB94				KH01		DI14	
	S/H		$\alpha = 3$		$\alpha = 2$		S/H		S/H	
PN	$\times 10^{-6}$	ICF(S)	S/H $\times 10^{-6}$	ICF(S)	S/H $\times 10^{-6}$	ICF(S)	$\times 10^{-6}$	ICF(S)	$\times 10^{-6}$	ICF(S)
K3-66	$1.7 \pm 0.6^{*\dagger\ddagger}$	1.18	$1.4 \pm 1.0^{*\dagger}$	1.10	$1.6 \pm 1.2^{*\dagger}$	1.29	#	...	#	...
K3-67	$2.2 \pm 0.7^{*\dagger\ddagger}$	1.18	$2.1 \pm 0.9^{*\dagger}$	1.98	$3.6 \pm 1.5^{*\dagger}$	3.38	$1.2 \pm 0.7^{*\dagger}$	1.22	$1.9 \pm 1.3^{*\dagger}$	1.91
K3-70	$3.7 \pm 1.8^{*\dagger\ddagger}$	1.18	$3.3 \pm 0.6^{*\dagger}$	1.33	$4.5 \pm 1.0^{*\dagger}$	1.79	$2.7 \pm 1.1^{*\dagger}$	1.09	$3.3 \pm 2.0^{*\dagger}$	1.31
K3-90	$2.7 \pm 1.2^{*\dagger\ddagger}$	1.18	$3.6 \pm 1.8^{*\dagger}$	5.39	$10.1 \pm 5.7^{*\dagger}$	15.3	$1.9 \pm 1.7^{*\dagger}$	2.86	$12.4 \pm 10.2^{*\dagger}$	18.7
K4-48	$2.2 \pm 0.7^{*\dagger\ddagger}$	1.18	$2.3 \pm 0.8^{*\dagger}$	1.51	$3.3 \pm 1.3^{*\dagger}$	2.20	$1.7 \pm 0.9^{*\dagger}$	1.13	$2.3 \pm 1.5^{*\dagger}$	1.52
M1-6	$1.6 \pm 0.6^{\dagger}$	1.11	#	...	#	...	#	...	#	...
M1-7	$4.4 \pm 2.6^{*\dagger\ddagger}$	1.18	$3.6 \pm 0.9^{*\dagger}$	1.21	$4.6 \pm 1.3^{*\dagger}$	1.53	$3.2 \pm 1.4^{*\dagger}$	1.07	$3.4 \pm 1.9^{*\dagger}$	1.15
M1-9	$2.0 \pm 1.0^{*\dagger\ddagger}$	1.00	$2.2 \pm 1.5^{*\dagger}$	1.21	$2.9 \pm 2.0^{*\dagger}$	1.53	#	...	#	...
M1-14	$2.5 \pm 1.0^{*\dagger\ddagger}$	1.00	$2.7 \pm 1.5^{*\dagger}$	1.14	$3.3 \pm 1.9^{*\dagger}$	1.39	$2.6 \pm 2.1^{*\dagger}$	1.06	$2.6 \pm 2.4^{*\dagger}$	1.04
M1-16	$1.8 \pm 0.9^{*\dagger\ddagger}$	1.18	$1.7 \pm 0.5^{*\dagger}$	1.37	$2.3 \pm 0.8^{*\dagger}$	1.90	$1.3 \pm 0.6^{*\dagger}$	1.10	$1.7 \pm 1.0^{*\dagger}$	1.38
M2-2	$2.1 \pm 0.5^{*\dagger\ddagger}$	1.18	$1.3 \pm 0.2^{*\dagger}$	2.47	$2.5 \pm 0.5^{*\dagger}$	4.72	$0.72 \pm 0.25^{*\dagger}$	1.35	$1.2 \pm 0.7^{*\dagger}$	2.28

Notes: B80 = Barker (1980); KB94 = Kingsburgh and Barlow (1994); KH01 = Kwitter and Henry (2001); DI14 = Delgado-Inglada et al. (2014). In all cases, ICFs are applied to the sulphur ionic abundances from Table 3.10. Superscript symbols show the ions considered in the calculations: $^{*} = S^{+}$; $^{\dagger} = S^{2+}$; $^{\ddagger} = S^{3+}$. $^{\#}$ Uncertainties >100%, likely due to uncertainties in the ICF and S^{+} abundances given from Henry et al. (2010).

$$\mathrm{ICF}(\mathrm{Ar}^{2+}+\mathrm{Ar}^{3+}+\mathrm{Ar}^{4+}) = \frac{1}{1-(\mathrm{N}^{+}/\mathrm{N})} \tag{3.11}$$

$$\mathrm{ICF}(\mathrm{Ar}^{2+}) = 1.87 \pm 0.41 \tag{3.12}$$

Kwitter and Henry (2001) built upon equation (3.11) by considering the ICF when only the Ar^{2+} and Ar^{3+} ionic states could be observed:

$$\mathrm{ICF}(\mathrm{Ar}^{2+}+\mathrm{Ar}^{3+}) = \frac{1}{1-(\mathrm{N}^{+}/\mathrm{N})} \times \frac{\mathrm{He}^{+}+\mathrm{He}^{2+}}{\mathrm{He}^{+}} \tag{3.13}$$

Delgado-Inglada et al. (2014) calculated their abundances in terms of Ar/O, before multiplying by the O/H abundance calculated with the ICF from equation (3.10):

$$\log \mathrm{ICF}\Big(\frac{\mathrm{Ar}^{2+}}{\mathrm{O}^{+}+\mathrm{O}^{2+}}\Big) = \frac{0.03\omega}{0.4-0.3\omega} - 0.05 \qquad (0.5 < \omega < 0.95) \tag{3.14}$$

Table 3.15 shows a comparison between the Ar/H abundances using ICFs from all studies. In general, the empirical ICFs agree well with those from each of the three comparative studies. The uncertainties from Delgado-Inglada et al. (2014) are large, particularly when $\omega > 0.95$. As the ω values for the PNe in the Galactic anti-centre sample are all large due to high ionisation fields and relatively large O^{2+} abundances, Delgado-Inglada et al. (2014) state that their ICF is not appropriate for this situation as only Ar^{2+} is required, resulting in more ionisation states for which corrections are needed.

Overall, the abundances calculated with empirically determined ICFs in all three considered elements compare well with those using ICFs from the literature. The main advantage of using the empirical method is that there is no need for large ICFs due to the number of ionisation states for which there are data. While much larger ICFs are applied in the literature to account for missing ionisation states that contribute more to the elemental abundances, the resulting values relate well to those calculated empirically in which some or all of these missing ionisation states have been observed.

Table 3.15 Comparison of the argon abundances and ICFs used in this study with those in which ICFs from other sources have been applied – see equations (3.11) to (3.14).

	This work		KB94		KH01		DI14	
PN	Ar/H $\times 10^{-7}$	ICF(Ar)	Ar/H $\times 10^{-7}$	ICF(Ar)	Ar/H $\times 10^{-7}$	ICF(Ar)	Ar/H $\times 10^{-7}$	ICF(Ar)
K3-66	$11.2 \pm 4.4^{*\dagger}$	1.35	$10.5 \pm 2.5^{\dagger}$	1.87	...	...	$6.2 \pm 2.6^{\dagger}$	1.10
K3-67	$6.7 \pm 2.0^{*\dagger\ddagger}$	1.00	$8.4 \pm 2.0^{\dagger}$	1.87	$6.5 \pm 3.3^{\dagger\ddagger}$	1.05	$7.2 \pm 2.1^{\dagger}$	1.60
K3-70	$13.0 \pm 6.6^{*\dagger\ddagger}$	1.00	$15.3 \pm 4.1^{\dagger}$	1.87	$16.7 \pm 9.5^{\dagger\ddagger}$	1.47	$11.5 \pm 5.7^{\dagger}$	1.40
K3-90	$7.5 \pm 3.4^{*\dagger\ddagger\#}$	1.00	$4.2 \pm 1.1^{\dagger}$	1.87	...	...	...	...
K4-48	$16.2 \pm 5.3^{*\dagger\ddagger}$	1.00	$19.1 \pm 4.6^{\dagger}$	1.87	$18.8 \pm 8.5^{\dagger\ddagger}$	1.30	$15.3 \pm 4.7^{\dagger}$	1.50
M1-6	$18.3 \pm 7.2^{*\dagger}$	1.35	$9.7 \pm 2.3^{\dagger}$	1.87	...	...	...	...
M1-7	$16.2 \pm 9.5^{*\dagger}$	1.00	$19.1 \pm 4.6^{\dagger}$	1.87	$20.3 \pm 7.2^{\dagger\ddagger}$	1.51	$12.9 \pm 7.7^{\dagger}$	1.26
M1-9	$7.5 \pm 3.7^{*\dagger\ddagger}$	1.00	$9.1 \pm 2.4^{\dagger}$	1.87	$6.7 \pm 4.0^{\dagger\ddagger}$	1.31	$5.9 \pm 1.9^{\dagger}$	1.21
M1-14	$12.3 \pm 4.9^{*\dagger}$	1.35	$14.3 \pm 3.5^{\dagger}$	1.87	$11.0 \pm 8.6^{\dagger\ddagger}$	1.44	$8.7 \pm 3.6^{\dagger}$	1.14
M1-16	$22.2 \pm 11.1^{*\dagger\ddagger\#}$	1.00	$21.0 \pm 6.1^{\dagger\ddagger\#}$	1.18	$25.4 \pm 11.7^{\dagger\ddagger}$	1.46	$20.2 \pm 12.7^{\dagger}$	1.45
M2-2	$8.7 \pm 2.0^{*\dagger\ddagger}$	1.35	$6.2 \pm 1.5^{\dagger}$	1.87	$7.0 \pm 4.6^{\dagger\ddagger}$	1.10	$5.8 \pm 2.0^{\dagger}$	1.74
Y-C 2-5	$5.4 \pm 3.4^{\dagger}$	1.64	$6.2 \pm 1.6^{\dagger}$	1.87	...	...	$11.3 \pm 3.1^{\dagger}$	3.42

Notes: KB94 = Kingsburgh and Barlow (1994); KH01 = Kwitter and Henry (2001); DI14 = Delgado-Inglada et al. (2014). In all cases, ICFs are applied to the argon ionic abundances from Table 3.11. Superscript symbols show the ions considered in the calculations: $^{*} = Ar^{+}$; $^{\dagger} = Ar^{2+}$; $^{\ddagger} = Ar^{3+}$; $^{\#} = Ar^{4+}$.

Table 3.16 Comparison of heliocentric distances from Giammanco et al. (2011) and Frew et al. (2016).

PN	R_h / kpc (Giammanco+'11)	R_h / kpc (Frew+'16)
K3-65	3.7	13.0
K3-68	2.2	7.4
K3-69	>6.0	...
K3-70	>6.0	15.8
K3-71	2.5	18.2
K3-90	<1.0	7.0
M1-6	2.0	5.2
M2-2	>2.0	5.2

3.3.7 Galactocentric distances

Distances to Galactic PNe are known to be notoriously difficult to measure owing to the variation of bolometric luminosity and effective temperature values within the sources. The distances relative to the Galactic centre are considered, and the PNe in this sample are located towards the anti-centre, which somewhat reduces the errors relative to those of their respective heliocentric distances (R_h).

R_h is converted to R_g using the following equation:

$$|\overrightarrow{R_g}| = ([R_h \cos(b)\cos(l) - R_\odot]^2 + R_h^2 \cos^2(b)\sin^2(l) + R_h^2 \sin^2(b))^{0.5} \quad (3.15)$$

where $R_\odot = 8.0 \pm 0.5$ kpc.

Table 3.1 shows the distance values used for each PN. In this chapter, values from Frew et al. (2016) are primarily adopted, which have been measured through statistical means. Where possible, the use of directly determined distances from Giammanco et al. (2011) is prioritised. Table 3.16 shows the R_h values of the PNe in the anti-centre sample with distance values given by Giammanco et al. (2011), alongside those from Frew et al. (2016). While there are strong disagreements in most cases, the abundances towards the anti-centre remain lower than elsewhere in the Galactic disk. The choice of data set will not affect the overall conclusions as each case presents a similar level of dispersion around the overall gradient, part of which comes from uncertainties in the distance measurements.

The uncertainties quoted by Frew et al. (2016) are estimated to be $\sim$ 20–30%, which seem small for statistical values, though larger uncertainties will not affect the outcomes of the discussion.

3.4 Discussion

3.4.1 Comparison of abundances with literature

In Tables 3.9–3.11, the elemental abundances of neon, sulphur and argon are compared with those available from literature. Average uncertainties of 17.5% in neon abundances for the missing Ne^{3+} ionisation state, 25% in sulphur abundances for S^{+} and S^{4+}, and 30% in argon for Ar^{3+} and occasionally Ar^{+} have been accounted for. The sample of Henry et al. (2010) is used as the main comparison, as this is a recent study involving 12 of the 23 PNe in the anti-centre sample, though the abundances shown within the study of Sterling and Dinerstein (2008) are also considered. Both of these studies involved the use of optical spectra.

In most cases, there is good agreement between all sets of abundances. Where the abundance values calculated for this sample are lower than those found in the literature, this likely comes from over-estimated ICFs from optical studies; for example, the neon abundance of K3-90 from the literature (Table 3.9) has an ICF of 23.8 (from equation 3.5) applied to an uncorrected value relatively similar to ours (Henry et al., 2010), resulting in our elemental abundances disagreeing with theirs by a factor of 8. The neon ICF was high because the oxygen ICF was comparatively large (22.3), which was calculated from the ratio of (He^{+} + He^{2+})/He^{+} abundances (Kwitter and Henry, 2001). Kingsburgh and Barlow (1994) give the same oxygen ICF to the power of 2/3, which would have decreased the ICF from 22.3 to 7.9 and the neon abundance to $(4.7 \pm 2.6) \times 10^{-5}$. This is narrowly within the uncertainty range of our Ne/H value ($(1.8 \pm 0.8) \times 10^{-5}$).

Conversely, the neon abundance that has been calculated in this study for M4-18 is a factor of 20 greater than that given in the literature by De Marco and Crowther (1999). Their abundance was calculated using the 12.8 μm [Ne II] line flux from Aitken and Roche (1982)

(3.6×10^{-12} erg cm^{-2} s^{-1}), which compares well with the value calculated from the *Spitzer* data, 3.3×10^{-12} erg cm^{-2} s^{-1}. However, the value of log $I(H\beta)$ used by De Marco and Crowther (1999) is lower than ours (-11.44 and -11.24, respectively), accounting for a discrepancy of factor 1.6. The $I(H\beta)$ and $C(H\beta)$ values for this PN have been applied from Henry et al. (2010), but we are unable to directly compare our neon abundances for this source as they are unable to observe the dominant Ne^{+} ion, and Ne^{2+} is barely observable, if at all (they give its ionic abundance with a 90% uncertainty).

M1-1 also shows relatively large discrepancies between our abundances and those given in literature for neon and argon. By considering its high ionisation field, from which Ne^{5+} can be observed, it is expected that Ne^{3+} and Ar^{3+} will contribute significantly to their overall abundances. Aller et al. (1986) estimate the abundances of Ne^{2+}, Ne^{3+} and Ne^{4+} in M1-1, obtaining values of a factor ~ 3 lower than those calculated in this study, with Ne^{+3} contributing 40% of the total of those three ions (taken from measurements of the 2424 Å [Ne IV] line). They also estimate Ar^{3+} to contribute 31% of the total argon abundance. ICFs of 1.12 and 2.1, for neon and argon respectively, are applied to their overall abundances. Even so, there are still significant discrepancies between both sets of abundance values.

The abundances of the anti-centre PNe agree well with those from literature. Notably, they also agree well with the elemental abundances of the ISM, as predicted by Wilms et al. (2000) and shown in Table 3.17. Not only does this reinforce the idea that these elements are not produced over the course of stellar evolution, but it also suggests that the chemical compositions of the PNe have not been affected by changes in galactocentric position, hence the orbits of most of these sources are likely to be circular (Pottasch and Bernard-Salas, 2006).

Table 3.17 Elemental abundances of neon, sulphur and argon from the ISM, as estimated by Wilms et al. (2000).

Element	Interstellar abundance
Ne	8.7×10^{-5}
S	1.2×10^{-5}
Ar	2.6×10^{-6}

For the few cases in which there are discrepancies between these abundances and those from the literature, they are likely to come from the larger ICFs used from other studies.

3.4.2 The abundance gradient

Figure 3.2 shows the abundances of neon, sulphur and argon plotted against R_g for the PNe in the anti-centre sample (open circles) and for those of Pottasch and Bernard-Salas (2006) from

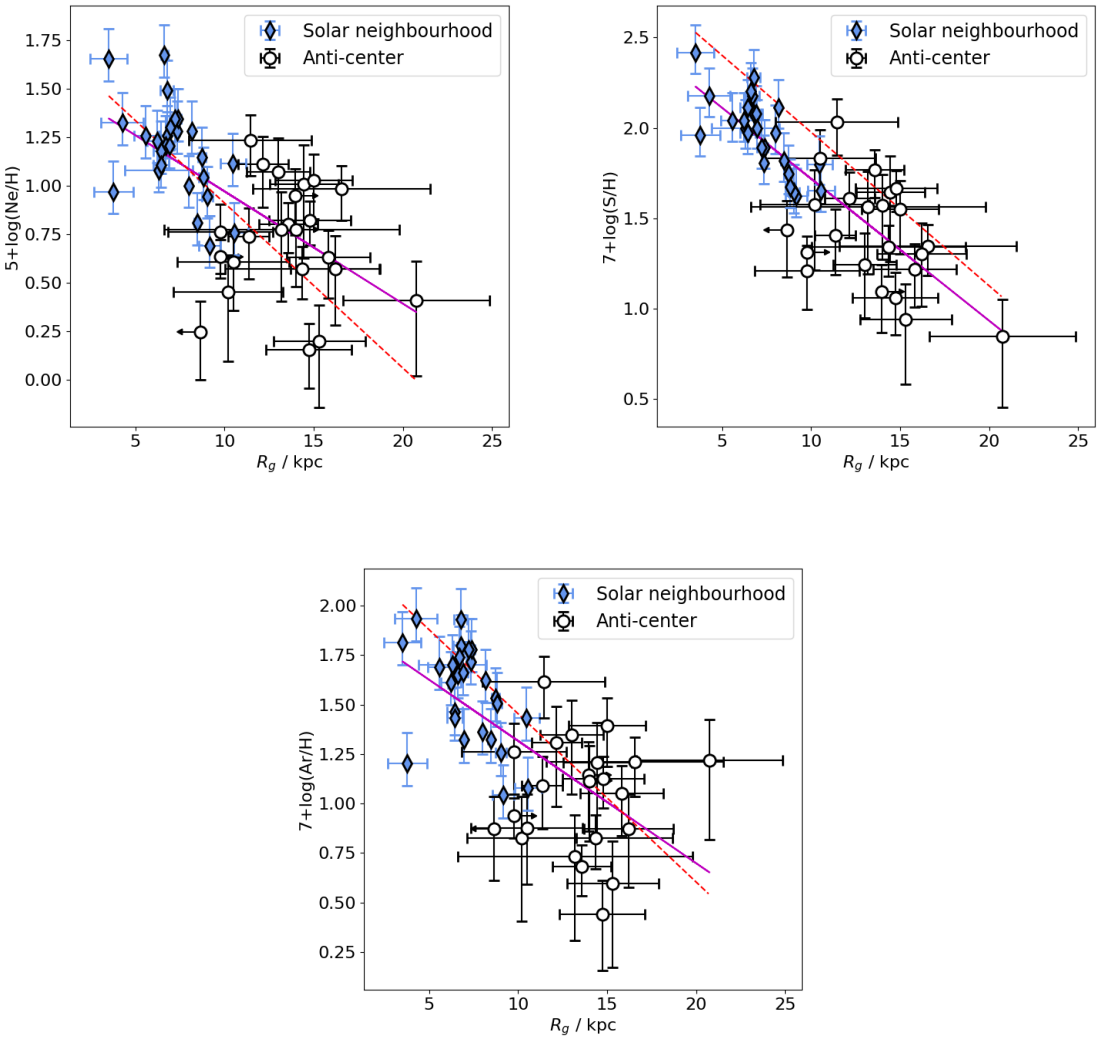

Fig. 3.2 The abundance gradients of neon, sulphur and argon in the Milky Way. The dashed lines represent the oxygen abundance gradient from within the Galactic disk with a slope of -0.085 dex/kpc (Pottasch and Bernard-Salas, 2006), passing through the solar value at 8.0 kpc (Asplund et al., 2005). The solid lines represent the line of best fit in each plot, with gradients of -0.058 ± 0.021, -0.079 ± 0.012 and -0.062 ± 0.023 dex/kpc respectively.

the solar neighbourhood (filled diamonds). Both of these samples were analysed and reduced in a similar way.

The abundances are lower than those of the Galactic bulge and the solar neighbourhood, and are consistent with a continuation of the metallicity gradient up to $R_g \sim 20$ kpc, albeit with a large dispersion within the data. However, when analysing the neon and argon anti-centre data separately from the solar neighbourhood data, there is no clear correlation, with Pearson correlation coefficients (R_{PCC}) of ~ -0.05 in each case. Hence, these data cannot discern whether there is a gradient in the anti-centre ($R_g > 10$ kpc). For sulphur, the anti-centre data show $R_{PCC} = -0.45$ with a corresponding p-value of 0.032, showing that there is a slight negative correlation in the anti-centre that is statistically significant. Together with the solar neighbourhood data, $R_{PCC} = -0.64$, -0.82 and -0.66 for neon, sulphur and argon respectively.

Table 3.18 compares the radial metallicity gradients from a selection of studies over multiple wavebands, including PNe, H II regions, young B-type stars and Cepheid variables. This analysis includes studies of neon, sulphur and argon gradients. Oxygen is also considered; even though its abundance changes over the course of stellar evolution in PNe, Pottasch and Bernard-Salas (2006) suggested that the oxygen gradient of sources that had not undergone hot bottom burning was identical to those of the other three elements from their PN sample. The metallicity gradient slopes from this work compare well with those from most other studies, though ours have greater uncertainties which arise from the dispersion at greater R_g, primarily due to the uncertainties in the distance measurements. Despite this, the slopes calculated from the PN studies of Maciel and Quireza (1999), Pottasch and Bernard-Salas (2006) and this study are typically steeper than those of other source types. Our metallicity gradients are consistent with a continuation at high R_g, though the slopes suggest an eventual flattening or steepening with distance is possible, particularly for neon and argon. While some of the studies that are considered rule out flattening as a possibility, the studies of Andrievsky et al. (2002a,b,c) and Luck et al. (2003), analysing Cepheid variables, find discontinuities in the abundance gradient with R_g. They show that the gradient is seen to be steeper in regions

Table 3.18 Comparison of several abundance gradient studies which use various sources.

Study	Sources	Waveband	Element	Slope (dex/kpc)	R_g range (kpc)
This work	PNe	IR, Optical	Ne	-0.058 ± 0.021	3–21*
			S	-0.079 ± 0.012	3–21*
			Ar	-0.062 ± 0.023	3–21*
Maciel and Quireza (1999)	PNe	IR, Optical	O	-0.058 ± 0.007	4–14
			Ne	-0.036 ± 0.010	4–14
			S	-0.077 ± 0.011	4–13
			Ar	-0.051 ± 0.010	4–13
Pottasch and Bernard-Salas (2006)	PNe	IR, Optical, UV	O, Ne, S, Ar	-0.085	3–11
Maciel et al. (2015)	PNe	multiple	O	-0.025 ± 0.006	0–15
Martín-Hernández et al. (2002)	H II regions	Optical	Ne	-0.039 ± 0.007	0–14
			Ar	-0.045 ± 0.011	0–13
Esteban et al. (2017)	H II regions	Optical	O	-0.040 ± 0.005	5–17†
Fernández-Martín et al. (2017)	H II regions	Optical	O	-0.053 ± 0.009	11–18
			S	-0.106 ± 0.006	11–18
			Ar	-0.074 ± 0.006	11–18
Fitzsimmons et al. (1992)	B-type stars	multiple	O	-0.03 ± 0.02	5–14
Rolleston et al. (2000)	B-type stars	Optical	O	-0.067 ± 0.008	6–18
Andrievsky et al. (2002b)	Cepheids	Optical	O	-0.022 ± 0.009	6–11
			S	-0.051 ± 0.008	6–11
Lemasle et al. (2013)	Cepheids	Optical, near-IR	S	-0.095 ± 0.015	4–19‡
Henry et al. (2004)	PNe, H II regions, B-type stars, Cepheids	multiple	O	-0.037 ± 0.008	0–18
			Ne	-0.044 ± 0.014	2–14
			S	-0.048 ± 0.010	0–17
			Ar	-0.030 ± 0.010	2–17

Notes: Studies with 'multiple' wavebands use data from several references. * Includes data from Pottasch and Bernard-Salas (2006); † Includes data from Esteban et al. (2015); ‡ Includes data from Luck and Lambert (2011).

closer to the Galactic centre ($R_g \sim$ 4–6 kpc) and towards the anti-centre ($R_g \sim$ 10–15 kpc) for 25 different elements, including oxygen and sulphur. Several studies that analyse sources beyond $\sim$ 15 kpc (e.g. Fernández-Martín et al. 2017; Lemasle et al. 2013; Rolleston et al. 2000; this work) show steeper gradients than those found in most other studies. While this appears to agree with the findings of Andrievsky et al. (2002a,b,c), there are relatively few sources at these distances in each named study, hence the effect of the large distance sources on the respective gradients is likely to be minimal. By factoring in the large uncertainties in distance measurements for most sources in these samples, the abundance gradients do not steepen with R_g in the direction of the anti-centre.

Analysis of the time evolution of the Galactic abundance gradient from this PN sample is also difficult, due to the large uncertainties in abundances and Galactocentric distances. The data in this study are consistent with a continuation of the gradient at large distances, so there is no suggestion that the inner and outer disks of the Milky Way evolved separately (e.g. Kubryk et al. 2015; Stanghellini and Haywood 2010).

3.4.3 α-process elements

In the evolution of low- to intermediate-mass stars, the abundances of elements heavier than carbon are generally not affected, except for those formed during the slow neutron-capture process (known as the *s*-process) which can occur during the AGB phase (e.g. Lugaro et al. 2012). As a result, the abundances of neon, sulphur and argon should trace each other. Figure 3.3 shows that there is good agreement between these abundances, hence proving that they do trace each other well, though it is clear that the plot of sulphur against argon shows a greater dispersion. This could be explained by the need to account for two ions for argon (Ar^+ and Ar^{3+}), for which Ar^{3+} can be the dominant ion.

Included on these plots are the abundances of Ne, S and Ar from the Magellanic Clouds. The mean abundance values for neon and sulphur were taken from an IR *Spitzer* sample of PNe from Bernard-Salas et al. (2008), and those for argon were taken from an optical PN sample from Leisy and Dennefeld (2006). The anti-centre sample shows abundances scattered

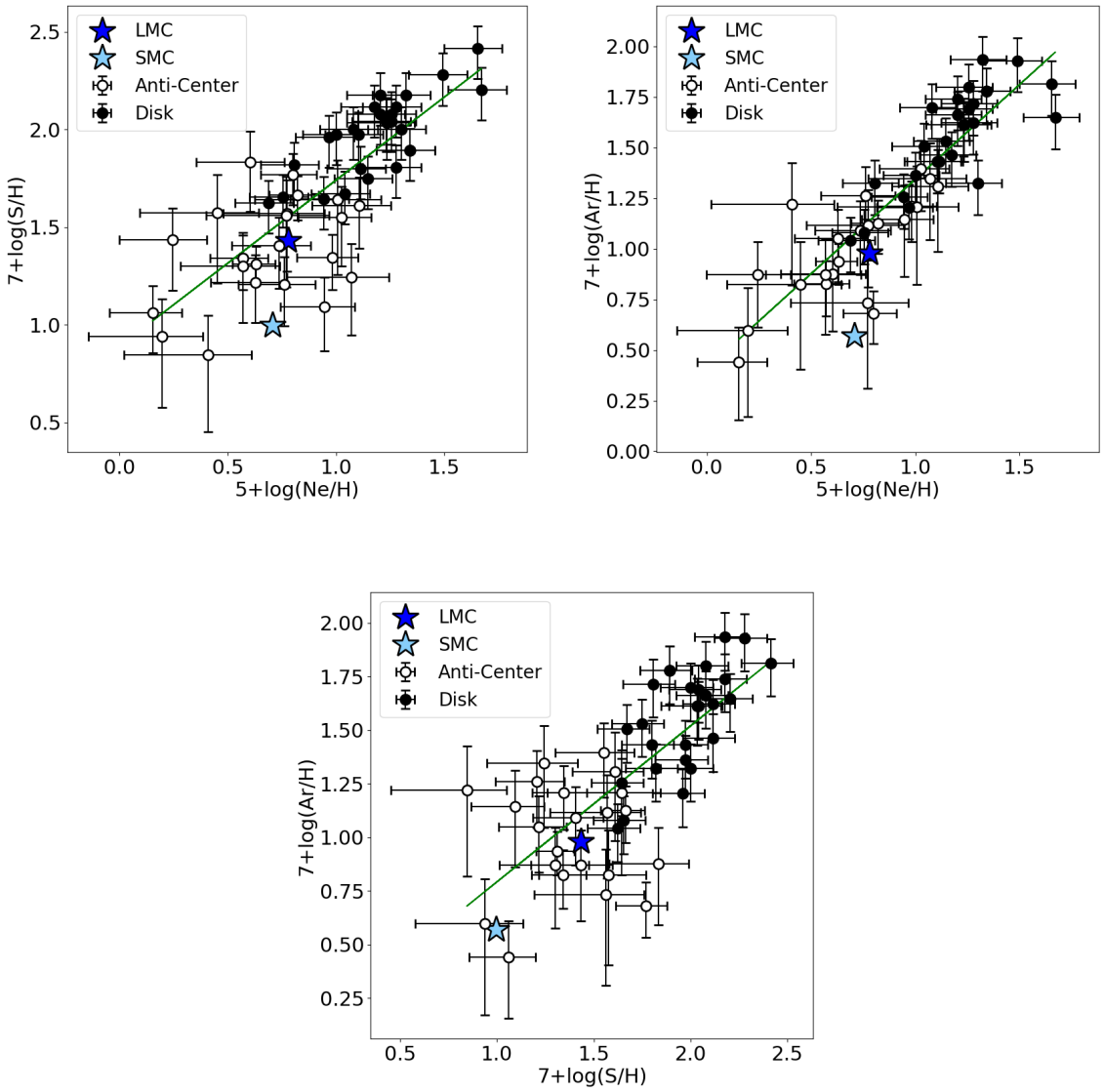

Fig. 3.3 Plots comparing the neon, sulphur and argon abundances. The Galactic Disk sample was analysed by Pottasch and Bernard-Salas (2006). The average abundances for the LMC and SMC are also shown, with those of neon and sulphur obtained from Bernard-Salas et al. (2008) and argon from Leisy and Dennefeld (2006).

around the LMC metallicity for each of the three elements, with few reaching values below those of the SMC.

The sulphur anomaly

The 'sulphur anomaly' is the term coined by Henry et al. (2004), used to describe the observed sulphur abundances in PNe being lower than those of H II regions at the same metallicity (see

also e.g. Henry et al. 2012). It was originally suggested that this could be explained by the lack of measured emission lines of ionisation states of S^{3+} and above in optical spectra and the need to account for them, particularly as S^{3+} can be a key stage of ionisation for sulphur. The sulphur anomaly has been seen in multiple galaxies; García-Rojas et al. (2016) observe this anomaly from four H II regions with abundances greater than most of the thirteen PNe in their sample from NGC 6822. Shaw et al. (2012) find the anomaly in the Magellanic Clouds from a combination of IR, optical and UV data, and Shingles and Karakas (2013) find the anomaly in the Milky Way from the PN sample of Pottasch and Bernard-Salas (2010), also from spectra in the same wavebands, compared to the ISM trend of H II regions and blue compact galaxies from the optical sample of Milingo et al. (2010).

In Figure 3.4, the sulphur abundances of PNe in the Galactic anti-centre and solar neighbourhood (Pottasch and Bernard-Salas, 2006) are compared with the sulphur abundances in two samples of Galactic H II regions, one derived from IR data (Martín-Hernández et al., 2002) and the other from optical data (Fernández-Martín et al., 2017). Both of these samples cover a similar range of Galactocentric distance values to the anti-centre PNe.

The IR H II region data from Martín-Hernández et al. (2002) agree well with the PN abundances, inferring that the sulphur anomaly is not observed from these data. However, their H II region abundances disagree with the interstellar and solar values of sulphur by a factor of $\sim$ 2–4. Based on this, they argue that their abundances are underestimated by up to a factor 4, from which they ascribe to uncertainties in n_e and T_e, with the lack of S^+ abundance values from their IR data from *ISO* accounting for a further $\sim$ 15% discrepancy. It is noted that since the release of the paper of Martín-Hernández et al. (2002), the most widely used solar sulphur abundance value from the literature shows a decrease of $\sim$ 20% from the value they used (Asplund et al., 2009; Snow and Witt, 1996), though both the abundances of the anti-centre PNe and the H II regions remain low in comparison.

On comparing the infrared PN abundances with the optical H II region abundance data of Fernández-Martín et al. (2017), with Galactocentric distances of 11–17 kpc, there is a clear discrepancy between the two sets of data. The PN abundances are lower than those of the

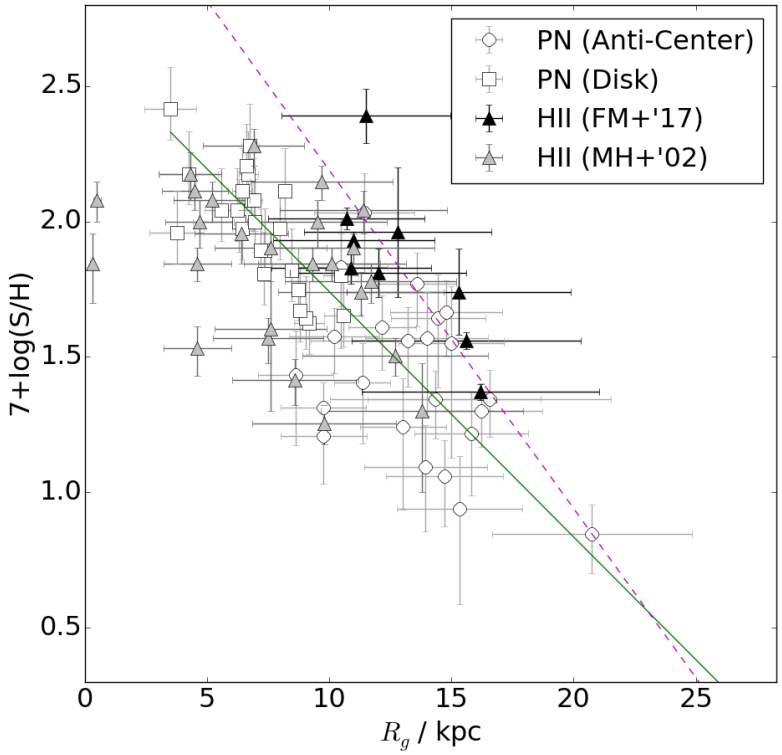

Fig. 3.4 The sulphur abundances of the PNe in the Galactic anti-centre sample, alongside those of H II regions from Fernández-Martín et al. (2017) (FM+'17) and Martín-Hernández et al. (2002) (MH+'02), and solar neighbourhood PNe from Pottasch and Bernard-Salas (2006). The solid line is the line of best fit for PN abundances. The dashed line represents that for the H II regions of the FM+'17 sample.

H II regions by a factor ~ 2, as shown by the two lines of best fit in Fig. 3.4. In this case, the sulphur anomaly is clearly observed.

3.5 Summary

An infrared spectroscopic study of 23 PNe towards the Galactic anti-centre with R_g values of 8–21 kpc has been presented, in which *Spitzer* IRS has been used to determine the abundances of neon, sulphur and argon in a region that is *a priori* assumed to be metal-poor.

The abundances have been calculated in two ways: using empirically calculated ICFs from a combination of IR and optical data, and using more well-established ICFs from the literature. The two methods produce similar results; the empirical ICFs consider a wider range of ionic states and are therefore small in value. The abundances of neon, sulphur and

argon are lower in the anti-centre than those in the Solar neighbourhood. The metallicity gradients of these elements seem to continue beyond $R_g = 10$ kpc despite a large spread of data values. The abundances of the α-process elements trace each other well, though there is a slightly larger dispersion between those of sulphur and argon.

Spitzer IRS has enabled the study of abundances from observations of PNe in the bulge, disk and halo of the Milky Way, as well as in nearby galaxies (primarily the Magellanic Clouds) at infrared wavelengths. With its greater sensitivity, the James Webb Space Telescope (*JWST*) will be able to continue obtaining spectra for PNe as far as the Local Group of galaxies, enabling us to carry out abundance studies over a wider range of parameter space. In addition, *JWST* will be able to spatially resolve PNe in the Milky Way, allowing us to investigate how the gas and dust content varies within these nebulae.

This chapter has further confirmed that the abundances within a sample of PNe in the Galactic anti-centre are lower than elsewhere in the Galactic disk, exhibiting a metallicity range incorporating those of the LMC and SMC. The next chapter will explore how the dust composition of this sample of PNe compares to sources closer to the Galactic centre and in the Magellanic Clouds.

Chapter 4

Dust composition of PNe in the Galactic anti-centre

(This chapter is based on a paper in preparation, to be submitted to *Astronomy & Astrophysics* by G. J. S. Pagomenos and J. Bernard-Salas (Open University, UK), E. Peeters (University of Western Ontario, Canada and SETI Institute, USA) and G. C. Sloan (Cornell University, University of North Carolina and Space Telescope Science Institute, USA). A preliminary version of the work in this chapter has also been published in a conference proceedings as Pagomenos et al. 2017.)

4.1 Introduction

Dust plays important roles in the interstellar medium (ISM), such as the reprocessing of stellar UV light to infrared and sub-millimetre wavelengths, and the catalysis of molecular formation. Much of the dust in the local ISM is formed during the evolutionary phase of low- to intermediate-mass stars ($\sim$ 0.8–8 $M_{\odot}$) known as the asymptotic giant branch (AGB). The most commonly observed types of emission features associated with dust are those of polycyclic aromatic hydrocarbons (PAHs), which are widely spread throughout the Universe, having been detected spectroscopically up to redshifts of z $\sim$ 2.8 (Lutz et al., 2008). Together with over 60 molecular species (e.g. Olofsson 2005; Kwok 2011), these dust grains originate

from within the circumstellar envelope of the AGB star, from which they are ejected primarily by stellar winds, enriching the ISM.

The composition of dust from AGB stars is characterised as either carbon-rich or oxygen-rich, depending on the efficiency of the third dredge-up mixing process and the resulting C/O ratio of the star. Carbon and oxygen in the convective envelope will preferentially form CO. An excess of carbon (i.e. C/O $>$ 1) will lead to the production of C-rich dust, which includes PAHs, fullerenes and silicon carbide. Conversely, an excess of oxygen (i.e. C/O $<$ 1) leads to O-rich dust, consisting of amorphous and crystalline silicates. Some sources also show dual-dust chemistry, in which both C-rich and O-rich dust emission are observed from their spectra; the reasons for this dual-dust chemistry are still in debate (see Chapter 1). The abundance of oxygen in the ISM is greater than that of carbon, so all stars will be born O-rich. In low- to intermediate-mass stars, the third dredge-up brings carbon from the stellar interior to the outer envelope, and the overall dust composition of the star will become C-rich if the amount of carbon in the envelope is greater than that of oxygen. In metal-poor regions, the amount of oxygen in the ISM will be low, hence the amount of dredged-up carbon required for the star to become C-rich is reduced. Therefore, regions of lower metallicity will theoretically favour the production of C-rich dust.

In the Milky Way, PNe located towards the metal-rich Galactic bulge ($0 < R_g < 4$ kpc) show significantly more dual-dust chemistry than elsewhere in our Galaxy (Gutenkunst et al., 2008; Perea-Calderón et al., 2009; Pottasch and Bernard-Salas, 2015). In the solar neighbourhood ($4 < R_g < 10$ kpc) and towards the Galactic anti-centre ($R_g > 8$ kpc), the distribution of the dust emission from PNe with Galactocentric distance is not well defined, though both C-rich and O-rich sources have been observed in these regions (e.g. Ishihara et al. 2011, Delgado-Inglada and Rodríguez 2014; García-Hernández and Górny 2014).

Studies of post-AGB stars and PNe in the Large and Small Magellanic Cloud galaxies (LMC/SMC) within the Local Group have shown that C-rich dust is more commonly observed than O-rich dust in these regions (e.g. Bernard-Salas et al. 2009; Matsuura et al. 2014; Sloan et al. 2014). These galaxies have average metallicity values of around 1/3 $Z_{\odot}$ and

1/6 $Z_{\odot}$, respectively (Bernard-Salas et al., 2008). There is also a greater inventory of C-rich dust emission features that have been observed in the Magellanic Clouds than in the solar neighbourhood. For instance, features attributed to silicon carbide (SiC) and fullerenes are not commonly observed around evolved stars in the disk of the Milky Way, yet they have been more readily detected in samples of PNe from the LMC and SMC (e.g. Bernard-Salas et al. 2009; Sloan et al. 2014). Hence, these studies further suggest a relationship between the formation of C-rich dust and low metallicity regions. This also ties in with a study by Stanghellini et al. (2012), who suggested that the number of O-rich and dual-dust chemistry sources decreases, while that of C-rich sources increases, with increasing Galactocentric distance.

The results from the previous chapter have shown that the Galactic anti-centre covers a range of sub-solar metallicity values, encompassing the average metallicities from both the LMC and SMC. In this chapter, we analyse the dust composition of the same sample of PNe and compare it with the dust emission from samples of PNe from the Galactic disk and the Magellanic Clouds that have been analysed in a similar way. In § 4.2, the full *Spitzer* spectra of the 23 PNe are shown, and an inventory is given of the dust features present. The main PAH emission profiles are examined in § 4.3, and these are further analysed through Gaussian decomposition methods in § 4.4. In § 4.5–4.8, the silicon carbide, fullerene, 30 μm and silicate features in the sample are respectively analysed. In § 4.9, the PNe with no clear dust emission features in the sample are investigated. In § 4.10, the relationship between the dust composition and the metallicity of the Galactic anti-centre is explored. The conclusions are given in § 4.11.

4.2 Sample overview

This chapter investigates the dust composition of a sample of 23 PNe from the Galactic anti-centre, as observed by *Spitzer* IRS. The full list of the sources is given in Chapter 3 and a description of the data reduction and extraction methods can be found in Chapter 2. The spectra for each of these sources are shown in Appendix A.

Table 4.1 An overview of the carbon-rich dust features observed in the sample.

Source	PAH	SiC	30μm	C_{60}	Silicates
J320	...	...	...	...	...
K3-65	Y	...	...	...	...
K3-66	Y	Y	...	...	...
K3-67	Y?	...	...	...	...
K3-68	Y	...	...	...	...
K3-69	Y	...	...	...	...
K3-70	Y?	...	...	...	...
K3-71	Y	...	...	...	...
K3-90	...	...	...	...	...
K4-48	Y	...	...	...	...
M1-1	...	...	...	...	...
M1-6	Y	Y	Y	Y	...
M1-7	Y	...	...	...	...
M1-8	Y	...	...	...	...
M1-9	Y	Y	Y	Y	...
M1-14	...	Y	Y	...	...
M1-16	Y	...	...	...	...
M1-17	Y	...	...	...	...
M2-2	...	...	Y?	...	...
M3-2	...	...	...	...	...
M4-18	Y	...	Y	Y	Y?
SaSt2-3	11.2	Y	Y	Y	...
Y-C 2-5	...	...	...	...	...

Table 4.1 shows the catalogue of the main dust features observed in the entire sample. Of the 23 PNe in this sample, 15 show C-rich dust features, including PAHs, fullerenes, SiC and the so-called '30 μm feature'. A further three sources show tentative C-rich emission (PAHs in K3-67 and K3-70, and the 30 μm feature in M2-2), in which the uncertainty in their detections comes from continuum noise and profiles that are difficult to characterise. Only one PN, M4-18, potentially shows amorphous silicates as well as C-rich dust emission, hence we consider it as a dual-dust chemistry source. For the remainder of this chapter, these tentative identifications are considered as certain detections.

4.3 Polycyclic aromatic hydrocarbons (PAHs)

PAHs are the most commonly detected C-rich dust emission features in both circumstellar and interstellar environments, with the main features observed at 3.3, 6.2, 7.7, 8.6, 11.2 and 12.7 μm (e.g. Allamandola et al. 1999; Moutou et al. 2000; Peeters et al. 2002), each representing either C–C or C–H bond vibrations within the molecule (see Chapter 1). Other PAH emission features representing C–C–C bond vibrations within the carbon skeleton may be seen at wavelengths > 15 μm, though they are comparatively weak in PNe (e.g. Shannon et al. 2015). These higher wavelength features are not observed in the Galactic anti-centre sample.

In this section, the profiles of the PAH features are investigated, and the changes in particular PAH intensity ratios with radiation field are examined. The continua were modelled by two different splines, as per the study of Peeters et al. (2017). These are shown in Figure 4.1. The first is a local spline, with continuum points placed at approximately 5.5, 5.9, 6.6, 7.1, 8.3, 8.8, 9.1, 9.6, 9.9, 10.2, 10.7, 11.7, 12.1 and 13.3 μm, from which the PAH flux measurements in Table 4.2 have been obtained. The second is a global spline with no continuum points within the 7–9 μm and 11–13 μm regions, which is considered in § 4.4. In both cases, no points were placed within a wavelength region that was being measured.

4.3.1 Profiles

The profiles of PAH emission features vary between different sources, and may hence be related to the physical conditions of the environments in which they are observed. As discussed in Chapter 1, Peeters et al. (2002) categorised PAH emission by their peak positions, where Classes *A*, *B* and *C* represent peaks at increasing wavelengths. On average, from Class *A* through to Class *C*, the relative strengths of the 6.2 μm PAH features decreases and the full-width at half-maximum (FWHM) of the 7.7 μm features increases. Indeed, Class *C* emission of the 7.7 μm PAH feature blends in with the accompanying 8.6 μm feature. PAH emission of Class *C* is rare, and has been observed around post-AGB stars and proto-planetary nebulae (e.g. Peeters et al. 2002; Sloan et al. 2007) but not around PNe. In their study of post-AGB

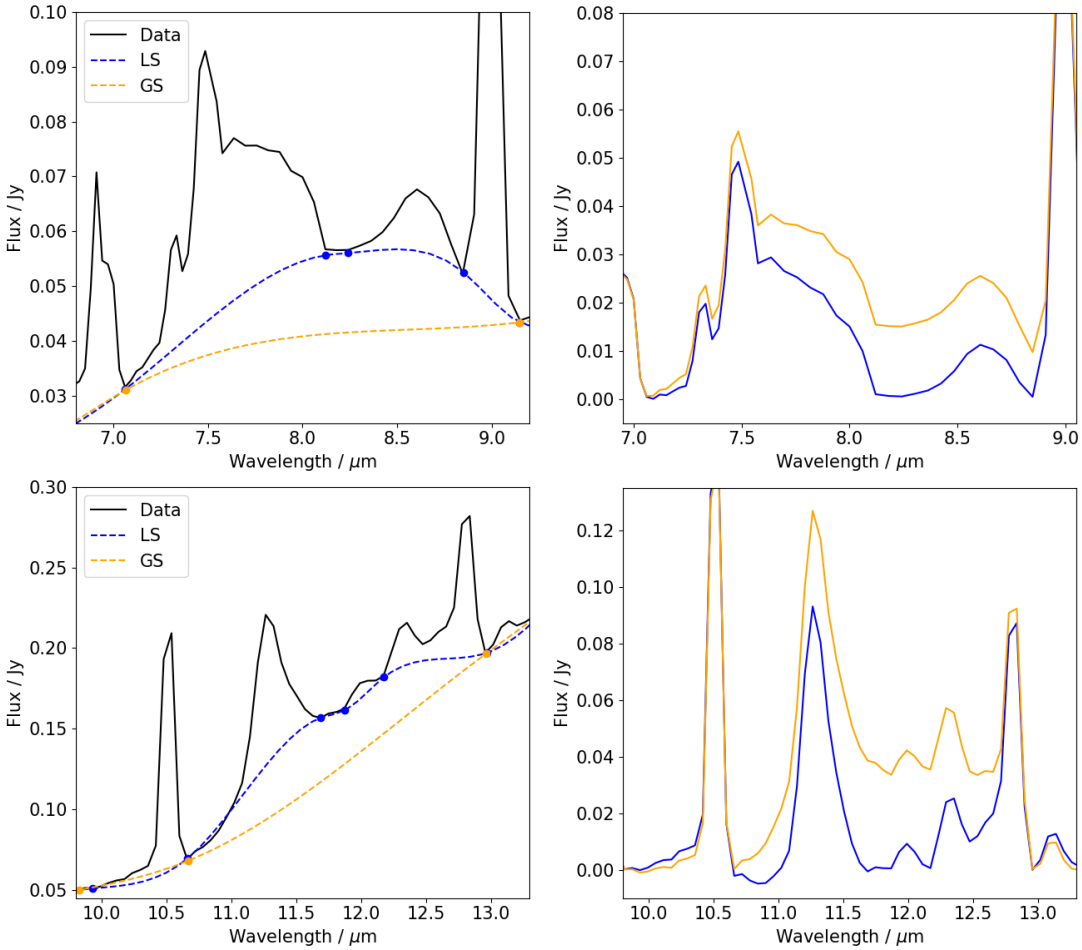

Fig. 4.1 The two methods of continuum fitting for K4-48: local splines (LS, blue) and global splines (GS, orange). The 7–9 μm (top) and 11–13 μm (bottom) regions are highlighted as the two spline fits differ within these wavelength ranges. The continua fitted as splines on the left-hand spectra are subtracted to produce the right-hand spectra.

stars in the Magellanic Clouds, Matsuura et al. (2014) have since provided classifications for PAHs in the 10–14 μm wavelength region, and have introduced a new Class *D* in the 6–9 μm region, which considers PAH profiles that cannot accurately be categorised as either Class *A*, *B* or *C*.

Figure 4.2 shows the continuum-subtracted spectra of the PAH-emitting PNe in our sample, which show emission of Classes *A* and *B* for all PAHs in the wavelength range 6–9 μm. The 7.7 μm features of M1-7 and M1-8 have been omitted from this analysis as they show several emission lines that are stronger than this PAH feature, particularly the H_2 0–0 S(4) line at 8.0 μm, the [Na III] line at 7.3 μm and the H I 6–5 line at 7.5 μm, making the classification of these profiles uncertain. The 7.7 μm profiles of M1-6, M1-9 and K3-66 showed particularly

Table 4.2 Intensity values of the main PAH emission features (with atomic line emission subtracted) in units of 10^{-17} W m^{-2}.

PN	6.2μm		7.7μm		8.6μm		11.2μm	
	I(λ)	EW	I(λ)	EW	I(λ)	EW	I(λ)	EW
K3-65	21.1	0.632	46.4	0.819	3.05	0.055	18.6	0.524
K3-66	38.1	0.255	69.0	0.405	11.6	0.058	27.3	0.059
K3-67	5.94	0.064*	17.4	0.650	...	...	7.07	0.025
K3-68	47.9	0.798	92.6	0.652	5.01	0.029	40.7	0.872
K3-69	142	0.290	253	0.303	19.5	0.025	179	0.305
K3-70	4.22	0.598*	7.29	1.249*	0.63	0.085	...	...
K3-71	11.8	1.998**	18.2	1.445*	2.22	0.112	3.77	0.452
K4-48	70.7	0.549	90.8	0.412	11.8	0.051	83.6	0.315
M1-6	323	0.034	295	0.125	102	0.034	...	...
M1-7	21.4	0.874*	32.5	1.599	0.92**	0.020**	8.55	0.253
M1-8	6.80	0.545	17.6	1.254*	3.21	0.089	9.01	0.350
M1-9	12.9	0.072	23.9	0.303	62.8	...	...	...
M1-16	145	0.345	279	0.529	17.1	0.032	189	0.483
M1-17	192	0.581	249	0.590	35.6	0.072	281	0.577
M4-18	1490	0.502	2870	0.438	474	0.071	1610	0.230
SaSt2-3	...	...	...	...	...	...	0.90	0.027

Notes: EW values are measured in microns. All uncertainties are assumed to be 10% for the 6.2, 7.7 and 11.2 μm PAH features and 15–20% for the 8.6 μm PAH feature unless otherwise specified. *: Uncertainties $\sim$ 20%; **: Uncertainties $\sim$ 50%.

strong H I emission that has been removed from Figure 4.2, hence there is an irregularity between $\sim$ 7.3–7.5 μm for these PNe. The profiles in K3-67 and K3-70 are not typical of PAHs, and are therefore hard to classify in all cases. It is assumed that these are sources of PAH emission. The 7.7 μm features in these two sources are also weak, as they are overshadowed by the H_2 0–0 S(4) line at 8.0 μm.

The 6–9 μm PAH classes are also shown in Table 4.3. From these data, there is a relatively even mix of both Classes *A* and *B* from the 6.2 and 7.7 μm components, whereas the 8.6 μm profiles are primarily of Class *B*. Although the wavelength ranges covered by the 7.7 μm features in M1-6 and M1-9 are slightly narrower ($\sim$ 7.2–8.0 μm, c.f. typical profiles in the range 7.2–8.2 μm), these two PNe are the only sources in the Galactic anti-centre sample to show all PAH emission in the range 6–9 μm as well as SiC, C_{60} and the 30 μm feature. Hence, it could be speculated that there may be a link between the extent of the 7.7 μm PAH

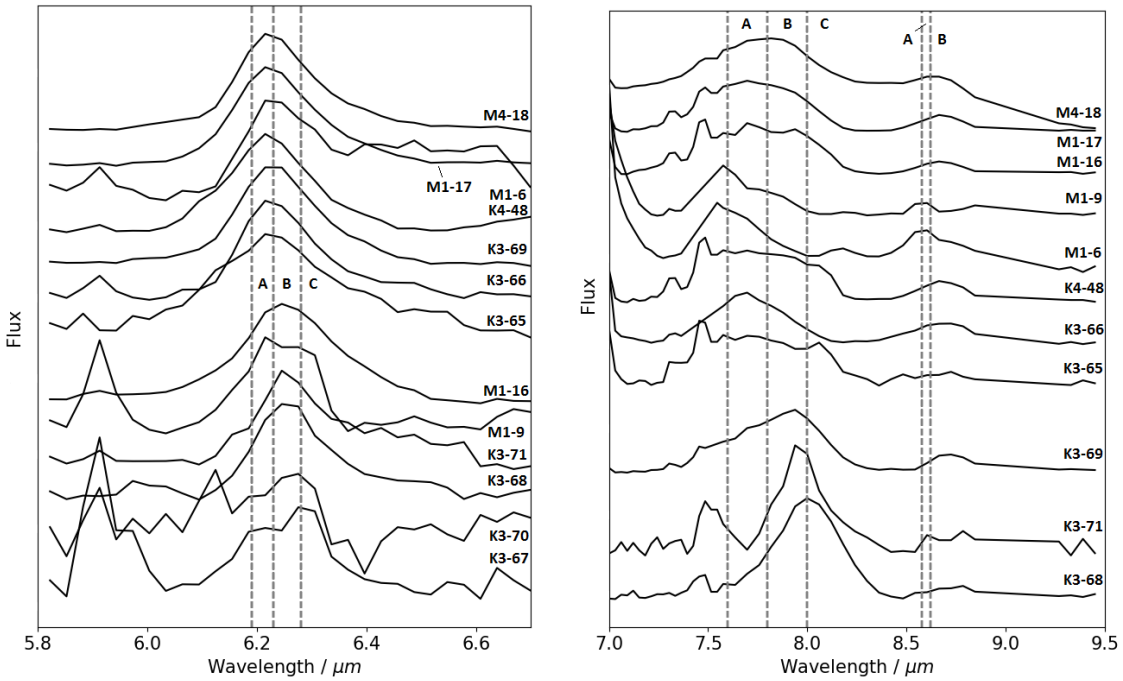

Fig. 4.2 Continuum-subtracted, normalised 6.2, 7.7 and 8.6 μm PAH profiles. The *A*, *B* and *C* regions indicate the wavelength ranges of peak positions in accordance with the classification system from Peeters et al. (2002). Strong atomic line emission that was observed at PAH emitting wavelengths, such as the H_2 0–0 S(6) line at 6.1 μm, H I 6–5 at 7.5 μm, and [Ar III] at 9.0 μm.

Table 4.3 PAH classes of Peeters et al. (2002) for the PNe in the Galactic anti-centre sample.

PN	6.2 μm Class	7.7 μm Class	8.6 μm Class
K3-65	A/B	A	A
K3-66	A	A	B
K3-67‡	B?	*	...
K3-68	B	B	B
K3-69	A/B	B	B
K3-70‡	A/B?	B?	B?
K3-71	B	B	B
K4-48	A	A/B	A/B
M1-6	A/B	A	†
M1-9	B	A	†
M1-16	B	A/B	B
M1-17	A	A	B
M4-18	A	A/B	B

Notes: * The [Na III] 7.3 μm and H I 6–5 line at 7.5 μm cover much of the PAH emission feature. † The 8.5 μm C_{60} feature covers this feature, which adds uncertainty to the observed profile of the PAH emission. ‡ It is unclear as to whether the emission observed in these sources is real, as the profiles are irregular.

features and the presence of the other C-rich dust emission features, although this may depend on the applied continuum.

The PAH emission within the wavelength range 6–9 μm in this sample of Galactic anti-centre PNe is typical of that observed in evolved stars from other regions. However, variations within the wavelength range of the 7.7 μm profile are seen in sources with a broader inventory of C-rich dust features, and these have not been observed in spectra from other samples of PNe.

4.3.2 Ionisation fractions

The charge of the PAH molecules directly affects the relative intensities of the main features; those attributed to C–C bonds (6.2 and 7.7 μm) are stronger in ionised PAHs, whereas those caused by C–H bond emission (3.3 and 11.2 μm) dominate in neutral molecules, and the 12.8 μm feature is emitted from both (Shannon et al., 2016). Figure 4.3 compares flux ratios of ionised-to-neutral PAH features (6.2 / 11.2 μm and 7.7 / 11.2 μm), including values from

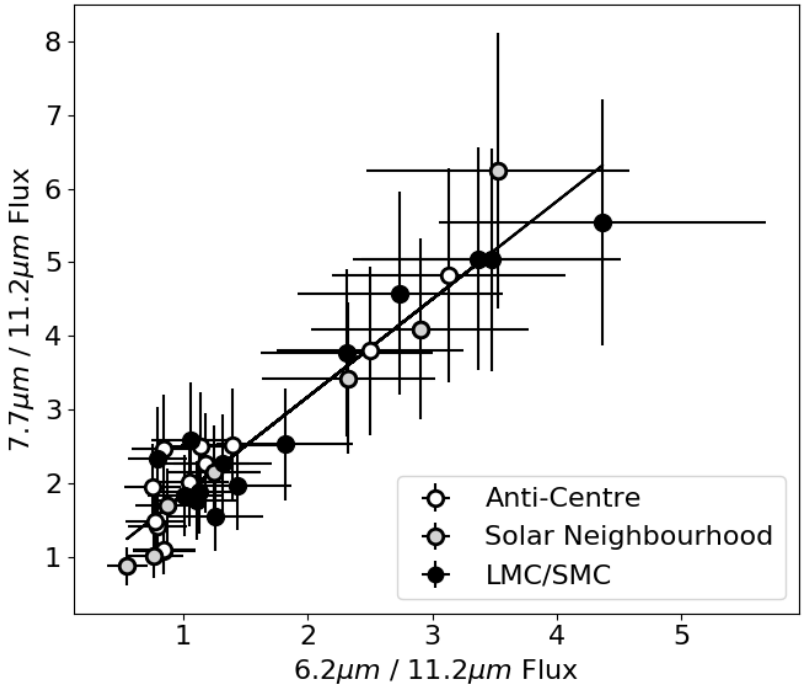

Fig. 4.3 The $I(6.2)$ / $I(11.2)$ PAH flux ratio plotted against the $I(7.7)$ / $I(11.2)$ ratio, both used as a reference for the degree of ionisation and hydrogenation of PAHs in their local environments.

the anti-centre sample and those from two other samples of PNe: one from the metal-poor Magellanic Clouds (Bernard-Salas et al. 2009, 2008) and a representative sample from the solar neighbourhood (Pottasch and Bernard-Salas, 2006). The figure shows a strong positive correlation between the two ratios, as has been observed previously (e.g. Bernard-Salas et al. 2009; Cerrigone et al. 2009). Most of the PNe in the Galactic anti-centre sample have low ionisation fractions, implying that the regions in which the PAHs are likely to be located (namely the photodissociation regions, or PDRs) around these PNe favour the presence of neutrally charged PAHs.

4.4 PAH decomposition

The profiles of broad PAH emission features cannot accurately be fitted by a single Gaussian, unlike those of atomic lines. Indeed, these profiles are asymmetric and differ between sources, as there are hundreds of potential molecular structures for PAHs that can be observed in circumstellar and interstellar environments. Recent studies have investigated these subcomponents in reflection nebulae and H II regions (e.g. Ricca et al. 2012, Peeters et al. 2017; Stock and Peeters 2017, Ricca et al. 2018), which have shown correlations between different sets of components for different source types. By fitting these features as sums of multiple Gaussians with set parameters (e.g. FWHM, approximate peak wavelength), relationships can be inferred between these molecules based on correlations of the relative intensity values of these components. This may provide information regarding the molecular families of these PAHs (e.g. coronene-based, ovalene-based, etc.) as well as their structure (e.g. the presence of bay regions), size and charge. This will be the first time in which this method has been applied to the spectra of evolved stars.

This section explains the technique used to measure these Gaussian components, what each component represents, the analysis of the PAH decomposition for the sample of PNe from the Galactic anti-centre, and the implications regarding the molecular structure of the PAHs in these sources. The spectral continua are fit as global splines, as shown in Figure 4.1.

In Figure 4.4, examples of measurements carried out over the three wavelength regions of interest are shown; atomic lines are masked before fitting the Gaussians.

For this work, only the decomposition of the 7–9 μm region will be analysed, as the 6 and 11 μm regions are difficult to accurately measure due to the smaller subcomponents at 6.0 and 11.0 μm, respectively, being too weak in almost all cases. The results of these decompositions will be shown, but more weight will be given to the analysis of the 7–9 μm PAH emission bands.

4.4.1 Gaussian curve fitting

Gaussian curves were fitted such that the wavelength of the central peak was a free parameter but the FWHM of the curves were fixed to values matching those of Peeters et al. (2017) for the reflection nebula NGC 2023, allowing for direct comparisons with their data (see § 4.4.3). The curves were measured separately in both nods of the SL spectra, and the corresponding flux values were averaged over the two values. Any atomic lines found within these wavelength regions were masked when applying the measurements, unless there was any uncertainty as to whether a particular feature could be attributed to dust emission.

A Gaussian curve is represented by the following equation:

$$y = A \times \exp\Big(\frac{-(x-\mu)^2}{2\sigma^2}\Big) \tag{4.1}$$

where A is the amplitude, μ is the peak wavelength and σ is the standard deviation of the corresponding normal distribution, of which the FWHM $= 2.355\ \sigma$.

4.4.2 Components

The 6.2 and 11.2 μm features are known to have smaller components centred around 6.0 and 11.0 μm, respectively. The 11.0 and 11.2 μm components represent C–H out-of-plane bend motions, which Hony et al. (2001) attributed to solo C–H bond movements in ionised and neutral PAHs, respectively. The origin of the smaller 6.0 μm component is not well defined.

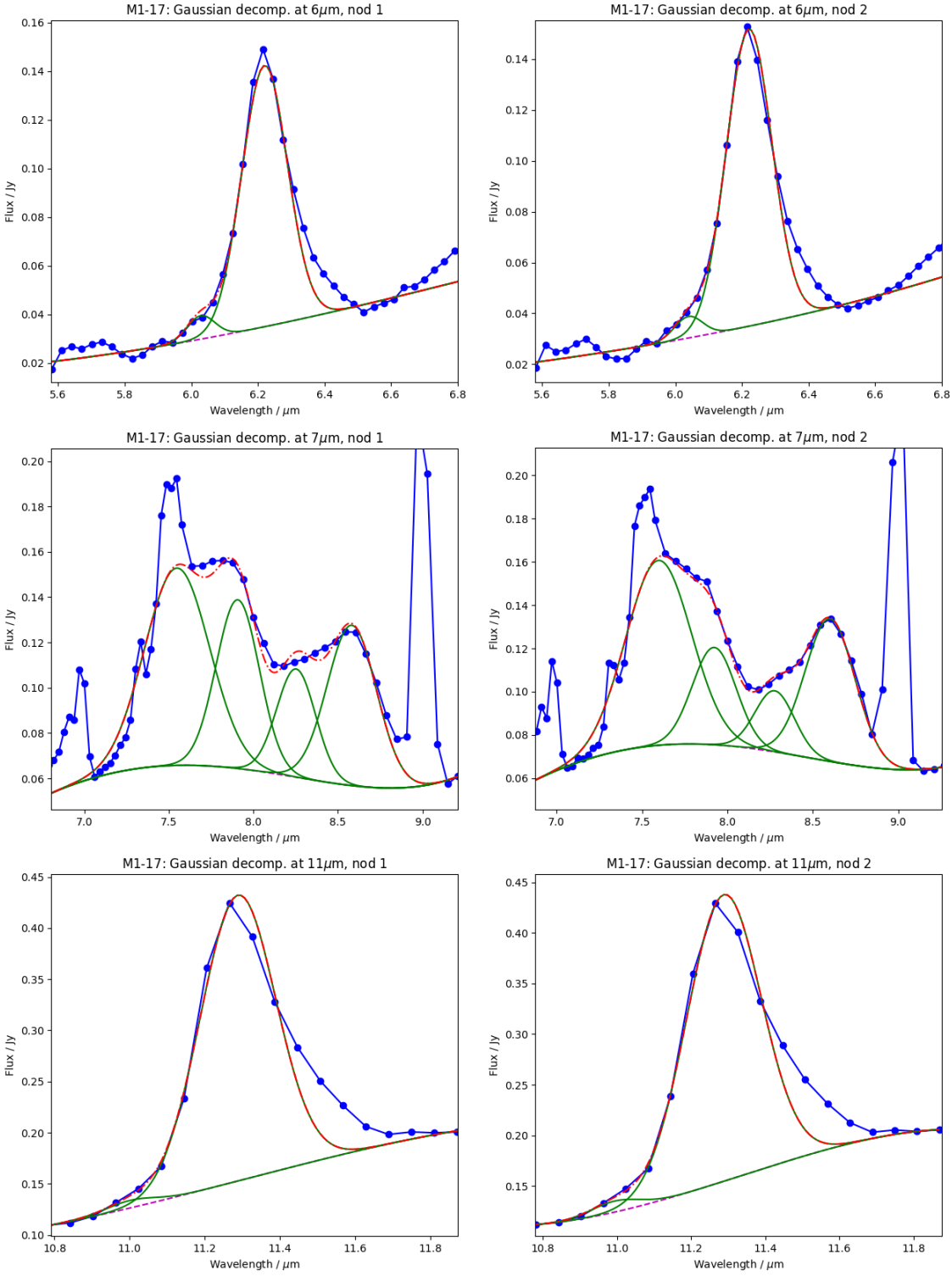

Fig. 4.4 The 6, 7 and 11 μm regions of PN M1-17, as seen through observing nods 1 and 2 of *Spitzer* IRS. The separate Gaussian components (green) are added together (red) in order to match the original data (blue). The fitted continua are shown as purple dashed lines.

Similarly, the 7–9 μm region can be separated into several Gaussian subcomponents. Previous studies have separated this complex into three components at 7.6, 7.8 and 8.6 μm (e.g. Bauschlicher et al. 2008, 2009; Ricca et al. 2012), though Peeters et al. (2017) and Stock and Peeters (2017) have since considered a fourth component at 8.2 μm. These four components of the 7–9 μm region have been designated as the following:

- **7.6 μm component**: Cationic and anionic PAHs with 20–100 carbon atoms;
- **7.8 μm component**: Cationic and anionic PAHs with 100–150 carbon atoms;
- **8.2 μm component**: C–H in-plane bending modes with numerous bay regions (predominantly neutral);
- **8.6 μm component**: C–H in-plane bending modes from large (96–150 carbon atoms), compact, symmetric molecules.

4.4.3 Decomposition analysis

From the sample of anti-centre PNe, the individual PAH components were measured in nine sources. This is because it was not always possible to differentiate the weaker 6.0 and 11.0 μm components from the stronger 6.2 and 11.2 μm features in the low resolution SL module, and occasionally the 8.2 μm component could not be observed. Table 4.4 shows these intensity values, with the associated uncertainties given as the difference between the values from the two positions from which observations are taken (see Chapter 2). The 6 and 11 μm complexes both show a red wing that cannot be well fitted using this Gaussian decomposition, as shown in Figure 4.4. In these cases, all flux is within the wavelength ranges $\sim$ 5.9–6.6 μm and $\sim$ 10.9–11.7 μm respectively (depending on continuum points). To account for this, Table 4.4 shows both the intensities of the associated Gaussian features, $I(\lambda)_G$, and intensities accounting for the "full" 6.2 and 11.2 μm components, $I(\lambda)_f$. The "full" components are calculated by subtracting the intensity of the 6.0 or 11.0 μm component from the intensity values of the 6 and 11 μm complexes, respectively, calculated from the flux values in Table 4.2.

Table 4.4 Intensity of the decomposed PAH Gaussian components for the 6–11 μm features, in units of 10^{-14} erg cm^{-2} s^{-1}, with the average peak wavelengths between the two nods, in μm. Continued on next page.

	7.6 μm		7.8 μm		8.2 μm		8.6 μm	
FWHM	*0.450 μm*		*0.300 μm*		*0.270 μm*		*0.344 μm*	
PN	λ	$I(\lambda)$	λ	$I(\lambda)$	λ	$I(\lambda)$	λ	$I(\lambda)$
K3-65	7.569 ± 0.023	44.6	7.968 ± 0.027	18.3	8.321 ± 0.001	3.99*	8.623 ± 0.001	9.53*
K3-66	7.604 ± 0.014	81.6	7.904 ± 0.040	10.6	8.229 ± 0.073	5.99*	8.622 ± 0.001	24.0*
K3-68	7.581 ± 0.051	35.7*	7.944 ± 0.014	103*	8.253 ± 0.058	39.7*	8.711 ± 0.010	60.4
K3-69	7.579 ± 0.003	295	7.915 ± 0.001	242	8.252 ± 0.003	112	8.627 ± 0.004	155
K3-71	7.442 ± 0.038	6.42‡	7.893 ± 0.003	14.6	8.229 ± 0.025	2.96†	8.738 ± 0.027	7.08†
K4-48	7.624 ± 0.013	93.7*	7.972 ± 0.003	34.8*	8.304 ± 0.002	16.4‡	8.622 ± 0.014	40.4*
M1-16	7.529 ± 0.021	216	7.887 ± 0.004	118*	8.217 ± 0.021	37.7*	8.603 ± 0.010	67.7‡
M1-17	7.573 ± 0.024	261*	7.916 ± 0.008	111†	8.265 ± 0.012	59.7†	8.592 ± 0.010	129
M4-18	7.591 ± 0.009	3210	7.887 ± 0.009	1640	8.222 ± 0.008	928	8.597 ± 0.003	1620

Notes: Uncertainties $< 10\%$ except for: * 10–20%; † 20–35%; ‡ 35–50%; $^{\#} > 50\%$.

Table 4.4 (Continued)

	6.0 μm		6.2 μm			11.0 μm		11.2 μm		
FWHM	*0.099 μm*		*0.1612 μm*			*0.154 μm*		*0.236 μm*		
PN	λ	$I(\lambda)$	λ	$I(\lambda)_G$	$I(\lambda)_f$	λ	$I(\lambda)$	λ	$I(\lambda)_G$	$I(\lambda)_f$
K3-65	6.093 ± 0.022	4.09*	6.242 ± 0.015	18.2	18.0	10.994 ± 0.014	0.56*	11.292 ± 0.004	19.3	20.6
K3-66	6.062 ± 0.019	0.94*	6.237 ± 0.008	34.9*	38.1	10.989 ± 0.001	$1.08^{\dagger}$	11.262 ± 0.005	29.5	28.2
K3-68	6.003 ± 0.015	4.10	6.258 ± 0.001	33.9	44.8	11.073 ± 0.013	$1.12^{\dagger}$	11.287 ± 0.002	33.4	42.0
K3-69	6.052 ± 0.003	5.75	6.239 ± 0.001	135	141	11.042 ± 0.003	8.42	11.279 ± 0.002	158	188
K3-71	6.077 ± 0.033	0.50*	6.269 ± 0.011	$6.63^{\dagger}$	11.6	11.100 ± 0.053	$0.13^{\ddagger}$	11.269 ± 0.004	3.45	3.96
K4-48	6.100 ± 0.010	7.82	6.231 ± 0.001	62.3	65.5	11.059 ± 0.009	5.76	11.297 ± 0.002	77.0	87.0
M1-16	6.096 ± 0.067	$6.60^{\#}$	6.251 ± 0.006	64.5*	141	11.058 ± 0.008	4.69	11.316 ± 0.003	128	192
M1-17	6.034 ± 0.006	9.54	6.220 ± 0.001	180	187	11.000 ± 0.004	4.73*	11.289 ± 0.001	210	296
M4-18	6.033 ± 0.001	69.8	6.234 ± 0.002	1480	1450	11.028 ± 0.015	103	11.264 ± 0.003	1270	1600

Notes: $I(\lambda)_G$ is the intensity of the Gaussian component; $I(\lambda)_f$ is the "full" intensity of the PAH feature, calculated by subtracting $I(\lambda)$ of the 6.0 μm (for the 6.2 μm feature) or 11.0 μm component (for the 11.2 μm feature) from the intensity of the entire PAH feature as calculated by the flux values in Table 4.2.

For the 7–9 μm complex, Figure 4.5 shows a series of correlation plots comparing ratios of the four Gaussian components in the anti-centre sample, as well as those from a set of comparison sources including the reflection nebula NGC 2023 as observed with *Spitzer* IRS (Peeters et al., 2017), and a selection of sources from the solar neighbourhood observed by the *ISO* Short Wavelength Spectrometer (SWS) including PNe, post-AGB stars, H II regions, Herbig Ae/Be stars, Seyfert galaxies and young stellar objects, as studied by Peeters et al. (2002). For ease of reference, this will be referred to as the "*ISO* sample" for the remainder of this chapter. The Pearson correlation coefficients of these plots are shown in Table 4.5. The correlation coefficients for the *ISO* sample with wavelengths fixed at 7.59, 7.93, 8.25 and 8.58 μm (for the 7.6, 7.8, 8.2 and 8.6 μm components, respectively) are given in the table as a comparison. Only values where the wavelengths are not fixed are considered.[1] However, the FWHM values have been fixed in all cases, with respective values of 0.450, 0.300, 0.270 and 0.344 μm, allowing for comparisons of the intensity values with those from Peeters et al. (2017), who applied the same FWHM values.

The plot comparing the 8.2 and 8.6 μm components shows the strongest correlation for the nine PNe in the Galactic anti-centre. This correlation is also strong in the *ISO* sample, but not for the NGC 2023 data. The 7.6 and 8.6 μm components also show a strong correlation, and this is observed within all samples. Conversely, the 7.6 and 7.8 μm components show no correlation in all samples except NGC 2023, in which the correlation is low-to-moderate. The 7.8 and 8.6 μm components are also not correlated in most of these samples, except for the *ISO* sample, in which there is a moderate-to-strong correlation. There are moderate correlations between the 7.8 and 8.2 μm components and between the 7.6 and 8.2 μm components, though the latter comparison shows a negative correlation for the anti-centre and *ISO* samples.

The sample of Stock and Peeters (2017), which contained both H II regions and RNe, showed different correlations between the two types of sources; the H II regions showed strong correlations between the neghbouring components (i.e. 7.6 and 7.8 μm, 7.8 and 8.2 μm, 8.2 and 8.6 μm) whereas the strongest correlations from the RNe were between the 7.6

[1]This is because the anti-centre sample contains a range of PAH profiles from Classes *A* and *B*, and the fixed wavelengths were exclusively applied to samples of Class *A* sources, hence these are not fully representative.

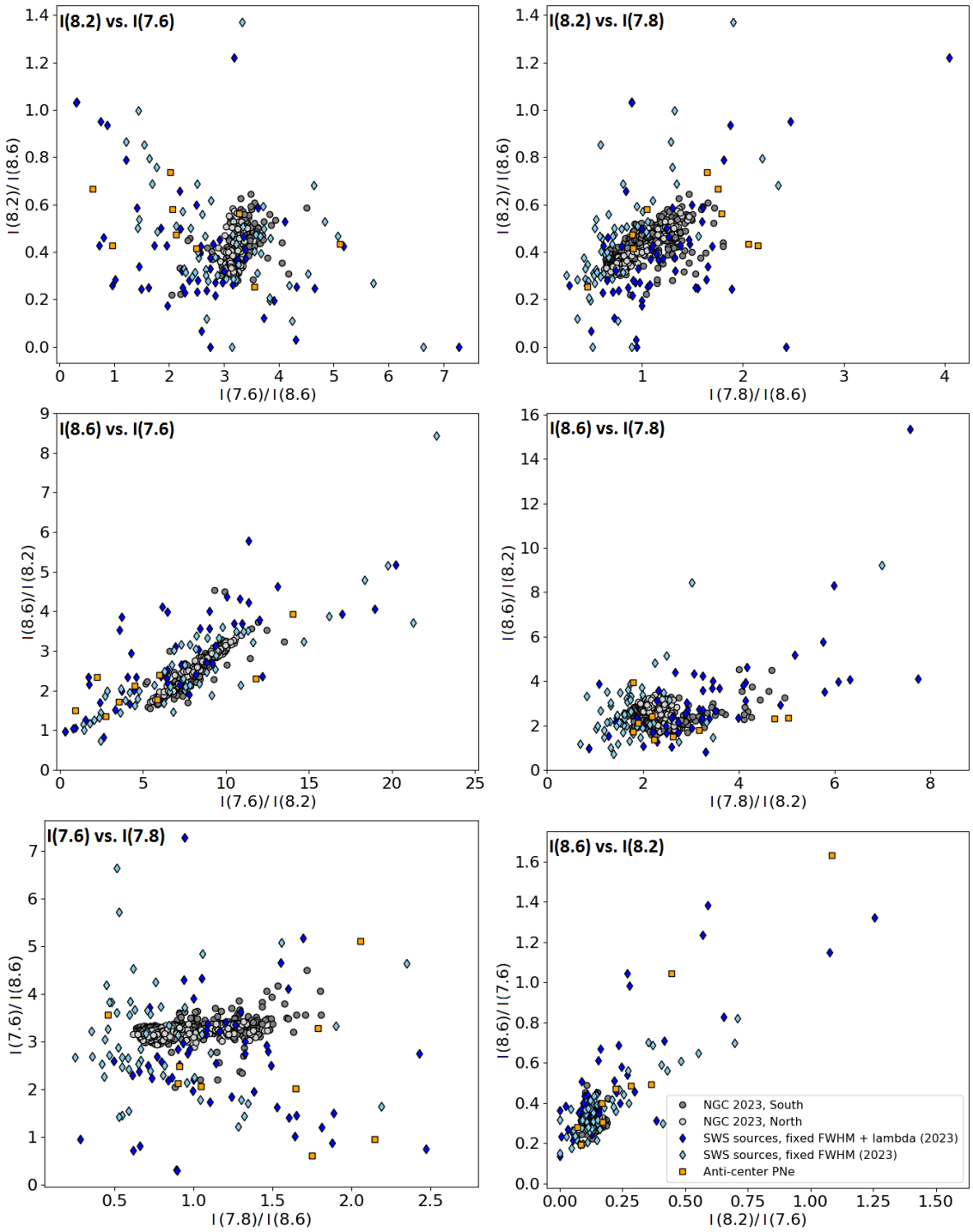

Fig. 4.5 Correlation plots between the flux ratios of 7–9 μm components. The dark grey and light grey circles represent data points from NGC 2023, as analysed by Peeters et al. (2017); dark blue and light blue diamonds represent data from a variety of sources as analysed by Peeters et al. (2002), where the peak wavelengths are either free (light blue) or fixed to 7.59, 7.93, 8.25 and 8.58 μm (dark blue). Orange squares represent the Galactic anti-centre data points.

Table 4.5 Pearson correlation coefficients of the plots in Figure 4.5.

Plot	NGC 2023	*ISO* (fixed λ)	*ISO* (free λ)	anti-centre	*ISO* + anti-centre	All
I(8.2) vs. I(7.6)	0.474	−0.450	−0.418	−0.449	−0.418	−0.151
I(8.2) vs. I(7.8)	0.760	0.482	0.674	0.429	0.601	0.659
I(8.6) vs. I(7.6)	0.926	0.977	0.916	0.798	0.910	0.897
I(8.6) vs. I(7.8)	−0.011	0.941	0.626	−0.043	0.456	0.195
I(7.6) vs. I(7.8)	0.409	0.008	−0.069	−0.086	−0.141	0.089
I(8.6) vs. I(8.2)	−0.116	0.961	0.853	0.964	0.890	0.834

Notes: The "*ISO* + anti-centre" and "all" data considered *ISO* values where the peak wavelengths were not set, as shown by the magenta diamonds in Figure 4.5, and did not consider the *ISO* data for which the peak wavelengths were fixed. The FWHM values were always set to those applied in Table 4.4; see also Peeters et al. (2017).

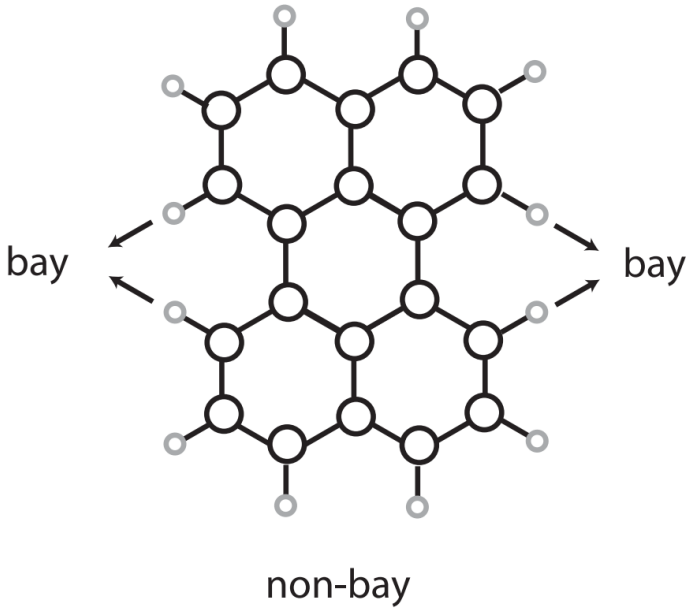

Fig. 4.6 Schematic of a PAH molecule with bay regions indicated. Figure reproduced from Candian et al. (2012).

and 8.6 μm components, and between the 7.8 and 8.2 μm components. They attributed the differences in correlations to the RNe having irradiated PDRs, whereas those of the H II regions were more quiescent.

In theory, there is no clear explanation for the strong correlations between the 7.6 and 8.6 μm PAH components, as the former represents smaller, charged molecules, and the latter indicates the presence of compact molecules that are larger in size. Ricca et al. (2018) investigated this relationship further by analysing density functional theory calculations to

predict the spectra of a range of PAH molecules, and found that these correlations were observed in those with straight edges (i.e. with no branches or bay regions, the latter as shown in Figure 4.6) consisting of $\sim$ 50–110 carbon atoms. This incorporates the representations of both components well. On the other hand, while the 8.2 and 8.6 μm components both represent C–H bond movements and are linked with PDRs within the quiescent ISM, some of the anti-centre PNe show large intensity values for these components with a strong correlation. This may require further investigation, as the PDRs of these PNe will be strongly irradiated.

4.5 Silicon carbide

Silicon carbide (SiC) is another form of C-rich dust emission, with its broad feature spanning the wavelength range $\sim$ 9–13 μm (e.g. Treffers and Cohen 1974, Lagadec et al. 2007, Bernard-Salas et al. 2009) , though its classification is still in debate. SiC is rarely observed around evolved stars in the Milky Way, with several detections from PNe in the Magellanic Clouds (e.g. Bernard-Salas et al. 2009; Sloan et al. 2014), and few studies reporting SiC observations in Galactic sources.

Silicon carbide has been detected in five of the 23 sources from the Galactic anti-centre sample, as shown in Figure 4.7. The profiles of each of these features are within the wavelength range $\sim$ 9.7–13.5 μm, and the peaks are observed at $\sim$ 11.6 μm. From a sample of PNe in the sub-solar metallicity Magellanic Clouds analysed by Bernard-Salas et al. (2009), nine of the 25 sources showed the SiC emission feature. Hence, SiC is readily observed around PNe in regions of sub-solar metallicity.

All five of the SiC-containing PNe have low radiation fields, as none show [Ne V] emission lines and only K3-66 shows a weak detection of the 25.9 μm [O IV] line. This reinforces the finding of Bernard-Salas et al. (2009), in which SiC was only detected in PNe with low radiation fields.

Casassus et al. (2001a,b) analysed observations of Galactic PNe from the *United Kingdom Infrared Telescope* (UKIRT) and reported to have detected the SiC feature in 30 sources out of a collective sample size of 99. However, these findings were published before the launch of

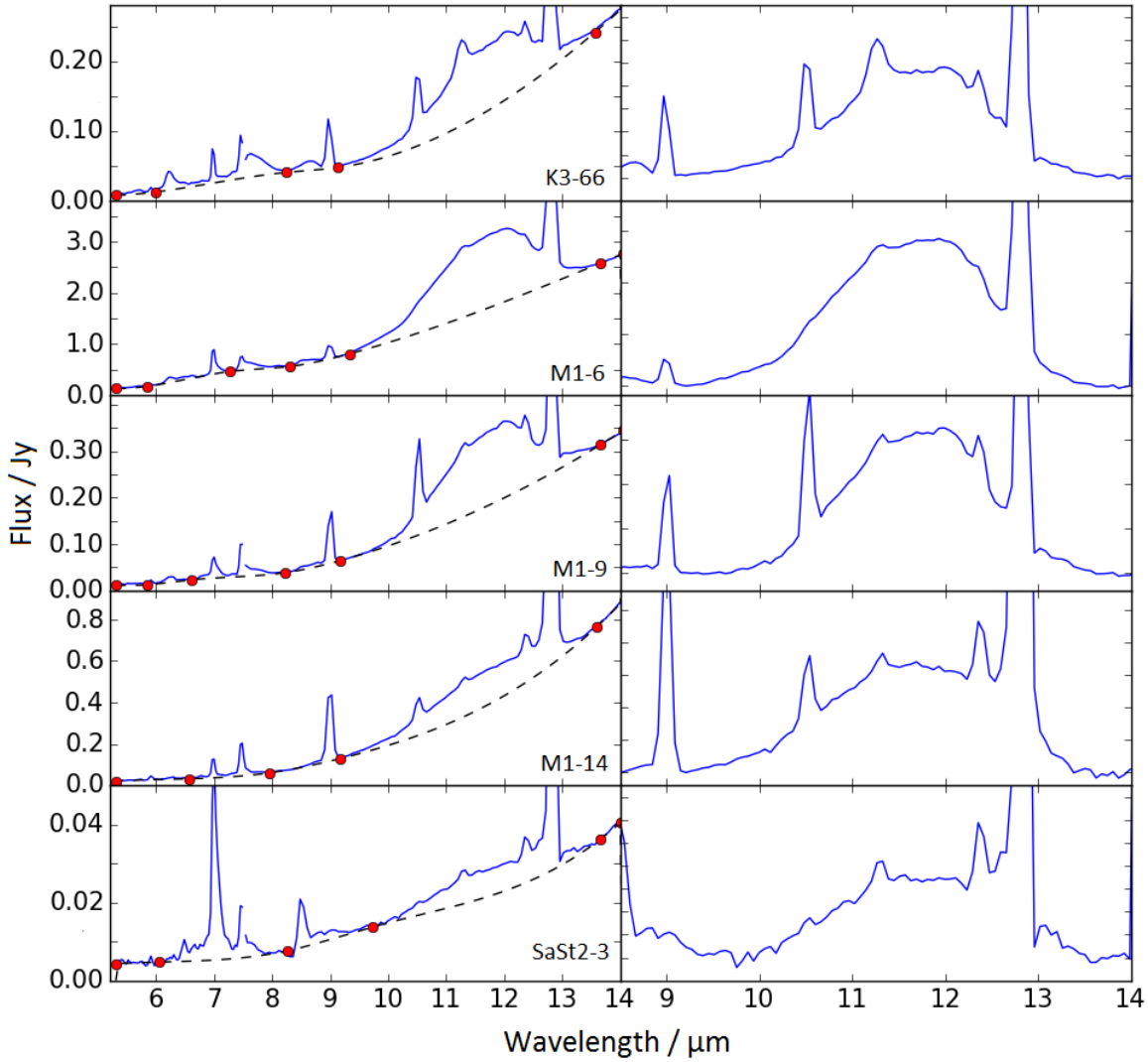

Fig. 4.7 The five PNe in our sample containing SiC. The left figures show the full LR range with the continuum shown as a dashed line fitted to the circle points. The right figures show the continuum subtracted spectra in the range 8.5–14 μm, in order to emphasise the SiC features.

the *Spitzer Space Telescope* in 2003, and hence the improved resolution and sensitivity offered by *Spitzer* may help in refining these quantities. I searched the *Spitzer* IRS archives and online *CASSIS* atlas[2] (Lebouteiller et al. 2011, Lebouteiller et al. 2015) for the 30 Galactic PNe reported to exhibit SiC emission, in order to investigate the rarity of this feature in evolved stars from the Milky Way. Table 4.6 shows results for the 24 PNe in the samples of Casassus et al. (2001a,b) with *Spitzer* IRS spectra. Including three new detections from our sample,

[2]The *Combined Atlas of Sources with Spitzer IRS Spectra* (CASSIS) is a product of the IRS instrument team, supported by NASA and JPL. Website: http://cassis.astro.cornell.edu

Table 4.6 Inventory of SiC-containing PNe observed by Casassus et al. (2001a,b), re-analysed with *Spitzer* IRS spectra. Detections of SiC are shown for the sample, alongside whether these PNe are located towards the Galactic anti-centre, in accordance with Galactocentric distances calculated from Frew et al. (2016).

PN	Anti-centre	SiC	PN	Anti-centre	SiC
K3-66**	Y	Y	Vy 2-2	N	Y†
M1-9**	Y	Y	Hu 2-1	N	Y†
SaSt2-3**	Y	Y	K3-69*	Y	N‡
M1-6*	Y	Y	M4-18*	Y	N‡
M1-14*	Y	Y	IC 2165	Y	N
M1-5	Y	Y	Hb 12	N	N
M1-11	Y	Y	BD $+30^{\circ}3639$	N	N
M1-12	Y	Y	NGC 5315	N	N
IC 418	N	Y	NGC 7027	N	N
IC 2501	N	Y	IC 2621	N	N‡
K3-62	N	Y	IC 5117	N	N‡
M1-20	N	Y	K3-52	N	N
M1-71	N	Y	M1-27	N	N
NGC 6790	N	Y			

Notes: * Analysed in our anti-centre PN sample. ** Not analysed by Casassus et al. (2001a,b). † Profile ends at bluer wavelengths than those of typical SiC features. ‡ Profile more reminiscent of Class α PAH emission (Matsuura et al., 2014).

at least 16 Galactic PNe show the broad SiC emission feature, of which eight are located towards the sub-solar metallicity anti-centre (i.e. $120^{\circ} < l < 240^{\circ}$, $-20^{\circ} < b < +20^{\circ}$).

In the Milky Way, there are IR spectra for hundreds of PNe (e.g. Otsuka et al. 2014), yet there is now a total of 16 Galactic sources of SiC that have so far been detected. Owing to the rarity of this emission feature in PNe, and the fact that 50% of all detections are within the third of the Galactic disk located towards the anti-centre, it can be concluded that the formation of SiC is favoured within regions of lower metallicity.

4.6 Fullerenes

Since the discovery of buckminsterfullerene (C_{60}) in the Galactic PN Tc 1 (Cami et al., 2010), fullerenes have remained the largest known molecules to be firmly identified in space. C_{60} shows strong emission features at 17.4 and 18.9 μm and weaker features at 7.0 and 8.5 μm, the latter two of which may blend with the 7.0 μm [Ar II] emission line and the 8.6 μm PAH

feature, respectively, in low-resolution spectra. Other weak features associated with fullerenes are located around 6.5, 7.6 and 8.1 μm (Sloan et al., 2014), as well as C_{60}^{+} at 6.4, 7.1 and 8.1 μm (Berné et al., 2013), though these are all located within the wavelength regions of the broad 6.2 and 7.7 μm PAH emission features and hence may be difficult to detect with the resolution of the SL module of *Spitzer* IRS.

Fullerenes have been observed in many diverse environments, including PNe, reflection nebulae (e.g. Sellgren et al. 2010) and H II regions (e.g. Castellanos et al. 2014). C_{60}^{+} has also been confirmed as a carrier of diffuse interstellar bands (DIBs; Campbell et al. 2015, Walker et al. 2015), implying that fullerenes may be common in the Universe. In Magellanic Cloud PNe, there is a reasonably high probability of observing fullerenes; García-Hernández et al. (2011) and Sloan et al. (2014) have together detected C_{60} emission in the *Spitzer* IRS spectra of 12 PNe from the 66 originally analysed by Stanghellini et al. (2007) and Bernard-Salas et al. (2009). However, fullerene-containing PNe are rarer in the Milky Way, with 11 out of 338 Galactic PNe from the *Spitzer* IRS archives ($\sim 3\%$) showing C_{60} emission (Otsuka et al., 2014). Of these 11 PNe, seven are located towards the anti-centre and three are within this data set: M1-6, M1-9 and SaSt2-3.

In addition to the three fullerene sources discovered in our sample by Otsuka et al. (2014), M4-18 also shows C_{60} emission. The 7.0 and 8.5 μm features are not observed in this PN, unlike with the other three, due to strong emission from the [Ar III] line centred at ~ 6.98 μm and an 8.6 μm PAH feature centred at ~ 8.60 μm (c.f. expected wavelengths of 7.04 ± 0.01 μm and 8.51 ± 0.01 μm for the two C_{60} features; Sloan et al. 2014). However, the emission from the 17.4 and 18.9 μm features is strong. Figure 4.8 shows these two emission features in all four of the PNe in our anti-centre sample. The number of detections of fullerenes in relatively small samples of PNe within the Galactic anti-centre and the Magellanic Clouds is relatively high, suggesting a relationship between fullerene sources and regions of low metallicity. Three of these four fullerene-containing PNe also show SiC emission, as do nine of the ten confirmed fullerene-containing PNe from the Magellanic

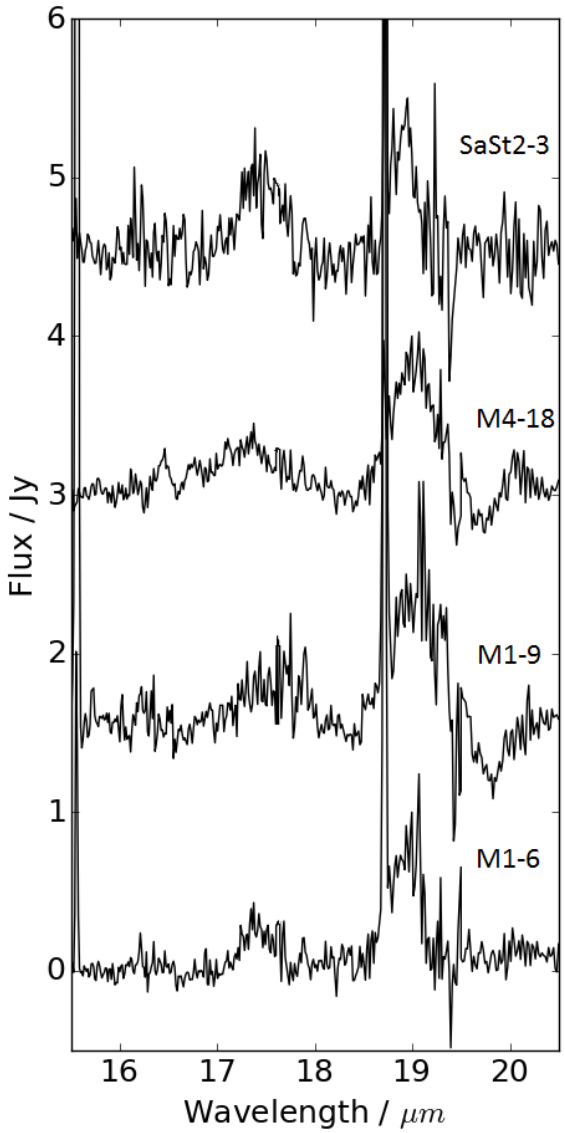

Fig. 4.8 Continuum-subtracted, normalised profiles of the 17.4 and 18.9 μm C_{60} features in the sample.

Clouds (Stanghellini et al. 2007; Bernard-Salas et al. 2009; García-Hernández et al. 2011), hence the presence of these features may also be linked.

4.7 The 30 μm feature

The 30 μm feature, spanning from $\sim$ 23–45 μm, is commonly observed in C-rich sources and is often attributed to MgS (e.g. Goebel and Moseley 1985; Hony et al. 2002; Sloan et al. 2014), though this classification is still in debate. Zhang et al. (2009) calculated that the

strength of the observed feature in the proto-planetary nebula HD 56126 would require a much larger mass of MgS than was present in order to confirm this classification. To overcome this, Lombaert et al. (2012) suggested that MgS could be used as a coating for SiC dust grains, which remains a widely accepted explanation for the presence of this feature.

While this feature is not observed in its entirety within our sample as the *Spitzer* IRS wavelength coverage cuts off at ~ 37 μm, there are six PNe with profiles rising from ~ 23 μm, indicating its presence: M1-6, M1-9, M1-14, M4-18, SaSt2-3 and (more tentatively) M2-2. A similar feature has been observed in M1-17, though the profile does not completely match that of typical 30 μm emission; the feature begins to rise away from the continuum around 27 μm. Hence, M1-17 is not considered as a source of the 30 μm feature.

In some sources from the literature, the broad 30 μm emission feature has been observed alongside a series of associated features. The most well known of these is found around 21 μm, with weaker features at 15.8 and 17.1 μm, typically associated with aliphatic carbonaceous compounds (e.g. Sloan et al. 2014). However, there have been claims that the 30 μm feature is not linked to the others (e.g. Mishra et al. 2015). None of the PNe in our sample show these accompanying features.

Sloan et al. (2014) suggested that these 30 μm features are always present alongside SiC emission. While this is true for four of the PNe in this sample, M2-2 and M4-18 both show 30 μm emission (only tentatively, in the case of M2-2) yet neither show SiC emission. In the sample of Bernard-Salas et al. (2009), there were three sources that showed the 30 μm feature, but did not show SiC emission. For these three sources and for M4-18, the spectral profiles of the emission in the wavelength range $\sim$ 9–13 μm are more closely related to PAH clusters than SiC.

In our sample, four of the five SiC sources show the 30 μm feature, hence if we assume the 30 μm feature is attributable to MgS, it is plausible that MgS could be coating SiC grains, as originally suggested by Lombaert et al. (2012).

4.8 Silicates

O-rich dust is observed in the form of amorphous or crystalline silicates (SiO and SiO_2). Amorphous silicates show broad features at $\sim$ 10 μm and 18 μm, whereas crystalline features are observed at 23, 28, 33, 40 and 60 μm.

There are no clear detections of silicates in our sample. Figure 4.9 shows one tentative detection of a 10 μm amorphous silicate absorption feature in M4-18, alongside a silicate absorption feature taken from a sample of ultra-luminous infrared galaxies (ULIRGs) analysed by Spoon et al. (2007) for comparison. The two profiles are consistent with each other. The corresponding 18 μm amorphous silicate feature is not observed in M4-18.

While other studies have not detected silicate dust absorption in this PN (e.g. Górny et al. 2001), the *Spitzer* IRS spectrum strongly suggests that it is present. A potential explanation for the presence of this feature is a cold silicate dust disk around M4-18, which would absorb much of the light within the wavelength range $\sim$ 9–11 μm emitted from the PN. If these

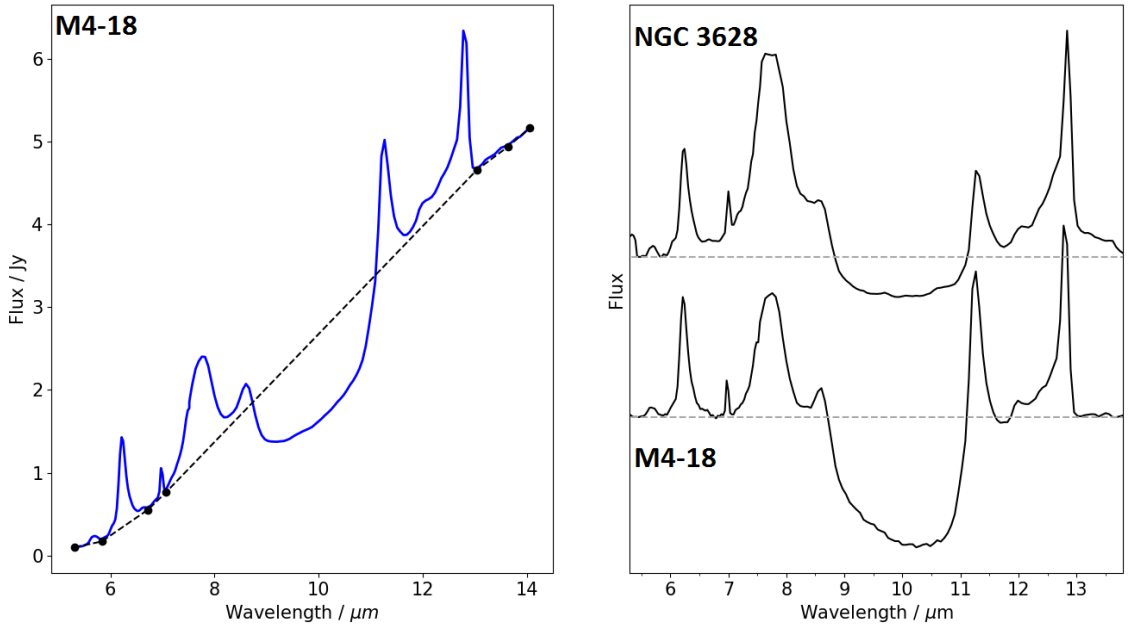

Fig. 4.9 (a) the SL spectrum of M4-18, with the fitted continuum shown as a dotted line. The continuum anchor points are shown as black circles. (b) the continuum-subtracted spectra of M4-18 and the ultra-luminous infrared galaxy NGC 3628. The NGC 3628 data comes from *Spitzer* observing program 14 (PI: J. Houck).

silicates were observed within close proximity of the PN, the features would have been observed in emission due to the high temperatures around the star. Hence, the silicate dust must be located far from the source such that this feature is not observed in emission, and there must be a relatively large amount of it to produce such a strong spectral feature.

4.9 Featureless spectra

Most of the PNe in our sample show spectra with a continuum that rises with increasing wavelength, indicating the presence of dust. However, some do not show particular emission bands attributable to C-rich or O-rich dust (e.g. PAHs, silicates, etc.) and these are classified as 'featureless'. In our sample, five of the 23 PNe are featureless: J320, K3-90, M1-1, Y-C 2-5 and M3-2, the last of which also does not show a rising dust continuum with wavelength.

Of the five PNe with featureless spectra, three experience strong radiation fields, in that they exhibit both [O IV] and [Ne V] emission. M1-1 also shows [Ne VI] emission (see Chapter 3), which has an ionisation potential of 126 eV. The only other source in our sample with this emission line is M1-16, which shows particularly strong PAH emission, indicating no relationship between the dust composition and the radiation field around the ionised regions of the PN.

It may be possible that these spectra are featureless because the dust emitting species have been destroyed. The methods by which dust grains can be destroyed are discussed further in Chapter 5, though studies have shown that C-rich molecules are more likely to be stable in stellar UV radiation fields with sizes greater than 30–40 carbon atoms (Jochims et al. 1994, Allain et al. 1996; Seon and Draine 2016). Hence, it may be speculated that the five featureless PNe in the Galactic anti-centre sample produced smaller dust grains earlier in their lifetimes that have since been destroyed.

4.10 The link between dust composition and metallicity

The dust compositions of the PNe from the Galactic anti-centre will now be compared to those from samples taken from regions of different metallicities from the Milky Way and Magellanic Clouds, in order to establish any links between them.

The variation of dust chemistry with location in the Milky Way suggests that the composition of this dust is linked with the metallicity of the local environment. These findings have been compared with other spectroscopic samples of PNe in the Milky Way and the Magellanic Clouds, which were analysed in the same way from the literature, in Table 4.7. The abundances of neon, sulfur and argon in the anti-centre PNe are comparable to those of the LMC and SMC (see Chapter 3), and these regions are more metal-poor than the Galactic bulge and solar neighbourhood.

The samples of PNe from the Magellanic Clouds, the Galactic anti-centre, the solar neighbourhood and the bulge show similar percentages of C-rich dust emission, predominantly from PAHs. However, it is clear that there are significantly more PNe with C-rich dust

Table 4.7 Comparison of dust inventories with studies from the solar neighbourhood and Magellanic Clouds.

	Galactic Bulge (0–4 kpc)	Solar Neighbourhood (4–10 kpc)	Magellanic Clouds	Galactic anti-centre (8–21 kpc)
Metallicity	High	Solar	Sub-solar	Sub-solar
Sample size	11	20*	25	23
C-rich emission	56%	60%	60%	78%
O-rich emission	100%	40%	8%	4%
Dual-dust chemistry	56%	20%	4%	4%
SiC	0%	5%	36%	22%

Notes: Bulge sample: Gutenkunst et al. (2008); Solar neighbourhood: Pottasch and Bernard-Salas (2006); Magellanic Cloud sample: Bernard-Salas et al. (2009). The percentages represent the PNe in the sample with these dust emission features and are not mutually exclusive. * The sample analysed in this work used *ISO* spectra and consisted of 26 PNe, in which most were obtained from the SWS02 observing mode which focused on particular line features instead of covering a broad wavelength range, hence mid-IR spectra were found for as many sources as possible from *IRS* programs 93 (PI: D. Cruikshank) and 30430 (PI: H. Dinerstein), and from the following sources: Delgado-Inglada and Rodríguez (2014); Bernard-Salas et al. (2001); Kemper et al. (2002); Pottasch et al. (2002); Matsuura et al. (2005); Chesneau et al. (2007); Ortiz et al. (2011); Mata et al. (2016).

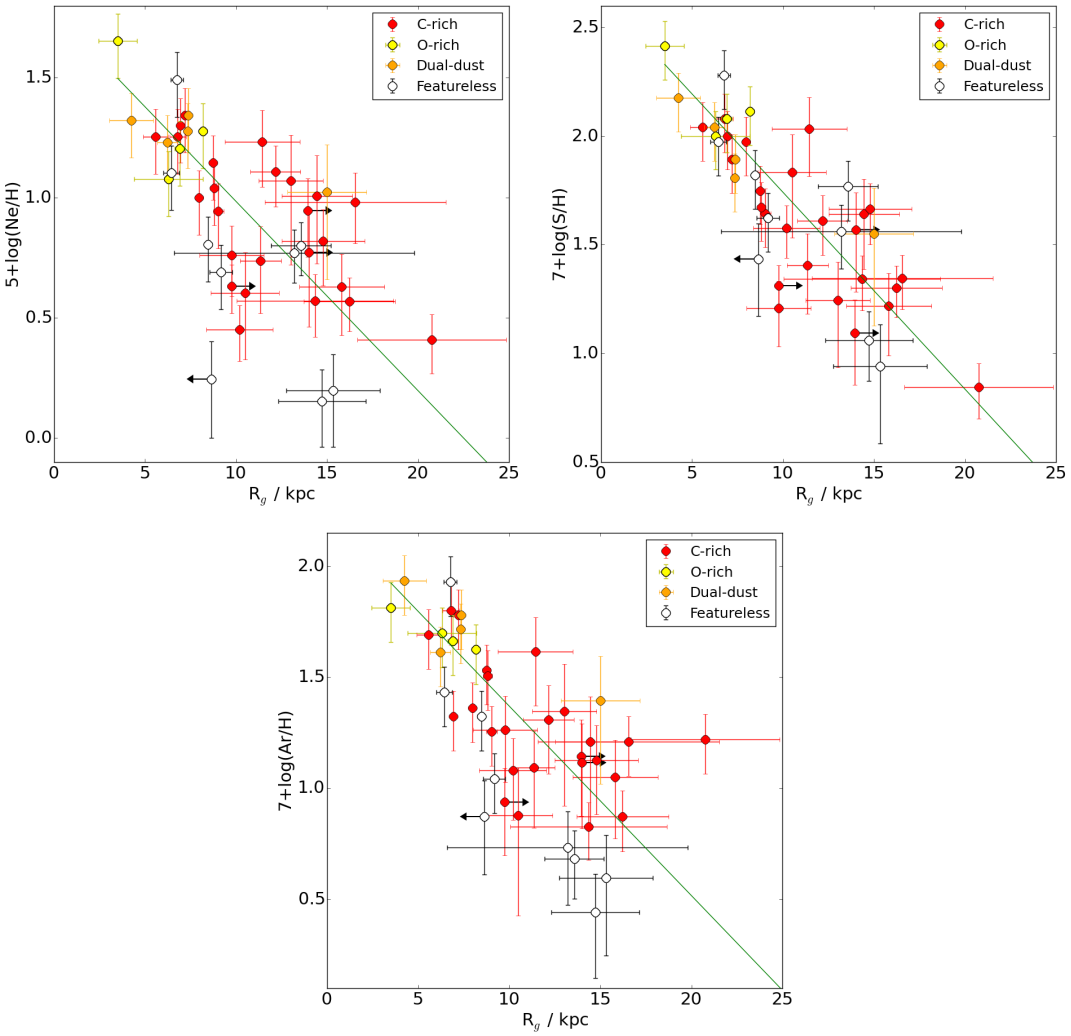

Fig. 4.10 The abundance gradients of neon, sulphur and argon in the Milky Way, with their dust composition shown. The solar neighbourhood data have been taken from Pottasch and Bernard-Salas (2006).

emission than O-rich emission in the sub-solar metallicity Magellanic Clouds and the Galactic anti-centre. The proportion of sources with emission from SiC is greater in these lower metallicity regions than elsewhere in the Milky Way, and the same is true for C_{60} emission; eight of the twelve known Galactic fullerene-containing PNe have been observed towards the anti-centre, and spectra for 12 out of the 66 PNe observed in the Magellanic Clouds from the studies of García-Hernández et al. (2011) and Sloan et al. (2014) have also shown these emission features.

Figure 4.10 shows the abundance gradients of neon, sulphur and argon with an indication of the overall dust composition of each PN shown. The samples of PNe from the solar

neighbourhood (Pottasch and Bernard-Salas, 2006) and Galactic bulge (Gutenkunst et al., 2008) are also shown. The R_g values for the anti-centre PNe are given in Chapter 3. The figure shows a mixture of C-rich, O-rich, featureless and dual-dust chemistry sources closer to the Galactic centre ($\sim$ 4–8 kpc). PNe with C-rich dust compositions dominate at lower abundances, with several featureless sources also observed.

The dust chemistry of the Galactic anti-centre resembles that of the Magellanic Clouds much more closely than elsewhere in the Galactic disk; both of these regions of sub-solar metallicity show more C-rich than O-rich PNe, and there is a diverse range of C-rich dust emission features observed in both regions. This reinforces the point that there is indeed a link between the dust composition of a region and its metallicity, and emphasises that low metallicity favours C-rich dust production.

4.11 Conclusions

A sample of 23 PNe have been observed in the metal-poor Galactic anti-centre with *Spitzer* IRS and the dust features have been examined. The main findings are as follows:

1. In this sample, 18 of the PNe show C-rich dust emission whereas only one may show amorphous silicate absorption, supporting the idea that low metallicity favours carbon-rich dust production.

2. The dust inventory of PNe in the anti-centre is also similar to that of the metal-poor Magellanic Clouds, with five detections of SiC and four of C_{60} from this sample alone. As the average metallicities of these galaxies are reached in the anti-centre sample, the relationship between dust composition and metallicity has become more evident.

3. The PAH emission observed in the anti-centre PN sample shows an even mixture of Class *A* and *B* profiles, as defined by Peeters et al. (2002).

4. The 7–9 μm PAH regions of the Galactic anti-centre PNe have been decomposed into four Gaussian components, as by Peeters et al. (2017) and Stock and Peeters (2017).

Each of these components represents the contributions of molecules from different bonding structures within the PAH molecules. From this sample, there are strong correlations between the intensities of the 7.6 and 8.6 μm components, as well as between those of the 8.2 and 8.6 μm components. These findings are consistent with those from samples of reflection nebulae and H II regions, respectively. While there are no clear links between the former two components, the latter two both represent C–H bonds, potentially suggesting links between the size of the PAH molecules and the number of bay regions.

5. An inventory of Galactic PNe containing the SiC emission feature was obtained from archival *Spitzer* IRS data, from the sources analysed by Casassus et al. (2001a,b). This emission feature is observed in 16 PNe, and eight of these sources are located towards the sub-solar metallicity anti-centre, three of which are new detections from our sample. It follows that the formation of SiC is favoured in regions of lower metallicity.

6. One new source of C_{60}, M4-18, has been detected. This brings the total number of PNe observed with *Spitzer* IRS containing these features to 12 out of 338, as originally investigated by Otsuka et al. (2014). 67% of these fullerene-containing PNe are found towards the sub-solar metallicity Galactic anti-centre, indicating a relationship between the presence of fullerenes and low metallicity.

7. Four of the six PNe with spectra showing the 30 μm feature also contain the SiC feature. Of the other two, one is a tentative detection and the other tentatively shows the 10 μm amorphous silicate absorption band, which partly covers the wavelength range of SiC. Hence, this finding is in agreement with previous suggestions that there is a relationship between the carriers of these two features.

Spectroscopic observations from the Milky Way and Magellanic Clouds have provided a detailed view of the dust composition of PNe in the Milky Way and Magellanic Clouds. With its enhanced sensitivity, the *James Webb Space Telescope* (JWST) will be able to extend these studies to the Local Group of galaxies, in which we can further analyse the dust composition

of evolved stars within a broader metallicity range. With its high spatial resolution, *JWST* can also pinpoint the location of many dust emission features within a PN through IFU spectroscopy (0.6–28 μm), providing a better understanding of the formation and evolution of the emitting dust features as a function of the physical conditions of the gas, and of stellar parameters.

This chapter has reinforced the concept that the compositions of dust from PNe are closely related to their local metallicity. Spectral observations of PNe in regions as low as 1/6 $Z_{\odot}$, namely the Galactic anti-centre and the Magellanic Clouds, compare well in terms of both dust composition and elemental abundances, but what about those in regions where the metallicity is much lower? The next chapter investigates this conundrum with the analysis of a sample of PNe in the Galactic halo.

Chapter 5

Abundances and dust compositions of planetary nebulae from the Galactic halo

5.1 Introduction

Most of the gas and dust in the Milky Way is located within its spiral-shaped disk. Surrounding this region is the spheroidal Galactic halo, which contains a large amount of dark matter but little stellar activity. The halo has an age of approximately 13.8 Gyr and a metallicity of Fe/H $\sim -1.78 \pm 0.50$, i.e. the iron abundance is $\sim 10^{-1.78}$ times that of the Sun. This is an order of magnitude lower than the mean metallicity of the Galactic thick disk (Robin et al., 2003).

Despite its metal-poor nature and low stellar population, the halo may not contain the oldest stars in our Galaxy. This depends on the original formation of the Milky Way. If the Galaxy was formed inside-out (e.g. Bovy et al. 2012; Larson 1976; Sommer-Larsen et al. 2003), the oldest stars may be found around the Galactic bulge (e.g. Koch et al. 2016; Tumlinson 2010). However, the bulge cannot have been directly formed from the halo (e.g. Clarkson et al. 2008; Fulbright et al. 2007) as the metallicities of α-elements like silicon, calcium and titanium are more enhanced in the bulge (see also Gutenkunst et al. 2008; Pottasch and Bernard-Salas 2015). Knowledge of the kinematics of these regions may help constrain the star formation history (e.g. Gilmore et al. 1989); indeed, those of the Galactic halo are

different to those within the disk of the Milky Way. The movement of sources in the Galactic disk are likely due to rotation around the Galactic bulge, whereas the halo does not rotate; the observed motions of sources in the halo are primarily due to the reflex component caused by interactions between the observer and the Sun (e.g. Malhan and Ibata 2017).

Only $\sim$ 12–14 PNe out of $\gtrsim$ 1100 in the Milky Way have been detected within the Galactic halo (e.g Henry et al. 2008; Howard et al. 1997; Otsuka et al. 2008; Otsuka and Tajitsu 2013; Stasińska et al. 2010). Interestingly, more halo PNe have an oxygen-rich composition (Howard et al., 1997; Stasińska et al., 2010), some of which exhibit silicate dust emission (e.g. Gesicki et al. 2010), contradicting the main outcome of Chapter 4: metal-poor environments favour the production of carbon-rich dust. García-Hernández and Górny (2014) found that both C-rich sources and O-rich PNe with amorphous silicate features are more likely to be metal-poor ($Z \sim 0.008$, c.f. $Z_{\odot} \sim 0.02$) than PNe with crystalline silicates or dual-dust chemistry. Alongside the metallicity, the mass of the star in its AGB phase (i.e. when it loses its circumstellar envelope) is also an important factor in determining its eventual dust composition; if $Z \sim Z_{\odot}$, the third dredge-up can only efficiently take place in stars where $M \gtrsim 1.5\ M_{\odot}$ (Lattanzio, 1989; Straniero et al., 1997).

Four of the PNe in the Galactic halo are also associated with globular clusters (GCs). These are groups of old ($\sim$ 12–13 Gyr) stars that formed during the first few Gyr of the lifetime of a galaxy (e.g. Canning et al. 2014). GCs orbit around the centre of their local galaxy over periods of $\sim 10^8$ years, during which they lose large amounts of mass. This is partly from ram pressure stripping as the GC crosses the galactic disk (e.g. Moore and Bildsten 2011; Naiman et al. 2013; Priestley et al. 2011; Tayler and Wood 1975), but also from Jeans escape (McDonald and Zijlstra, 2015), i.e. some of the gas in the GC travels faster than the escape velocity:

$$v_{\rm escape} = \sqrt{\frac{2GM}{R}} \tag{5.1}$$

where G is the gravitational constant, 6.67×10^{-11} m^3 kg^{-1} s^{-2}; M is the GC mass and R is its radius. Jeans escape occurs at distances beyond those at which the ram pressure is not effective.

In this chapter, the neon, sulphur and argon abundances of six PNe in the Galactic halo are analysed using data from *Spitzer* IRS, in order to examine the extent of the metal-poor nature of this region, and to analyse the dust emission of PNe at low metallicity. The dust compositions of these PNe are also determined and analysed with reference to the low metallicity of the Galactic halo and the potential origins of these sources.

In § 5.2, the sample of PNe from the Galactic halo are shown and the methods of data reduction are outlined. An analysis of the abundances of neon, sulphur and argon in these PNe is given in § 5.3, and the dust content is analysed in § 5.4. The origins of these PNe and their dust composition contextualised to the metallicity of the halo are discussed in § 5.5, and a summary is given in § 5.6.

5.2 Data

5.2.1 Sample

The sample analysed in this chapter consists of the six Galactic halo PNe observed with *Spitzer* IRS, as shown in Table 5.1, from observing programs 30652 (PI: J. Bernard-Salas) and 20049 (PI: K. Kwitter). We do not consider M2-29, which has long been considered a halo PN (e.g. Exter et al. 2004; Howard et al. 1997), as it has since been reclassified as a bulge PN (Miszalski et al., 2011) due to its Galactocentric distance of $R_g \sim 0.8$ kpc (Frew et al., 2016) and its Galactic coordinates ($l = 4.0°$, $b = -3.0°$). We also do not analyse PNG 135.9+55.9 (also known as TS 01) in the same way, as low-resolution observations with *Spitzer* IRS have not clearly detected the source ($\leqslant 3\sigma$), and there are no off-position observations to subtract from the high-resolution spectra, resulting in many glitches. There are no *Spitzer* IRS spectra for the halo PNe JaFu 1, JaFu 2, NGC 2242, NGC 4361 or

Table 5.1 Sample of PNe from the Galactic halo, as observed by *Spitzer*.

Source *Name*	Source *PNG*	RA (J2000) *h m s*	Dec (J2000) *d m s*	v_{radial} *(km s^{-1})*	Proper motion (RA, Dec) *(milliarcsecs/yr)*	[Fe/H]	Observed Dust*
K648	065.0−27.3	21 29 59.38	+12 10 27.5	$-140.6^{(1)}$	$-0.46, -4.98^{\dagger}$	$-2.24 \pm 0.10^{(6)}$	C-rich
BoBn-1	108.4−76.1	00 37 16.03	−13 42 58.6	$+196.0^{(1)}$	...	$-2.39 \pm 0.14^{(7)}$	C-rich
H4-1	049.3+88.1	12 59 27.77	+27 38 10.5	$-141.0^{(1)}$	...	$-2.3^{(8)}$	C-rich
GJJC-1	009.8−07.5	18 36 22.82	−23 55 18.3	$-146.3^{\dagger(2,3)}$	$4.72, -3.59^{\dagger}$	$-1.75 \pm 0.08^{(9,10)\dagger}$	C-rich
DdDm-1	061.9+41.3	16 40 18.15	+38 42 20.0	$-309.1^{(4)}$	−2.04, −1.18	$-1.24 \pm 0.05^{(11)}$	O-rich
PRMG-1	006.0−41.9	21 05 53.56	−37 08 40.3	$+20^{(5)}$	0.16, −3.65	...	Featureless

Notes: (1) Schneider et al. (1983); (2) Harris (1996); (3) Jacoby et al. (2017); (4) Otsuka et al. (2009); (5) Zijlstra et al. (2006); (6) Otsuka et al. (2015); (7) Otsuka et al. (2010); (8) Otsuka and Tajitsu (2013); (9) Lee et al. (1994); (10) Muthumariappan et al. (2013); (11) Henry et al. (2008). † Data represents the globular clusters M15 for K648, and M22 for GJJC-1. Proper motion data for M15 and M22 from Kharchenko et al. (2013), and for DdDm-1 and PRMG-1 from *Gaia* DR2. * Discussed in § 5.4.

Table 5.1 (Continued)

Source *Name*	$R_h^{\#}$ *(kpc)*	R_g *(kpc)*	T_{eff} *(K)*	T_e *(K)*	Ions used for T_e	AORkey	AORkey *off position*
K648	14.2 ± 4.1	13.5 ± 3.2	$39000 \pm 2000^{(1,2,3)}$	10950 ± 2000	[N II], [O II], [O III], [Ne III], [Ar III]	18627840*	18628096
BoBn-1	22.7 ± 6.5	24.7 ± 6.0	$128000 \pm 12000^{(4,5)}$	12700 ± 5600	[N II], [O I], [O II], [O III], [Ne III], [Ne IV], [S II], [S III], [Ar III]	18628352	18628608
H4-1	16.8 ± 4.9	18.5 ± 4.2	$113000 \pm 21000^{(6,7,8)}$	11900 ± 2600	[N II], [O I], [O II], [O III], [Ne III], [S III]	18628864	18629120
GJJC-1	$3.3 \pm 0.3^{\ddagger}$	4.9 ± 0.3	$50000 \pm 10000^{(9,10)}$	...	...	18629376	18629632
DdDm-1	17.3 ± 5.0	16.4 ± 4.3	$48000 \pm 8000^{(3,10)}$	12600 ± 2000	[N II], [O III], [S III]	16808704	16808448†
PRMG-1	21.6 ± 6.3	16.6 ± 5.7	$70000 \pm 10000^{(9,10)}$	15000 ± 1500	[O III]	16809472	16809728†

Notes: (1) Alves et al. (2000); (2) Bianchi et al. (2001); (3) Rauch et al. (2002); (4) Zijlstra et al. (2006); (5) Otsuka et al. (2010); (6) Henry et al. (1996); (7) Mal'Kov (1997); (8) Otsuka and Tajitsu (2013); (9) Pena et al. (1992); (10) Pereyra et al. (2016). * SL data for K648 from AORkey 15733760 in *Spitzer* observing program 124 (PI: R. Gehrz). † AORkey contains SH and LH data for on- and off-positions. $^{\#}$ Values from Frew et al. (2016), except for GJJC-1. ‡ Distance given is to the globular cluster M22 (Lamb et al., 2017; Monaco et al., 2004b).

PNG 243.8−37.1. The full 5–37 μm spectra for all sources are shown in Figure 5.1, alongside the SL spectra.

Of the six PNe in the sample, four have been observed with *Spitzer* as part of a campaign to analyse C-rich sources in the halo. With the exception of the oxygen-deficient

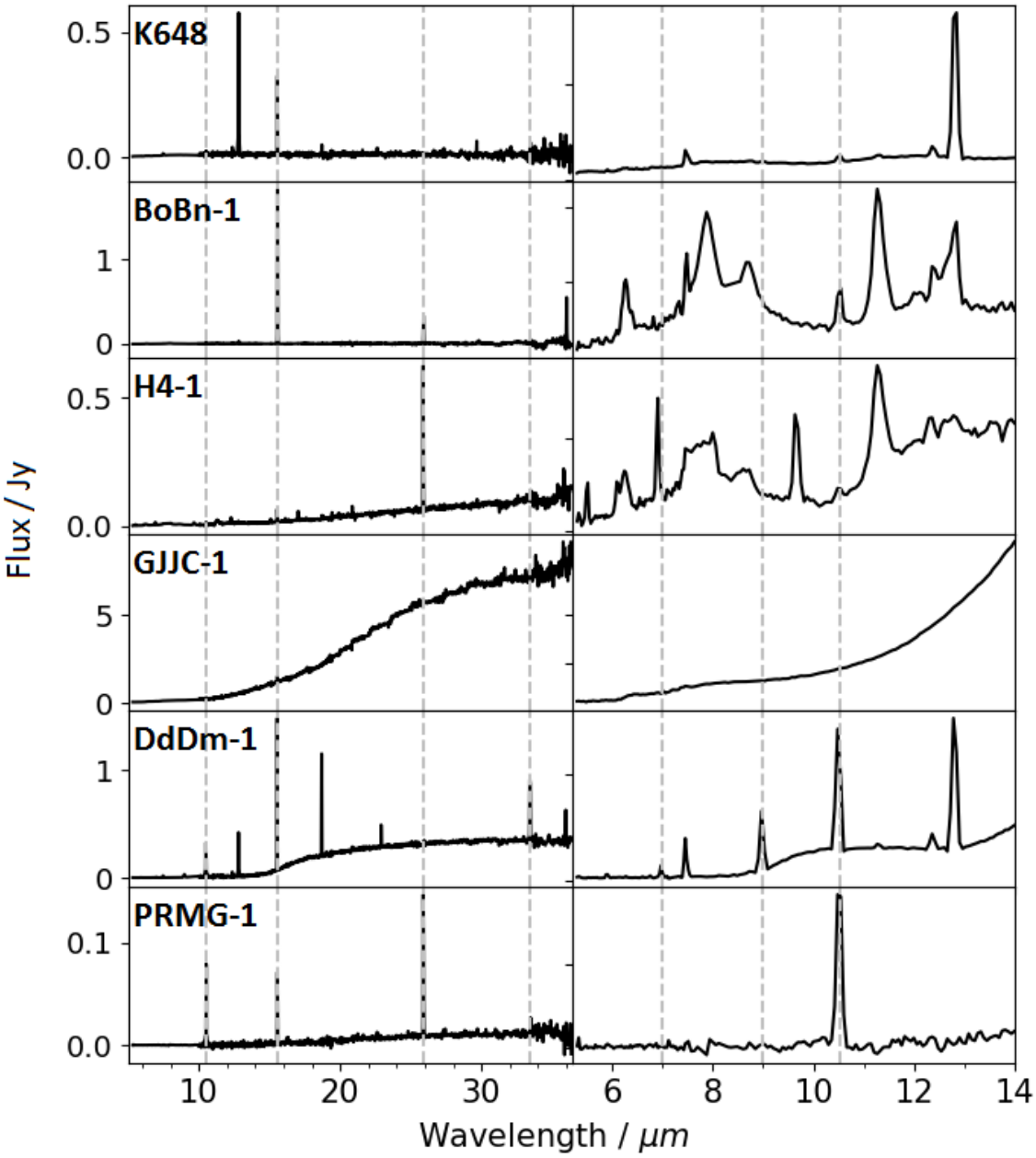

Fig. 5.1 The 5–37 μm spectra of each of the halo PNe. SL, SH and LH data are included on the left-hand side, SL data are plotted on the right. Dashed lines show a selection of atomic lines that are expected to be strong in PNe: 6.99 μm [Ar II]; 8.99 μm [Ar III]; 10.51 μm [S IV]; 15.56 μm [Ne III]; 25.89 μm [O IV]; 33.48 μm [S III].

PNG 135.9+55.9, all other known halo PNe have C/O < 1. Hence, there is an inevitable sample bias which will be considered when analysing the data in this chapter.

For these six sources, the *Spitzer* IRS spectra have been published for K648 (Otsuka et al., 2015), BoBn-1 (Otsuka et al., 2010), H4-1 (Otsuka and Tajitsu, 2013) and DdDm-1 (Henry et al., 2008), whereas the *Spitzer* spectra of GJJC-1 and PRMG-1 are presented here for the first time. In these studies, the abundances are derived using photoionisation models and the dust compositions are obtained for individual sources (except for H4-1), with analysis on a source-by-source basis. The work in this chapter involves the analysis of these Galactic halo sources, but with more of an emphasis on the halo as a region of low metallicity. The abundances of neon, sulphur and argon of these halo PNe are recalculated using the same methods as outlined in Chapter 3, and are then analysed in the context of metallicity compared to other PNe from the Galactic disk. The dust compositions of the halo PNe are similarly compared to those from the disk of the Milky Way. Their origins are then discussed based on their chemical compositions and their locations relative to the Sagittarius stream.

GJJC-1 is a particularly interesting source as its classification as a PN is tentative due to its H- and He-deficient composition (e.g. Jacoby et al. 2017; Zijlstra 2002) and its large dust-to-gas ratio of 0.3 ± 0.2 (c.f. ~ 0.005 for a typical PN; Muthumariappan et al. 2013). GJJC-1 was originally classified as a PN by Borkowski and Harrington (1991), due to its strong emission from [Ne III] and ionised oxygen (observations of [O IV] in its IR spectrum and [O III] in its optical, the latter shown by Gillett et al. 1989). The PN has also been considered as a potential neon nova or merger, though in both cases the progenitor star and the resulting white dwarf would be too massive. Jacoby et al. (2017) concluded that none of these designations (including that of a PN) suit GJJC-1 particularly well. It is assumed for the remainder of this chapter that this source is a PN.

Two of the PNe in this sample are located within GCs: K648 (Pease, 1928) and GJJC-1 (Gillett et al., 1989, 1986) are respectively located within the globular clusters M15 and M22. These are two of only four PNe located in Galactic GCs, the other two being JaFu 1 in Palomar 6 and JaFu 2 in NGC 6441 (e.g. Jacoby et al. 1997), both of which also reside

within the Galactic halo. M15 (NGC 7078) is one of a minority of GCs ($\sim 20\%$) which has undergone core-collapse (Djorgovski and King, 1986), i.e. its luminosity profile is largest at the core. It remains the only GC in which both dust and neutral intracluster H I gas have been observed (Boyer et al., 2006; Evans et al., 2003). M22 (NGC 6656) is one of few GCs in which internal abundance variations of iron have been observed (Da Costa et al., 2009). The PN GJJC-1 is located ~ 3.1 kpc from the centre of the GC (Frogel et al., 1983). There have also been two sightings of stellar-mass black holes in M22, and it has been argued that around 5–100 may be present throughout this GC (Strader et al., 2012).

5.2.2 Data handling and reduction

The data were downloaded from the *Spitzer Heritage Archive*, and the reader is referred to Chapter 2 for more information on their reduction and extraction through the *SMART* program. The observations used the SL, SH and LH modules in all cases, and the relevant scaling factors to account for aperture corrections are shown in Table 5.1. The SL data were extracted using the *AdOpt* package (Lebouteiller et al., 2010), and full aperture extractions were used for the high resolution data. In each case, the data in each module were scaled to those in the LH module, which is the largest of the three ($4.7'' \times 11.3''$) and is therefore able to detect more flux.

5.3 Abundances

Spitzer IRS is ideally suited for observing forbidden line emission from ions of neon, sulphur and argon. The processes of determining the abundances for these elements in PNe are explained in Chapter 3. The atomic data is given in Table 3.7 and primarily comes from TIPbase, part of the IRON project (Hummer et al., 1993), though the effective collision strength for [Ar IV] has been taken from Ramsbottom and Bell (1998). For the electron temperature (T_e) and electron density (n_e) values required to calculate the abundances, T_e values have been used from literature and are shown in Table 5.1, whereas n_e values have been

Table 5.2 Electron densities for the PNe in the sample (cm^{-3}).

PN	n_e (This work)	Line ratio	n_e (Lit.)	Ions	Sources
K648	350 ± 100	[S III]	4650	[O II], [S II], [S III]	1,2
BoBn-1	2200 ± 250	[Ne III]	2700	[N I], [O II], [S II], [Ar IV]	1,3
H4-1	...	...	2790	[N I], [O II], [S II]	4
GJJC-1	...	...	10	...	5
DdDm-1	3500 ± 500	[S III]	3750	[S II], [S III]	1,6
PRMG-1	...	...	750	[S II]	1

Notes: (1) Howard et al. (1997); (2) Otsuka et al. (2015); (3) Otsuka et al. (2010); (4) Otsuka and Tajitsu (2013); (5) Borkowski and Harrington (1991); (6) Henry et al. (2008). Line ratios of [S III] and [Ne III] come from the 18.7/33.5 μm and 36.0/15.6 μm intensities, respectively.

calculated from IR spectral line intensity ratios where possible and are shown in Table 5.2. The infrared line intensity values, $I(\lambda)$, are shown in Table 5.3. Literature values have been used for the electron densities of H4-1 and PRMG-1, for which a 20% uncertainty is assumed, as an approximation of the uncertainities in n_e for K648, BoBn-1 and DdDm-1. The $I(H\beta)$ values have been converted from the 7.5 and 12.4 μm H I line intensities, using conversions from Hummer and Storey (1987).

For GJJC-1, there are no emission lines in its IR spectrum aside from those of neon and oxygen (see also Harrington et al. 1997). Also, the lack of hydrogen emission in both IR and optical spectra suggests that $F(H\beta)$ will be low, leading to uncharacteristically large abundance values. For example, model estimates from Borkowski and Harrington (1991) give an uncharacteristically low value of $\log F(H\beta) = -15.82$ (where $F(H\beta)$ has units of erg cm^{-2} s^{-1}). For these reasons, we do not consider GJJC-1 in the upcoming abundance calculations.

Where possible, the IR abundances have been complemented with those from other studies at optical wavelengths, particularly for Ne^{3+}, S^{+}, S^{2+}, Ar^{2+} and Ar^{3+}. Though S^{2+} and Ar^{2+} are both observable at IR wavelengths, the relevant lines were not detected in the *Spitzer* spectra in a few cases.

The resulting ionic and elemental abundance values for all transitions are shown in Tables 5.4, 5.5 and 5.6. Ionisation correction factors of 1.11 ± 0.08 have been applied to the sulphur abundances in DdDm-1 and PRMG-1, as their ionic abundances of S^{+} have not

Table 5.3 Line intensity values for the halo PNe, in units of 10^{-15} erg cm^{-2} s^{-1}.

PN	$C(H\beta)$	log $I(H\beta)$	H I		[O IV]	[Ne II]	[Ne III]	
			7.5 μm	*12.4 μm*	*25.9 μm*	*12.8 μm*	*15.6 μm*	*36.0 μm*
K648	0.135[(1)]	−12.01	34.8*	9.56*	...	164	106	<20.1
BoBn-1	0.09[(2)]	−12.44	12.2*	3.67[†]	60.7	8.93	592	50.2
H4-1	0.09[(3)]	−12.40	16.2*	3.11*	117	<2.33*	13.7	<23.4
GJJC-1	0.47[(4,5)]	...	...	...	32.2*	<2.89	118	<502
DdDm-1	0.06[(6)]	−11.82	55.2[†]	13.9[‡]	...	132	476	36.2*
PRMG-1	0.09[(7)]	−13.49[(8)]	...	...	27.4[†]	<2.00*	21.3	<3.96*

Table 5.3 (Continued)

PN	[S III]		[S IV]	[Ar II]	[Ar III]	
	18.7 μm	*33.5 μm*	*10.5 μm*	*7.0 μm*	*9.0 μm*	*21.8 μm*
K648	11.2[†]	13.8*	8.51[†]	<2.84	...	...
BoBn-1	<1.90*	<4.45*	8.68*	<3.83*	...	...
H4-1	3.31[†]	<8.70*	4.89[†]	<7.76*	...	...
GJJC-1	...	...	...	<50.0	...	...
DdDm-1	217*	89.1	164*	16.9*	92.1*	<7.05
PRMG-1	<1.93	2.08[‡]	38.8*	<2.06	...	...

Notes: (1) Otsuka et al. (2015); (2) Otsuka et al. (2010); (3) Otsuka and Tajitsu (2013); (4) Gillett et al. (1989); (5) Muthumariappan et al. (2013); (6) Henry et al. (2008); (7) Frew et al. (2016); (8) Peña et al. (1989). Uncertainties <10%, except: * 10–20%; [†] 20–35%; [‡] 75%. $I(H\beta)$ values are given in erg cm^{-2} s^{-1}.

Table 5.4 Ionic and elemental abundances of neon for the halo PN sample.

PN	[Ne II] IP = 21.56 eV	[Ne III] IP = 40.96 eV	[Ne IV] IP = 63.45 eV	[Ne V] IP = 97.12 eV	Ne/H $\times 10^{-6}$	$\log\left(\frac{\mathrm{Ne/H}}{(\mathrm{Ne/H})_\odot}\right)^{\#}$	Ne/H lit. $\times 10^{-6}$	O/H lit. $\times 10^{-6}$	Ne/O
K648	21.0	6.48	...	...	27.5 ± 11.5	$-0.49^{+0.27}_{-0.49}$	$27.5^{(1)}$, $10^{(2)}$, $3.7^{(3)}$	$53.9^{(1)}$	0.51
BoBn-1	2.87	93.0	3.97*	0.198*	100 ± 60	$+0.07\ ^{+0.27}_{-0.78}$	$91.2^{(4)}$, $126^{(2)}$, $52.5^{(3)}$	$55.1^{(4)}$	1.82
H4-1	$0.450^{\dagger}$	2.08	...	...	2.53 ± 1.04	$-1.53\ ^{+0.23}_{-0.47}$	$2.67^{(5)}$, $4^{(2)}$, $1.9^{(3)}$	$150^{(5)}$	0.02
DdDm-1	9.67	18.3	...	...	28.0 ± 14.0	$-0.48\ ^{+0.24}_{-0.62}$	$21^{(6)}$, $14^{(7)}$, $16^{(3)}$	$115^{(6)}$	0.24
PRMG-1	<5.27	33.7	...	...	36.3 ± 13.7	$-0.37\ ^{+0.21}_{-0.44}$	$32^{(8)}$, $17^{(3)}$	$115^{(3)}$	0.32

Notes: (1) Otsuka et al. (2015); (2) Kwitter et al. (2003); (3) Howard et al. (1997); (4) Otsuka et al. (2010); (5) Otsuka and Tajitsu (2013); (6) Henry et al. (2008); (7) Dinerstein et al. (2003); (8) Peña et al. (1989). * from line flux values of Otsuka et al. (2010). # Estimated solar neon abundance from Asplund et al. 2009 ($12 + \log(\mathrm{Ne/H}) = 7.93 \pm 0.10$).

Table 5.5 Ionic and elemental abundances of sulphur for the halo PN sample.

PN	[S II] IP = 10.36 eV	[S III] IP = 23.34 eV	[S IV] IP = 34.79 eV	ICF	S/H $\times 10^{-7}$	$\log\left(\frac{\mathrm{S/H}}{(\mathrm{S/H})_\odot}\right)^{\#}$	S/H lit. $\times 10^{-7}$
K648	0.067*	1.22	0.198	1.00	1.64 ± 0.90	$-1.91^{+0.22}_{-0.42}$	$2.51^{(1)}$, $2^{(2)}$, $13^{(3)}$
BoBn-1	$0.103^{\dagger}$	$0.711^{\dagger}$	0.490	1.00	1.30 ± 0.84	$-2.01^{+0.24}_{-0.55}$	$2.09^{(4)}$, $1^{(2)}$, $3.2^{(3)}$
H4-1	$0.221^{\ddagger}$	0.898	0.252	1.00	1.37 ± 0.70	$-1.98^{+0.20}_{-0.39}$	$1.36^{(5)}$, $2^{(2)}$, $1.1^{(3)}$
DdDm-1	...	15.3	2.39	1.11	19.6 ± 9.8	$-0.83^{+0.20}_{-0.37}$	$21^{(6,7)}$, $40^{(3)}$
PRMG-1	...	5.71	20.8	1.11	29.4 ± 24.3	$-0.65^{+0.28}_{-1.02}$	$100^{(3)}$

Notes: * from line flux values of Otsuka et al. (2015); † from line flux values of Otsuka et al. (2010); ‡ from line flux values of Otsuka and Tajitsu (2013). # Solar sulphur abundance from Asplund et al. 2009 ($12 + \log(\mathrm{S/H}) = 7.12 \pm 0.03$). Literature references are those in Table 5.4.

Table 5.6 Ionic and elemental abundances of argon for the halo PN sample.

PN	[Ar II] IP = 15.76 eV	[Ar III] IP = 27.63 eV	[Ar IV] IP = 40.74 eV	Ar/H $\times 10^{-8}$	$\log\left(\frac{\mathrm{Ar/H}}{(\mathrm{Ar/H})_\odot}\right)^{\#}$	Ar/H lit. $\times 10^{-8}$
K648	<2.31	3.36*	...	4.52 ± 1.92	$-1.74^{+0.25}_{-0.67}$	$3.98^{(1)}$, $4^{(2)}$, $0.5^{(3)}$
BoBn-1	<7.63	$1.29^{\dagger}$	$0.756^{\dagger}$	5.86 ± 3.58	$-1.63^{+0.29}_{-1.54}$	$2.14^{(4)}$, $1^{(2)}$, $3.2^{(3)}$
H4-1	<15.0	$1.75^{\ddagger}$	$0.765^{\ddagger}$	10.0 ± 4.0	$-1.40^{+0.25}_{-0.62}$	$3.63^{(5)}$, $2^{(2)}$, $8.3^{(3)}$
DdDm-1	8.15	54.7	...	62.9 ± 30.1	$-0.60^{+0.26}_{-0.69}$	$59^{(3)}$
PRMG-1	<41.0	...	...	$<41.0 \pm 12.8$	$< -0.79^{+0.23}_{-0.48}$	$63^{(8)}$, $32^{(3)}$

Notes: * from line flux values of Otsuka et al. (2015); † from line flux values of Otsuka et al. (2010); ‡ from line flux values of Otsuka and Tajitsu (2013). $^{\#}$ Estimated solar argon abundance from Asplund et al. 2009 ($12 + \log(\mathrm{Ar/H}) = 6.40 \pm 0.13$). Literature references are those in Table 5.4.

been published. This ICF value was calculated from the mean contribution of S^+ towards the overall sulphur abundances in K648, BoBn-1 and H4-1. Upper limits are calculated in cases where particular lines cannot be observed from the continuum to $\gtrsim 3\sigma$, and half of these values are added to obtain the overall elemental abundances. The abundances measured from the *Spitzer* spectra generally agree well with those from the literature, though there are few exceptions. For instance, the upper limits for [Ar II] in BoBn-1 and H4-1 are particularly high as the continuum at 7.0 μm is noisy in these spectra. This leads to argon abundances that are larger than those observed from literature, though the use of mid-IR data means that the main ionisation states for each of the three examined elements are observed and require relatively small extinction corrections, hence the abundances obtained in this study are generally accurate.

5.4 Dust

In this sample, four of the PNe show C-rich dust emission: K648, BoBn-1, H4-1 and GJJC-1. DdDm-1 is the only source to show amorphous silicate emission, and PRMG-1 is featureless.

The continuum-subtracted profiles of the 6.2, 7.7 and 8.6 μm PAH features in the sample are shown in Figure 5.2. Using the classification system of Peeters et al. (2002), the 6.2 μm PAH features of K648, BoBn-1 and H4-1 all peak at wavelengths indicating Class *B* emission. The 6.2 μm emission in GJJC-1 is particularly unusual in that it peaks at $\sim$ 6.4 μm, which is redder than any such feature documented in the literature. This feature is not attributable to C_{60}, of which there is a weak feature centred at $\sim$ 6.54 μm (e.g. Sloan et al. 2014), or hydrogenated amorphous carbon (HAC), which shows emission features at $\sim$ 6.85 and 7.25 μm (e.g. Nardini and Risaliti 2011). The classification of this feature as one attributed to PAHs is reasonable given the presence of a 7.7 μm feature, which also represents emission from a C–C bond stretch. Analysis of the 7.7 and 8.6 μm features shows that BoBn-1 also shows Class *B* emission. The profile of the 7.7 μm feature from H4-1 is difficult to classify given that it may have been affected by glitches, or by artefacts resulting from the overlap of the SL1 and SL2 orders at $\sim$ 7.5 μm. This particular feature may be classified as either PAH

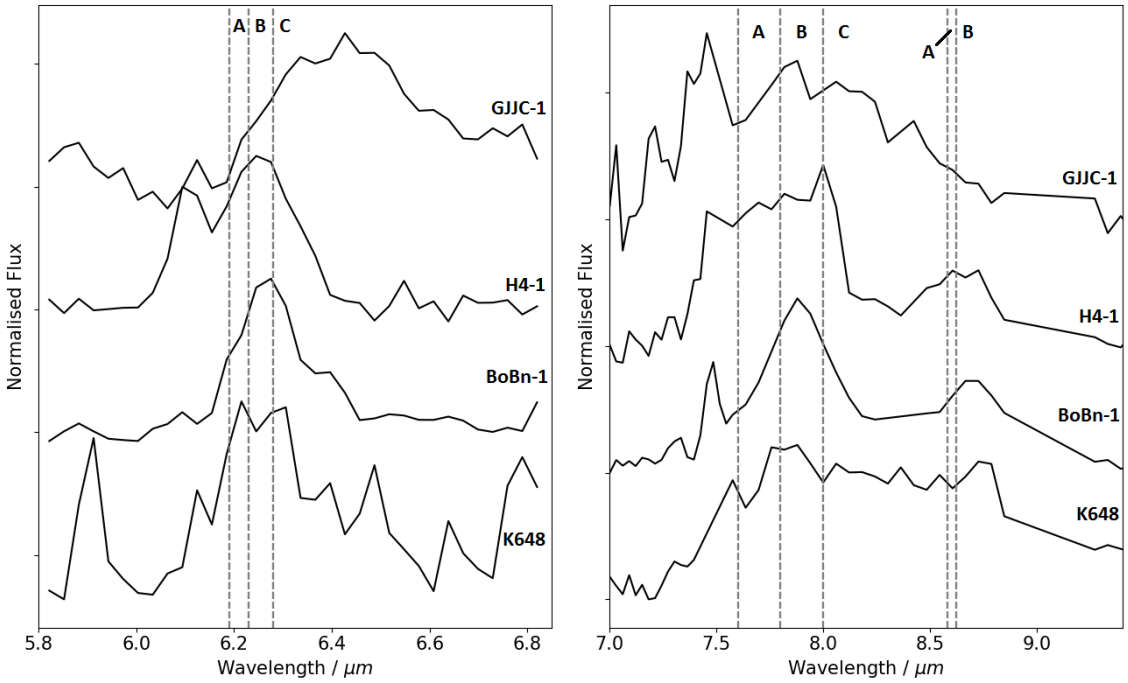

Fig. 5.2 The continuum-subtracted, normalised 6.2, 7.7 and 8.6 μm PAH emission profiles of the four C-rich PNe.

Class *A* or *B*, though its 8.6 μm feature is more typical of a Class *B* feature. Both K648 and GJJC-1 show broad features spanning from 7–9 μm, similar to a Class *D* feature (Matsuura et al., 2014). These have so far only been observed in objects within the sub-solar metallicity Magellanic Clouds (Matsuura et al., 2014; Sloan et al., 2014), and are part of a variety of different C-rich dust emission features observed only in such sources. It was also observed by Matsuura et al. (2014) that Class *D* emission was often detected alongside the 21 μm emission feature, though this has not been detected in any of the PNe in the Galactic halo sample. K648 also shows a separate 8.6 μm feature, potentially indicating the presence of C–H in-plane bends. The lack of this feature in GJJC-1 is expected due to its hydrogen-deficient composition.

The 11.2 and 12.7 μm PAH emission features are shown in Figure 5.3. No C-rich dust features are observed in GJJC-1 at these wavelengths. The 11.2 μm features are clearly observed in BoBn-1 and H4-1, whereas the line at $\sim$ 11.3 μm in K648 is the H I 9–7 recombination line. The 12.7 μm PAH feature is observed in both BoBn-1 and H4-1, though

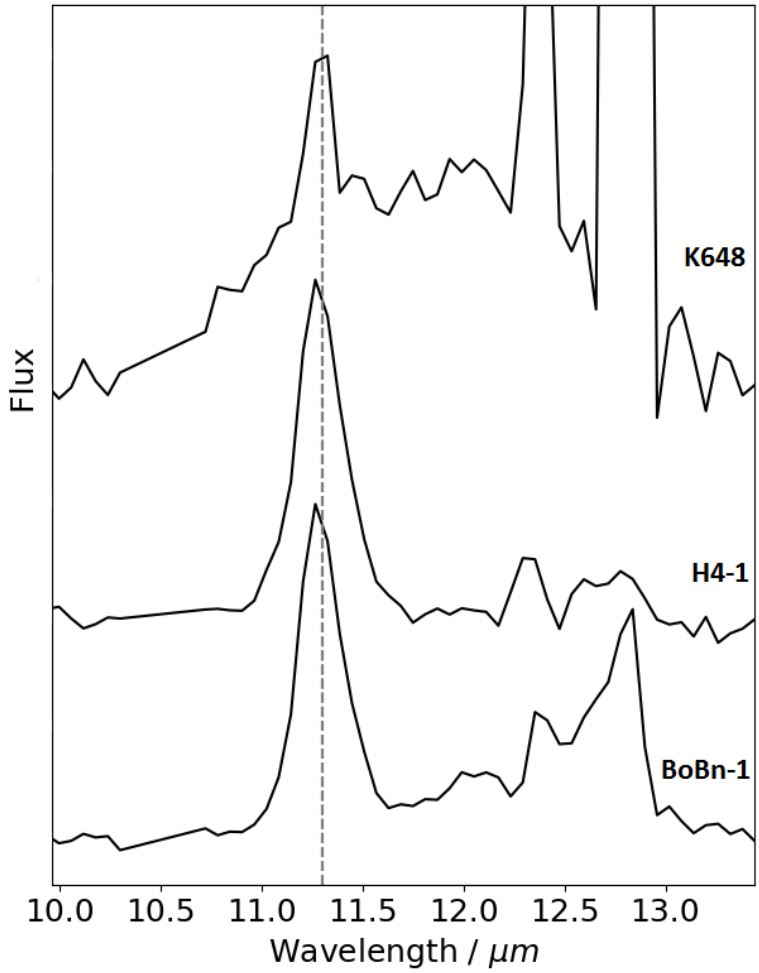

Fig. 5.3 The 11–13 μm continuum-subtracted spectra of the Galactic halo PN sample showing C-rich dust emission. The 10.5 μm [S IV] emission line has been masked in each of these spectra.

it is weak in both PNe. In K648, there is a broad feature in the wavelength range $\sim$ 10.0–12.9 μm, centred at $\sim$ 11.7 μm, which resembles SiC emission.

The intensities and peak wavelengths of the C-rich features are shown in Table 5.7, alongside the associated PAH classes. The PAH emission in the Galactic halo PN sample is primarily of Class *B* or *D* for the 6–9 μm region. The Class *D* emission, in particular, is relatively rare and may only be detected in sources of lower metallicity.

As mentioned previously, an inevitable sample bias towards C-rich sources means that the dust composition observed in this sample is not representative of all PNe in the Galactic halo. This has been considered in the following discussion.

Table 5.7 PAH and SiC intensities for the Galactic halo PNe. Intensities are given in 10^{-17} W m^{-2}; central wavelengths are given in μm. The PAH classes are as described by Peeters et al. (2002) and Matsuura et al. (2014).

PN	I(6.2)	$\lambda_{\rm central}$	PAH Class	I(7.7)	$\lambda_{\rm central}$	PAH Class
K648	3.93	6.265 ± 0.001	B	14.2	8.077 ± 0.066	D
BoBn-1	4.26	6.269 ± 0.004	B	9.77	7.864 ± 0.006	B
H4-1	5.27	6.246 ± 0.003	B	13.4	7.772 ± 0.010	A/B
GJJC-1	18.5	6.405 ± 0.012	?	81.8	7.897 ± 0.095	D

Table 5.7 (Continued)

PN	I(8.6)	$\lambda_{\rm central}$	PAH Class	I(11.2)	$\lambda_{\rm central}$	PAH Class	I(SiC)	$\lambda_{\rm central}$
K648	0.564	8.746 ± 0.001	B?	...	...	...	8.75	11.735 ± 0.025
BoBn-1	2.26	8.702 ± 0.006	B	5.35	11.284 ± 0.003	α	...	...
H4-1	2.68	8.623 ± 0.023	B	6.57	11.285 ± 0.006	α	...	...

Notes: Uncertainties in the intensity values are all in the range 10–20%. The central wavelengths were calculated by averaging those in the two nods of *Spitzer* IRS.

5.5 Discussion

5.5.1 Comparisons with other Galactic PNe

The Galactic halo and anti-centre regions both exhibit a lower metallicity than that of the solar neighbourhood. Figure 5.4 shows the abundances of five halo PNe (GJJC-1 not included) compared to those from elsewhere in the Galaxy, using data from Pottasch and Bernard-Salas (2006) and Chapter 3. The three PNe for which the abundances are known with C/O > 1 (K648, BoBn-1 and H4-1) all have relatively low sulphur and argon abundances. This was also noticed by Torres-Peimbert et al. (1990), who noted that K648, BoBn-1 and H4-1 were all argon-deficient. Indeed, all of the argon observed in PNe would have been present within their original molecular clouds, originating from the outbursts of heavier evolved stars (e.g. supernovae). Conversely, the two sources with C/O < 1 (PRMG-1 and DdDm-1) both show neon, sulphur and argon abundances comparative to those of the anti-centre and, in some cases, the solar neighbourhood.

Despite low sulphur and argon abundances, both K648 and BoBn-1 show relatively high neon abundances, matching those of PNe from the Galactic anti-centre and even the solar neighbourhood. This suggests that neon is formed in these stars (Milingo et al., 2010). This occurs through the following reaction mechanism (Karakas and Lattanzio, 2003; Marigo et al., 2003):

$$\begin{aligned} {}^{14}\mathrm{N} + {}^{4}\mathrm{He} &\longrightarrow {}^{18}\mathrm{F} + \gamma \\ {}^{18}\mathrm{F} + \beta^{+} &\longrightarrow {}^{18}\mathrm{O} + \nu \\ {}^{18}\mathrm{O} + {}^{4}\mathrm{He} &\longrightarrow {}^{22}\mathrm{Ne} + \gamma \end{aligned} \tag{5.2}$$

There is typically a direct correlation between the abundances of neon and oxygen in PNe from the Milky Way and M31, and the Ne/O ratios by mass are expected to be relatively constant at $\sim 0.20 \pm 0.05$ (e.g. Karakas and Lattanzio 2003; Wang and Liu 2008). The Ne/O abundance ratios for the PNe in this sample are given in Table 5.4, which show no agreement with one another. This may be a result of neon enrichment occurring in stars with masses

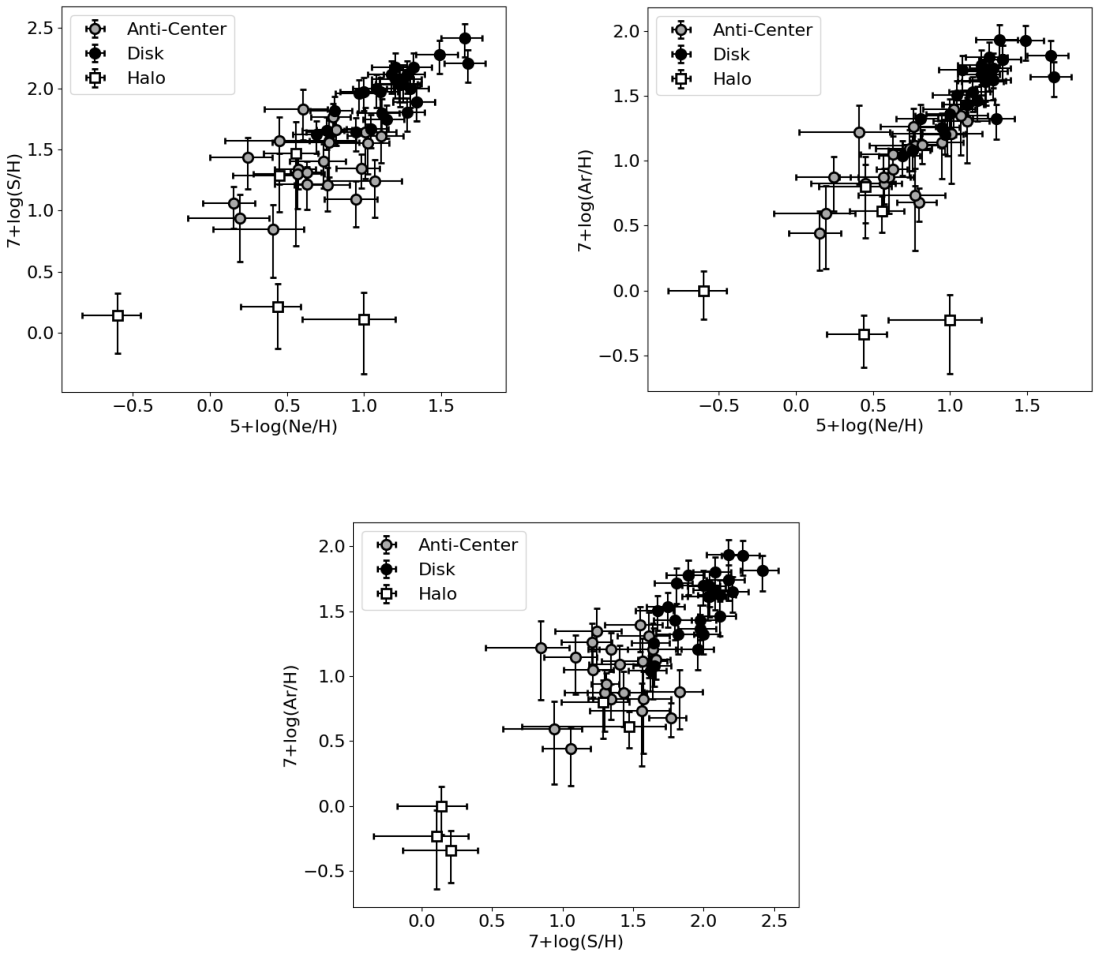

Fig. 5.4 Plots comparing the neon, sulphur and argon abundances in the anti-centre (grey) and solar neighbourhood (black, data from Pottasch and Bernard-Salas (2006)) with those from the Galactic halo (white squares).

between 2 and 4 $M_{\odot}$ due to an enhanced production of ^{22}Ne (Karakas and Lattanzio, 2003), or the oxygen abundances decreasing as an effect of the second dredge-up and hot-bottom burning processes (for stars with an initial mass of $\sim$ 4–8 $M_{\odot}$). However, there are many anomalies to this in our sample, as shown in Table 5.4. For instance, large Ne/O ratios are observed in BoBn-1 (Henry et al., 2004) and GJJC-1 (Borkowski and Harrington, 1991). This may also be due to oxygen-deficiency; the Galactic halo contains two of the most oxygen-deficient PNe, K648 and PNG 135.9+55.9 (Tovmassian et al., 2001). The low Ne/O ratio observed in H4-1 (see also Henry et al. 1996; Otsuka et al. 2003) originates from a combination of a low neon abundance and a relatively large oxygen abundance (see also Henry

et al. 2004). Whether these anomalies are due to the enhancement or suppression of either element, the variation in these abundance ratios challenges current nucleosynthesis theories.

5.5.2 The Sagittarius stream

In the Galactic halo, most of the PNe are O-rich; of the $\sim$ 14 known Galactic halo PNe, the four C-rich sources in this sample and PNG 135.9+55.9 are the only known C-rich PNe. However, studies of the gas and dust in PNe from the Galactic disk and Magellanic Clouds have shown that metal-poor sources are more likely to be C-rich, due to the increased efficiency of the third dredge-up mixing process. In these cases, the stars have masses $\gtrsim 1.5\ M_{\odot}$ and are within the age range of 0.5–5 Gyr (e.g. Marigo et al. 2008). DdDm-1 and PRMG-1 are both O-rich, which may suggest that the masses of their progenitors were too low for the third dredge-up to take place efficiently (e.g. Howard et al. 1997), or simply that they were formed in the Galactic halo.

The C-rich stars in the sample may not have formed or evolved in the Galactic halo; indeed, they may not have originated from the Galaxy at all. The Milky Way is close enough to the Sagittarius dwarf spheroidal galaxy (Ibata et al., 1994) and the Magellanic Clouds to tidally strip some of their galactic material to form sub-structure in the Galactic halo. The Sagittarius stream (Ibata et al., 2001) consists solely of stars, whereas the Magellanic stream (Mathewson et al., 1974; Wannier and Wrixon, 1972) is primarily a source of H I emission (e.g. Nidever et al. 2010). This is because the Milky Way is closer to the Sagittarius galaxy (26.3 $\pm$ 1.8 kpc, Monaco et al. 2004a) than it is to the Magellanic Clouds (50.0 $\pm$ 1.1 kpc for the LMC (Pietrzyński et al., 2013), 62.1 $\pm$ 1.9 kpc for the SMC (Graczyk et al., 2014)).

In order to determine whether the PNe in the sample originated from the Sagittarius galaxy, their location and radial velocity must be similar to that of the stream (Ibata et al., 2001). For instance, BoBn-1 is likely to have been a part of Sagittarius (Zijlstra et al., 2006) as its velocity is similar to those of the comoving stars in the tail at this location, $\sim$ +140–170 km s^{-1} (Ibata et al., 1994). Figure 5.5 shows the location of the Sagittarius stream with relation to

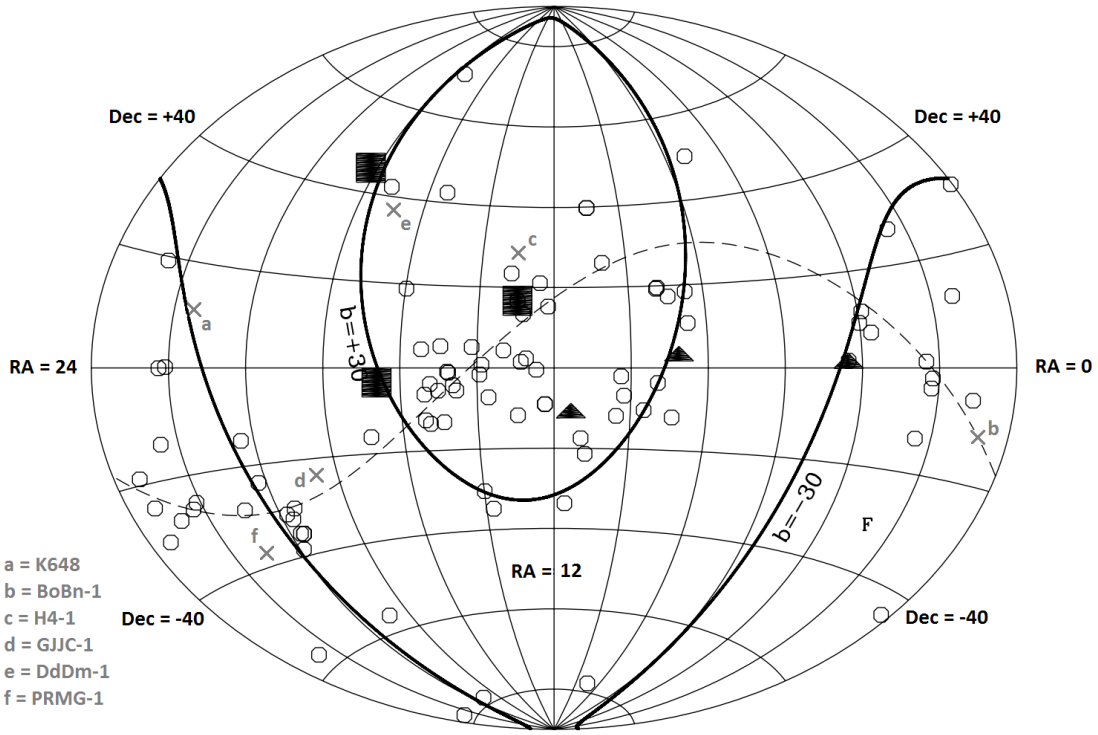

Fig. 5.5 Aitoff projection of the sky, showing the Sagittarius Dwarf Spheroidal Galaxy stream (dashed line) with a series of carbon stars from the halo (Mauron et al., 2004, 2007, 2005; Totten and Irwin, 1998) as open circles, those of Lagadec et al. (2010) as filled symbols. Thick lines represent $b = +30°$ (line approaching the North Celestial Pole) and $b = -30°$ (approaching the South Celestial Pole). The Magellanic stream roughly follows the $b = -30°$ line around the SCP (Mathewson et al., 1974; Nidever et al., 2010). The PNe in this sample are shown as grey crosses. Figure amended from Lagadec et al. (2010).

the six halo PNe in the sample and a selection of carbon stars from other studies. Aside from BoBn-1, the PNe GJJC-1, PRMG-1 and H4-1 are all located close to the stream. GJJC-1 and its globular cluster, M22, have a velocity of ~ -140 km s^{-1} and are located in an area where the stream reaches velocities of ~ -150–200 km s^{-1}. However, its association with the GC M22 rules out any association with the stream as M22 is not located within the Sagittarius dwarf spheroidal galaxy. Walsh et al. (1997) suggested that PRMG-1 may be a member of the Sagittarius galaxy, though Zijlstra et al. (2006) suggests that it is not a member of the stream as its velocity is ~ 20 km s^{-1} whereas the stream velocity is ~ 100 km s^{-1} at that location. However, Ibata et al. (2001) and Helmi and White (2001) show that the velocity of the stream around that area may be closer to ~ 0–50 km s^{-1}, hence PRMG-1 may potentially originate from Sagittarius. H4-1 is slightly faster than the progression of the Sagittarius stream, in

accordance with Ibata et al. (2001), which shows stream velocities of ~ -50–100 km s^{-1} at that location. Hence, it is doubtful that H4-1 is a member of Sagittarius.

Sources of C-rich chemistry in the Galactic halo are typically located closer to the Sagittarius stream. This may be a result of a younger stellar population from the Sagittarius galaxy being stripped away. This makes sense in the context of a minimum mass requirement for the third dredge-up; the metal-poor nature of the halo could not have provided enough material to form stars of sufficiently high mass to undergo this mixing process. However, an origin in the Sagittarius galaxy may suggest that the PNe are of a younger age, and a different chemical composition to that which would typically be observed from the Galactic halo. H4-1 is the only C-rich PN in this sample not associated with either a globular cluster or the Sagittarius stream, hence its origin will require further investigation.

Any links to be made between metallicity and association with the Sagittarius stream are tenuous; the stream experiences its own metallicity gradient (Chou et al., 2007; Martínez-Delgado et al., 2004), despite sources from the galactic disk of Sagittarius exhibiting metallicities as high as $\sim Z_{\odot}$ (e.g. Siegel et al. 2007).

5.5.3 Shocks and dust destruction

The featureless spectrum of PRMG-1 may have resulted from the destruction of dust grains, by dissociation from UV radiation or by shocks. Within the wavelength range of *Spitzer* IRS there is a rise in the overall continuum of this PN, suggesting that dust grains are present.

Shocks are formed when PN outflows of predominantly neutral (or low-ionisation) material interact with the lower density ISM. For instance, Figure 5.6 shows photometric data from the *Very Large Telescope* (VLT) run by *ESO* (program ID 60.A-9203), in which strong [O II] and [O III] emission have been observed around GJJC-1. The source itself is shown in black, as the stellar image has been subtracted. From these images, the [O II] emission is seen in an approximate SSE direction from the star, which follows the direction of proper motion for the M22 Galactic cluster (see Table 5.1). Most of the PNe in this sample exhibit shocks: GJJC-1 (see also Muthumariappan et al. 2013), K648 (Guerrero et al., 2013), BoBn-1 and

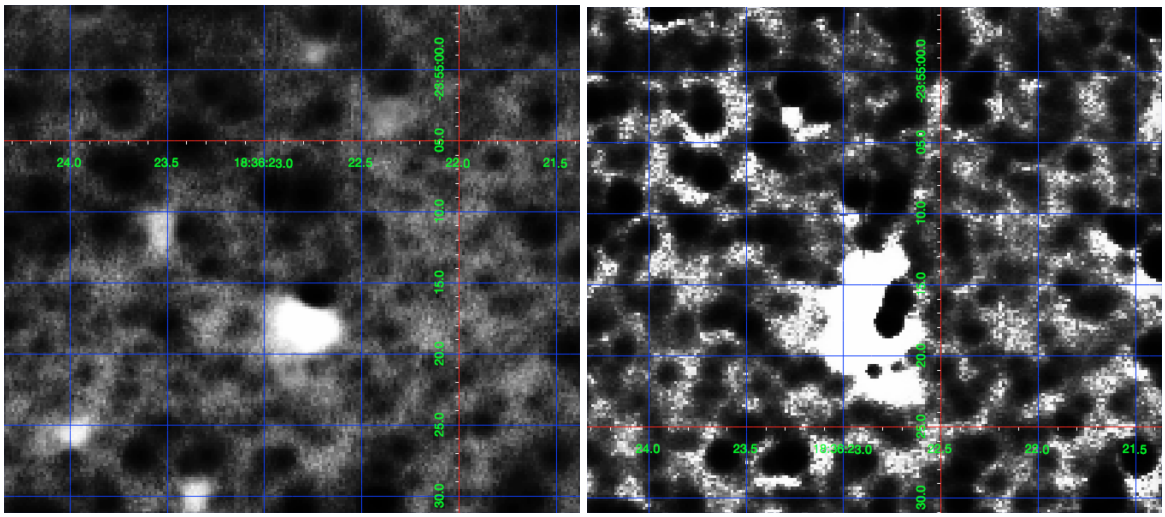

Fig. 5.6 *ESO* VLT photometric data of GJJC-1 through [O II] (left) and [O III] (right) filters. The stellar image has been subtracted from the background image by A. Zijlstra. Screenshots from *SAOImage DS9*.

PRMG-1 (Schönberner et al., 2014) and H4-1 (Tajitsu and Otsuka, 2004). Although DdDm-1 has a dual-lobe structure (Henry et al., 2008), no clear shocks have been observed in this PN.

Shocks with velocities of ~ 50 km s^{-1} can destroy dust grains (Draine, 1995), though this is partly dependent on the dust composition. For instance, Micelotta et al. (2010) found that PAHs with ~ 50 carbon atoms are completely destroyed in shocks with velocities of 100 km s^{-1}, whereas PAHs with ~ 200 carbon atoms are destroyed at shock velocities of $\geqslant 125$ km s^{-1}. Bow shocks from PNe can reach these speeds relatively easily (e.g. Meaburn et al. 2013). Accounting for these shock velocities, C-rich dust has an expected lifetime of few $\times\ 10^7$ years, whereas silicates are able to survive these faster shocks and last closer to 10^8 years (Bocchio et al., 2014). However, models have shown that amorphous carbon may have a similar lifetime to silicate grains (e.g. Jones et al. 1996). In any case, a large amount of information is required to accurately model this, such as the populations of C-rich and O-rich grains in a particular environment, or the rates at which these grains are destroyed (Jones and Nuth, 2011).

Regarding the relative O-rich dust composition of most PNe in the Galactic halo, it may be possible that the sources are old enough that the PAH molecules have been destroyed, whereas amorphous carbon is still present. Despite all of the C-rich PNe in this sample

originating from either the tidal tail of Sagittarius or a globular cluster, it may be possible that more C-rich PNe would have been located in the Galactic halo, but the PAH molecules have been destroyed over 10^7–10^8 years. Of course, this is somewhat speculative. The amount of carbonaceous dust observed from an evolved low- to intermediate-mass star depends mainly on the efficiency of the third dredge-up, which is unlikely to be efficient enough to make the composition of an AGB star C-rich if its mass is too low. This is more likely to have an overall impact on the chemical composition of halo PNe than the destruction of these grains by shocks. It is also more likely for dust to be destroyed by UV radiation (Hollenbach and Tielens, 1999), which is particularly significant in the dissociation of molecules from within GCs (McDonald et al., 2015).

5.6 Summary

A sample of six PNe from the Galactic halo were observed with *Spitzer* IRS in order to determine their dust compositions and abundances of neon, sulphur and argon. The origins of these PNe were also discussed with relation to their coordinates and radial velocities.

A relationship between the abundances and dust composition was observed; three of the four C-rich PNe (K648, BoBn-1 and H4-1) exhibited low sulphur and argon abundances. K648 and BoBn-1 showed higher neon abundances, similar to those of PNe in the Galactic anti-centre and Magellanic Clouds, whereas the neon abundance of H4-1 was at a similarly low level to its sulphur and argon abundances. The two O-rich sources (DdDm-1 and PRMG-1) exhibited similar abundances of all three elements, and all were similar to those observed from Galactic anti-centre PNe.

With the exception of PRMG-1, all of the PNe in the sample show C-rich or O-rich dust emission features. DdDm-1 shows amorphous silicate emission whereas the four C-rich sources show PAH emission (typically of Class *B* or *D*), and K648 also shows silicon carbide. It is noted that this is not expected of Galactic halo PNe, which are predominantly O-rich.

The origins of the PNe are discussed; BoBn-1 is known to originate from the Sagittarius dwarf spheroidal galaxy, of which its tidal tail produces sub-structure within the Galactic halo.

Based on its velocity and location, PRMG-1 is proposed as another PN that has originated from Sagittarius, despite Zijlstra et al. (2006) discounting it for these reasons. H4-1 is the only C-rich PN in the sample to not originate from Sagittarius or a globular cluster, and hence would make an interesting target for further investigation.

Following the previous chapters, which have shown that the production of C-rich dust is favoured in AGB stars of lower metallicity, the O-rich preference of the Galactic halo is most likely explained by the mass and age requirements for the third dredge-up to efficiently take place.

So far, the abundances and dust compositions in Galactic PNe at sub-solar metallicity have been analysed. This has shown that the observed dust emission is primarily C-rich in these sources, on the assumption that the metallicity is still high enough for there to be sufficient mass to carry out the third dredge-up efficiently. Hence, the first key question of this thesis, regarding the influence of metallicity on dust composition, has been answered. In the next chapter, the question regarding the chemical diversity of large organic molecules in circumstellar environments is addressed by using IFU spectroscopy from *SOFIA* FIFI-LS to investigate the PDRs of PNe with fullerene emission.

Chapter 6

Investigating the astrophysical environments of fullerene emission around PNe

The work presented in this chapter is currently being written as a paper to be submitted to *The Astrophysical Journal* by G. J. S. Pagomenos and J. Bernard-Salas (Open University, UK), J. Cami and E. Peeters (University of Western Ontario, Canada and SETI Institute, USA), F. Kemper (ASIAA, Taiwan), A. A. Zijlstra (University of Manchester, UK), R. Klein and W. D. Vacca (*SOFIA*-USRA, USA).

6.1 Introduction

Fullerenes are spheroidal molecules consisting of only carbon atoms. They were first discovered by Kroto et al. (1985) from experiments aimed at understanding the processes regarding the formation of aliphatic carbonaceous molecules in space; the buckminsterfullerene (C_{60}) molecule was formed from the vaporisation of graphite. Upon its discovery, Kroto's team suggested that fullerenes may be stable enough to survive the harsh conditions of the Universe. However, after 25 years of searching for these molecules, the first confirmed detections of C_{60} and C_{70} were from the young Galactic PN Tc 1 by Cami et al. (2010).

Since then, fullerenes have also been detected in several different stellar environments, such as reflection nebulae (e.g. Peeters et al. 2017; Sellgren et al. 2010), young stellar objects (e.g. Roberts et al. 2012), and other evolved stars in the Milky Way and Magellanic Clouds (e.g. García-Hernández et al. 2011, 2010; Sloan et al. 2014). However, despite the numerous sources in which fullerenes have been seen, detections of these molecules have been relatively rare. Features attributed to the buckminsterfullerene cation, C_{60}^{+}, were technically first detected in the interstellar medium by Foing and Ehrenfreund (1994), though Campbell et al. (2015) were the first to unequivocally confirm these features as carriers of two of the diffuse interstellar bands (DIBs), providing an approach to answering one of the biggest mysteries in astronomy over the past hundred years (Heger, 1922) whilst also proving the existence of fullerenes in the ISM (e.g. Cordiner et al. 2017; Galazutdinov and Krełowski 2017; Galazutdinov et al. 2017; Lallement et al. 2018; Spieler et al. 2017; Walker et al. 2015, 2017). This also suggests that fullerenes are more widespread throughout the Universe than originally expected, despite their rarity.

Fullerenes are the largest molecules that have been identified in space, and hence understanding their formation mechanisms will help in determining the methods by which complex organic molecules form in astronomical environments. Some of the proposed chemical pathways for their formation include the bottom-up process of closed network growth, in which a small PAH or fullerene molecule grows with the addition of atomic carbon and C_2 (Dunk et al., 2012a,b), and the top-down photo-processing of PAHs (Berné et al., 2015; Berné and Tielens, 2012), in which the hydrogen atoms are removed from a PAH molecule by UV irradiation, resulting in the bonded structure of carbon atoms curving in on itself to form a fullerene molecule (see Chapter 1). From a study of the reflection nebula NGC 7023, Berné and Tielens (2012) showed that a greater fraction of the carbon closer to the illuminating star (HD 200775) took the form of C_{60}, though this decreased with distance from the star. Conversely, the fraction of carbon in PAHs increased with distance from the star. Hence, photo-processing of PAHs from stellar UV radiation may be a legitimate route to astronomical fullerene formation. Zhen et al. (2014) have also confirmed that this can happen in a laboratory environment.

However, there still remains a missing link between their potential formation mechanisms and the astrophysical environments in which they form.

For the young, well-studied PN Tc 1, the C_{60} emission is extended by $\sim 5''$ from the central star (Bernard-Salas et al., 2012). Indeed, mid-IR photometric data from the *Thermal Region Camera Spectrograph* (T-ReCS) of the *Gemini* telescope have shown that this emission comes from a ring structure at this radius around the central star (Cami et al., in prep). Tc 1 has a radius of $\sim$ 5–6$''$ (e.g. Acker et al. 1992; Pottasch et al. 2011; Tylenda et al. 2003), and hence these are observed near the edge of the region of ionised emission. This means that the observed C_{60} emission may originate from the surrounding photodissociation region (PDR). PDRs are areas of neutral material in which the heating is dominated by far-UV photons, and the main cooling mechanism is the emission of far-IR photons, particularly those of [O I] at 63 and 146 μm, and [C II] at 158 μm, as well as emission from CO and H_2 molecules (Tielens and Hollenbach, 1985). The emission of these cooling lines infer the physical conditions occurring in the PDR, and so by studying these lines in a sample of PNe that are known to show emission from fullerenes, the environments in which these molecules inhabit can be probed, leading to a better understanding of their potential formation and evolution routes.

In this chapter, the PDRs of a sample of four fullerene-containing Galactic PNe (M1-6, M1-11, M1-12 and IC 2501) are investigated from *SOFIA* FIFI-LS observations of the cooling line emission, namely the [O I] 146 μm and [C II] 158 μm emission lines. The [O III] 52 μm lines are also analysed, which represent the ionised regions of these PNe. This study is the first to analyse the PDRs around fullerene-containing PNe using spatial maps and spectra from integral field unit (IFU) data.

This chapter is organised as follows: in § 6.2, the methods of handling the *SOFIA* data are outlined. In § 6.3, the data for each of the four PNe are analysed. In § 6.4, the intensities of the PDR emission lines are compared to those predicted by PDR models. The discussion and conclusions are shown in § 6.5.

6.2 Data acquisition and handling

The *SOFIA* FIFI-LS data were obtained between February and July 2016 as part of program ID 04_0162 (PI: J. Cami). The data were processed and reduced following the standard pipeline, as described in Chapter 2. The PDRs of the PNe M1-6, M1-11, M1-12 and IC 2501 are analysed through IFU spectroscopy for the first time, and the main physical conditions in these sources are shown in Table 6.1. The other Galactic fullerene-containing PNe either have existing data from *ISO* LWS or *Herschel* PACS (IC 418 and Tc 1), are too faint to be detected (M1-9, M1-20, SaSt2-3) or are due to be observed in Cycle 6 of *SOFIA* observations (Hen 2-68 and K3-62) using both FIFI-LS and the HAWC+ camera (PI: J. Cami).

Figure 6.1 shows images of these sources, as observed at optical wavelengths with the *Wide Field and Planetary Camera 2* (WFPC2) for M1-6, M1-11 and M1-12, and at mid-IR wavelengths with *Gemini* TReC-S for IC 2501. All of these PNe have physical diameters of 2–4″ at these wavelengths, which fits within one pixel of both the blue (6″ × 6″ per pixel) and red (12″ × 12″ per pixel) channels of FIFI-LS. These two channels respectively cover the wavelength ranges 51–120 μm and 115–203 μm, allowing for detections of the [O I] at 146 μm, [C II] at 158 μm, and [O III] at 52 and 88 μm. While the [O I] 63 μm line is theoreticaly observable from *SOFIA* FIFI-LS, its wavelength coincides with atmospheric water contamination, and hence the corresponding data points are removed in the reduction pipeline.

6.3 Analysis

The *SOFIA* FIFI-LS data of the [O I] 146 μm, [C II] 158 μm, [O III] 52 and 88 μm lines were analysed with the *FLUXER*[1] program, version 2.69. The full methods of data analysis with *FLUXER* are explained in Chapter 2, but to summarise: a pixel from the IFU spectrum for each data cube was selected, and upper and lower wavelength bounds were specified for the measured lines and continuum regions. These were applied to the spectra in all pixels, from

[1]IDL routine created by Christoph Iserlohe, available from http://www.ciserlohe.de/fluxer/fluxer.html .

Table 6.1 Fullerene-containing PNe observed with *SOFIA* FIFI-LS.

Source *Name*	Source *PNG*	RA (J2000) *(h m s)*	Dec (J2000) *(d m s)*	R_g *(kpc)*	Diameter *(arcsecs)*	$C(H\beta)$	n_e *(cm^{-3})*	T_e *(K)*	T_{eff} *(K)*	log(C/O)	F(C_{60})
M1-6	211.2−03.5	06 35 45.13	−00 05 37.5	9.8 ± 1.8	4	$1.57^{(1)}$	11450*	$9800^{(1,2)}$	$34960^{(3)}$	$0.16^{(3)}$	2.93
M1-11	232.8−04.7	07 11 16.69	−19 51 02.6	10.7 ± 0.9	2	$1.63^{(1)}$	$10700^{(4)}$	$10400^{(1)}$	$31830^{(3)}$	$0.19^{(3)}$	10.5
M1-12	235.3−03.9	07 19 21.47	−21 43 55.4	14.5 ± 2.3	2	$0.97^{(1)}$	2550†	$9300^{(1)}$	$31660^{(3)}$	$0.24^{(3)}$	3.50
IC 2501	281.0−05.7	09 38 47.15	−60 05 30.5	8.0 ± 0.1	4	$0.55^{(5)}$	$11000^{(6)}$	$10800^{(6)}$	$51650^{(3)}$	$0.19^{(3)}$	5.90

Notes: (1) Henry et al. (2010); (2) Costa et al. (2004); (3) Otsuka et al. (2014); (4) Koeppen et al. (1991); (5) Sterling et al. (2015); (6) Sharpee et al. (2007). The electron density values for M1-6 and M1-12 were calculated using [S III] 18.7 / 33.5 μm line ratios from *Spitzer* IRS data: * AORkey 21953024 (PI: J. Bernard-Salas, program ID: 40035); † AORkey 25849856 (PI: L. Stanghellini, program ID: 50261). The C_{60} flux values are calculated by addition of the 17.4 and 18.9 μm flux values, as done by Otsuka et al. 2014 (units: 10^{-15} W m^{-2}).

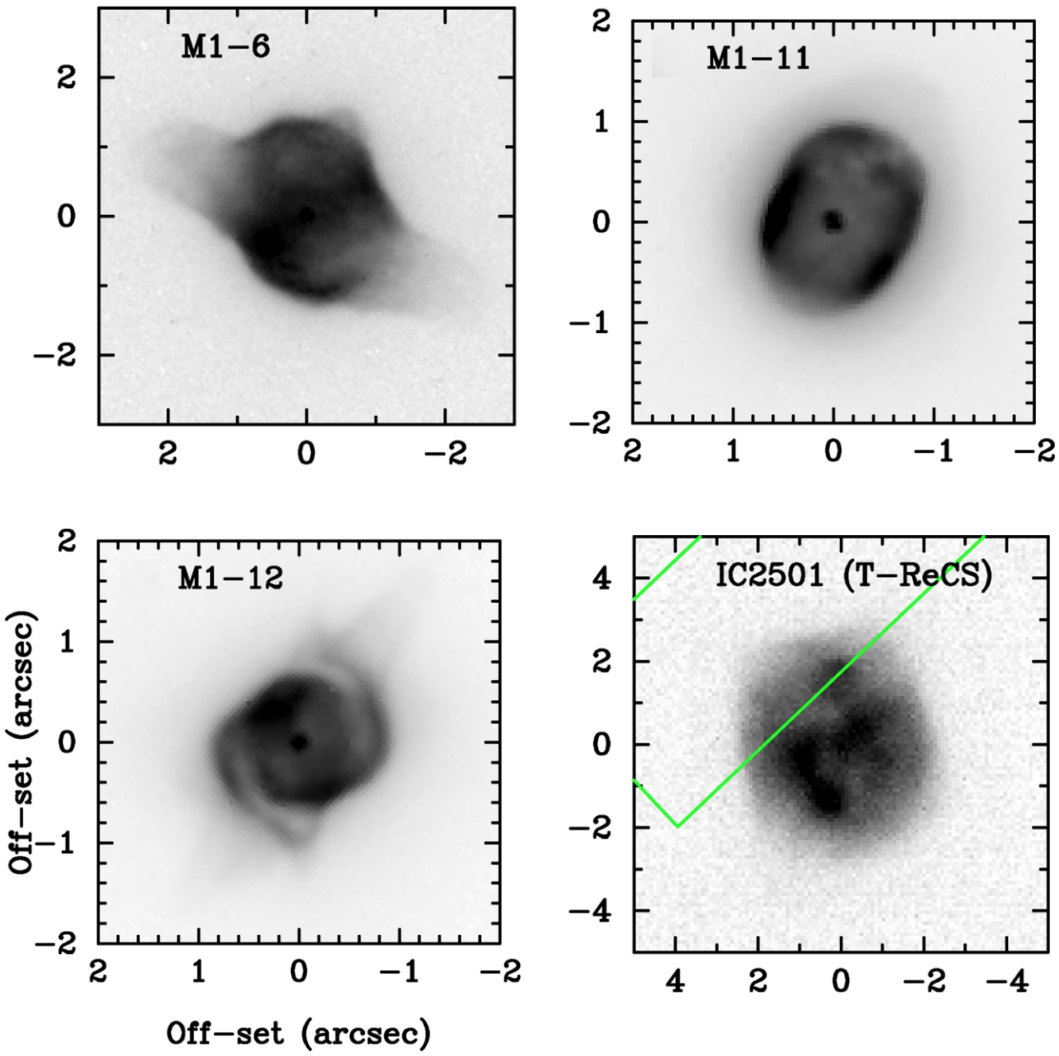

Fig. 6.1 Photometric images of the four fullerene-containing PNe from the *Hubble Space Telescope* (R-band) and *Gemini* T-ReCS (mid-IR). Figure reproduced from Otsuka et al. (2014); the green rectangle represents the size and position of the SH module of *Spitzer* IRS from their observations.

which spatial maps could be produced by adding the flux within the specified wavelength range for each pixel.

The beam sizes for the [O I] 146 μm, [C II] 158 μm and [O III] 52 μm lines were respectively around 14.7$''$, 15.9$''$ and 5.2$''$. This is in accordance with the angular resolution of the telescope at these wavelengths (see equation 2.12). The largest angular size of a PN in this sample is $\sim 4''$, and hence all of the sources are detected in their entirety.

The intensity and velocity maps of the observed emission lines from around the fullerene-containing PNe are analysed below.

6.3.1 Intensity maps

The emission line intensities were obtained by adding together the total flux between the specified wavelength range for each pixel within a ring, and applying the extinction corrections of Fluks et al. (1994) (these are particularly small at far-IR wavelengths). The parameters of these fitted rings are shown in Table 6.2, along with the intensity values of the emission lines. The beam sizes are shown on these figures for each line, and in all cases the line emission is more extended than the beam.

The maps for each PN are shown in Figures 6.2 to 6.5. Uncertainties in intensity values are estimated to be $\sim$ 10–20% in each case, in order to balance the non-circular morphologies of these sources measured within the applied rings with the minimisation of flux loss in the outer pixels. The 52 μm [O III] emission line was not observed in M1-11 and M1-12. Pixels are masked if they provide flux values less than zero, or are clearly not a part of the main PN. In some cases, there are other emission sources that are observed within the IFU spectral map, hence these have also been masked. These figures show that there is a general change in morphology between the two cooling lines ([O I] and [C II]) in all sources except M1-11. This may reflect the greater flux emission from this source (e.g. the C_{60} flux in Table 6.1), but this may also be affected by a variety of signal-to-noise ratios in some of the pixels in a given

Table 6.2 Ring parameters applied to measure intensities for each of the atomic lines of interest. Intensity values are given in units of 10^{-16} W m^{-2}; ring radii are given in pixels.

PN	Line	Central pixel	Ring radius	Intensity
M1-6	[O I] 146 μm	18,16	6	1.03
	[C II] 158 μm	14,15	7	2.93
	[O III] 52 μm	18,20	9	38.4
M1-11	[O I] 146 μm	12,15	9	6.59
	[C II] 158 μm	12,15	9	15.2
M1-12	[O I] 146 μm	16,16	7	0.934
	[C II] 158 μm	13,14	6	2.53
IC 2501	[O I] 146 μm	16,12	7	9.54
	[C II] 158 μm	12,13	9	5.82
	[O III] 52 μm	16,17	9	305
	[O III] 88 μm	16,17	9	50.8

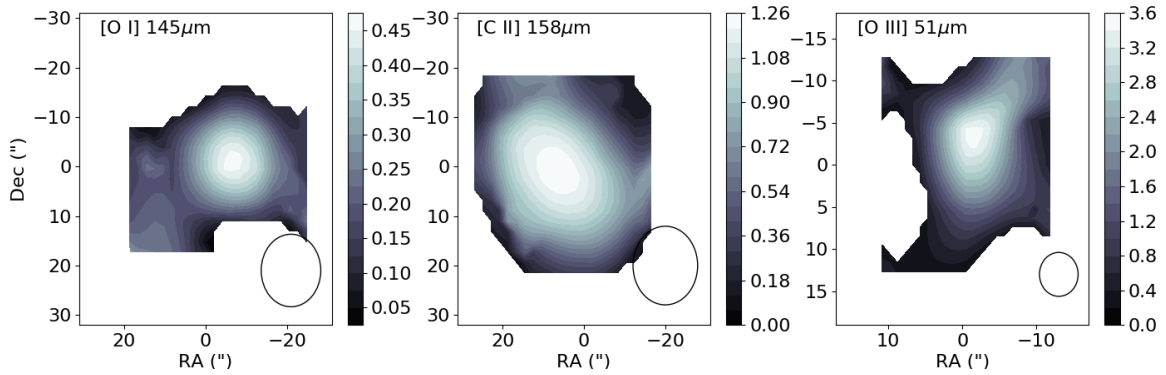

Fig. 6.2 The [O I] 146 μm, [C II] 158 μm and [O III] 52 μm intensity maps of M1-6. The circles indicate the beam sizes at each wavelength.

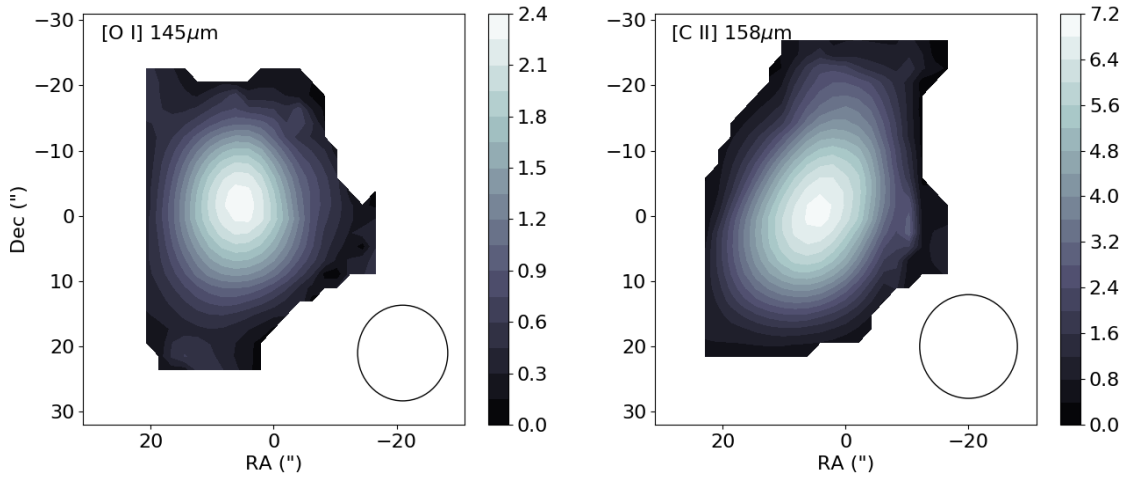

Fig. 6.3 The [O I] 146 μm and [C II] 158 μm intensity maps of M1-11. The circles indicate the beam sizes at each wavelength.

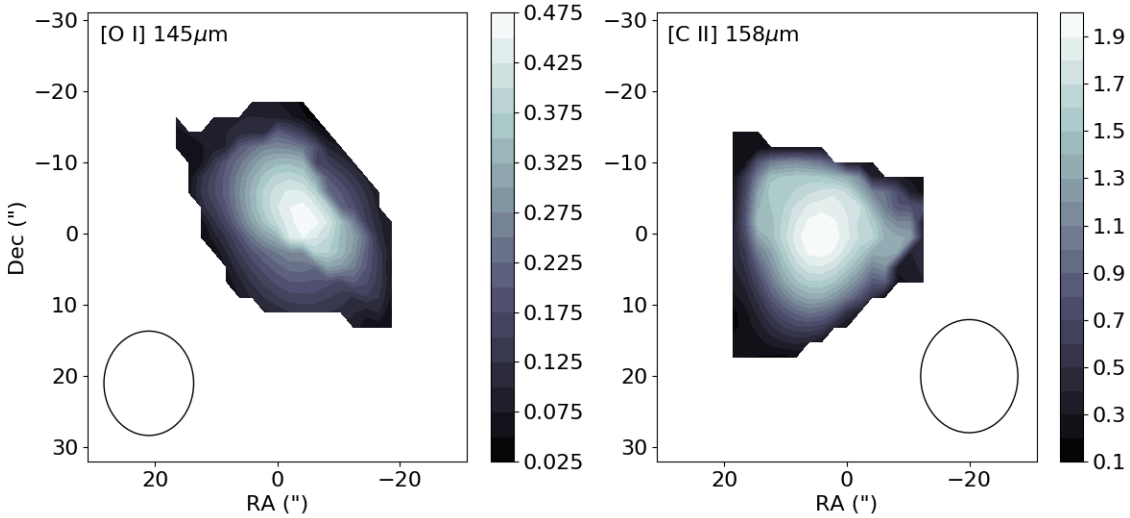

Fig. 6.4 The [O I] 146 μm and [C II] 158 μm intensity maps of M1-12. The circles indicate the beam sizes at each wavelength.

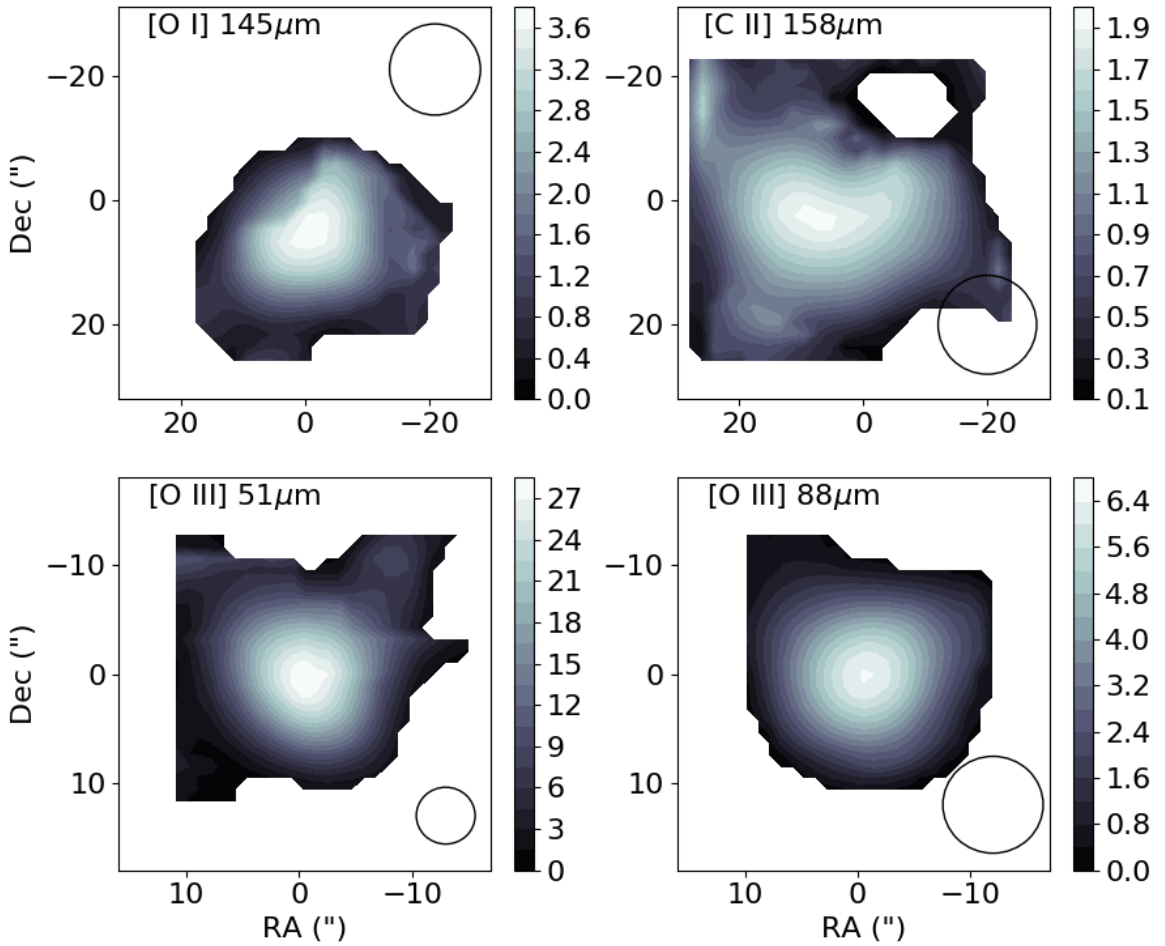

Fig. 6.5 The [O I] 146 μm, [C II] 158 μm, [O III] 52 μm and [O III] 88 μm intensity maps of IC 2501. The circles indicate the beam sizes at each wavelength.

IFU map. For IC 2501, the two observed [O III] emission lines at 52 and 88 μm show almost identical morphologies, as expected.

Figure 6.6 shows all of the observed emission lines for each source plotted over each other. Again, the centres of emission for the [O I] and [C II] lines in M1-11 overlap well. The peak of the [O III] emission is close to those for the cooling emission lines in M1-6 and IC 2501, suggesting that the emission from the PDRs is close to that from the ionised region of these PNe.

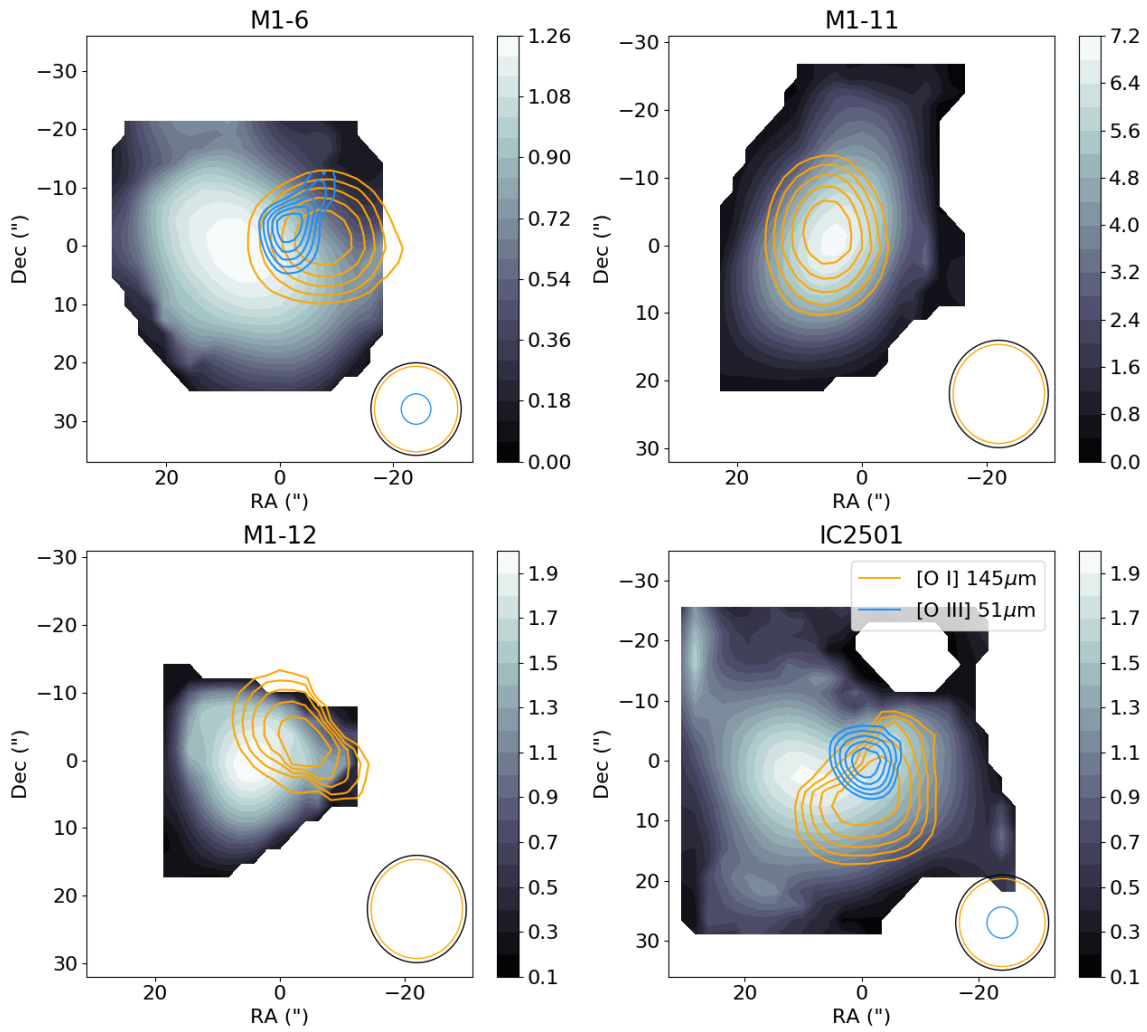

Fig. 6.6 Spatial maps of the [C II] 158 μm emission in the four fullerene-containing PNe, with [O I] 146 μm and [O III] 52 μm emission superimposed. Flux values are given in Janskys. Contours represent 50, 60, 70, 80 and 90% of the maximum detected flux in each case.

6.3.2 Line intensity offsets

Figure 6.6 also shows that there are notable offsets between the central positions of the [O I] 146 μm and [C II] 158 μm emission lines for all sources except M1-11; [O I] is typically centred around 4–5 pixels to the west (right) of [C II].

Due to the systematic nature of the offsets between the two cooling lines, there is some doubt as to whether or not they are real. If they are real, they are most likely an effect of the different critical densities between the two lines (see § 6.4.3), but may also result from shocks or outflows.

I have contacted the *SOFIA* team for clarification. It emerged that this was a non-trivial issue. After several months of analysis from their end, they suggested that these offsets may arise from relatively low signal-to-noise in the [O I] 146 μm line data. They also detected offsets between the [O I] 63 (pre-reduction) and 146 μm lines, respectively observed through the blue and red channels of FIFI-LS, inferring that these channels may have been misaligned.

No definitive answer has yet been given from the *SOFIA* team regarding these offsets, so for the rest of this chapter I will be ignoring the spatial offsets and treating them as instrumental artefacts.

6.3.3 Line velocities

Velocity maps for each of the PNe in the sample were obtained in *FLUXER* by specifying a wavelength range for the peak emission flux and measuring deviations from the wavelengths of the observed lines in a vacuum (λ_{vac}) using the Doppler redshift equation:

$$\frac{v}{c} = \frac{\lambda_{obs} - \lambda_{vac}}{\lambda_{vac}} \tag{6.1}$$

where λ_{obs} is the observed wavelength and λ_{vac} = 145.53, 157.74, 51.81 and 88.36 μm for the [O I], [C II], and two [O III] lines respectively. The velocity maps for each of these lines are shown in Figures 6.7 to 6.10.

The [O III] emission in M1-6 and IC 2501 shows velocity gradients, as observed in Figures 6.11 and 6.12. The variations in velocity within these two PNe suggest rotation of the ionised regions, with differences of $\sim$ 150 km s^{-1} between the two highlighted pixels in each case. From Figures 6.9 and 6.10, it also appears that the [C II] 158 μm lines are rotating, though these are less convicing due to relatively high noise in the continua of many of these pixels. Also, the profiles of the lines vary between pixels, unlike those in Figure 6.12, implying that these profiles are not representative of the [C II] emission line. In this sample, the rotation of the [O III] 52 μm lines in M1-6 and IC 2501 suggests a discontinuity between the PDR and ionised regions of the PNe. This may also indicate the presence of outflows (see § 6.5).

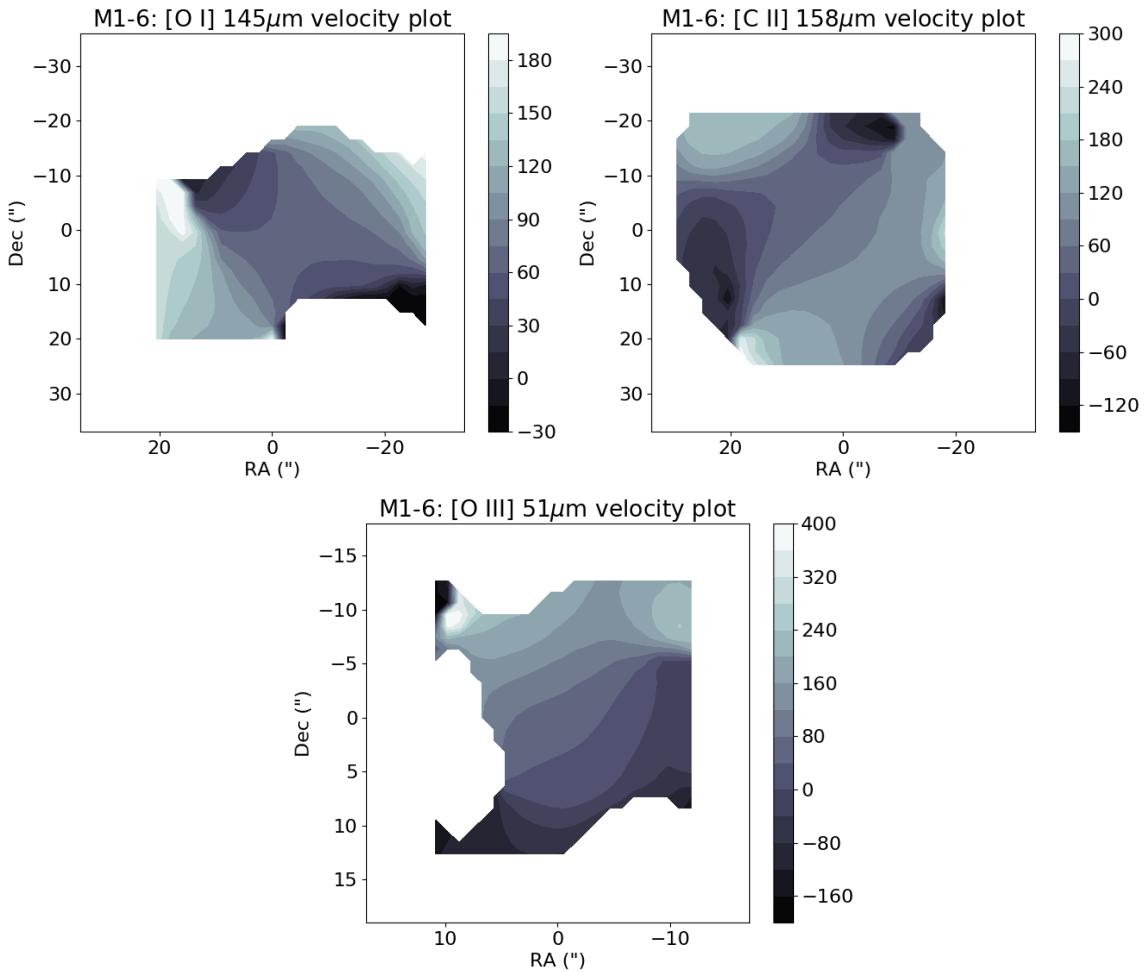

Fig. 6.7 The [O I] 146 μm, [C II] 158 μm and [O III] 52 μm velocity maps of M1-6, as measured by *SOFIA* FIFI-LS, with units of km s^{-1}.

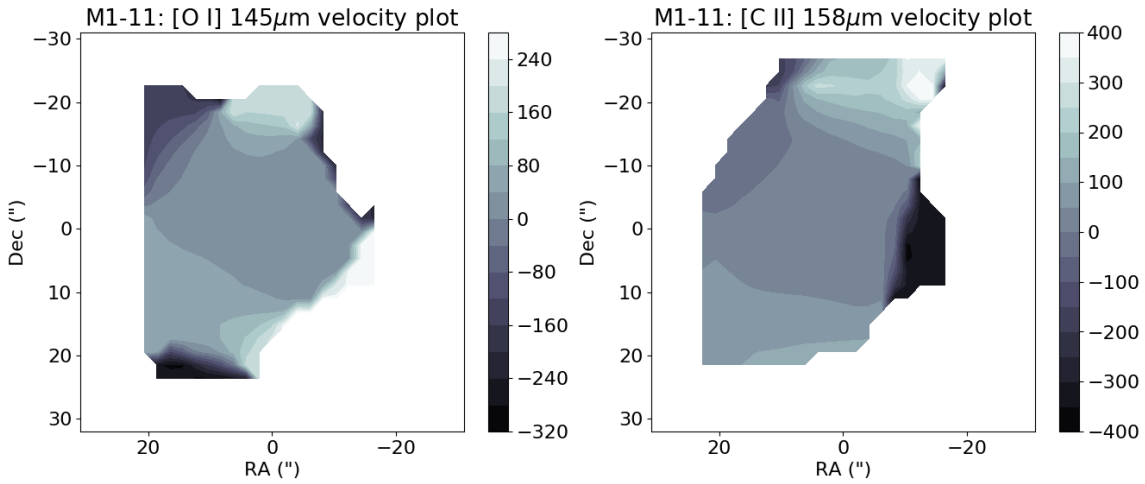

Fig. 6.8 The [O I] 146 μm and [C II] 158 μm velocity maps of M1-11, as measured by *SOFIA* FIFI-LS, with units of km s^{-1}.

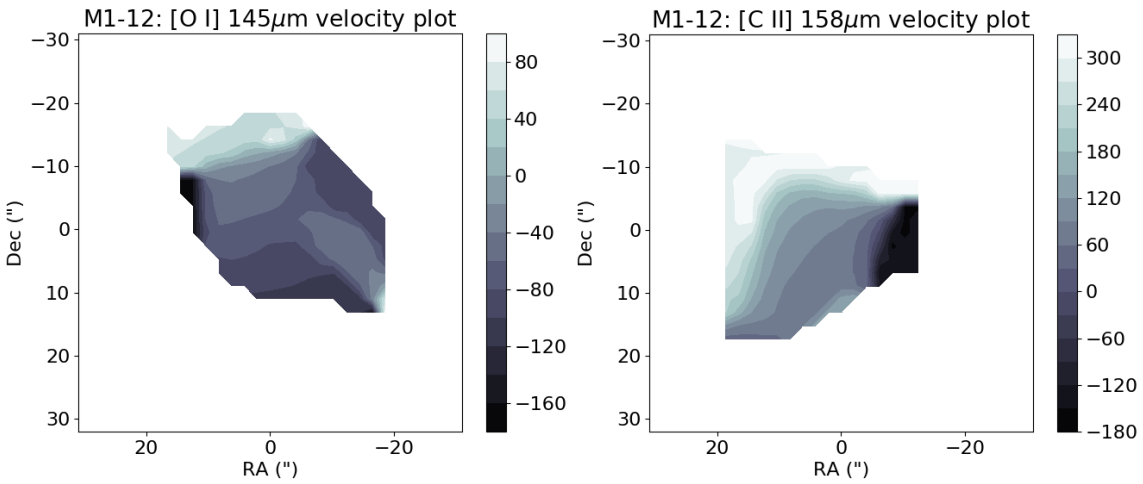

Fig. 6.9 The [O I] 146 μm and [C II] 158 μm velocity maps of M1-12, as measured by *SOFIA* FIFI-LS, with units of km s^{-1}.

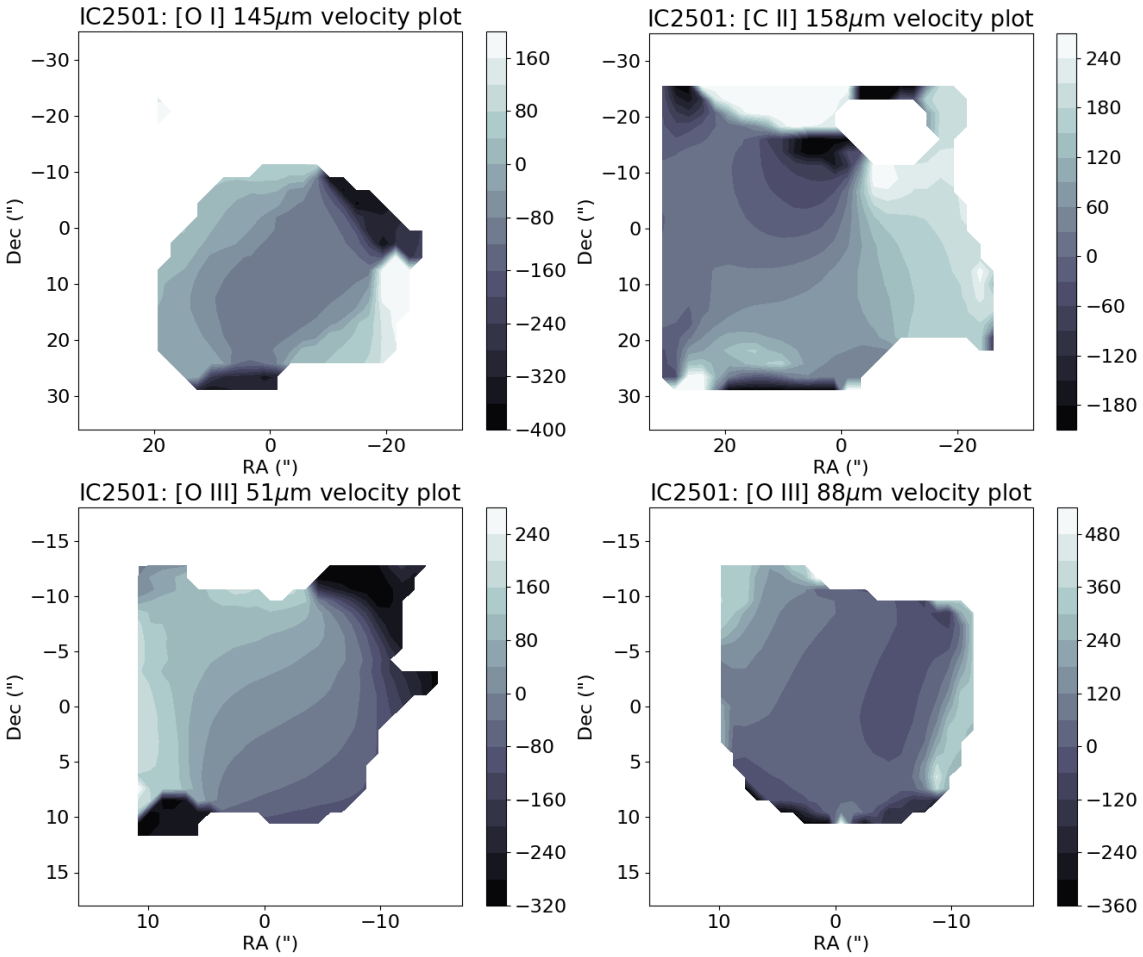

Fig. 6.10 The [O I] 146 μm, [C II] 158 μm, [O III] 52 μm and [O III] 88 μm velocity maps of IC 2501, as measured by *SOFIA* FIFI-LS, with units of km s^{-1}.

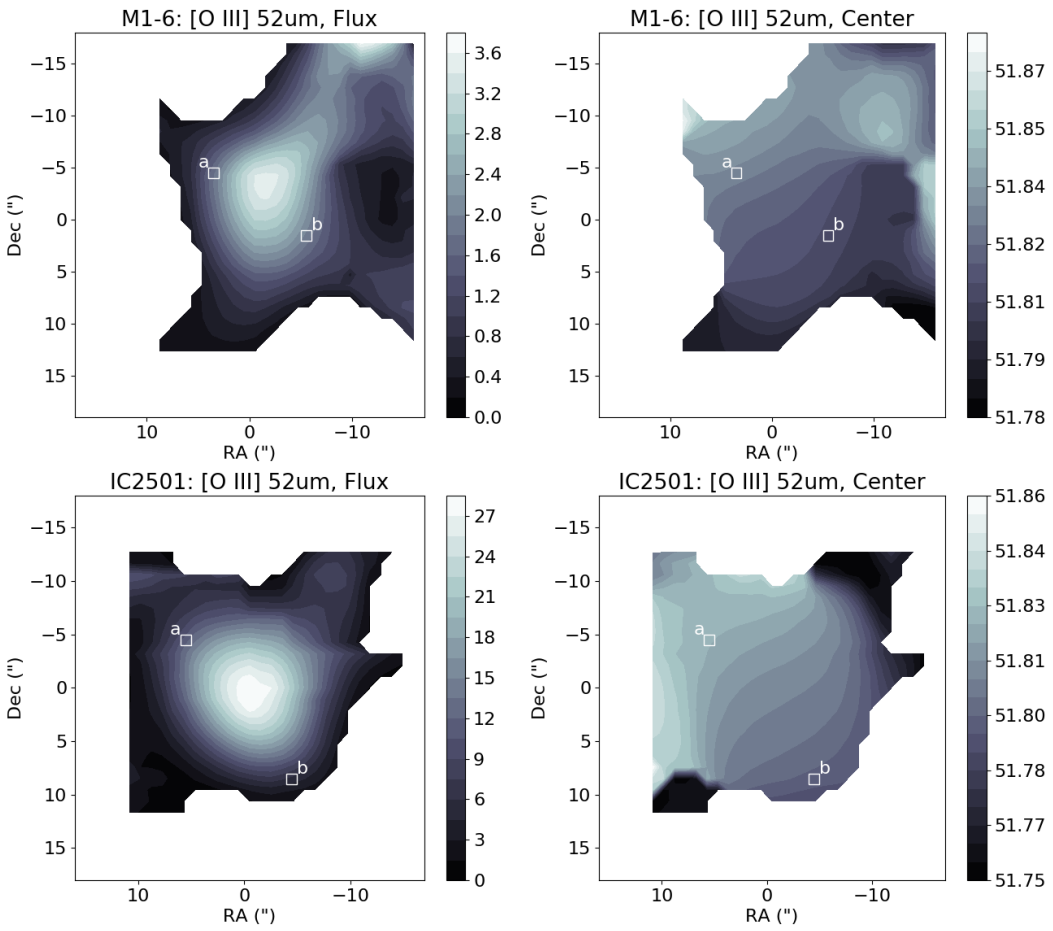

Fig. 6.11 Full spatial maps of the [O III] 52 μm emission in M1-6 (top) and IC 2501 (bottom), in terms of flux (left) and central wavelength (right). Pixels 'a' and 'b' have been highlighted for use in Figure 6.12.

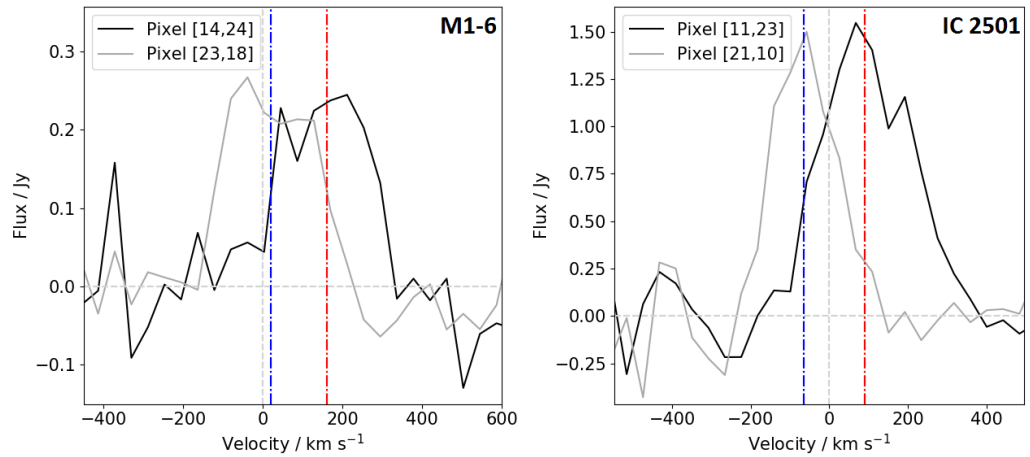

Fig. 6.12 Continuum-subtracted velocity spectra from pixels 'a' (black) and 'b' (grey) from Figure 6.11. The red and blue lines show the average velocities of the [O III]$_{52\ \mu m}$ lines from the two respective spectra. A velocity of 0 km s^{-1} represents the λ_{vac} = 51.81 μm in each case.

6.4 PDR modelling

A PDR model will now be applied to the observed cooling line intensities around fullerene-containing PNe, in order to derive the densities and radiation fields of these regions. PDR models consider aspects such as the chemical abundances, heating and cooling, and radiation transport processes occurring within these regions. Given certain physical conditions, such as the hydrogen density ($n_{\rm H}$) and the Habing flux (G_0), i.e. the total UV flux between the Lyman limit (912 Å) and 2400 Å, normalised to the average interstellar radiation field (Habing, 1968), the intensities of certain lines within the PDR can be predicted. However, the main interest of this work is to determine the physical conditions of these fullerene-containing PNe. Hence, in a similar way to Bernard-Salas and Tielens (2005), values of G_0 and $n_{\rm H}$ will be obtained from observational line intensities.

This section explains the purposes of the models used and the inputs required for them to work, before analysing the predictions for the physical conditions of the PDRs around the fullerene-containing PNe.

6.4.1 Model description

This work uses the PDR model of W. Latter, as published in Fong et al. (2001), which was the first model of circumstellar C-rich PDRs around evolved stars (particularly AGB stars, proto-PNe and PNe). To emphasise the main differences between this PDR model for evolved stars and other models for interstellar sources, the initial abundances considered by the PDR model for C-rich evolved stars are shown alongside those of the model for interstellar O-rich PDRs around molecular clouds by Kaufman et al. (1999) in Table 6.3. In particular, the initial carbon abundance is an order of magnitude greater in the C-rich model than that of the O-rich model, and the C/O abundance ratios are ~ 3.0 and 0.5 for the evolved star and molecular cloud models, respectively. An equivalent PDR model for O-rich evolved stars was published alongside this model (Castro-Carrizo et al., 2001), though we do not consider it here since the sample only contains C-rich sources.

Table 6.3 Comparison of the main parameters of the PDR model for evolved stars by W. Latter (Fong et al., 2001) and the PDR model for molecular clouds by Kaufman et al. (1999).

Parameter	Evolved star model	Molecular cloud model
Carbon abundance	1.5×10^{-3}	1.4×10^{-4}
Oxygen abundance	5.0×10^{-4}	3.0×10^{-4}
Sulphur abundance	7.9×10^{-6}	2.8×10^{-5}
Silicon abundance	3.5×10^{-6}	1.7×10^{-6}
Magnesium abundance	1.3×10^{-6}	1.1×10^{-6}
PAH abundance (n_{PAH} / n_{H})	1×10^{-7}	4×10^{-7}
Turbulent Doppler velocity (km s^{-1})	0.75	1.5
Gas density range (cm^{-3})	10^2–10^6	10^1–10^7

Unlike most existing models at the time, which considered PDRs in interstellar environments (e.g. Black and Dalgarno 1977; Kaufman et al. 1999; Tielens and Hollenbach 1985) and were primarily O-rich, the C-rich model considers the chemistry of a greater range of carbonaceous molecules, such as C_2, C_2H_2 and ionised PAHs. The gas temperatures are around three times greater than those of oxygen-rich models, due to the photoelectric heating from large PAH molecules (Bakes and Tielens, 1994; Kaufman et al., 1999). Another condition of this model is that the carbon abundance is always greater than that of oxygen. The carbon and oxygen in the modelled PDRs are primarily in the C^+ and O^0 (i.e. neutrally charged oxygen) states, respectively; most of the oxygen reacts with C^+ to form CO, whereas much of the carbon recombines to form C^0.

6.4.2 Inputs

The network of chemical reactions used in this C-rich model includes 1270 reactions between 94 different chemical species, and includes both charged (positive and negative) and neutral PAH molecules.

Estimates of the PDR density around the fullerene-containing PNe require both line intensities (see § 6.3) and the Habing flux. This works under the assumption that all of the UV light has been absorbed and re-emitted at IR wavelengths from the PDR. The Habing flux is calculated by:

$$G_0 = \frac{4\,F_{IR}}{1.6\,\times\,10^{-6} \times 2.35\,\times\,10^{-11} \times d^2} \tag{6.2}$$

where F_{IR} is the total far-IR flux of the source, 1.6×10^{-6} W m^{-2} is the average flux of the interstellar radiation field, 2.35×10^{-11} arcsec^{-2} is equal to an inverse steradian, and d is the diameter of the PN in arcseconds (Bernard-Salas and Tielens, 2005). Note that for M1-6, M1-11 and M1-12, the PN diameters used for these predictions may add extra uncertainties, given that the applied values were calculated from photometry at optical wavelengths.

The F_{IR} values of M1-6, M1-11 and M1-12 calculated by Otsuka et al. (2014) have been applied in this work for consistency. These values were obtained by integrating under the spectrum in the wavelength range 5–200 μm, assisted by the use of photometric data points. However, no F_{IR} value was given for IC 2501 due to the lack of spectroscopic data from *Spitzer* IRS (only SH data are available). Few photometric data points are available from sources such as *IRAS* and *AKARI*, and as there are no data points around 30–50 μm it is difficult to determine the peak of the spectral energy distribution (SED). Hence, a range of G_0 values encompassing those of the other three PNe is assumed for IC 2501 in the following model predictions, in order to account for the large uncertainties.

6.4.3 Analysis of model outputs

Here, PDR model predictions are compared to observations through two different methods. The first method considers the [C II] / [O I] line intensity ratio, compared to the sum of the two intensity values divided by F_{IR}. The former quantity is a metric for the PDR density due to the different critical densities of the two lines (i.e. the densities above which the main source of emission changes from spontaneous radiative transitions to collisional de-excitations), which are respectively $\sim 1 \times 10^5$ cm^{-3} and $\sim 3 \times 10^3$ cm^{-3} for the [O I] 146 μm and [C II] 158 μm lines (e.g. Hollenbach and Tielens 1999; Malhotra et al. 2001; Stacey et al. 2010). The latter quantity represents the ratio of main cooling processes against the total infrared emission from around the PN. These lead to estimates for both G_0 and $n_{\rm H}$. These comparisons are displayed in Figure 6.13. With the exception of IC 2501, for which the [C II] / [O I] ratio

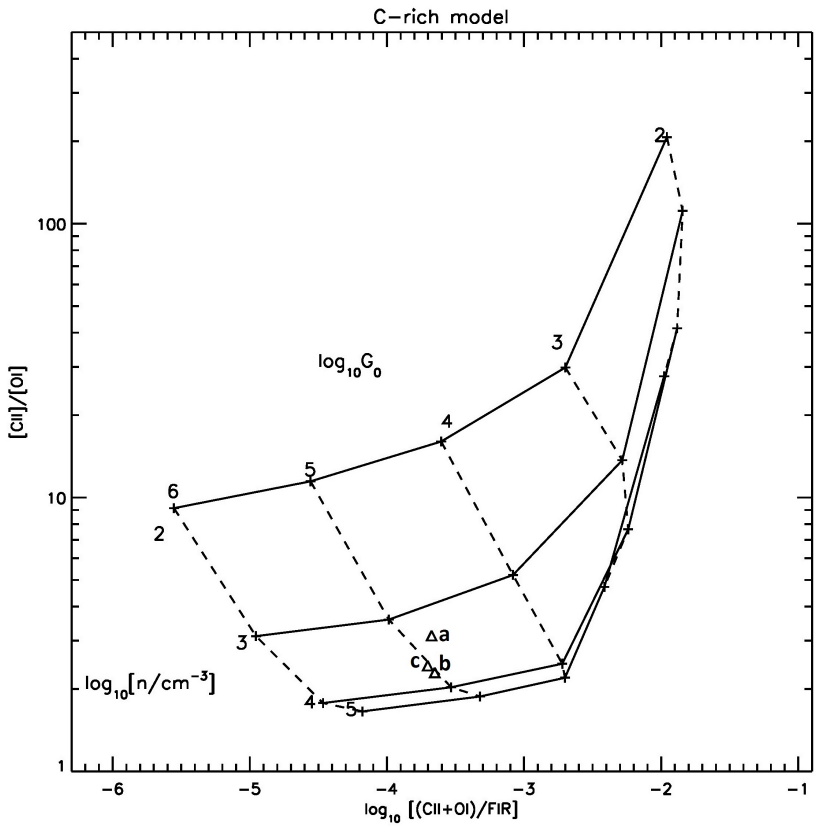

Fig. 6.13 Plot of the [C II] 158 μm / [O I] 146 μm line flux ratio against the sum of these two lines divided by the far-IR flux, compared to the PDR model of Fong et al. (2001).

was too low for the bounds of the model, the other three fullerene-containing PNe show very similar predictions for both density and G_0.

The second method takes advantage of the line intensities increasing with G_0 in order to estimate the PDR density. Figure 6.14 shows the intensities of the [O I] 146 μm and [C II] 158 μm lines compared to the G_0 values calculated from equation (6.2). The two examined lines originate from the PDR and are hence expected to show similar densities.

The results from both methods of applying the model are shown in Table 6.4. Both methods of interpreting the PDR model predictions show reasonable agreement for the density of M1-11, for which $\log(n_{\rm H}/{\rm cm}^{-3}) \sim 3.8$–$4.0$, whereas for M1-6 and M1-12 there are larger disagreements. For the two I vs. G_0 plots, there is good agreement between the two predicted densities in M1-11 and reasonable agreement in M1-12, though there is little agreement between those in IC 2501. This may be a result of the high intensities obtained from M1-11, and the somewhat unusual [C II] 158 μm / [O I] 146 μm ratio in IC 2501.

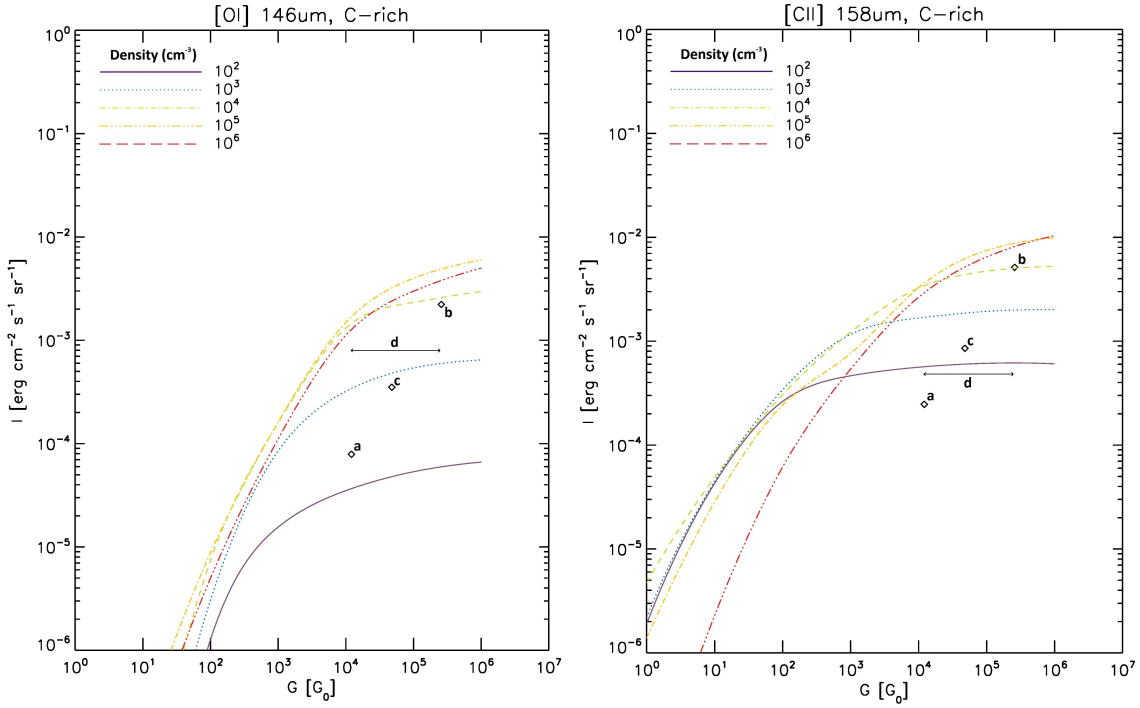

Fig. 6.14 Comparison of the [O I] 146 μm and [C II] 158 μm line flux values with the C-rich PDR model by W. Latter (Fong et al., 2001). Key: a = M1-6; b = M1-11; c = M1-12; d = IC 2501.

Table 6.4 The far-IR flux values of M1-6, M1-11 and M1-12 as given in Otsuka et al. (2014), the G_0 values calculated from these quantities, and model predictions of $n_{\rm H}$ and G_0 from Fong et al. (2001), as shown in Figures 6.13 and 6.14.

	$\log(F_{IR})$	$\log(G_0)$	Grid model		I vs. G_0: $\log(n_{\rm H})$	
PN	(W m^{-2})	(*)	$\log(n_H)$	$\log(G_0)$	[O I] 146 μm	[C II] 158 μm
M1-6	$-11.73^{(1)}$	4.083	3.3	4.8	2.3	<2
M1-11	$-11.01^{(1)}$	5.412	3.8	5.0	3.9	4.0
M1-12	$-11.74^{(1)}$	4.680	3.7	5.0	2.8	2.3
IC 2501	...	...	...	...	3.2–3.6	<2

Notes: (1) Otsuka et al. (2014). * G_0 given in units of 1.6×10^{-6} W m^{-2}. Logarithmic values have uncertainties of $\pm$ 0.2.

However, these methods of predicting the physical conditions are somewhat limited due to the lack of consideration of critical densities. Hence, the [C II] emission may not be suitable as a metric for determining the densities of PNe, and the [O I] plot in Figure 6.14 may provide more reliable predictions in this respect. The measured electron density values of the fullerene-containing PNe in this sample are all between 10^2 and 10^4 cm^{-3}, which is on the lower end of those expected for PNe.

6.5 Discussion and conclusions

The main aim of this work has been to obtain IFU spectra of the PDRs around four PNe with known C_{60} emission, in order to analyse the spatial morphologies of the environments in which fullerenes form and evolve. The intensities of the [O I] 146 μm and [C II] 158 μm lines were then used in a PDR model for C-rich evolved stars, in order to obtain the physical conditions of the regions in which the fullerenes are located.

The peaks of the [O I] and [C II] emission lines are centred close to those of the [O III] 52 μm emission from the ionised regions in M1-6 and IC 2501. In both cases, this [O III] line is observed to be rotating, whereas the cooling lines are not (except potentially for the [C II] line in IC 2501, though this particular case is likely an effect of relatively high noise). The cooling line emission in M1-11 and M1-12 also does not rotate. Indeed, the velocities of the cooling lines from all four sources are relatively uniform within the direction of our line of sight, and do not appear to take the form of outflows, hence these fullerene-containing PDRs are assumed to be quiescent.

Another key result of this chapter has come from comparing the predictions of the PDR model with those from the sample of C-rich and O-rich PNe studied by Bernard-Salas and Tielens (2005), the estimated hydrogen densities of the fullerene-containing PNe typically have lower values (10^2 to 10^4 cm^{-3}) than those predicted for the other sample (4×10^3 to $> 10^7$ cm^{-3}). This likely indicates that fullerene formation prefers environments with lower hydrogen densities. On the other hand, the G_0 values in this sample, ranging from $\log(G_0) \sim 4.0$–5.5, are relatively normal for PDRs around PNe (in accordance with the

sample of Bernard-Salas and Tielens 2005, with $\log(G_0) \sim 3.3$–6.9), and hence there is no relationship between the presence of fullerenes and the local UV radiation field.

With regard to the potential formation mechanisms of fullerenes, closed network growth scales with n^2 (where n is the density; e.g. Micelotta et al. 2012), hence this is unlikely to be a viable method of fullerene production due to the low densities observed in this sample of PNe. The top-down photo-processing method of forming fullerenes appears more likely, as this is dependent on the UV radiation field.

The IFU spectral maps have shown that the spatial distribution of the [O I] and [C II] emission in the PDRs of M1-6, M1-12 and IC 2501 are not consistent with one another. This is unexpected, as the two species represent the two strongest cooling species in these regions, and both require weak radiation fields. The [O I] 63 μm line is expected to be much stronger, and hence would have been a better metric for comparison. Ideally, a space telescope is required to detect this particular line, in order to avoid the need to remove data points due to atmospheric water corrections.

This is the first time in which PDRs around fullerene-containing PNe have been analysed both spatially and spectroscopically in order to interpret the physical conditions required for their formation. The eventual launch of *JWST* will provide access to near- and mid-IR integral field unit spectroscopy, from which the C_{60} emission can be directly mapped around these sources in the Milky Way and Magellanic Clouds. If accepted, *SPICA* will also be able to take IFU spectra from space for these cooling lines, including the strong [O I] 63 μm line.

Chapter 7

Conclusions and future work

At the beginning of Chapter 1, two major questions were posed:

- How does metallicity influence dust composition?
- How diverse is the chemistry of large organic molecules in circumstellar environments?

I have addressed these questions via a series of studies investigating planetary nebulae at low metallicity with the *Spitzer Space Telescope* and the *Stratospheric Observatory for Infrared Astronomy*. In § 7.1, the conclusions from each of the previous science chapters are recapped. These findings are put into context by answering the above questions in § 7.2. The future of this research is discussed in § 7.3 and some concluding remarks are given in § 7.4.

7.1 Summary of findings

In Chapter 3, the potential continuation of the Galactic abundance gradients of neon, sulphur and argon in the outskirts of the Milky Way, a region *a priori* assumed to be of low metallicity, were investigated from a sample of 23 PNe with the *Spitzer Space Telescope*. The main findings were:

- The continuations of the abundance gradients in the Galactic anti-centre were not agreed upon in the literature. This work showed that abundance gradients continued

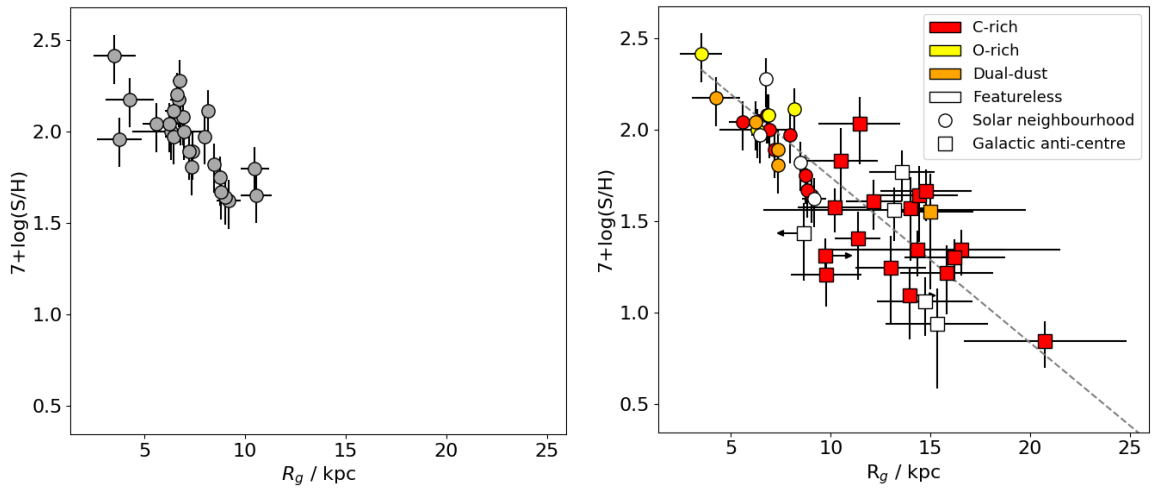

Fig. 7.1 The advancement of the Galactic abundance gradient of sulphur throughout this thesis. The plot on the left shows the knowledge of PNe within the Galactic disk before this thesis (Pottasch and Bernard-Salas, 2006), whereas the plot on the right includes these points (circles) alongside the anti-centre PNe investigated in Chapters 3 and 4 (squares). The observed dust compositions of all available sources are included. Some data points on the left are not included on the right, as their dust compositions are not obtainable due to lack of data from *Spitzer* IRS and *ISO* SWS (particularly SWS01). The same general trends are also observed for neon and argon.

beyond Galactocentric distances of $R_g \sim 20$ kpc, although the dispersion increased with distance, as shown in Figure 7.1.

- The metallicities in these regions reached values as low as the averages observed from the Magellanic Clouds ($\sim$ 1/3 and 1/6 $Z_\odot$ for the LMC and SMC, respectively).

- The sulphur anomaly was clearly observed when comparing the optical abundances of a sample of H II regions with the infrared abundances from the anti-centre PN sample. This was not observed when comparing the sulphur abundances of anti-centre PNe and H II regions that were both measured at IR wavelengths, though the H II region abundances may have been underestimated.

In Chapter 4, the dust emission in the same sample of PNe in the sub-solar metallicity Galactic anti-centre was analysed. The main results were:

- 78% of the PNe in the sample showed C-rich dust emission, only one of which also showed potential O-rich dust absorption.

- The emission of fullerenes and silicon carbide is more commonly observed towards the Galactic anti-centre and in the Magellanic Clouds than in the solar neighbourhood and towards the Galactic bulge, suggesting that the formation of these molecules is favoured in environments of sub-solar metallicity.

- For nine of the PNe, the main PAH emission features in the wavelength range 7–9 μm have been decomposed into four subcomponents. These trace the size, charge and structure of the molecules. The intensities of the 8.2 and 8.6 μm components show a strong positive correlation, which represents C–H bond movements indicating links between the number of bay regions and carbon atoms in the PAH molecules. The 7.6 and 8.6 μm components are also strongly correlated, likely representing PAH molecules with $\sim$ 50–110 carbon atoms and fewer bay regions.

In Chapter 5, the studies of the dust content and abundances in Galactic PNe of low metallicity were extended to the metal-poor Galactic halo, with the following results:

- Most of the PNe in the Galactic halo are O-rich.

- All of the C-rich sources show PAH emission of Class *B* or *D*. One source shows an as yet unclassified 6.2 μm profile, and another shows emission from both silicon carbide and PAHs.

- Of the four C-rich sources in the sample, two originate from globular clusters and another was tidally stripped from the Sagittarius dwarf spheroidal galaxy.

In Chapter 6, the PDRs of four Galactic planetary nebulae with known fullerene emission were studied with *SOFIA*, in order to characterise the environments in which these molecules form. Fullerenes are the largest known organic molecules, hence the investigation into their PDRs may provide insight into how many organic species form and evolve. The findings were as follows:

- The intensity maps of the two observed cooling lines from the PDR (namely [O I] at 146 μm and [C II] at 158 μm) showed that the emission was extended compared to the sizes of the sources. In three of the four PNe, the spatial morphologies of the two emission lines were different from each other.

- The velocity maps of these lines suggested that the PDRs around these fullerene-containing PNe are quiescent.

- A PDR model for C-rich evolved stars showed that the hydrogen densities of these PNe are low, ranging from $n_{\rm H} \sim 10^2$–10^4 cm^{-3}.

7.2 Overall conclusions

7.2.1 Influence of metallicity on dust composition

The studies of the sample of PNe from the Galactic anti-centre have shown that low metallicity favours C-rich dust production. This is because the oxygen abundances in these metal-poor stars are lower, and hence less carbon needs to be brought to the convective envelope of the star by the third dredge-up. An important caveat is that AGB stars may not be massive enough to efficiently dredge enough carbon up to the circumstellar envelope if the region is too metal-poor. Hence, the Galactic halo contains more O-rich PNe. It follows that the C-rich PNe in the halo are expected to have originated from elsewhere. The origins of three of the four sources investigated in the halo sample can be accounted for, whereas those of the C-rich halo PN H4-1 are unclear; its location does not coincide with the Sagittarius stream as with BoBn-1, and it does not originate from a globular cluster like K648 and GJJC-1.

There is also a greater chance to find a greater diversity of C-rich dust emission from around PNe in low metallicity regions than elsewhere, as explained below.

7.2.2 Diversity of large organic molecules

PAHs remained the most commonly observed carbonaceous emission features towards the Galactic anti-centre and halo, whereas SiC, fullerenes and the 30 μm features were detected in $\sim$ 20% of the anti-centre sample. All of the fullerene sources in this sample also showed the 30 μm feature, and many of these also showed SiC.

Of the PAH emission from the anti-centre sample, each of the 6.2, 7.7 and 8.6 μm features were of Classes *A* and *B* (as defined by Peeters et al. 2002), which are typical for those observed in PNe. The PAH profiles observed from the Galactic halo sample are distinctly different in some cases, as until now Class *D* emission (Matsuura et al., 2014) has only been observed from samples of PNe in the Magellanic Clouds. Hence, PAH emission of Class *D* is likely to be linked to regions with a particularly low metallicity. The two sources showing PAHs with these emission profiles are those located within globular clusters, which may also contribute to the origins of this profile.

The decomposition of the broad 7–9 μm PAH complex has been carried out for the first time with the anti-centre PNe. This has shown correlations which correspond with both quiescent (8.2 and 8.6 μm) and irradiated (7.6 and 8.6 μm) PDRs.

Regarding the environments in which fullerene features are observed, the [O I] 146 μm and [C II] 158 μm emission lines were used to predict the PDR densities from a model of these regions around C-rich evolved stars; similar G_0 and $n_{\rm H}$ values were obtained for the three PNe in which these quantities could be measured. The hydrogen density values are on the lower end of those expected for the PDRs around PNe, in accordance with Bernard-Salas and Tielens (2005). This may suggest that fullerenes are prefentially formed in PDRs where the hydrogen density is low, and hence the bottom-up fullerene formation mechanism of closed network growth cannot explain the formation of these molecules *in situ*. The low hydrogen densities of these environments are similar to those in which fullerenes were originally formed from the study of Kroto et al. (1985). The G_0 values of these sources were typical for PNe, suggesting that there is no relationship between the presence of fullerenes and the UV flux within a PDR.

7.3 Future work

7.3.1 The immediate future

Studies of the circumstellar gas around PNe provide accurate abundances for particular elements. However, the application of these abundances to studies of the Galactic metallicity gradient are somewhat inhibited by the large uncertainties attributed to the distances of these sources. Recently, the second data release of *Gaia* has provided parallax measurements for many Galactic sources, allowing for the refinement of these gradients.

While we wait for the launch of *JWST*, the archival data from *Spitzer* and *ISO* can be used to study the fractions of the total IR flux from features such as those from PAHs, SiC, fullerenes and the 30 μm feature, and how these features evolve with the star. This will be important for understanding the evolutionary links in the short, but important, transition period in which an AGB star becomes a planetary nebula.

A *SOFIA* proposal has been accepted to expand on the investigation into the physical conditions of PDRs around Galactic fullerene-containing PNe (PI: J. Cami), with the addition of two more sources to be observed with FIFI-LS (K3-62 and Hen 2-68). Photometric data for these PNe are also due to be obtained from the *High-resolution Airborne Wideband Camera-plus* (HAWC+) instrument, which takes diffraction-limited images in five wavelength bands between 50 and 240 μm; together with the FIFI-LS data, better estimates for the far-IR flux values of these PNe can be obtained by further constraining the Rayleigh-Jeans fit ($F_\lambda \propto \lambda^{-4}$) at redder wavelengths. From this, we can obtain more accurate values for G_0, and hence the ultraviolet radiation fields in the PDR can be further constrained, leading to a better understanding of the processing of organic molecules. These values can also be used in PDR models for improved calculations of $n_{\rm H}$ in these environments, improving our understanding of the physical conditions in these regions.

The study of dust emission in low metallicity regions of the Milky Way has been a major focus of this thesis. While this has all been written in the context of the mid-IR features of PAHs, fullerenes etc. around evolved stars, dust grains emit in a variety of environments.

For instance, protoplanetary disks show variations of PAH profiles similar to those observed around PNe (e.g. Berné et al. 2009; Seok and Li 2017). Hence, studies of dust emission around PNe can be extrapolated to various types of sources.

While not a focus of this thesis, a major question in astronomy regards the origins of dust. AGB stars are important contributors of interstellar dust, although there are other contributing sources such as supernovae and red supergiants (e.g. Boyer et al. 2012; Dharmawardena et al. 2018). To better understand the contributions from AGB stars, mass-loss rates are required; these can be inferred from sub-millimetre studies of the CO molecule, which can be observed from AGB envelopes with the *Atacama Large Millimeter/submillimeter Array* (ALMA). These studies can be extended to examining how mass-loss changes as a function of metallicity.

7.3.2 Longer term

The next few years promise significant advances in spectral resolution and sensitivity, allowing more in-depth infrared studies of sources in the Milky Way and the Local Group of galaxies, and providing the resources to investigate PNe at greater distances.

In particular, the *James Webb Space Telescope* (JWST), which is due for launch in March 2021 (at time of writing), will be able to observe at wavelengths of 0.6 to 28 μm, with a spectral resolution of R $\sim$ 1000 for the *Near-Infrared Spectrograph* (NIRSpec, 0.6–5 μm) and R $\sim$ 100 or 1500–3200 for the *Mid-Infrared Instrument* (MIRI, 5–28 μm). With its increased sensitivity over *Spitzer*, *JWST* will be able to carry out abundance and dust studies in more distant sources, enabling coverage of a broader range of parameter space. The near-IR wavelength range provides access to emission such as the 3.3 and 3.4 μm PAH and HAC features, enabling us to study how aliphatic and arophatic compounds (i.e. consisting of both rings and chains) evolve into aromatic structures in astronomical environments (e.g. García-Hernández et al. 2010; Micelotta et al. 2012; Scott and Duley 1996). *JWST* will also have IFU capabilities; *NIRSpec* offers a $3'' \times 3''$ field of view, whereas *MIRI* has four IFUs, with fields of view ranging from $3.9'' \times 3.9''$ to $7.7'' \times 7.7''$. Hence, for the first time Galactic PNe

can be spatially resolved at mid-IR wavelengths, allowing for the mapping of dust emission and providing the means to interpret how the dust evolves as a function of the local physical conditions traced by the gas.

The *Space Infrared Telescope for Cosmology and Astrophysics* (SPICA) is currently one of three candidates for the fifth medium-class mission run by the *European Space Agency* (ESA), as part of its *Cosmic Vision* program. It has been proposed that *SPICA* will launch (pending acceptance) in 2032. Its main science goals are to investigate the evolution of galaxies up to redshifts of $z \sim 3$, and to observe features for molecules such as water, CO, H_2 and those attributed to dust in proto-planetary disks. The instruments that are of particular interest to PN studies are the *SPICA Far-Infrared Instrument* (SAFARI) and the *SPICA Mid-Infrared Instrument* (SMI). *SAFARI* has a spectral wavelength range of 34–230 μm with $R \sim 300$ in low-resolution and $R \sim 3000$–11000 in high-resolution, whereas the *SMI* obtains spectra from 12–36 μm, reaching a maximum sensitivity of a few μJy and a resolution as high as $R \sim 28000$ [1]. Hence, *SPICA* will be able to determine the physical conditions in the PDRs of more distant PNe, which can provide a deeper understanding on the regions in which molecules and dust reside. The PDRs can be spatially mapped from the cooling line emission with even greater resolution than *SOFIA* currently offers. Dust will also be detectable at higher redshifts, which will be useful in determining its formation and evolution as galaxies evolve.

7.4 Concluding remarks

This thesis has shown that studies of the chemical composition of circumstellar material around PNe are important, as they probe the history of the local stellar environments. Most of the observed ionic emission originates from the outbursts of massive stars (e.g. supernovae), and the dust composition is largely dependent on the metallicity of the environment.

JWST will revolutionise the study of gas, dust and molecules in circumstellar environments, with its ability to physically map the dust emission in AGB stars and PNe within the Galaxy,

[1] http://www.spica-mission.org/index.html

while also being able to detect the dust emission in local extragalactic sources. If *SPICA* is approved, it will greatly enhance our knowledge of the physical conditions in which the diversity of carbonaceous dust emission can be located in the photodissociation regions of PNe.

Much of the material in the interstellar medium has been produced from evolved stars. Hence, by studying the molecules, gas and dust in the circumstellar envelopes of AGB stars and PNe, we are learning about the material that enriches the ISM. Here, this material can contribute to the formation of new stars, which can be traced by the emission of PAHs in these interstellar environments. The applications of the science carried out on this circumstellar material are far-reaching and may benefit many areas of astronomy.

Appendix A

Spitzer IRS spectra of Galactic anti-centre PNe

The spectra of the 23 PNe analysed in Chapters 2 and 3 are shown in Figure A.1. The full 5–37 μm spectra are shown on the left of the figure, which include SL, SH and LH data. The SL data are shown on the right.

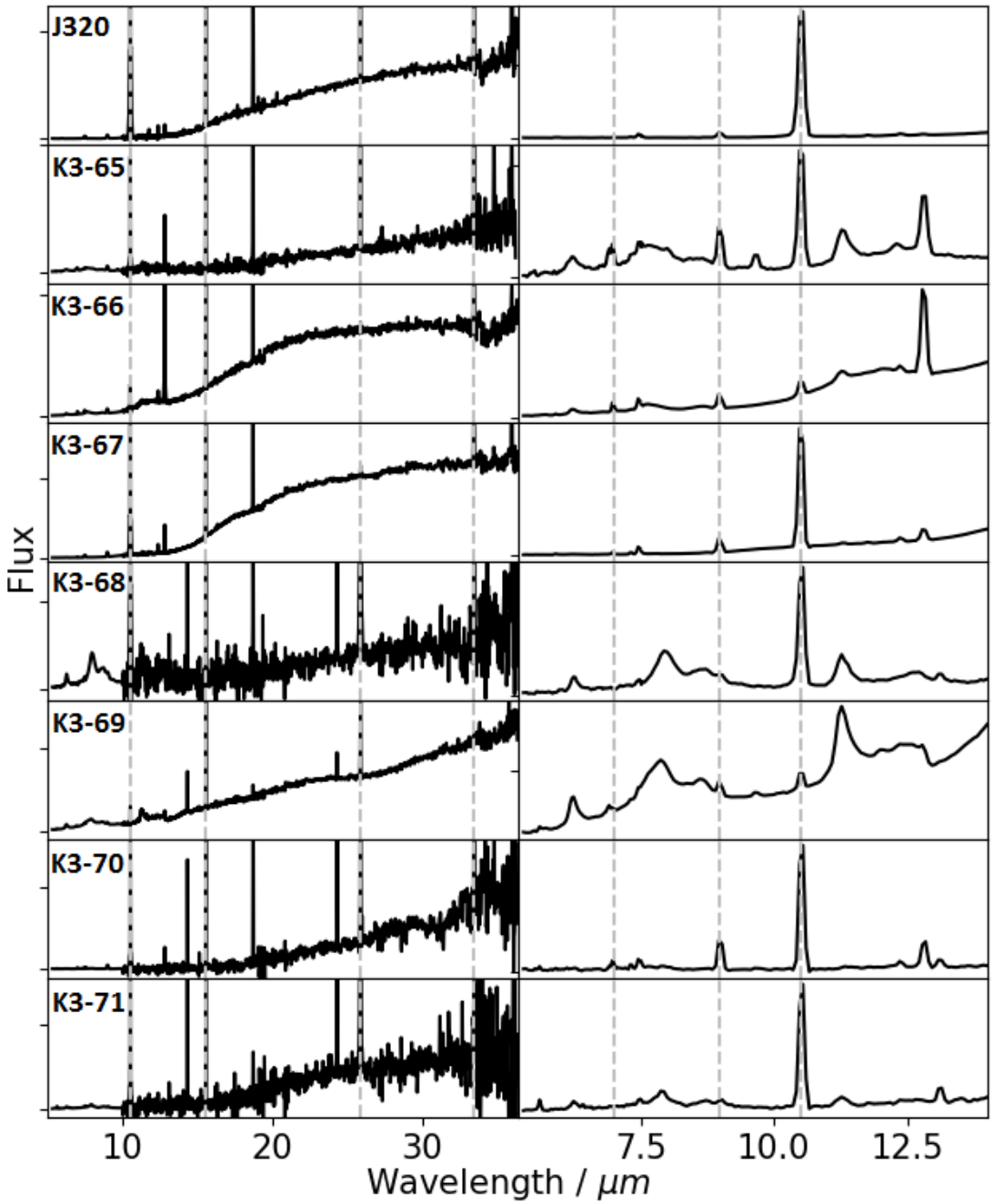

Fig. A.1 The 5–37 μm spectra of each of the 23 PNe. Dashed lines show a selection of strong atomic lines: 6.99 μm [Ar II]; 8.99 μm [Ar III]; 10.51 μm [S IV]; 15.56 μm [Ne III]; 25.89 μm [O IV]; 33.48 μm [S III]. Continued over next two pages.

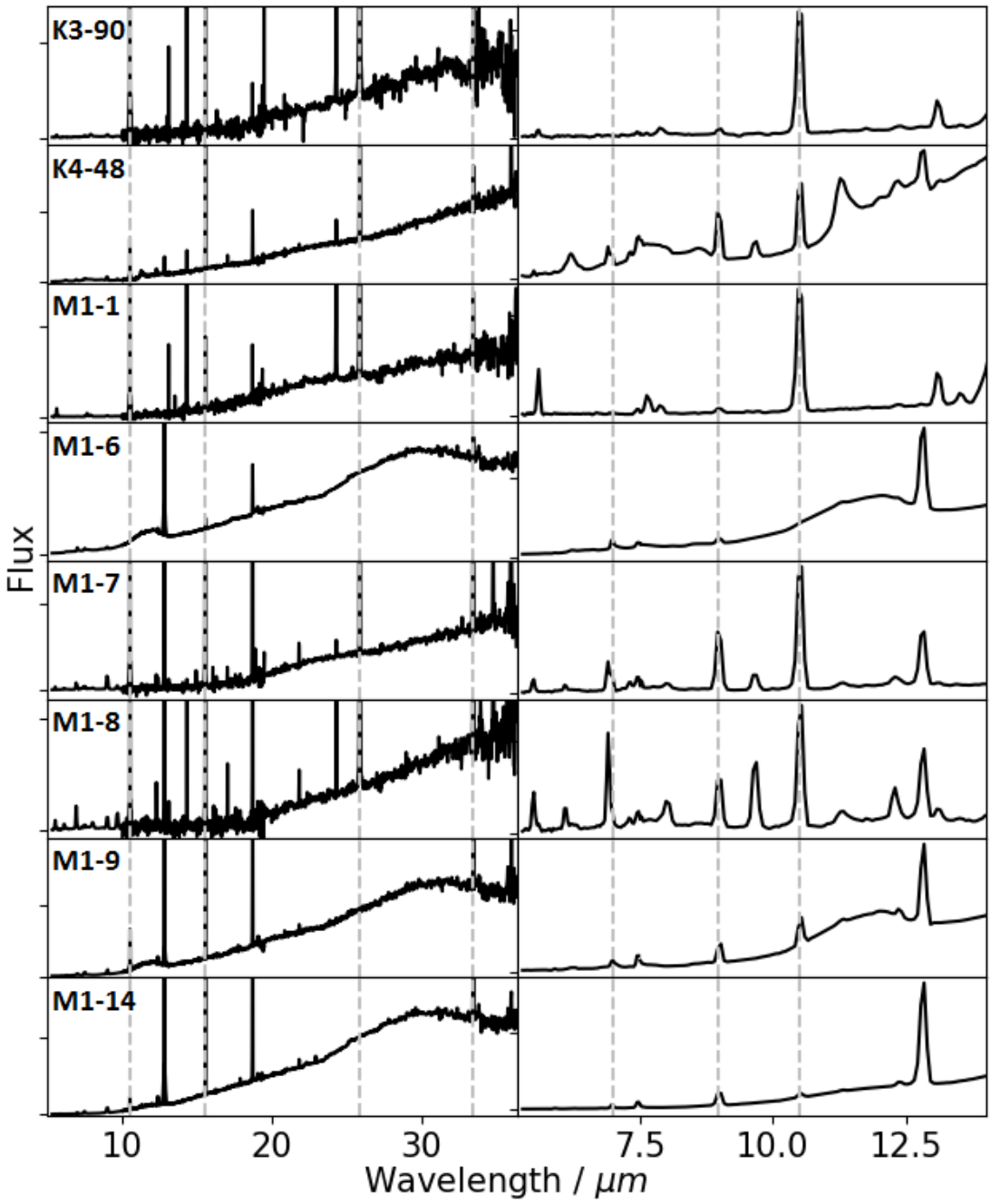

Fig. A.1 (Continued)

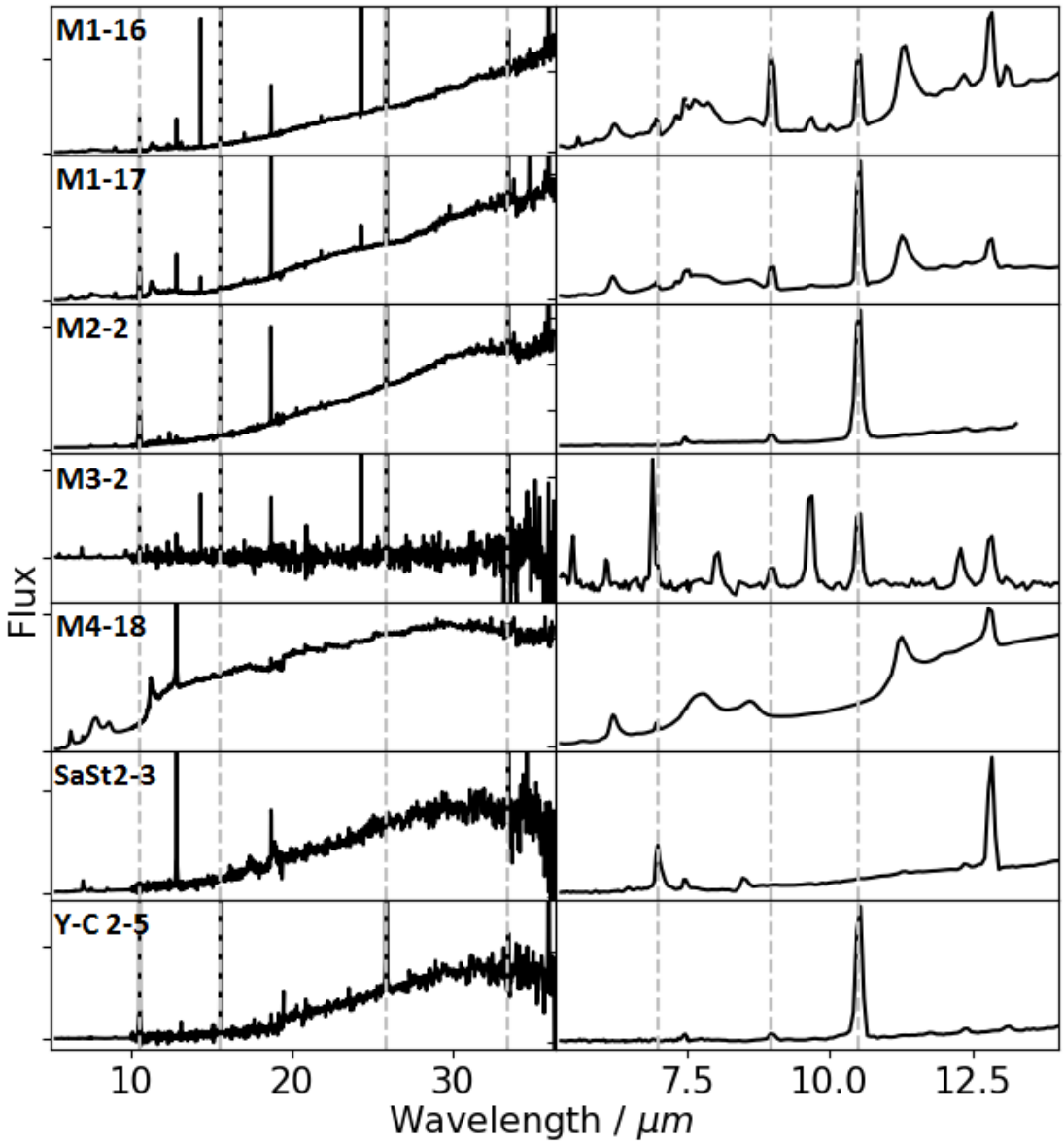

Fig. A.1 (Continued)

References

Abate, C., Pols, O. R., Karakas, A. I., and Izzard, R. G. (2015). Carbon-enhanced metal-poor stars: a window on AGB nucleosynthesis and binary evolution. I. Detailed analysis of 15 binary stars with known orbital periods. *A&A*, 576:A118.

Acker, A., Marcout, J., Ochsenbein, F., Stenholm, B., Tylenda, R., and Schohn, C. (1992). *The Strasbourg-ESO Catalogue of Galactic Planetary Nebulae. Parts I, II.*

Acker, A., Raytchev, B., Stenholm, B., and Tylenda, R. (1991). The absolute H-beta fluxes for galactic planetary nebulae. *A&AS*, 90:89.

Aitken, D. K. and Roche, P. F. (1982). 8-13 micron spectrophotometry of compact planetary nebulae and emission line objects. *MNRAS*, 200:217.

Akashi, M. and Soker, N. (2017). Shaping planetary nebulae with jets in inclined triple stellar systems. *MNRAS*, 469:3296.

Aksaker, N., Yerli, S. K., Kızıloğlu, Ü., and Atalay, B. (2015). Emission-Line Fluxes of Northern Planetary Nebulae. *PASA*, 32:e003.

Allain, T., Leach, S., and Sedlmayr, E. (1996). Photodestruction of PAHs in the interstellar medium. I. Photodissociation rates for the loss of an acetylenic group. *A&A*, 305:602.

Allamandola, L. J., Hudgins, D. M., and Sandford, S. A. (1999). Modeling the Unidentified Infrared Emission with Combinations of Polycyclic Aromatic Hydrocarbons. *ApJL*, 511:L115.

Aller, L. H. and Czyzak, S. J. (1983). Chemical compositions of planetary nebulae. *ApJS*, 51:211.

Aller, L. H. and Keyes, C. D. (1987). A spectroscopic survey of 51 planetary nebulae. *ApJS*, 65:405.

Aller, L. H., Keyes, C. D., and Feibelman, W. A. (1986). Ultraviolet Spectrum and Probable Chemical Composition of the High-Excitation Planetary Nebula M1-1. *Proceedings of the National Academy of Science*, 83:2777.

Alves, D. R., Bond, H. E., and Livio, M. (2000). Hubble Space Telescope Observations of the Planetary Nebula K648 in the Globular Cluster M15. *AJ*, 120:2044.

Anders, F., Chiappini, C., Minchev, I., Miglio, A., Montalbán, J., Mosser, B., Rodrigues, T. S., Santiago, B. X., Baudin, F., Beers, T. C., da Costa, L. N., García, R. A., García-Hernández, D. A., Holtzman, J., Maia, M. A. G., Majewski, S., Mathur, S., Noels-Grotsch, A., Pan, K., Schneider, D. P., Schultheis, M., Steinmetz, M., Valentini, M., and Zamora, O. (2017). Red giants observed by CoRoT and APOGEE: The evolution of the Milky Way's radial metallicity gradient. *A&A*, 600:A70.

Andrievsky, S. M., Bersier, D., Kovtyukh, V. V., Luck, R. E., Maciel, W. J., Lépine, J. R. D., and Beletsky, Y. V. (2002a). Using Cepheids to determine the galactic abundance gradient. II. Towards the galactic center. *A&A*, 384:140.

Andrievsky, S. M., Kovtyukh, V. V., Luck, R. E., Lépine, J. R. D., Bersier, D., Maciel, W. J., Barbuy, B., Klochkova, V. G., Panchuk, V. E., and Karpischek, R. U. (2002b). Using Cepheids to determine the galactic abundance gradient. I. The solar neighbourhood. *A&A*, 381:32.

Andrievsky, S. M., Kovtyukh, V. V., Luck, R. E., Lépine, J. R. D., Maciel, W. J., and Beletsky, Y. V. (2002c). Using Cepheids to determine the galactic abundance gradient. III. First results for the outer disc. *A&A*, 392:491.

Asplund, M., Grevesse, N., and Sauval, A. J. (2005). The Solar Chemical Composition. In Barnes, III, T. G. and Bash, F. N., editors, *Cosmic Abundances as Records of Stellar Evolution and Nucleosynthesis*, volume 336 of *Astronomical Society of the Pacific Conference Series*, page 25.

Asplund, M., Grevesse, N., Sauval, A. J., and Scott, P. (2009). The Chemical Composition of the Sun. *ARA&A*, 47:481.

Atkins, P. W. and de Paula, J. (2002). *Physical Chemistry*. Oxford University Press, 7th edition.

Bakes, E. L. O. and Tielens, A. G. G. M. (1994). The Photoelectric Heating Mechanism for Very Small Graphitic Grains and Polycyclic Aromatic Hydrocarbons. *ApJ*, 427:822.

Balick, B. (1987). The Evolution of Planetary Nebulae. I. Structures, Ionizations, and Morphological Sequences. *AJ*, 94:671.

Barker, T. (1980). The ionization structure of the ring nebula. I - Sulfur and argon. *ApJ*, 240:99.

Bauschlicher, Jr., C. W., Peeters, E., and Allamandola, L. J. (2008). The Infrared Spectra of Very Large, Compact, Highly Symmetric, Polycyclic Aromatic Hydrocarbons (PAHs). *ApJ*, 678:316.

Bauschlicher, Jr., C. W., Peeters, E., and Allamandola, L. J. (2009). The Infrared Spectra of Very Large Irregular Polycyclic Aromatic Hydrocarbons (PAHs): Observational Probes of Astronomical PAH Geometry, Size, and Charge. *ApJ*, 697:311.

Becker, S. A. and Iben, Jr., I. (1979). The asymptotic giant branch evolution of intermediate-mass stars as a function of mass and composition. I - Through the second dredge-up phase. *ApJ*, 232:831.

Belloche, A., Garrod, R. T., Müller, H. S. P., and Menten, K. M. (2014). Detection of a branched alkyl molecule in the interstellar medium: iso- propyl cyanide. *Science*, 345:1584.

Belloche, A., Garrod, R. T., Müller, H. S. P., Menten, K. M., Comito, C., and Schilke, P. (2009). Increased complexity in interstellar chemistry: detection and chemical modeling of ethyl formate and n-propyl cyanide in Sagittarius B2(N). *A&A*, 499:215.

Bernard-Salas, J. (2003). *Physics and Chemistry of Gas in Planetary Nebulae*. PhD thesis, University of Groningen, The Netherlands.

Bernard-Salas, J., Cami, J., Peeters, E., Jones, A. P., Micelotta, E. R., and Groenewegen, M. A. T. (2012). On the Excitation and Formation of Circumstellar Fullerenes. *ApJ*, 757:41.

Bernard-Salas, J., Peeters, E., Sloan, G. C., Cami, J., Guiles, S., and Houck, J. R. (2006). The Spitzer IRS spectrum of SMP LMC 11. *ApJ*, 652:L29.

Bernard-Salas, J., Peeters, E., Sloan, G. C., Gutenkunst, S., Matsuura, M., Tielens, A. G. G. M., Zijlstra, A. A., and Houck, J. R. (2009). Unusual Dust Emission from Planetary Nebulae in the Magellanic Clouds. *ApJ*, 699:1541.

Bernard-Salas, J., Pottasch, S. R., Beintema, D. A., and Wesselius, P. R. (2001). The ISO-SWS spectrum of planetary nebula NGC 7027. *A&A*, 367:949.

Bernard-Salas, J., Pottasch, S. R., Gutenkunst, S., Morris, P. W., and Houck, J. R. (2008). Neon and Sulfur Abundances of Planetary Nebulae in the Magellanic Clouds. *ApJ*, 672:274.

Bernard-Salas, J. and Tielens, A. G. G. M. (2005). Physical conditions in Photo-Dissociation Regions around Planetary Nebulae. *A&A*, 431:523.

Berné, O., Joblin, C., Fuente, A., and Ménard, F. (2009). What can we learn about protoplanetary disks from analysis of mid- infrared carbonaceous dust emission? *A&A*, 495:827.

Berné, O., Montillaud, J., and Joblin, C. (2015). Top-down formation of fullerenes in the interstellar medium. *A&A*, 577:A133.

Berné, O., Mulas, G., and Joblin, C. (2013). Interstellar C_{60}^{+}. *A&A*, 550:L4.

Berné, O. and Tielens, A. G. G. M. (2012). Formation of buckminsterfullerene (C60) in interstellar space. *Proceedings of the National Academy of Science*, 109:401.

Bianchi, L., Bohlin, R., Catanzaro, G., Ford, H., and Manchado, A. (2001). Hubble Space Telescope and Ground-based Spectroscopy of K648 in M15. *AJ*, 122:1538.

Black, J. H. and Dalgarno, A. (1977). Models of interstellar clouds. I. The Zeta Ophiuchi cloud. *ApJS*, 34:405.

Bocchio, M., Jones, A. P., and Slavin, J. D. (2014). A re-evaluation of dust processing in supernova shock waves. *A&A*, 570:A32.

Boersma, C., Bauschlicher, C. W., Allamandola, L. J., Ricca, A., Peeters, E., and Tielens, A. G. G. M. (2010). The 15-20 μm PAH emission features: probes of individual PAHs? *A&A*, 511:A32.

Böhm-Vitense, E. (1958). Über die Wasserstoffkonvektionszone in Sternen verschiedener Effektivtemperaturen und Leuchtkräfte. Mit 5 Textabbildungen. *ZA*, 46:108.

Bond, H. E. and Livio, M. (1990). Morphologies of Planetary Nebulae Ejected by Close-Binary Nuclei. *ApJ*, 355:568.

Borkowski, K. J. and Harrington, J. P. (1991). A grain-heated, dusty planetary nebula in M22. *ApJ*, 379:168.

Bovy, J., Rix, H.-W., Liu, C., Hogg, D. W., Beers, T. C., and Lee, Y. S. (2012). The Spatial Structure of Mono-abundance Sub-populations of the Milky Way Disk. *ApJ*, 753:148.

Boyer, M. L., Srinivasan, S., Riebel, D., McDonald, I., van Loon, J. T., Clayton, G. C., Gordon, K. D., Meixner, M., Sargent, B. A., and Sloan, G. C. (2012). The Dust Budget of the Small Magellanic Cloud: Are Asymptotic Giant Branch Stars the Primary Dust Source at Low Metallicity? *ApJ*, 748:40.

Boyer, M. L., Woodward, C. E., van Loon, J. T., Gordon, K. D., Evans, A., Gehrz, R. D., Helton, L. A., and Polomski, E. F. (2006). Stellar Populations and Mass Loss in M15: A Spitzer Space Telescope Detection of Dust in the Intracluster Medium. *AJ*, 132:1415.

Burton, M. G., Hollenbach, D. J., and Tielens, A. G. G. M. (1990). Line Emission from Clumpy Photodissociation Regions. *ApJ*, 365:620.

Butler, K. and Zeippen, C. J. (1994). Atomic data from the IRON Project. V. Effective collision strengths for transitions in the ground configuration of oxygen-like ions. *A&AS*, 108:1.

Calvet, N. and Peimbert, M. (1983). Bipolar nebulae and Type I planetary nebulae. *RMxAA*, 5:319.

Cami, J., Bernard-Salas, J., Peeters, E., and Malek, S. E. (2010). Detection of C_{60} and C_{70} in a Young Planetary Nebula. *Science*, 329:1180.

Campbell, E. K., Holz, M., Gerlich, D., and Maier, J. P. (2015). Laboratory confirmation of C_{60}^+ as the carrier of two diffuse interstellar bands. *Nature*, 523:322.

Candian, A., Kerr, T. H., Song, I.-O., McCombie, J., and Sarre, P. J. (2012). Spatial distribution and interpretation of the 3.3 μm PAH emission band of the Red Rectangle. *MNRAS*, 426:389.

Canning, R. E. A., Ryon, J. E., Gallagher, J. S., Kotulla, R., O'Connell, R. W., Fabian, A. C., Johnstone, R. M., Conselice, C. J., Hicks, A., Rosario, D., and Wyse, R. F. G. (2014). Filamentary star formation in NGC 1275. *MNRAS*, 444:336.

Cardiel, N., Elbaz, D., Schiavon, R. P., Willmer, C. N. A., Koo, D. C., Phillips, A. C., Gallego, J., and Ranalli, P. (2003). Comparing sfr indicators from multiwavelength data in galaxies at intermediate redshifts. In Gallego, J., Zamorano, J., and Cardiel, N., editors, *Highlights of Spanish Astrophysics III*, page 39. Kluwer Academic Publishers.

Carpentier, Y., Féraud, G., Dartois, E., Brunetto, R., Charon, E., Cao, A.-T., d'Hendecourt, L., Bréchignac, P., Rouzaud, J.-N., and Pino, T. (2012). Nanostructuration of carbonaceous dust as seen through the positions of the 6.2 and 7.7 μm AIBs. *A&A*, 548:A40.

Carrasco, L., Serrano, A., and Costero, R. (1983). Photoelectric Absolute H-Beta Fluxes for 55 Planetary Nebulae. *RMxAA*, 8:187.

Casassus, S., Roche, P. F., Aitken, D. K., and Smith, C. H. (2001a). 8-13 μm dust emission features in Galactic bulge planetary nebulae. *MNRAS*, 327:744.

Casassus, S., Roche, P. F., Aitken, D. K., and Smith, C. H. (2001b). The Galactic disc distribution of planetary nebulae with warm dust emission features - I. *MNRAS*, 320:424.

Castellanos, P., Berné, O., Sheffer, Y., Wolfire, M. G., and Tielens, A. G. G. M. (2014). C_{60} in Photodissociation Regions. *ApJ*, 794:83.

Castro-Carrizo, A., Bujarrabal, V., Fong, D., Meixner, M., Tielens, A. G. G. M., Latter, W. B., and Barlow, M. J. (2001). Low-excitation atomic gas around evolved stars. II. ISO observations of O-rich nebulae. *A&A*, 367:674.

Cerrigone, L., Hora, J. L., Umana, G., and Trigilio, C. (2009). Spitzer Detection of Polycyclic Aromatic Hydrocarbons and Silicate Features in Post-AGB Stars and Young Planetary Nebulae. *ApJ*, 703:585.

Chen, Z., Nordhaus, J., Frank, A., Blackman, E. G., and Balick, B. (2016). Three-dimensional hydrodynamic simulations of L_2 Puppis. *MNRAS*, 460:4182.

Chesneau, O., Lykou, F., Balick, B., Lagadec, E., Matsuura, M., Smith, N., Spang, A., Wolf, S., and Zijlstra, A. A. (2007). A silicate disk in the heart of the Ant. *A&A*, 473:L29.

Chiappini, C., Matteucci, F., and Gratton, R. (1997). The Chemical Evolution of the Galaxy: The Two-Infall Model. *ApJ*, 477:765.

Chiappini, C., Matteucci, F., and Romano, D. (2001). Abundance Gradients and the Formation of the Milky Way. *ApJ*, 554:1044.

Chokshi, A., Tielens, A. G. G. M., Werner, M., and Castelaz, M. W. (1988). C II 158 Micron and O i 63 Micron Observations of NGC 7023: A Model for Its Photodisscoiation Region. *ApJ*, 334:803.

Chou, M.-Y., Majewski, S. R., Cunha, K., Smith, V. V., Patterson, R. J., Martínez-Delgado, D., Law, D. R., Crane, J. D., Muñoz, R. R., Garcia López, R., Geisler, D., and Skrutskie, M. F. (2007). A 2MASS All-Sky View of the Sagittarius Dwarf Galaxy. V. Variation of the Metallicity Distribution Function along the Sagittarius Stream. *ApJ*, 670:346.

Clarkson, W., Sahu, K., Anderson, J., Smith, T. E., Brown, T. M., Rich, R. M., Casertano, S., Bond, H. E., Livio, M., Minniti, D., Panagia, N., Renzini, A., Valenti, J., and Zoccali, M. (2008). Stellar Proper Motions in the Galactic Bulge from Deep Hubble Space Telescope ACS WFC Photometry. *ApJ*, 684:1110.

Condon, J. J. and Kaplan, D. L. (1998). Planetary Nebulae in the NRAO VLA Sky Survey. *ApJS*, 117:361.

Cordiner, M. A., Cox, N. L. J., Lallement, R., Najarro, F., Cami, J., Gull, T. R., Foing, B. H., Linnartz, H., Lindler, D. J., Proffitt, C. R., Sarre, P. J., and Charnley, S. B. (2017). Searching for Interstellar C_{60}^{+} Using a New Method for High Signal-to-noise HST/STIS Spectroscopy. *ApJ*, 843:L2.

Costa, R. D. D., Chiappini, C., Maciel, W. J., and de Freitas Pacheco, J. A. (1996). New abundances of southern planetary nebulae. *A&AS*, 116:249.

Costa, R. D. D., Uchida, M. M. M., and Maciel, W. J. (2004). Chemical abundances of planetary nebulae towards the Galactic anticenter. *A&A*, 423:199.

Cox, P., Huggins, P. J., Maillard, J. P., Habart, E., Morisset, C., Bachiller, R., and Forveille, T. (2002). High resolution near-infrared spectro-imaging of NGC 7027. *A&A*, 384:603.

Crowther, P. A. (2007). Physical Properties of Wolf-Rayet Stars. *ARA&A*, 45:177.

Cuisinier, F., Acker, A., and Koeppen, J. (1996). Spectrophotometric observations of planetary nebulae high above the Galactic plane. *A&A*, 307:215.

Curtis, H. D. (1918). The Planetary Nebulae. *Publications of Lick Observatory*, 13:55.

Da Costa, G. S., Held, E. V., Saviane, I., and Gullieuszik, M. (2009). M22: An [Fe/H] Abundance Range Revealed. *ApJ*, 705:1481.

de Freitas Pacheco, J. A., Maciel, W. J., Costa, R. D. D., and Barbuy, B. (1991). Abundances of southern type I planetary nebulae. *A&A*, 250:159.

De Marco, O. and Crowther, P. A. (1999). M4-18: the planetary nebula and its WC10 central star. *MNRAS*, 306:931.

Delgado-Inglada, G., Morisset, C., and Stasińska, G. (2014). Ionization correction factors for planetary nebulae - I. Using optical spectra. *MNRAS*, 440:536.

Delgado-Inglada, G. and Rodríguez, M. (2014). C/O Abundance Ratios, Iron Depletions, and Infrared Dust Features in Galactic Planetary Nebulae. *ApJ*, 784:173.

Delgado-Inglada, G., Rodríguez, M., Peimbert, M., Stasińska, G., and Morisset, C. (2015). Oxygen enrichment in carbon-rich planetary nebulae. *MNRAS*, 449:1797.

Dharmawardena, T. E., Kemper, F., Scicluna, P., Wouterloot, J. G. A., Trejo, A., Srinivasan, S., Cami, J., Zijlstra, A., and Marshall, J. P. (2018). Extended dust emission from nearby evolved stars. *MNRAS*, 479:536.

Dinerstein, H. L. (1980). Infrared line measurements and the abundance of sulfur in planetary nebulae. *ApJ*, 237:486.

Dinerstein, H. L., Richter, M. J., Lacy, J. H., and Sellgren, K. (2003). Observations of [S IV] 10.5 μm and [Ne II] 12.8 μm in Two Halo Planetary Nebulae: Implications for Chemical Self-Enrichment. *AJ*, 125:265.

Djorgovski, S. and King, I. R. (1986). A Preliminary Survey of Collapsed Cores in Globular Clusters. *ApJ*, 305:L61.

Doan, L., Ramstedt, S., Vlemmings, W. H. T., Höfner, S., De Beck, E., Kerschbaum, F., Lindqvist, M., Maercker, M., Mohamed, S., Paladini, C., and Wittkowski, M. (2017). The extended molecular envelope of the asymptotic giant branch star π^1 Gruis as seen by ALMA. I. Large- scale kinematic structure and CO excitation properties. *A&A*, 605:A28.

Draine, B. T. (1980). Interstellar shock waves with magnetic precursors. *ApJ*, 241:1021.

Draine, B. T. (1995). Grain Destruction in Interstellar Shock Waves. *Ap&SS*, 233:111.

Duley, W. W. and Williams, D. A. (1983). A 3.4 micron absorption band in amorphous carbon Implications for interstellar dust. *MNRAS*, 205:67P.

Dunk, P. W., Kaiser, N. K., Hendrickson, C. L., Quinn, J. P., Ewels, C. P., Nakanishi, Y., Sasaki, Y., Shinohara, H., Marshall, A. G., and Kroto, H. W. (2012a). Closed network growth of fullerenes. *Nature Communications*, 3:855.

Dunk, P. W., Kaiser, N. K., Mulet-Gas, M., Rodríguez-Fortea, A., Poblet, J. M., Shinohara, H., Hendrickson, C. L., Marshall, A. G., and Kroto, H. W. (2012b). The smallest stable fullerene, m@c28 (m = ti, zr, u): Stabilization and growth from carbon vapor. *Journal of the American Chemical Society*, 134(22):9380. PMID: 22519801.

Elliot, J. L., Dunham, E., and Mink, D. (1977). The rings of Uranus. *Nature*, 267:328.

Elliot, J. L., Dunham, E. W., Bosh, A. S., Slivan, S. M., Young, L. A., Wasserman, L. H., and Millis, R. L. (1989). Pluto's atmosphere. *Icarus*, 77:148.

Endres, C. P., Schlemmer, S., Schilke, P., Stutzki, J., and MÃŒller, H. S. (2016). The cologne database for molecular spectroscopy, cdms, in the virtual atomic and molecular data centre, vamdc. *Journal of Molecular Spectroscopy*, 327:95. New Visions of Spectroscopic Databases, Volume II.

Erickson, E. F. (1992). SOFIA - Stratospheric Observatory For Infrared Astronomy. *Space Science Reviews*, 61:61.

Esteban, C., Fang, X., García-Rojas, J., and Toribio San Cipriano, L. (2017). The radial abundance gradient of oxygen towards the Galactic anti-centre. *MNRAS*, 471:987.

Esteban, C., García-Rojas, J., and Pérez-Mesa, V. (2015). The radial abundance gradient of chlorine in the Milky Way. *MNRAS*, 452:1553.

Evans, A., Stickel, M., van Loon, J. T., Eyres, S. P. S., Hopwood, M. E. L., and Penny, A. J. (2003). Far infra-red emission from NGC 7078: First detection of intra-cluster dust in a globular cluster. *A&A*, 408:L9.

Exter, K. M., Barlow, M. J., and Walton, N. A. (2004). The abundance distributions of Galactic bulge and disc planetary nebulae. *MNRAS*, 349:1291.

Fajardo-Acosta, S., Carey, S., Helou, G., Hurt, R., Rebull, L., Soifer, B. T., Squires, G., and Storrie-Lombardi, L. (2007). Hot Science With A "warm" Telescope: Galactic Studies With The Spitzer "warm" Mission. In *American Astronomical Society Meeting Abstracts*, volume 39 of *Bulletin of the American Astronomical Society*, page 763.

Falceta-Gonçalves, D. and Monteiro, H. (2014). On the alignment of PNe and local magnetic field at the Galactic centre: magnetohydrodynamical numerical simulations. *MNRAS*, 438:2853.

Fazio, G. G., Hora, J. L., Allen, L. E., Ashby, M. L. N., Barmby, P., Deutsch, L. K., Huang, J.-S., Kleiner, S., Marengo, M., Megeath, S. T., Melnick, G. J., Pahre, M. A., Patten, B. M., Polizotti, J., Smith, H. A., Taylor, R. S., Wang, Z., Willner, S. P., Hoffmann, W. F., Pipher, J. L., Forrest, W. J., McMurty, C. W., McCreight, C. R., McKelvey, M. E., McMurray, R. E., Koch, D. G., Moseley, S. H., Arendt, R. G., Mentzell, J. E., Marx, C. T., Losch, P., Mayman, P., Eichhorn, W., Krebs, D., Jhabvala, M., Gezari, D. Y., Fixsen, D. J., Flores, J., Shakoorzadeh, K., Jungo, R., Hakun, C., Workman, L., Karpati, G., Kichak, R., Whitley, R., Mann, S., Tollestrup, E. V., Eisenhardt, P., Stern, D., Gorjian, V., Bhattacharya, B., Carey, S., Nelson, B. O., Glaccum, W. J., Lacy, M., Lowrance, P. J., Laine, S., Reach, W. T., Stauffer, J. A., Surace, J. A., Wilson, G., Wright, E. L., Hoffman, A., Domingo, G., and Cohen, M. (2004). The Infrared Array Camera (IRAC) for the Spitzer Space Telescope. *ApJS*, 154:10.

Ferland, G. J., Chatzikos, M., Guzmán, F., Lykins, M. L., van Hoof, P. A. M., Williams, R. J. R., Abel, N. P., Badnell, N. R., Keenan, F. P., Porter, R. L., and Stancil, P. C. (2017). The 2017 Release Cloudy. *RMxAA*, 53:385.

Ferland, G. J., Korista, K. T., Verner, D. A., Ferguson, J. W., Kingdon, J. B., and Verner, E. M. (1998). CLOUDY 90: Numerical Simulation of Plasmas and Their Spectra. *PASP*, 110:761.

Ferland, G. J., Porter, R. L., van Hoof, P. A. M., Williams, R. J. R., Abel, N. P., Lykins, M. L., Shaw, G., Henney, W. J., and Stancil, P. C. (2013). The 2013 Release of Cloudy. *RMxAA*, 49:137.

Fernández-Martín, A., Pérez-Montero, E., Vílchez, J. M., and Mampaso, A. (2017). Chemical distribution of h ii regions towards the galactic anticentre. *A&A*, 597:A84.

Fitzsimmons, A., Dufton, P. L., and Rolleston, W. R. J. (1992). A comparison of oxygen and nitrogen abundances in young clusters and associations and in the interstellar gas. *MNRAS*, 259:489.

Fluks, M. A., Plez, B., The, P. S., de Winter, D., Westerlund, B. E., and Steenman, H. C. (1994). On the spectra and photometry of M-giant stars. *A&AS*, 105:311.

Foing, B. H. and Ehrenfreund, P. (1994). Detection of two interstellar absorption bands coincident with spectral features of C_{60}^{+}. *Nature*, 369:296.

Fong, D., Meixner, M., Castro-Carrizo, A., Bujarrabal, V., Latter, W. B., Tielens, A. G. G. M., Kelly, D. M., and Sutton, E. C. (2001). Low-excitation atomic gas around evolved stars. I. ISO observations of C-rich nebulae. *A&A*, 367:652.

French, H. B. (1981). The ionization structure and abundance of argon in gaseous nebulae. *ApJ*, 246:434.

Frew, D. J., Bojičić, I. S., and Parker, Q. A. (2013). A catalogue of integrated Hα fluxes for 1258 Galactic planetary nebulae. *MNRAS*, 431:2.

Frew, D. J., Parker, Q. A., and Bojičić, I. S. (2016). The Hα surface brightness-radius relation: a robust statistical distance indicator for planetary nebulae. *MNRAS*, 455:1459.

Friel, E. D. (1995). The Old Open Clusters Of The Milky Way. *ARA&A*, 33:381.

Frogel, J. A., Cohen, J. G., and Persson, S. E. (1983). Globular cluster giant branches and the metallicity scale. *ApJ*, 275:773.

Fulbright, J. P., McWilliam, A., and Rich, R. M. (2007). Abundances of Baade's Window Giants from Keck HIRES Spectra. II. The Alpha and Light Odd Elements. *ApJ*, 661:1152.

Furton, D. G., Laiho, J. W., and Witt, A. N. (1999). The Amount of Interstellar Carbon Locked in Solid Hydrogenated Amorphous Carbon. *ApJ*, 526:752.

Galavis, M. E., Mendoza, C., and Zeippen, C. J. (1995). Atomic data from the IRON Project. X. Effective collision strengths for infrared transitions in silicon- and sulphur-like ions. *A&AS*, 111:347.

Galavis, M. E., Mendoza, C., and Zeippen, C. J. (1997). Atomic data from the IRON Project. XXII. Radiative rates for forbidden transitions within the ground configuration of ions in the carbon and oxygen isoelectronic sequences. *A&AS*, 123:159.

Galavis, M. E., Mendoza, C., and Zeippen, C. J. (1998). Atomic data from the IRON Project. XXIX. Radiative rates for transitions within the N = 2 complex in ions of the boron isoelectronic sequence. *A&AS*, 131:499.

Galazutdinov, G. A. and Krełowski, J. (2017). Looking for the Weak Members of the C_{60}^{+} Family in the Interstellar Medium. *Acta Astronomica*, 67:159.

Galazutdinov, G. A., Shimansky, V. V., Bondar, A., Valyavin, G., and Krełowski, J. (2017). C_{60}^{+} - looking for the bucky-ball in interstellar space. *MNRAS*, 465:3956.

García-Hernández, D. A. and Górny, S. K. (2014). Chemical abundances in Galactic planetary nebulae with Spitzer spectra. *A&A*, 567:A12.

García-Hernández, D. A., Iglesias-Groth, S., Acosta-Pulido, J. A., Manchado, A., García-Lario, P., Stanghellini, L., Villaver, E., Shaw, R. A., and Cataldo, F. (2011). The Formation of Fullerenes: Clues from New C_{60}, C_{70}, and (Possible) Planar C_{24} Detections in Magellanic Cloud Planetary Nebulae. *ApJL*, 737:L30.

García-Hernández, D. A., Manchado, A., García-Lario, P., Stanghellini, L., Villaver, E., Shaw, R. A., Szczerba, R., and Perea-Calderón, J. V. (2010). Formation of Fullerenes in H-containing Planetary Nebulae. *ApJL*, 724:L39.

García-Hernández, D. A., Ventura, P., Delgado-Inglada, G., Dell'Agli, F., Di Criscienzo, M., and Yagüe, A. (2016). Probing O-enrichment in C-rich dust planetary nebulae. *MNRAS*, 458:L118.

García-Rojas, J., Peña, M., Flores-Durán, S., and Hernández-Martínez, L. (2016). The planetary nebulae and H II regions in NGC 6822 revisited. Clues to AGB nucleosynthesis. *A&A*, 586:A59.

García-Segura, G., Villaver, E., Langer, N., Yoon, S. C., and Manchado, A. (2014). Single Rotating Stars and the Formation of Bipolar Planetary Nebula. *ApJ*, 783:74.

García-Segura, G., Villaver, E., Manchado, A., Langer, N., and Yoon, S. C. (2016). Rotating Stars and the Formation of Bipolar Planetary Nebulae. II. Tidal Spin-up. *ApJ*, 823:142.

Garnett, D. R. (1989). The abundance of sulfur in extragalactic H II regions. *ApJ*, 345:282.

Gehrz, R. (1989). Sources of Stardust in the Galaxy. In Allamandola, L. J. and Tielens, A. G. G. M., editors, *Interstellar Dust*, volume 135 of *IAU Symposium*, page 445.

Genovali, K., Lemasle, B., da Silva, R., Bono, G., Fabrizio, M., Bergemann, M., Buonanno, R., Ferraro, I., François, P., Iannicola, G., Inno, L., Laney, C. D., Kudritzki, R.-P., Matsunaga, N., Nonino, M., Primas, F., Romaniello, M., Urbaneja, M. A., and Thévenin, F. (2015). On the α-element gradients of the Galactic thin disk using Cepheids. *A&A*, 580:A17.

Genzel, R., Harris, A. I., and Stutzki, J. (1989). Photodissociation regions: Observations and theory. In *Infrared Spectroscopy in Astronomy*, page 115.

Gesicki, K., Zijlstra, A. A., Szyszka, C., Hajduk, M., Lagadec, E., and Guzman Ramirez, L. (2010). Disk evaporation in a planetary nebula. *A&A*, 514:A54.

Giammanco, C., Sale, S. E., Corradi, R. L. M., Barlow, M. J., Viironen, K., Sabin, L., Santander-García, M., Frew, D. J., Greimel, R., Miszalski, B., Phillipps, S., Zijlstra, A. A., Mampaso, A., Drew, J. E., Parker, Q. A., and Napiwotzki, R. (2011). IPHAS extinction distances to planetary nebulae. *A&A*, 525:A58.

Gillett, F. C., Jacoby, G. H., Joyce, R. R., Cohen, J. G., Neugebauer, G., Soifer, B. T., Nakajima, T., and Matthews, K. (1989). The optical/infrared counterpart(s) of IRAS 18333-2357. *ApJ*, 338:862.

Gillett, F. C., Neugebauer, G., Emerson, J. P., and Rice, W. L. (1986). IRAS 18333-2357 - an unusual source in M22. *ApJ*, 300:722.

Gilmore, G. and Reid, N. (1983). New light on faint stars. III - Galactic structure towards the South Pole and the Galactic thick disc. *MNRAS*, 202:1025.

Gilmore, G., Wyse, R. F. G., and Kuijken, K. (1989). Kinematics, chemistry, and structure of the Galaxy. *ARA&A*, 27:555.

Glassgold, A. E. and Langer, W. D. (1974). Model calculations for diffuse molecular clouds. *ApJ*, 193:73.

Goebel, J. H. and Moseley, S. H. (1985). MgS grain component in circumstellar shells. *ApJL*, 290:L35.

Goodrich, R. W. and Dahari, O. (1985). M4-18 - A young, cool planetary nebula. *ApJ*, 289:342.

Górny, S. K., Perea-Calderón, J. V., García-Hernández, D. A., García-Lario, P., and Szczerba, R. (2010). New groups of planetary nebulae with peculiar dust chemistry towards the Galactic bulge. *A&A*, 516:A39.

Górny, S. K., Stasińska, G., Szczerba, R., and Tylenda, R. (2001). Infrared properties of planetary nebulae with [WR] central stars. *A&A*, 377:1007.

Gould, R. J. and Salpeter, E. E. (1963). The Interstellar Abundance of the Hydrogen Molecule. I. Basic Processes. *ApJ*, 138:393.

Graczyk, D., Pietrzyński, G., Thompson, I. B., Gieren, W., Pilecki, B., Konorski, P., Udalski, A., Soszyński, I., Villanova, S., Górski, M., Suchomska, K., Karczmarek, P., Kudritzki, R.-P., Bresolin, F., and Gallenne, A. (2014). The Araucaria Project. The Distance to the Small Magellanic Cloud from Late-type Eclipsing Binaries. *ApJ*, 780.

Green, S. F., Eaton, N., Meadows, A. J., Davies, J. K., and Stewart, B. C. (1985). The detection of fast-moving asteroids and comets by IRAS. *Icarus*, 64:517.

Greig, W. E. (1971). The morphological classification of symmetrical nebulae. *A&A*, 10:161.

Griffin, D. C. and Badnell, N. R. (2000). Electron-impact excitation of Ne^{4+}. *Journal of Physics B Atomic Molecular Physics*, 33:4389.

Griffin, D. C., Mitnik, D. M., and Badnell, N. R. (2001). Electron-impact excitation of Ne^{+}. *Journal of Physics B Atomic Molecular Physics*, 34:4401.

Guerrero, M. A., Miranda, L. F., Riera, A., Velázquez, P. F., Olguín, L., Vázquez, R., Chu, Y.-H., Raga, A., and Benítez, G. (2008). Multiple and Precessing Collimated Outflows in the Planetary Nebula IC 4634. *ApJ*, 683:272.

Guerrero, M. A., Toalá, J. A., Medina, J. J., Luridiana, V., Miranda, L. F., Riera, A., and Velázquez, P. F. (2013). Unveiling shocks in planetary nebulae. *A&A*, 557:A121.

Gutenkunst, S., Bernard-Salas, J., Pottasch, S. R., Sloan, G. C., and Houck, J. R. (2008). Chemical Abundances and Dust in Planetary Nebulae in the Galactic Bulge. *ApJ*, 680:1206.

Guzman-Ramirez, L., Lagadec, E., Wesson, R., Zijlstra, A. A., Müller, A., Jones, D., Boffin, H. M. J., Sloan, G. C., Redman, M. P., Smette, A., Karakas, A. I., and Nyman, L.-Å. (2015). Witnessing the emergence of a carbon star. *MNRAS*, 451:L1.

Habing, H. J. (1968). The interstellar radiation density between 912 A and 2400 A. *BAN*, 19:421.

Harrington, J. P., Borkowski, K. J., and Tsvetanov, Z. I. (1997). Modelling hydrogen-deficient Planetary Nebulae. In Habing, H. J. and Lamers, H. J. G. L. M., editors, *Planetary Nebulae*, volume 180 of *IAU Symposium*, page 235.

Harris, W. E. (1996). A Catalog of Parameters for Globular Clusters in the Milky Way. *AJ*, 112:1487.

Heger, M. L. (1922). The spectra of certain class B stars in the regions 5630A-6680A and 3280A-3380A. *Lick Observatory Bulletin*, 10:146.

Helmi, A. and White, S. D. M. (2001). Simple dynamical models of the Sagittarius dwarf galaxy. *MNRAS*, 323:529.

Henry, R. B. C., Kwitter, K. B., and Balick, B. (2004). Sulfur, Chlorine, and Argon Abundances in Planetary Nebulae. IV. Synthesis and the Sulfur Anomaly. *AJ*, 127:2284.

Henry, R. B. C., Kwitter, K. B., Dufour, R. J., and Skinner, J. N. (2008). A Multiwavelength Analysis of the Halo Planetary Nebula DdDm-1. *ApJ*, 680:1162.

Henry, R. B. C., Kwitter, K. B., and Howard, J. W. (1996). A New Look at Carbon Abundances in Planetary Nebulae. I. PB 6, HU 2–1, K648, and H4–1. *ApJ*, 458:215.

Henry, R. B. C., Kwitter, K. B., Jaskot, A. E., Balick, B., Morrison, M. A., and Milingo, J. B. (2010). Abundances of Galactic Anticenter Planetary Nebulae and the Oxygen Abundance Gradient in the Galactic Disk. *ApJ*, 724:748.

Henry, R. B. C., Speck, A., Karakas, A. I., Ferland, G. J., and Maguire, M. (2012). The Curious Conundrum Regarding Sulfur Abundances in Planetary Nebulae. *ApJ*, 749:61.

Herwig, F., Bloecker, T., Schoenberner, D., and El Eid, M. (1997). Stellar evolution of low and intermediate-mass stars. IV. Hydrodynamically-based overshoot and nucleosynthesis in AGB stars. *A&A*, 324:L81.

Higdon, S. J. U., Devost, D., Higdon, J. L., Brandl, B. R., Houck, J. R., Hall, P., Barry, D., Charmandaris, V., Smith, J. D. T., Sloan, G. C., and Green, J. (2004). The SMART Data Analysis Package for the Infrared Spectrograph on the Spitzer Space Telescope. *PASP*, 116:975.

Hillwig, T. C., Jones, D., De Marco, O., Bond, H. E., Margheim, S., and Frew, D. (2016). Observational Confirmation of a Link Between Common Envelope Binary Interaction and Planetary Nebula Shaping. *ApJ*, 832:125.

Hollenbach, D. and Salpeter, E. E. (1971). Surface Recombination of Hydrogen Molecules. *ApJ*, 163:155.

Hollenbach, D. J. and Tielens, A. G. G. M. (1997). Dense Photodissociation Regions (PDRs). *ARA&A*, 35:179.

Hollenbach, D. J. and Tielens, A. G. G. M. (1999). Photodissociation regions in the interstellar medium of galaxies. *Reviews of Modern Physics*, 71:173.

Hony, S., Van Kerckhoven, C., Peeters, E., Tielens, A. G. G. M., Hudgins, D. M., and Allamandola, L. J. (2001). The CH out-of-plane bending modes of PAH molecules in astrophysical environments. *A&A*, 370:1030.

Hony, S., Waters, L. B. F. M., and Tielens, A. G. G. M. (2002). The carrier of the "30μm" emission feature in evolved stars. A simple model using magnesium sulfide. *A&A*, 390:533.

Hora, J. L., Latter, W. B., and Deutsch, L. K. (1999). Investigating the Near-Infrared Properties of Planetary Nebulae. II. Medium-Resolution Spectra. *ApJS*, 124:195.

Houck, J. R., Roellig, T. L., van Cleve, J., Forrest, W. J., Herter, T., Lawrence, C. R., Matthews, K., Reitsema, H. J., Soifer, B. T., Watson, D. M., Weedman, D., Huisjen, M., Troeltzsch, J., Barry, D. J., Bernard-Salas, J., Blacken, C. E., Brandl, B. R., Charmandaris, V., Devost, D., Gull, G. E., Hall, P., Henderson, C. P., Higdon, S. J. U., Pirger, B. E., Schoenwald, J., Sloan, G. C., Uchida, K. I., Appleton, P. N., Armus, L., Burgdorf, M. J., Fajardo-Acosta, S. B., Grillmair, C. J., Ingalls, J. G., Morris, P. W., and Teplitz, H. I. (2004). The Infrared Spectrograph (IRS) on the Spitzer Space Telescope. *ApJS*, 154:18.

Howard, J. W., Henry, R. B. C., and McCartney, S. (1997). A detailed abundance analysis of nine halo planetary nebulae. *MNRAS*, 284:465.

Hrivnak, B. J., Volk, K., and Kwok, S. (2000). 2-45 Micron Infrared Spectroscopy of Carbon-rich Proto-Planetary Nebulae. *ApJ*, 535:275.

Huang, Z.-Y., Hasegawa, T. I., Dinh-V-Trung, Kwok, S., Muller, S., Hirano, N., Lim, J., Muthu Mariappan, C., and Lyo, A. (2010). Detection of Multiple Bipolar Flows in NGC 7027 with Submillimeter Array. *ApJ*, 722:273.

Huggins, P. J. (2007). Jets and Tori in Proto-Planetary Nebulae. *ApJ*, 663:342.

Hugoniot, P. H. (1887). Mémoire sur la propagation du mouvement dans les corps et ples spécialement dans les gaz parfaits, 1e partie. *Journal de l'École Polytechnique*, 57.

Hugoniot, P. H. (1889). Mémoire sur la propagation du mouvement dans les corps et plus spécialement dans les gaz parfaits, 2e partie. *Journal de l'École Polytechnique*, 58.

Hummer, D. G., Berrington, K. A., Eissner, W., Pradhan, A. K., Saraph, H. E., and Tully, J. A. (1993). Atomic data from the IRON Project. 1: Goals and methods. *A&A*, 279:298.

Hummer, D. G. and Storey, P. J. (1987). Recombination-line intensities for hydrogenic ions. I - Case B calculations for H I and He II. *MNRAS*, 224:801.

Ibata, R., Irwin, M., Lewis, G. F., and Stolte, A. (2001). Galactic Halo Substructure in the Sloan Digital Sky Survey: The Ancient Tidal Stream from the Sagittarius Dwarf Galaxy. *ApJ*, 547:L133.

Ibata, R. A., Gilmore, G., and Irwin, M. J. (1994). A dwarf satellite galaxy in Sagittarius. *Nature*, 370:194.

Icke, V. (1988). Blowing bubbles. *A&A*, 202:177.

Icke, V., Preston, H. L., and Balick, B. (1989). The Evolution of Planetary Nebulae. III. Position-Velocity Images of Butterfly-Type Nebulae. *AJ*, 97:462.

Ishihara, D., Kaneda, H., Onaka, T., Ita, Y., Matsuura, M., and Matsunaga, N. (2011). Galactic distributions of carbon- and oxygen-rich AGB stars revealed by the AKARI mid-infrared all-sky survey. *A&A*, 534:A79.

Jacoby, G. H., De Marco, O., Davies, J., Lotarevich, I., Bond, H. E., Harrington, J. P., and Lanz, T. (2017). Masses of the Planetary Nebula Central Stars in the Galactic Globular Cluster System from HST Imaging and Spectroscopy. *ApJ*, 836:93.

Jacoby, G. H., Morse, J. A., Fullton, L. K., Kwitter, K. B., and Henry, R. B. C. (1997). Planetary Nebulae in the Globular Cluster PAL 6 and NGC 6441. *AJ*, 114:2611.

Jochims, H. W., Ruhl, E., Baumgartel, H., Tobita, S., and Leach, S. (1994). Size effects on dissociation rates of polycyclic aromatic hydrocarbon cations: Laboratory studies and astophysical implications. *ApJ*, 420:307.

John, T. L. (1988). Continuous absorption by the negative hydrogen ion reconsidered. *A&A*, 193:189.

Johnson, C. T., Kingston, A. E., and Dufton, P. L. (1986). Atomic data for the S IV 10.5-micron fine-structure transition. *MNRAS*, 220:155.

Jones, A. P. and Nuth, J. A. (2011). Dust destruction in the ISM: a re-evaluation of dust lifetimes. *A&A*, 530:A44.

Jones, A. P., Tielens, A. G. G. M., and Hollenbach, D. J. (1996). Grain Shattering in Shocks: The Interstellar Grain Size Distribution. *ApJ*, 469:740.

Jones, D. (2015). Planetary Nebulae: What Can They Tell Us About Close Binary Evolution? In *EAS Publications Series*, volume 71-72, page 113.

Kakinami, Y., Yamamoto, M., Chen, C.-H., Watanabe, S., Lin, C., Liu, J.-Y., and Habu, H. (2013). Ionospheric disturbances induced by a missile launched from North Korea on 12 December 2012. *Journal of Geophysical Research (Space Physics)*, 118:5184.

Karakas, A. I. and Lattanzio, J. C. (2003). AGB Stars and the Observed Abundance of Neon in Planetary Nebulae. *PASA*, 20:393.

Karakas, A. I. and Lattanzio, J. C. (2014). The Dawes Review 2: Nucleosynthesis and Stellar Yields of Low- and Intermediate-Mass Single Stars. *PASA*, 31:e030.

Kaufman, M. J. and Neufeld, D. A. (1996). Far-Infrared Water Emission from Magnetohydrodynamic Shock Waves. *ApJ*, 456:611.

Kaufman, M. J., Wolfire, M. G., Hollenbach, D. J., and Luhman, M. L. (1999). Far-Infrared and Submillimeter Emission from Galactic and Extragalactic Photodissociation Regions. *ApJ*, 527:795.

Kawada, M., Baba, H., Barthel, P. D., Clements, D., Cohen, M., Doi, Y., Figueredo, E., Fujiwara, M., Goto, T., Hasegawa, S., Hibi, Y., Hirao, T., Hiromoto, N., Jeong, W.-S., Kaneda, H., Kawai, T., Kawamura, A., Kester, D., Kii, T., Kobayashi, H., Kwon, S. M., Lee, H. M., Makiuti, S., Matsuo, H., Matsuura, S., Müller, T. G., Murakami, N., Nagata, H., Nakagawa, T., Narita, M., Noda, M., Oh, S. H., Okada, Y., Okuda, H., Oliver, S., Ootsubo, T., Pak, S., Park, Y.-S., Pearson, C. P., Rowan-Robinson, M., Saito, T., Salama, A., Sato, S., Savage, R. S., Serjeant, S., Shibai, H., Shirahata, M., Sohn, J., Suzuki, T., Takagi, T., Takahashi, H., Thomson, M., Usui, F., Verdugo, E., Watabe, T., White, G. J., Wang, L., Yamamura, I., Yamauchi, C., and Yasuda, A. (2007). The Far-Infrared Surveyor (FIS) for AKARI. *PASJ*, 59:S389.

Kemper, F., Molster, F. J., Jäger, C., and Waters, L. B. F. M. (2002). The mineral composition and spatial distribution of the dust ejecta of NGC 6302. *A&A*, 394:679.

Kessler, M. F., Steinz, J. A., Anderegg, M. E., Clavel, J., Drechsel, G., Estaria, P., Faelker, J., Riedinger, J. R., Robson, A., Taylor, B. G., and Ximénez de Ferrán, S. (1996). The Infrared Space Observatory (ISO) mission. *A&A*, 315:L27.

Kharchenko, N. V., Piskunov, A. E., Schilbach, E., Röser, S., and Scholz, R.-D. (2013). Global survey of star clusters in the Milky Way. II. The catalogue of basic parameters. *A&A*, 558:A53.

Kingsburgh, R. L. and Barlow, M. J. (1994). Elemental abundances for a sample of southern galactic planetary nebulae. *MNRAS*, 271:257.

Koch, A., McWilliam, A., Preston, G. W., and Thompson, I. B. (2016). Metal-poor stars towards the Galactic bulge: A population potpourri. *A&A*, 587:A124.

Koeppen, J., Acker, A., and Stenholm, B. (1991). Spectrophotometric survey of southern planetary nebulae. II - Chemical compositions. *A&A*, 248:197.

Kroto, H. W., Heath, J. R., Obrien, S. C., Curl, R. F., and Smalley, R. E. (1985). C(60): Buckminsterfullerene. *Nature*, 318:162.

Kubryk, M., Prantzos, N., and Athanassoula, E. (2015). Evolution of the Milky Way with radial motions of stars and gas. II. The evolution of abundance profiles from H to Ni. *A&A*, 580:A127.

Kwitter, K. B. and Henry, R. B. C. (2001). Sulfur, Chlorine, and Argon in Planetary Nebulae. I. Observations and Abundances in a Northern Sample. *ApJ*, 562:804.

Kwitter, K. B., Henry, R. B. C., and Milingo, J. B. (2003). Sulfur, Chlorine, and Argon Abundances in Planetary Nebulae. III. Observations and Results for a Final Sample. *PASP*, 115:80.

Kwitter, K. B., Méndez, R. H., Peña, M., Stanghellini, L., Corradi, R. L. M., De Marco, O., Fang, X., Henry, R. B. C., Karakas, A. I., Liu, X. W., López, J. A., Manchado, A., and Parker, Q. A. (2014). The Present and Future of Planetary Nebula Research. A White Paper by the IAU Planetary Nebula Working Group. *RMxAA*, 50:203.

Kwok, S. (2011). Molecular Evolution from AGB Stars to Planetary Nebulae. In Cernicharo, J. and Bachiller, R., editors, *The Molecular Universe*, volume 280 of *IAU Symposium*, page 203.

Lagadec, E., Zijlstra, A. A., Mauron, N., Fuller, G., Josselin, E., Sloan, G. C., and Riggs, A. J. E. (2010). The low wind expansion velocity of metal-poor carbon stars in the Halo and the Sagittarius stream†. *MNRAS*, 403:1331.

Lagadec, E., Zijlstra, A. A., Sloan, G. C., Matsuura, M., Wood, P. R., van Loon, J. T., Harris, G. J., Blommaert, J. A. D. L., Hony, S., Groenewegen, M. A. T., Feast, M. W., Whitelock, P. A., Menzies, J. W., and Cioni, M.-R. (2007). Spitzer spectroscopy of carbon stars in the Small Magellanic Cloud. *MNRAS*, 376:1270.

Lallement, R., Cox, N. L. J., Cami, J., Smoker, J., Fahrang, A., Elyajouri, M., Cordiner, M. A., Linnartz, H., Smith, K. T., Ehrenfreund, P., and Foing, B. H. (2018). The EDIBLES survey II. The detectability of C_{60}^{+} bands. *A&A*, 614:A28.

Lamb, M., Venn, K., Andersen, D., Oya, S., Shetrone, M., Fattahi, A., Howes, L., Asplund, M., Lardière, O., Akiyama, M., Ono, Y., Terada, H., Hayano, Y., Suzuki, G., Blain, C., Jackson, K., Correia, C., Youakim, K., and Bradley, C. (2017). Using the multi-object adaptive optics demonstrator RAVEN to observe metal-poor stars in and towards the Galactic Centre. *MNRAS*, 465:3536.

Landau, L., D. and Lifshitz, E. M. (1959). *Fluid Mechanics*, volume 1. Pergamon Press.

Larson, R. B. (1976). Models for the formation of disc galaxies. *MNRAS*, 176:31.

Lattanzio, J. C. (1989). Carbon Dredge-up in Low-Mass Stars and Solar Metallicity Stars. *ApJ*, 344:L25.

Lattanzio, J. C. and Wood, P. R. (2003). Evolution, Nucleosynthesis, and Pulsation of AGB Stars. In *Asymptotic giant branch stars, by Harm J. Habing and Hans Olofsson. Astronomy and astrophysics library, New York, Berlin: Springer*, page 23.

Latter, W. B., Dayal, A., Bieging, J. H., Meakin, C., Hora, J. L., Kelly, D. M., and Tielens, A. G. G. M. (2000). Revealing the Photodissociation Region: HST/NICMOS Imaging of NGC 7027. *ApJ*, 539:783.

Lebouteiller, V., Barry, D. J., Goes, C., Sloan, G. C., Spoon, H. W. W., Weedman, D. W., Bernard-Salas, J., and Houck, J. R. (2015). CASSIS: The Cornell Atlas of Spitzer/Infrared Spectrograph Sources. II. High-resolution Observations. *ApJS*, 218:21.

Lebouteiller, V., Barry, D. J., Spoon, H. W. W., Bernard-Salas, J., Sloan, G. C., Houck, J. R., and Weedman, D. W. (2011). CASSIS: The Cornell Atlas of Spitzer/Infrared Spectrograph Sources. *ApJS*, 196:8.

Lebouteiller, V., Bernard-Salas, J., Sloan, G. C., and Barry, D. J. (2010). Advanced Optimal Extraction for the Spitzer/IRS. *PASP*, 122:231.

Lee, Y.-W., Demarque, P., and Zinn, R. (1994). The Horizontal-Branch Stars in Globular Clusters. II. The Second Parameter Phenomenon. *ApJ*, 423:248.

Leisy, P. and Dennefeld, M. (2006). Planetary nebulae in the Magellanic Clouds. II. Abundances and element production. *A&A*, 456:451.

Lemasle, B., François, P., Genovali, K., Kovtyukh, V. V., Bono, G., Inno, L., Laney, C. D., Kaper, L., Bergemann, M., Fabrizio, M., Matsunaga, N., Pedicelli, S., Primas, F., and Romaniello, M. (2013). Galactic abundance gradients from Cepheids. α and heavy elements in the outer disk. *A&A*, 558:A31.

Li, A. (2009). Optical properties of dust. In Mann, I., Nakamura, A., and Mukai, T., editors, *Small Bodies in Planetary Systems*, volume 758 of *Lecture Notes in Physics*, page 167. Springer.

Lombaert, R., de Vries, B. L., de Koter, A., Decin, L., Min, M., Smolders, K., Mutschke, H., and Waters, L. B. F. M. (2012). Observational evidence for composite grains in an AGB outflow. MgS in the extreme carbon star LL Pegasi. *A&A*, 544:L18.

Luck, R. E., Gieren, W. P., Andrievsky, S. M., Kovtyukh, V. V., Fouqué, P., Pont, F., and Kienzle, F. (2003). The galactic abundance gradient from Cepheids. IV. New results for the outer disc. *A&A*, 401:939.

Luck, R. E. and Lambert, D. L. (2011). The Distribution of the Elements in the Galactic Disk. III. A Reconsideration of Cepheids from l = 30° to 250°. *AJ*, 142:136.

Lugaro, M., Karakas, A. I., Stancliffe, R. J., and Rijs, C. (2012). The s-process in Asymptotic Giant Branch Stars of Low Metallicity and the Composition of Carbon-enhanced Metal-poor Stars. *ApJ*, 747:2.

Lutz, D., Sturm, E., Tacconi, L. J., Valiante, E., Schweitzer, M., Netzer, H., Maiolino, R., Andreani, P., Shemmer, O., and Veilleux, S. (2008). Star Formation in the Hosts of High-z QSOs: Evidence from Spitzer PAH Detections. *ApJ*, 684:853.

Maciel, W. J., Costa, R. D. D., and Cavichia, O. (2015). Radial abundance gradients from planetary nebulae at different distances from the galactic plane. *RMxAA*, 51:165.

Maciel, W. J., Costa, R. D. D., and Uchida, M. M. M. (2003). An estimate of the time variation of the O/H radial gradient from planetary nebulae. *A&A*, 397:667.

Maciel, W. J. and Quireza, C. (1999). Abundance gradients in the outer galactic disk from planetary nebulae. *A&A*, 345:629.

Macquorn Rankine, W. J. (1870). On the Thermodynamic Theory of Waves of Finite Longitudinal Disturbance. *Philosophical Transactions of the Royal Society of London Series I*, 160:277.

Magrini, L., Coccato, L., Stanghellini, L., Casasola, V., and Galli, D. (2016). Metallicity gradients in local Universe galaxies: Time evolution and effects of radial migration. *A&A*, 588:A91.

Magrini, L., Randich, S., Kordopatis, G., Prantzos, N., Romano, D., Chieffi, A., Limongi, M., François, P., Pancino, E., Friel, E., Bragaglia, A., Tautvaišienė, G., Spina, L., Overbeek, J., Cantat-Gaudin, T., Donati, P., Vallenari, A., Sordo, R., Jiménez-Esteban, F. M., Tang, B., Drazdauskas, A., Sousa, S., Duffau, S., Jofré, P., Gilmore, G., Feltzing, S., Alfaro, E., Bensby, T., Flaccomio, E., Koposov, S., Lanzafame, A., Smiljanic, R., Bayo, A., Carraro, G., Casey, A. R., Costado, M. T., Damiani, F., Franciosini, E., Hourihane, A., Lardo, C., Lewis, J., Monaco, L., Morbidelli, L., Sacco, G., Sbordone, L., Worley, C. C., and Zaggia, S. (2017). The Gaia-ESO Survey: radial distribution of abundances in the Galactic disc from open clusters and young-field stars. *A&A*, 603:A2.

Malhan, K. and Ibata, R. A. (2017). Measuring the Sun's motion with stellar streams. *MNRAS*, 471:1005.

Malhotra, S., Kaufman, M. J., Hollenbach, D., Helou, G., Rubin, R. H., Brauher, J., Dale, D., Lu, N. Y., Lord, S., Stacey, G., Contursi, A., Hunter, D. A., and Dinerstein, H. (2001). Far-Infrared Spectroscopy of Normal Galaxies: Physical Conditions in the Interstellar Medium. *ApJ*, 561:766.

Mal'Kov, Y. F. (1997). A self-consistent determination of the distances, physical parameters, and chemical composition for a large sample of galactic planetary nebulae: The distances and parameters of central stars and the optical depths of envelopes. *Astronomy Reports*, 41:760.

Manchado, A., Villaver, E., Stanghellini, L., and Guerrero, M. A. (2000). The Morphological and Structural Classification of Planetary Nebulae. In *Asymmetrical Planetary Nebulae II: From Origins to Microstructures*, volume 199, page 17.

Marigo, P. (2001). Chemical yields from low- and intermediate-mass stars: Model predictions and basic observational constraints. *A&A*, 370:194.

Marigo, P., Bernard-Salas, J., Pottasch, S. R., Tielens, A. G. G. M., and Wesselius, P. R. (2003). Probing AGB nucleosynthesis via accurate Planetary Nebula abundances. *A&A*, 409:619.

Marigo, P., Girardi, L., Bressan, A., Groenewegen, M. A. T., Silva, L., and Granato, G. L. (2008). Evolution of asymptotic giant branch stars. II. Optical to far-infrared isochrones with improved TP-AGB models. *A&A*, 482:883.

Marshall, J. R., van Loon, J. T., Matsuura, M., Wood, P. R., Zijlstra, A. A., and Whitelock, P. A. (2004). Asymptotic giant branch superwind speed at low metallicity. *MNRAS*, 355:1348.

Martín-Hernández, N. L., Peeters, E., Morisset, C., Tielens, A. G. G. M., Cox, P., Roelfsema, P. R., Baluteau, J.-P., Schaerer, D., Mathis, J. S., Damour, F., Churchwell, E., and Kessler, M. F. (2002). ISO spectroscopy of compact H II regions in the Galaxy. II. Ionization and elemental abundances. *A&A*, 381:606.

Martínez-Delgado, D., Gómez-Flechoso, M. Á., Aparicio, A., and Carrera, R. (2004). Tracing Out the Northern Tidal Stream of the Sagittarius Dwarf Spheroidal Galaxy. *ApJ*, 601:242.

Mata, H., Ramos-Larios, G., Guerrero, M. A., Nigoche-Netro, A., Toalá, J. A., Fang, X., Rubio, G., Kemp, S. N., Navarro, S. G., and Corral, L. J. (2016). Spitzer mid-infrared spectroscopic observations of planetary nebulae. *MNRAS*, 459:841.

Mathewson, D. S., Cleary, M. N., and Murray, J. D. (1974). The Magellanic Stream. *ApJ*, 190:291.

Matsuura, M., Bernard-Salas, J., Lloyd Evans, T., Volk, K. M., Hrivnak, B. J., Sloan, G. C., Chu, Y.-H., Gruendl, R., Kraemer, K. E., Peeters, E., Szczerba, R., Wood, P. R., Zijlstra, A. A., Hony, S., Ita, Y., Kamath, D., Lagadec, E., Parker, Q. A., Reid, W. A., Shimonishi, T., Van Winckel, H., Woods, P. M., Kemper, F., Meixner, M., Otsuka, M., Sahai, R., Sargent, B. A., Hora, J. L., and McDonald, I. (2014). Spitzer Space Telescope spectra of post-AGB stars in the Large Magellanic Cloud - polycyclic aromatic hydrocarbons at low metallicities. *MNRAS*, 439:1472.

Matsuura, M., Zijlstra, A. A., Gray, M. D., Molster, F. J., and Waters, L. B. F. M. (2005). The symmetric dust shell and the central star of the bipolar planetary nebula NGC6537*. *MNRAS*, 363:628.

Matthews, G. P. (1985). *Experimental Physical Chemistry*. Oxford University Press, 1st edition.

Mauron, N., Azzopardi, M., Gigoyan, K., and Kendall, T. R. (2004). Cool carbon stars in the halo: A new survey based on 2MASS. *A&A*, 418:77.

Mauron, N., Gigoyan, K. S., and Kendall, T. R. (2007). Cool carbon stars in the halo: new very red or distant objects. *A&A*, 475:843.

Mauron, N., Kendall, T. R., and Gigoyan, K. (2005). Cool carbon stars in the halo. II. A study of 25 new objects. *A&A*, 438:867.

McDonald, I. and Zijlstra, A. A. (2015). Globular cluster interstellar media: ionized and ejected by white dwarfs. *MNRAS*, 446:2226.

McDonald, I., Zijlstra, A. A., Lagadec, E., Sloan, G. C., Boyer, M. L., Matsuura, M., Smith, R. J., Smith, C. L., Yates, J. A., van Loon, J. T., Jones, O. C., Ramstedt, S., Avison, A., Justtanont, K., Olofsson, H., Blommaert, J. A. D. L., Goldman, S. R., and Groenewegen, M. A. T. (2015). ALMA reveals sunburn: CO dissociation around AGB stars in the globular cluster 47 Tucanae. *MNRAS*, 453:4324.

Meaburn, J., Boumis, P., and Akras, S. (2013). The bow-shock and high-speed jet in the faint, 40 arcmin diameter, outer halo of the evolved Helix planetary nebula (NGC 7293). *MNRAS*, 435:3462.

Meadows, A. (1984). Department of Astronomy, University of Leicester (Reports of Observatories). *QJRAS*, 25:498.

Meixner, M., Zalucha, A., Ueta, T., Fong, D., and Justtanont, K. (2004). The Molecular and Dust Envelope of HD 56126. *ApJ*, 614:371.

Mendoza, C. (1983). Recent advances in atomic calculations and experiments of interest in the study of planetary nebulae. In Flower, D. R., editor, *Planetary Nebulae*, volume 103 of *IAU Symposium*, page 143.

Mendoza, C. and Zeippen, C. J. (1982). Transition probabilities for forbidden lines in the 3p/2/ configuration. - II. *MNRAS*, 199:1025.

Mendoza, C. and Zeippen, C. J. (1983). Transition probabilities for forbidden lines in the 3p4 configuration. III. *MNRAS*, 202:981.

Micelotta, E. R., Jones, A. P., Cami, J., Peeters, E., Bernard-Salas, J., and Fanchini, G. (2012). The Formation of Cosmic Fullerenes from Arophatic Clusters. *ApJ*, 761:35.

Micelotta, E. R., Jones, A. P., and Tielens, A. G. G. M. (2010). Polycyclic aromatic hydrocarbon processing in interstellar shocks. *A&A*, 510:A36.

Milingo, J. B., Henry, R. B. C., and Kwitter, K. B. (2002). Sulfur, Chlorine, and Argon Abundances in Planetary Nebulae. IIB. Abundances in a Southern Sample. *ApJS*, 138:285.

Milingo, J. B., Kwitter, K. B., Henry, R. B. C., and Souza, S. P. (2010). Alpha Element Abundances in a Large Sample of Galactic Planetary Nebulae. *ApJ*, 711:619.

Minchev, I., Chiappini, C., and Martig, M. (2013). Chemodynamical evolution of the Milky Way disk. I. The solar vicinity. *A&A*, 558:A9.

Minchev, I., Chiappini, C., and Martig, M. (2014). Chemodynamical evolution of the Milky Way disk. II. Variations with Galactic radius and height above the disk plane. *A&A*, 572:A92.

Minchev, I., Famaey, B., Quillen, A. C., Dehnen, W., Martig, M., and Siebert, A. (2012). Radial migration does little for Galactic disc thickening. *A&A*, 548:A127.

Mishra, A., Li, A., and Jiang, B. W. (2015). A Tale of Three Mysterious Spectral Features in Carbon-rich Evolved Stars: The 21 μm, 30 μm, and Unidentified Infrared Emission Features. *ApJ*, 802:39.

Miszalski, B., Mikołajewska, J., Köppen, J., Rauch, T., Acker, A., Cohen, M., Frew, D. J., Moffat, A. F. J., Parker, Q. A., Jones, A. F., and Udalski, A. (2011). The influence of binarity on dust obscuration events in the planetary nebula M 2-29 and its analogues. *A&A*, 528:A39.

Mitnik, D. M., Griffin, D. C., and Badnell, N. R. (2001). Electron-impact excitation of Ne^{5+}. *Journal of Physics B Atomic Molecular Physics*, 34:4455.

Molster, F. J., Waters, L. B. F. M., Tielens, A. G. G. M., and Barlow, M. J. (2002). Crystalline silicate dust around evolved stars. I. The sample stars. *A&A*, 382:184.

Monaco, L., Bellazzini, M., Ferraro, F. R., and Pancino, E. (2004a). The distance to the Sagittarius dwarf spheroidal galaxy from the red giant branch tip. *MNRAS*, 353:874.

Monaco, L., Pancino, E., Ferraro, F. R., and Bellazzini, M. (2004b). Wide-field photometry of the Galactic globular cluster M22. *MNRAS*, 349:1278.

Moore, K. and Bildsten, L. (2011). Clearing the Gas from Globular Clusters and Dwarf Spheroidals with Classical Novae. *ApJ*, 728:81.

Moutou, C., Verstraete, L., Léger, A., Sellgren, K., and Schmidt, W. (2000). New PAH mode at 16.4 mu m. *A&A*, 354:L17.

Müller, H. S., Schlöder, F., Stutzki, J., and Winnewisser, G. (2005). The cologne database for molecular spectroscopy, cdms: a useful tool for astronomers and spectroscopists. *Journal of Molecular Structure*, 742(1):215.

Müller, H. S. P., Thorwirth, S., Roth, D. A., and Winnewisser, G. (2001). The Cologne Database for Molecular Spectroscopy, CDMS. *A&A*, 370:L49.

Murakami, H., Baba, H., Barthel, P., Clements, D. L., Cohen, M., Doi, Y., Enya, K., Figueredo, E., Fujishiro, N., Fujiwara, H., Fujiwara, M., Garcia-Lario, P., Goto, T., Hasegawa, S., Hibi, Y., Hirao, T., Hiromoto, N., Hong, S. S., Imai, K., Ishigaki, M., Ishiguro, M., Ishihara, D., Ita, Y., Jeong, W.-S., Jeong, K. S., Kaneda, H., Kataza, H., Kawada, M., Kawai, T., Kawamura, A., Kessler, M. F., Kester, D., Kii, T., Kim, D. C., Kim, W., Kobayashi, H., Koo, B. C., Kwon, S. M., Lee, H. M., Lorente, R., Makiuti, S., Matsuhara, H., Matsumoto, T., Matsuo, H., Matsuura, S., MÜller, T. G., Murakami, N., Nagata, H., Nakagawa, T., Naoi, T., Narita, M., Noda, M., Oh, S. H., Ohnishi, A., Ohyama, Y., Okada, Y., Okuda, H., Oliver, S., Onaka, T., Ootsubo, T., Oyabu, S., Pak, S., Park, Y.-S., Pearson, C. P., Rowan-Robinson, M., Saito, T., Sakon, I., Salama, A., Sato, S., Savage, R. S., Serjeant, S., Shibai, H., Shirahata, M., Sohn, J., Suzuki, T., Takagi, T., Takahashi, H., TanabÉ, T., Takeuchi, T. T., Takita, S., Thomson, M., Uemizu, K., Ueno, M., Usui, F., Verdugo, E., Wada, T., Wang, L., Watabe, T., Watarai, H., White, G. J., Yamamura, I., Yamauchi, C., and Yasuda, A. (2007). The Infrared Astronomical Mission AKARI*. *PASJ*, 59:S369.

Muthumariappan, C., Parthasarathy, M., and Ita, Y. (2013). Radiative transfer modelling of dust in IRAS 18333-2357: the only planetary nebula in the metal-poor globular cluster M22. *MNRAS*, 435:606.

Naiman, J., Soares-Furtado, M., and Ramirez-Ruiz, E. (2013). Modeling the Tenuous Intracluster Medium in Globular Clusters. *ArXiv e-prints*, page arXiv:1310.8301.

Nardini, E. and Risaliti, G. (2011). Compton-thick active galactic nuclei inside local ultraluminous infrared galaxies. *MNRAS*, 415:619.

Natta, A., Preite-Martinez, A., and Panagia, N. (1980). The problem of sulfur abundance determination in gaseous nebulae. *ApJ*, 242:596.

Nemes, L. and Jelski, D. A. (2012). Anharmonicity in the vibrational spectra of c_{60} and its implications in laboratory spectroscopy and astrophysics. In J., D., Sarka, K., and Cohen, E. A., editors, *Spectroscopy from Space*, page 301. Springer.

Neugebauer, G., Habing, H. J., van Duinen, R., Aumann, H. H., Baud, B., Beichman, C. A., Beintema, D. A., Boggess, N., Clegg, P. E., de Jong, T., Emerson, J. P., Gautier, T. N., Gillett, F. C., Harris, S., Hauser, M. G., Houck, J. R., Jennings, R. E., Low, F. J., Marsden, P. L., Miley, G., Olnon, F. M., Pottasch, S. R., Raimond, E., Rowan-Robinson, M., Soifer, B. T., Walker, R. G., Wesselius, P. R., and Young, E. (1984). The Infrared Astronomical Satellite (IRAS) mission. *ApJ*, 278:L1.

Nidever, D. L., Majewski, S. R., Butler Burton, W., and Nigra, L. (2010). The 200° Long Magellanic Stream System. *ApJ*, 723:1618.

Nordhaus, J. and Blackman, E. G. (2006). Low-mass binary-induced outflows from asymptotic giant branch stars. *MNRAS*, 370:2004.

Olofsson, H. (2005). Molecular abundances in AGB circumstellar envelopes. In Wilson, A., editor, *ESA Special Publication*, volume 577 of *ESA Special Publication*, page 223.

Onaka, T., Matsuhara, H., Wada, T., Fujishiro, N., Fujiwara, H., Ishigaki, M., Ishihara, D., Ita, Y., Kataza, H., Kim, W., Matsumoto, T., Murakami, H., Ohyama, Y., Oyabu, S., Sakon, I., Tanabé, T., Takagi, T., Uemizu, K., Ueno, M., Usui, F., Watarai, H., Cohen, M., Enya, K., Ootsubo, T., Pearson, C. P., Takeyama, N., Yamamuro, T., and Ikeda, Y. (2007). The Infrared Camera (IRC) for AKARI – Design and Imaging Performance. *PASJ*, 59:S401.

Ortiz, R., Copetti, M. V. F., and Lorenz-Martins, S. (2011). A distance scale of planetary nebulae based on mid-infrared data. *MNRAS*, 418:2004.

Osterbrock, D. E. and Ferland, G. J. (2006). *Astrophysics of Gaseous Nebulae and Active Galactic Nuclei*. University Science Books, 2nd edition.

Otsuka, M., Hyung, S., Lee, S.-J., Izumiura, H., and Tajitsu, A. (2009). High-dispersion Spectrum of the Halo Planetary Nebula DdDm 1. *ApJ*, 705:509.

Otsuka, M., Hyung, S., and Tajitsu, A. (2015). Chemical Abundances and Dust in the Halo Planetary Nebula K648 in M15: Its Origin and Evolution Based on an Analysis of Multiwavelength Data. *ApJS*, 217:22.

Otsuka, M., Izumiura, H., Tajitsu, A., and Hyung, S. (2008). Detection of Fluorine in the Halo Planetary Nebula BoBn 1: Evidence for a Binary Progenitor Star. *ApJL*, 682:L105.

Otsuka, M., Kemper, F., Cami, J., Peeters, E., and Bernard-Salas, J. (2014). Physical properties of fullerene-containing Galactic planetary nebulae. *MNRAS*, 437:2577.

Otsuka, M. and Tajitsu, A. (2013). Chemical Abundances in the Extremely Carbon-rich and Xenon-rich Halo Planetary Nebula H4-1. *ApJ*, 778:146.

Otsuka, M., Tajitsu, A., Hyung, S., and Izumiura, H. (2010). The Origin and Evolution of the Halo PN BoBn 1: From a Viewpoint of Chemical Abundances Based on Multiwavelength Spectra. *ApJ*, 723:658.

Otsuka, M., Tamura, S., Yadoumaru, Y., and Tajitsu, A. (2003). Analysis of Internal Motions in the Halo Planetary Nebula H4-1. *PASP*, 115:67.

Pagomenos, G. J. S., Bernard-Salas, J., and Pottasch, S. R. (2018). Neon, sulphur and argon abundances of planetary nebulae in the sub-solar metallicity Galactic anti-centre. *A&A*, 615:A29.

Pagomenos, G. J. S., Bernard-Salas, J., and Sloan, G. C. (2017). Dust & Abundances of Metal-Poor Planetary Nebulae in the Galactic Anti-Centre. In Liu, X., Stanghellini, L., and Karakas, A., editors, *Planetary Nebulae: Multi-Wavelength Probes of Stellar and Galactic Evolution*, volume 323 of *IAU Symposium*, page 341.

Peña, M., Ruíz, M. T., Maza, J., and González, L. E. (1989). A new halo planetary nebula. *RMxAA*, 17:25.

Pease, F. G. (1928). A Planetary Nebula in the Globular Cluster Messier 15. *PASP*, 40:342.

Peeters, E. (2002). *Polycyclic Aromatic Hydrocarbons and Dust in Regions of Massive Star Formation*. PhD thesis, University of Groningen, The Netherlands.

Peeters, E., Bauschlicher, Jr., C. W., Allamandola, L. J., Tielens, A. G. G. M., Ricca, A., and Wolfire, M. G. (2017). The PAH Emission Characteristics of the Reflection Nebula NGC 2023. *ApJ*, 836:198.

Peeters, E., Hony, S., Van Kerckhoven, C., Tielens, A. G. G. M., Allamandola, L. J., Hudgins, D. M., and Bauschlicher, C. W. (2002). The rich 6 to 9 μm spectrum of interstellar PAHs. *A&A*, 390:1089.

Peimbert, M. (1978). Chemical abundances in planetary nebulae. In *IAU Symp. 76, held at Cornell University, Ithaca, New York, USA, june 6-10, 1977. Planetary nebulae. Observations and theory. Ed by Y. Terzian., 215-224 (1978)*, volume 76, page 215.

Peimbert, M. and Costero, R. (1969). Chemical Abundances in Galactic HII Regions. *Boletin de los Observatorios Tonantzintla y Tacubaya*, 5:3.

Peimbert, M., Luridiana, V., and Torres-Peimbert, S. (1995). Temperature fluctuations and the chemical composition of planetary nebulae of Type I. *RMxAA*, 31:147.

Pelan, J. and Berrington, K. A. (1995). Atomic data from the IRON Project. IX. Electron excitation of the $^2P^o_{3/2}$–$^2P_{1/2}$ fine-structure transition in chlorine-like ions, from AR II to NI XII. *A&AS*, 110:209.

Pena, M., Torres-Peimbert, S., and Ruiz, M. T. (1992). Ultraviolet and optical spectra of central stars of halo planetary nebulae. *A&A*, 265:757.

Perea-Calderón, J. V., García-Hernández, D. A., García-Lario, P., Szczerba, R., and Bobrowsky, M. (2009). The mixed chemistry phenomenon in Galactic Bulge PNe. *A&A*, 495:L5.

Pereira, C.-B. and Miranda, L.-F. (2007). Identification of PN G232.0+05.7 as a new halo planetary nebula and of IRAS 19336-0400 as a new type III planetary nebula. *A&A*, 467:1249.

Pereyra, M., López, J. A., and Richer, M. G. (2016). The Kinematics of the Nebular Shells Around Low Mass Progenitors of PNe with Low Metallicity. *AJ*, 151:53.

Perinotto, M. and Corradi, R. L. M. (1998). The chemical structure of bipolar planetary nebulae. II. 13 objects. *A&A*, 332:721.

Phillips, J. P. and Márquez-Lugo, R. A. (2011). Mid- and Far-Infrared Photometry of Galactic Planetary Nebulae with the AKARI All-Sky Survey. *RMxAA*, 47:83.

Pietrzyński, G., Graczyk, D., Gieren, W., Thompson, I. B., Pilecki, B., Udalski, A., Soszyński, I., Kozłowski, S., Konorski, P., Suchomska, K., Bono, G., Moroni, P. G. P., Villanova, S., Nardetto, N., Bresolin, F., Kudritzki, R. P., Storm, J., Gallenne, A., Smolec, R., Minniti, D., Kubiak, M., Szymański, M. K., Poleski, R., Wyrzykowski, Ł., Ulaczyk, K., Pietrukowicz, P., Górski, M., and Karczmarek, P. (2013). An eclipsing-binary distance to the Large Magellanic Cloud accurate to two per cent. *Nature*, 495:76.

Pignatari, M., Herwig, F., Hirschi, R., Bennett, M., Rockefeller, G., Fryer, C., Timmes, F. X., Ritter, C., Heger, A., Jones, S., Battino, U., Dotter, A., Trappitsch, R., Diehl, S., Frischknecht, U., Hungerford, A., Magkotsios, G., Travaglio, C., and Young, P. (2016). NuGrid Stellar Data Set. I.Stellar Yields from H to Bi for Stars with Metallicities Z = 0.02 and Z = 0.01. *ApJS*, 225:24.

Pilbratt, G. L., Riedinger, J. R., Passvogel, T., Crone, G., Doyle, D., Gageur, U., Heras, A. M., Jewell, C., Metcalfe, L., Ott, S., and Schmidt, M. (2010). Herschel Space Observatory. An ESA facility for far-infrared and submillimetre astronomy. *A&A*, 518:L1.

Pottasch, S. R. and Beintema, D. A. (1999). The ISO spectrum of the planetary nebula NGC 6302. II. Nebular abundances. *A&A*, 347:975.

Pottasch, S. R., Beintema, D. A., Bernard Salas, J., Koornneef, J., and Feibelman, W. A. (2002). Abundances of Planetary Nebula NGC 5315. *A&A*, 393:285.

Pottasch, S. R. and Bernard-Salas, J. (2006). Planetary nebulae abundances and stellar evolution. *A&A*, 457:189.

Pottasch, S. R. and Bernard-Salas, J. (2010). Planetary nebulae abundances and stellar evolution II. *A&A*, 517:A95.

Pottasch, S. R. and Bernard-Salas, J. (2015). Abundances of planetary nebulae in the Galactic bulge. *A&A*, 583:A71.

Pottasch, S. R. and Surendiranath, R. (2005). Abundances in planetary nebulae: NGC 6886. *A&A*, 432:139.

Pottasch, S. R., Surendiranath, R., and Bernard-Salas, J. (2011). Abundances in planetary nebulae: NGC 1535, NGC 6629, He2-108, and Tc1. *A&A*, 531:A23.

Predehl, P. and Schmitt, J. H. M. M. (1995). X-raying the interstellar medium: ROSAT observations of dust scattering halos. *A&A*, 293:889.

Priestley, W., Ruffert, M., and Salaris, M. (2011). On the evolution of intracluster gas within Galactic globular clusters. *MNRAS*, 411:1935.

Ramsbottom, C. A. and Bell, K. L. (1998). Effective Collision Strengths for Electron-Impact Excitation of Ne IV. *Atomic Data and Nuclear Data Tables*, 68:203.

Rauch, T., Heber, U., and Werner, K. (2002). Spectral analysis of the sdO K 648, the exciting star of the planetary nebula Ps 1 in the globular cluster M 15 (NGC 7078). *A&A*, 381:1007.

Ricca, A., Bauschlicher, Jr., C. W., Boersma, C., Tielens, A. G. G. M., and Allamandola, L. J. (2012). The Infrared Spectroscopy of Compact Polycyclic Aromatic Hydrocarbons Containing up to 384 Carbons. *ApJ*, 754:75.

Ricca, A., Bauschlicher, Charles W., J., Roser, J. E., and Peeters, E. (2018). Polycyclic Aromatic Hydrocarbons with Straight Edges and the 7.6/6.2 and 8.6/6.2 Intensity Ratios in Reflection Nebulae. *ApJ*, 854:115.

Rieke, G. H., Young, E. T., Engelbracht, C. W., Kelly, D. M., Low, F. J., Haller, E. E., Beeman, J. W., Gordon, K. D., Stansberry, J. A., Misselt, K. A., Cadien, J., Morrison, J. E., Rivlis, G., Latter, W. B., Noriega-Crespo, A., Padgett, D. L., Stapelfeldt, K. R., Hines, D. C., Egami, E., Muzerolle, J., Alonso-Herrero, A., Blaylock, M., Dole, H., Hinz, J. L., Le Floc'h, E., Papovich, C., Pérez-González, P. G., Smith, P. S., Su, K. Y. L., Bennett, L., Frayer, D. T., Henderson, D., Lu, N., Masci, F., Pesenson, M., Rebull, L., Rho, J., Keene, J., Stolovy, S., Wachter, S., Wheaton, W., Werner, M. W., and Richards, P. L. (2004). The Multiband Imaging Photometer for Spitzer (MIPS). *ApJS*, 154:25.

Roberts, K. R. G., Smith, K. T., and Sarre, P. J. (2012). Detection of C_{60} in embedded young stellar objects, a Herbig Ae/Be star and an unusual post-asymptotic giant branch star. *MNRAS*, 421:3277.

Robin, A. C., Reylé, C., Derrière, S., and Picaud, S. (2003). A synthetic view on structure and evolution of the Milky Way. *A&A*, 409:523.

Rolleston, W. R. J., Smartt, S. J., Dufton, P. L., and Ryans, R. S. I. (2000). The Galactic metallicity gradient. *A&A*, 363:537.

Röllig, M., Abel, N. P., Bell, T., Bensch, F., Black, J., Ferland, G. J., Jonkheid, B., Kamp, I., Kaufman, M. J., Le Bourlot, J., Le Petit, F., Meijerink, R., Morata, O., Ossenkopf, V., Roueff, E., Shaw, G., Spaans, M., Sternberg, A., Stutzki, J., Thi, W. F., van Dishoeck, E. F., van Hoof, P. A. M., Viti, S., and Wolfire, M. G. (2007). A photon dominated region code comparison study. *A&A*, 467:187.

Rubin, R. H., Simpson, J. P., Erickson, E. F., and Haas, M. R. (1988). Determination of N/O from far-infrared line observations of Galactic H II regions. *ApJ*, 327:377.

Ryan, R. S. and Norton, A. J. (2010). *Stellar Evolution and Nucleosynthesis*. Cambridge University Press.

Sabin, L., Zijlstra, A. A., and Greaves, J. S. (2007). Magnetic fields in planetary nebulae and post-AGB nebulae. *MNRAS*, 376:378.

Saraph, H. E. and Storey, P. J. (1999). Atomic data from the IRON Project. XXX. Collision data for the $^2P^o_{1/2}$ - $^2P^o_{3/2}$ fine-structure lines of P III, S IV and CL V. *A&AS*, 134:369.

Savage, B. D. and Mathis, J. S. (1979). Observed properties of interstellar dust. *ARA&A*, 17:73.

Schneider, S. E., Terzian, Y., Purgathofer, A., and Perinotto, M. (1983). Radial velocities of planetary nebulae. *ApJS*, 52:399.

Schönberner, D., Jacob, R., Lehmann, H., Hildebrandt, G., Steffen, M., Zwanzig, A., Sandin, C., and Corradi, R. L. M. (2014). A hydrodynamical study of multiple-shell planetary nebulae. III. Expansion properties and internal kinematics: Theory versus observation. *Astronomische Nachrichten*, 335:378–408.

Scott, A. and Duley, W. W. (1996). The Decomposition of Hydrogenated Amorphous Carbon: A Connection with Polycyclic Aromatic Hydrocarbon Molecules. *ApJ*, 472:L123.

Sellgren, K., Werner, M. W., Ingalls, J. G., Smith, J. D. T., Carleton, T. M., and Joblin, C. (2010). C_{60} in Reflection Nebulae. *ApJL*, 722:L54.

Sellwood, J. A. and Binney, J. J. (2002). Radial mixing in galactic discs. *MNRAS*, 336:785.

Seok, J. Y. and Li, A. (2017). Polycyclic Aromatic Hydrocarbons in Protoplanetary Disks around Herbig Ae/Be and T Tauri Stars. *ApJ*, 835:291.

Seon, K.-I. and Draine, B. T. (2016). Radiative Transfer Model of Dust Attenuation Curves in Clumpy, Galactic Environments. *ApJ*, 833:201.

Shannon, M. J., Stock, D. J., and Peeters, E. (2015). Probing the Ionization States of Polycyclic Aromatic Hydrocarbons via the 15-20 μm Emission Bands. *ApJ*, 811:153.

Shannon, M. J., Stock, D. J., and Peeters, E. (2016). Interpreting the Subtle Spectral Variations of the 11.2 and 12.7 μm Polycyclic Aromatic Hydrocarbon Bands. *ApJ*, 824:111.

Sharpee, B., Zhang, Y., Williams, R., Pellegrini, E., Cavagnolo, K., Baldwin, J. A., Phillips, M., and Liu, X.-W. (2007). s-Process Abundances in Planetary Nebulae. *ApJ*, 659:1265.

Shaver, P. A., McGee, R. X., Newton, L. M., Danks, A. C., and Pottasch, S. R. (1983). The galactic abundance gradient. *MNRAS*, 204:53.

Shaw, R. A., Lee, T.-H., Stanghellini, L., Davies, J. E., García-Hernández, D. A., García-Lario, P., Perea-Calderón, J.-V., Villaver, E., Manchado, A., Palen, S., and Balick, B. (2012). A detailed look at chemical abundances in the Magellanic Clouds. In *IAU Symposium*, volume 283 of *IAU Symposium*, page 502.

Shingles, L. J. and Karakas, A. I. (2013). Is the sulphur anomaly in planetary nebulae caused by the s-process? *MNRAS*, 431:2861.

Shu, F. H. (1982). *The Physical Universe*. University Science Books, 1st edition.

Siegel, M. H., Dotter, A., Majewski, S. R., Sarajedini, A., Chaboyer, B., Nidever, D. L., Anderson, J., Marín-Franch, A., Rosenberg, A., Bedin, L. R., Aparicio, A., King, I., Piotto, G., and Reid, I. N. (2007). The ACS Survey of Galactic Globular Clusters: M54 and Young Populations in the Sagittarius Dwarf Spheroidal Galaxy. *ApJ*, 667:L57.

Simpson, J. P. (1975). Infrared forbidden lines in H II regions and planetary nebulae. *A&A*, 39:43.

Sloan, G. C., Jura, M., Duley, W. W., Kraemer, K. E., Bernard-Salas, J., Forrest, W. J., Sargent, B., Li, A., Barry, D. J., Bohac, C. J., Watson, D. M., and Houck, J. R. (2007). The Unusual Hydrocarbon Emission from the Early Carbon Star HD 100764: The Connection between Aromatics and Aliphatics. *ApJ*, 664:1144.

Sloan, G. C., Kraemer, K. E., Matsuura, M., Wood, P. R., Price, S. D., and Egan, M. P. (2006). Mid-Infrared Spectroscopy of Carbon Stars in the Small Magellanic Cloud. *ApJ*, 645:1118.

Sloan, G. C., Lagadec, E., Zijlstra, A. A., Kraemer, K. E., Weis, A. P., Matsuura, M., Volk, K., Peeters, E., Duley, W. W., Cami, J., Bernard-Salas, J., Kemper, F., and Sahai, R. (2014). Carbon-rich Dust Past the Asymptotic Giant Branch: Aliphatics, Aromatics, and Fullerenes in the Magellanic Clouds. *ApJ*, 791:28.

Smartt, S. J. (2000). Abundance Gradients along the Galactic Disk. In Matteucci, F. and Giovannelli, F., editors, *Astrophysics and Space Science Library*, volume 255 of *Astrophysics and Space Science Library*, page 323.

Snow, T. P. and Witt, A. N. (1996). Interstellar Depletions Updated: Where All the Atoms Went. *ApJL*, 468:L65.

Soker, N. (2002). Spherical planetary nebulae. *A&A*, 386:885.

Soker, N. (2005). Can We Ignore Magnetic Fields in Studies of PN Formation, Shaping and Interaction with the ISM? In *PLANETARY NEBULAE AS ASTRONOMICAL TOOLS: International Conference on Planetary Nebulae as Astronomical Tools. AIP Conference Proceedings*, volume 804, page 89.

Soker, N. (2006). Why Magnetic Fields Cannot Be the Main Agent Shaping Planetary Nebulae. *PASP*, 118:260.

Soker, N. (2016). Planetary nebula progenitors that swallow binary systems. *MNRAS*, 455:1584.

Soker, N. and Rappaport, S. (2000). The Formation of Very Narrow Waist Bipolar Planetary Nebulae. *ApJ*, 538:241.

Soker, N., Zucker, D. B., and Balick, B. (1992). The Density Profile of the Elliptical Planetary Nebula NGC 3242. *AJ*, 104:2151.

Sommer-Larsen, J., Götz, M., and Portinari, L. (2003). Galaxy Formation: Cold Dark Matter, Feedback, and the Hubble Sequence. *ApJ*, 596:47.

Spieler, S., Kuhn, M., Postler, J., Simpson, M., Wester, R., Scheier, P., Ubachs, W., Bacalla, X., Bouwman, J., and Linnartz, H. (2017). C_{60}^+ and the Diffuse Interstellar Bands: An Independent Laboratory Check. *ApJ*, 846:168.

Spoon, H. W. W., Marshall, J. A., Houck, J. R., Elitzur, M., Hao, L., Armus, L., Brandl, B. R., and Charmandaris, V. (2007). Mid-Infrared Galaxy Classification Based on Silicate Obscuration and PAH Equivalent Width. *ApJL*, 654:L49.

Squires, G. K., Carey, S., Helou, G., Hurt, R., Rebull, L., Soifer, T., and Storrie-Lombardi, L. (2007). Hot Science With a "Warm" Telescope - Archival Research Opportunities in the Spitzer "Warm" Mission. In *American Astronomical Society Meeting Abstracts*, volume 39 of *Bulletin of the American Astronomical Society*, page 808.

Stacey, G. J., Charmandaris, V., Boulanger, F., Wu, Y., Combes, F., Higdon, S. J. U., Smith, J. D. T., and Nikola, T. (2010). The Energetics of Molecular Gas in NGC 891 from H_2 and Far-infrared Spectroscopy. *ApJ*, 721:59.

Stanghellini, L., Corradi, R. L. M., and Schwarz, H. E. (1993). The correlations between planetary nebula morphology and central star evolution. *A&A*, 279:521.

Stanghellini, L., García-Hernández, D. A., García-Lario, P., Davies, J. E., Shaw, R. A., Villaver, E., Manchado, A., and Perea-Calderón, J. V. (2012). The Nature of Dust in Compact Galactic Planetary Nebulae from Spitzer Spectra. *ApJ*, 753:172.

Stanghellini, L., García-Lario, P., García-Hernández, D. A., Perea-Calderón, J. V., Davies, J. E., Manchado, A., Villaver, E., and Shaw, R. A. (2007). Spitzer Infrared Spectrograph Observations of Magellanic Cloud Planetary Nebulae: The Nature of Dust in Low-Metallicity Circumstellar Ejecta. *ApJ*, 671:1669.

Stanghellini, L. and Haywood, M. (2010). The Galactic Structure and Chemical Evolution Traced by the Population of Planetary Nebulae. *ApJ*, 714:1096.

Stanghellini, L., Shaw, R. A., and Villaver, E. (2016). Compact Galactic Planetary Nebulae: An HST/WFC3 Morphological Catalog, and a Study of Their Role in the Galaxy. *ApJ*, 830:33.

Stasińska, G. (1978). Empirical methods for determining elemental abundances tested on model H II regions. *A&A*, 66:257.

Stasińska, G., Morisset, C., Tovmassian, G., Rauch, T., Richer, M. G., Peña, M., Szczerba, R., Decressin, T., Charbonnel, C., Yungelson, L., Napiwotzki, R., Simón-Díaz, S., and Jamet, L. (2010). The chemical composition of TS 01, the most oxygen-deficient planetary nebula. AGB nucleosynthesis in a metal-poor binary star. *A&A*, 511:A44.

Sterling, N. C. and Dinerstein, H. L. (2008). The Abundances of Light Neutron-Capture Elements in Planetary Nebulae. II. s-Process Enrichments and Interpretation. *ApJS*, 174:158.

Sterling, N. C., Porter, R. L., and Dinerstein, H. L. (2015). The Abundances of Light Neutron-capture Elements in Planetary Nebulae. III. The Impact of New Atomic Data on Nebular Selenium and Krypton Abundance Determinations. *ApJS*, 218:25.

Stock, D. J. and Peeters, E. (2017). Polycyclic Aromatic Hydrocarbon Emission in Spitzer/IRS Maps. II. A Direct Link between Band Profiles and the Radiation Field Strength. *ApJ*, 837:129.

Strader, J., Chomiuk, L., Maccarone, T. J., Miller-Jones, J. C. A., and Seth, A. C. (2012). Two stellar-mass black holes in the globular cluster M22. *Nature*, 490:71.

Straniero, O., Chieffi, A., Limongi, M., Busso, M., Gallino, R., and Arlandini, C. (1997). Evolution and Nucleosynthesis in Low-Mass Asymptotic Giant Branch Stars. I. Formation of Population I Carbon Stars. *ApJ*, 478:332.

Sturm, E., Bauer, O. H., Brauer, J., Buckley, M., Harwood, A., Helou, G., Khan, I., Li, J., Lord, S., Lutz, D., Mazzarella, J., Morris, P. W., Narron, B., Sidher, S., Swinyard, B., Unger, S. J., Verstraete, L., Vivares, F., Wieprecht, E., and Wiezorrek, E. (1998). The ISO Spectral Analysis Package ISAP. In Albrecht, R., Hook, R. N., and Bushouse, H. A., editors, *Astronomical Data Analysis Software and Systems VII*, volume 145 of *Astronomical Society of the Pacific Conference Series*, page 161.

Surendiranath, R., Pottasch, S. R., and García-Lario, P. (2004). Abundances in planetary nebulae: Me 2-1. *A&A*, 421:1051.

Tajitsu, A. and Otsuka, M. (2004). The Multiple Outflows in the Galactic Halo PN H4-1. In *Asymmetrical Planetary Nebulae III: Winds, Structure and the Thunderbird, Edited by Margaret Meixner, Joel H. Kastner, Bruce Balick and Noam Soker. ASP Conference Proceedings*, volume 313, page 202.

Tamura, S. and Shaw, R. A. (1987). Spectroscopic analyses of the stellar planetary nebulae K3-66, K3-67, and K3-71. *PASP*, 99:1264.

Tayler, R. J. and Wood, P. R. (1975). The gas and horizontal branch star content of globular clusters. *MNRAS*, 171:467.

Tennyson, J. (2011). *Astronomical Spectroscopy*. World Scientific Publishing Co. Pte. Ltd., 2nd edition.

Thuan, T. X., Izotov, Y. I., and Lipovetsky, V. A. (1995). Heavy element abundances in a new sample of low-metallicity blue compact galaxies. *ApJ*, 445:108.

Tielens, A. G. G. M. (2005). *The Physics and Chemistry of the Interstellar Medium*. Cambridge University Press, 1st edition.

Tielens, A. G. G. M. (2014). Diffuse Interstellar Bands: The Way Forward. In *The Diffuse Interstellar Bands*, volume 297, page 399.

Tielens, A. G. G. M. and Hollenbach, D. (1985). Photodissociation regions. I - Basic model. *ApJ*, 291:722.

Torres-Peimbert, S. and Peimbert, M. (1997). Planetary Nebulae of type I revisited (Invited Review). In *Planetary nebulae, Proceedings of the 180th Symposium of the International Astronomical Union (IAU), edited by H. J. Habing and H. J. G. L. M. Lamers.*, volume 180, page 175.

Torres-Peimbert, S., Peimbert, M., and Pena, M. (1990). Planetary nebulae with a high degree of ionization : NGC 2242 and NGC 4361. *A&A*, 233:540.

Totten, E. J. and Irwin, M. J. (1998). The APM survey for cool carbon stars in the Galactic halo - I. *MNRAS*, 294:1.

Tovmassian, G. H., Stasińska, G., Chavushyan, V. H., Zharikov, S. V., Gutierrez, C., and Prada, F. (2001). SBS 1150+599A: An extremely oxygen-poor planetary nebula in the Galactic halo? *A&A*, 370:456.

Treffers, R. and Cohen, M. (1974). High-resolution spectra of cool stars in the 10- and 20-micron regions. *ApJ*, 188:545.

Trumpler, R. J. (1930). Absorption of Light in the Galactic System. *PASP*, 42:214.

Tsamis, Y. G., Flores-Fajardo, N., Henney, W. J., Walsh, J. R., and Mesa-Delgado, A. (2013). Chemical abundances in Orion protoplanetary discs: integral field spectroscopy and photoevaporation models of HST 10. *MNRAS*, 430:3406.

Tumlinson, J. (2010). Chemical Evolution in Hierarchical Models of Cosmic Structure. II. The Formation of the Milky Way Stellar Halo and the Distribution of the Oldest Stars. *ApJ*, 708:1398.

Tylenda, R., Siódmiak, N., Górny, S. K., Corradi, R. L. M., and Schwarz, H. E. (2003). Angular dimensions of planetary nebulae. *A&A*, 405:627.

Ueta, T., Ladjal, D., Exter, K. M., Otsuka, M., Szczerba, R., Siódmiak, N., Aleman, I., van Hoof, P. A. M., Kastner, J. H., Montez, R., McDonald, I., Wittkowski, M., Sandin, C., Ramstedt, S., De Marco, O., Villaver, E., Chu, Y.-H., Vlemmings, W., Izumiura, H., Sahai, R., Lopez, J. A., Balick, B., Zijlstra, A., Tielens, A. G. G. M., Rattray, R. E., Behar, E., Blackman, E. G., Hebden, K., Hora, J. L., Murakawa, K., Nordhaus, J., Nordon, R., and Yamamura, I. (2014). The Herschel Planetary Nebula Survey (HerPlaNS). I. Data overview and analysis demonstration with NGC 6781. *A&A*, 565:A36.

van Dishoeck, E. F. (2017). Astrochemistry: overview and challenges. *ArXiv e-prints*, page arXiv:1710.05940.

van Dishoeck, E. F. and Black, J. H. (1988). The Photodissociation and Chemistry of Interstellar CO. *ApJ*, 334:771.

van Loon, J. T., Groenewegen, M. A. T., de Koter, A., Trams, N. R., Waters, L. B. F. M., Zijlstra, A. A., Whitelock, P. A., and Loup, C. (1999). Mass-loss rates and luminosity functions of dust-enshrouded AGB stars and red supergiants in the LMC. *A&A*, 351:559.

van Loon, J. T., Marshall, J. R., Matsuura, M., and Zijlstra, A. A. (2003). The superwind mass-loss rate of the metal-poor carbon star LI-LMC 1813 in the LMC cluster KMHK 1603. *MNRAS*, 341:1205.

van Marle, A. J., Cox, N. L. J., and Decin, L. (2014). Eyes in the sky. Interactions between asymptotic giant branch star winds and the interstellar magnetic field. *A&A*, 570:A131.

Vasta, M. (2010). *Modelling ionised and photodissociated regions*. PhD thesis, University of London, University College London (United Kingdom).

Venemans, B. P., McMahon, R. G., Walter, F., Decarli, R., Cox, P., Neri, R., Hewett, P., Mortlock, D. J., Simpson, C., and Warren, S. J. (2012). Detection of Atomic Carbon [C II] 158 μm and Dust Emission from a z = 7.1 Quasar Host Galaxy. *ApJL*, 751:L25.

Ventura, P., Stanghellini, L., Di Criscienzo, M., García-Hernández, D. A., and Dell'Agli, F. (2016). Planetary nebulae in the Small Magellanic Cloud. *MNRAS*, 460:3940.

Vera-Ciro, C., D'Onghia, E., Navarro, J., and Abadi, M. (2014). The Effect of Radial Migration on Galactic Disks. *ApJ*, 794:173.

Verhoelst, T., van der Zypen, N., Hony, S., Decin, L., Cami, J., and Eriksson, K. (2009). The dust condensation sequence in red supergiant stars. *A&A*, 498:127.

Vermeij, R. and van der Hulst, J. M. (2002). The physical structure of Magellanic Cloud H II regions. II. Elemental abundances. *A&A*, 391:1081.

Volk, K., Hrivnak, B. J., Matsuura, M., Bernard-Salas, J., Szczerba, R., Sloan, G. C., Kraemer, K. E., van Loon, J. T., Kemper, F., Woods, P. M., Zijlstra, A. A., Sahai, R., Meixner, M., Gordon, K. D., Gruendl, R. A., Tielens, A. G. G. M., Indebetouw, R., and Marengo, M. (2011). Discovery and Analysis of 21 μm Feature Sources in the Magellanic Clouds. *ApJ*, 735:127.

Walker, G. A. H., Bohlender, D. A., Maier, J. P., and Campbell, E. K. (2015). Identification of More Interstellar C_{60}^+ Bands. *ApJL*, 812:L8.

Walker, G. A. H., Campbell, E. K., Maier, J. P., and Bohlender, D. (2017). The 9577 and 9632 Å Diffuse Interstellar Bands: C_{60}^+ as a Carrier. *ApJ*, 843:56.

Walsh, J. R., Dudziak, G., Minniti, D., and Zijlstra, A. A. (1997). Chemical Abundances of Planetary Nebulae in the Sagittarius Dwarf Elliptical Galaxy. *ApJ*, 487:651.

Wang, W. and Liu, X. W. (2008). Are oxygen and neon enriched in PNe and is the current solar Ne/O abundance ratio underestimated? *MNRAS*, 389:L33.

Wannier, P. and Wrixon, G. T. (1972). An Unusual High-Velocity Hydrogen Feature. *ApJ*, 173:L119.

Waters, L. B. F. M., Beintema, D. A., Zijlstra, A. A., de Koter, A., Molster, F. J., Bouwman, J., de Jong, T., Pottasch, S. R., and de Graauw, T. (1998). Crystalline silicates in planetary nebulae with [WC] central stars. *A&A*, 331:L61.

Werner, M. W., Roellig, T. L., Low, F. J., Rieke, G. H., Rieke, M., Hoffmann, W. F., Young, E., Houck, J. R., Brandl, B., Fazio, G. G., Hora, J. L., Gehrz, R. D., Helou, G., Soifer, B. T., Stauffer, J., Keene, J., Eisenhardt, P., Gallagher, D., Gautier, T. N., Irace, W., Lawrence, C. R., Simmons, L., Van Cleve, J. E., Jura, M., Wright, E. L., and Cruikshank, D. P. (2004). The Spitzer Space Telescope Mission. *ApJS*, 154:1.

Wheeler, J. C., Sneden, C., and Truran, J. W., J. (1989). Abundance ratios as a function of metallicity. *ARA&A*, 27:279.

Wilms, J., Allen, A., and McCray, R. (2000). On the Absorption of X-Rays in the Interstellar Medium. *ApJ*, 542:914.

Witteborn, F. C. and Young, L. S. (1976). Spacelab infrared telescope facility (SIRTF). *Journal of Spacecraft and Rockets*, 13:667.

Zhang, H. L., Graziani, M., and Pradhan, A. K. (1994). Atomic data from the IRON project. 3: Rate coefficients for electron impact excitation of boron-like ions: Ne VI, Mg VIII, Al IX, Si X, S XII, Ar XIV, Ca XVI and Fe XXII. *A&A*, 283:319.

Zhang, K., Jiang, B. W., and Li, A. (2009). On Magnesium Sulfide as the Carrier of the 30 μm Emission Feature in Evolved Stars. *ApJ*, 702:680.

Zhen, J., Castellanos, P., Paardekooper, D. M., Linnartz, H., and Tielens, A. G. G. M. (2014). Laboratory Formation of Fullerenes from PAHs: Top-down Interstellar Chemistry. *ApJ*, 797:L30.

Zhukovska, S. and Henning, T. (2013). Dust input from AGB stars in the Large Magellanic Cloud. *A&A*, 555:A99.

Zijlstra, A. A. (2002). Hydrogen-poor planetary nebulae. *Ap&SS*, 279:171.

Zijlstra, A. A., Gaylard, M. J., te Lintel Hekkert, P., Menzies, J., Nyman, L.-A., and Schwarz, H. E. (1991). IRAS 07027 - 7934 - The link between OH/IR stars and carbon-rich planetary nebulae. *A&A*, 243:L9.

Zijlstra, A. A., Gesicki, K., Walsh, J. R., Péquignot, D., van Hoof, P. A. M., and Minniti, D. (2006). The planetary nebula population of the Sagittarius dwarf spheroidal galaxy. *MNRAS*, 369:875.